

Dissertation  
zur Erlangung des Doktorgrades  
der Naturwissenschaften

# Investigation of Novel Condensed Matter Systems by Means of Fluctuation Spectroscopy



vorgelegt beim Fachbereich Physik  
der Goethe-Universität Frankfurt am Main

von

Martin Lonsky  
geboren in Hanau

Frankfurt am Main, 2018  
(D30)

Vom Fachbereich Physik der Goethe-Universität Frankfurt am Main als Dissertation angenommen.

**Dekan:**

Prof. Dr. Owe Philipsen

**Gutachter:**

Prof. Dr. Jens Müller

Prof. Dr. Cornelius Krellner

**Datum der Disputation:**

05.07.2018

## Abstract

This thesis is concerned with systematic investigations of electronic noise in novel condensed matter systems. Although fluctuations are frequently considered a nuisance, that is, a disturbance limiting the accuracy of scientific measurements, in many cases they can reveal fundamental information about the inherent system dynamics. During the past decades, the study of electronic fluctuations has evolved into an indispensable tool in condensed matter physics.

The focus of the present work lies both in a further development of the fluctuation spectroscopy technique and in the study of materials of current interest. In particular, a comprehensive study of the charge carrier dynamics in the archetypal diluted magnetic semiconductors (Ga,Mn)As and (Ga,Mn)P was performed. In spite of extensive research work carried out during the last years, there still exists no theoretical consensus on the precise mechanism of ferromagnetic order and the electronic structure in these materials. Moreover, disorder and correlation effects complicate the understanding of these compounds. Fluctuation spectroscopy experiments presented in this work provide strong evidence that a percolation transition is observed in samples with localized charge carriers, since the normalized resistance noise magnitude displays a significant enhancement around the Curie temperature. In addition, this quantity exhibits a power law scaling behavior as a function of the resistance, which is in good agreement with theoretical models of percolating systems. By contrast, it was found that the resistance noise in metallic samples is mainly dominated by the physics of defects such as manganese interstitials and arsenic antisites.

Furthermore, first noise studies were carried out on hafnia- and yttria-based resistive random-access memories. In these memristor devices, the rupture and re-formation of oxygen deficient conducting filaments caused by the electric field and Joule heating driven motion of mobile anions lead to an unusual resistance switching behavior. For the first time, comparative noise measurements on oxygen deficient and stoichiometric hafnium oxide devices, as well as on novel yttrium oxide based devices were performed in this work.

Finally, new strategies for noise measurements of highly insulating and extremely low-resistive samples were developed and realized. In detail, an experimental setup for the measurements of dielectric polarization fluctuations in insulating systems was designed and successfully tested. Here, the polarization noise of a sample is measured as current or voltage fluctuations produced within a capacitance cell. The study of dielectric polarization noise allows for conclusions to be drawn regarding equilibrium structural dynamics in insulators such as relaxor ferroelectrics. On the other hand, as successfully demonstrated for a heavy-fermion compound, focused ion beam etching enables to introduce a meander-shaped geometry in single crystal platelets, in order to strongly enhance the sample resistance and thus make resistance noise measurements possible. First results indicate a connection of the noise properties with the Kondo effect in the investigated material.



# Contents

<b>1</b>	<b>Introduction</b>	<b>1</b>
<b>2</b>	<b>Electronic Noise in Solids</b>	<b>5</b>
2.1	Fluctuations in the time domain . . . . .	5
2.2	Autocorrelation function . . . . .	7
2.3	Power spectral density . . . . .	9
2.4	Types of noise . . . . .	11
2.4.1	Thermal noise . . . . .	11
2.4.2	Shot noise . . . . .	13
2.4.3	Generation-recombination noise . . . . .	13
2.4.4	1/f noise . . . . .	15
2.5	Second spectrum . . . . .	24
2.6	Electronic noise in percolating systems . . . . .	25
2.6.1	Percolation in random resistor networks . . . . .	26
2.6.2	Resistance fluctuations in lattice percolation systems . . . . .	27
2.6.3	Percolation of magnetic polarons in $\text{EuB}_6$ . . . . .	29
2.7	Dielectric polarization fluctuations . . . . .	31
2.7.1	Fluctuation-dissipation theorem . . . . .	31
2.7.2	Dielectric spectroscopy . . . . .	32
2.7.3	Dielectric polarization noise in selected model systems . . . . .	35
<b>3</b>	<b>Experimental Realization of Electronic Transport and Noise Measurements</b>	<b>41</b>
3.1	Cryostats and low-temperature physics . . . . .	41
3.2	Fluctuation spectroscopy . . . . .	44
3.2.1	Analysis of noise spectra . . . . .	44
3.2.2	Parasitic sources of noise . . . . .	47
3.2.3	Four-terminal DC and AC noise spectroscopy . . . . .	49
3.2.4	Five-terminal AC noise spectroscopy . . . . .	51
3.2.5	Two-terminal DC noise spectroscopy . . . . .	53
3.3	Dielectric polarization noise measurements . . . . .	54
3.3.1	Electrical circuit and operational amplifier . . . . .	54
3.3.2	Experimental realization in a closed cycle refrigerator . . . . .	57

3.3.3	First results on pressed pellet samples . . . . .	60
<b>4</b>	<b>Magnetic Semiconductors <math>\text{Ga}_{1-x}\text{Mn}_x\text{As}</math> and <math>\text{Ga}_{1-x}\text{Mn}_x\text{P}</math> Studied by Noise Spectroscopy</b>	<b>63</b>
4.1	Basic properties and fabrication . . . . .	64
4.1.1	Crystal structure and defects . . . . .	64
4.1.2	Low-temperature molecular beam epitaxy . . . . .	66
4.1.3	He-ion irradiation . . . . .	67
4.1.4	Ion implantation and pulsed laser melting . . . . .	68
4.2	Ferromagnetism and Electronic Transport in $\text{Ga}_{1-x}\text{Mn}_x\text{As}$ and $\text{Ga}_{1-x}\text{Mn}_x\text{P}$ . .	69
4.2.1	Theoretical models . . . . .	69
4.2.2	Percolation of bound magnetic polarons . . . . .	73
4.2.3	Metal-insulator transition and magnetotransport . . . . .	75
4.2.4	Related compounds . . . . .	78
4.3	Investigated samples . . . . .	78
4.4	Results . . . . .	83
4.4.1	Metallic $\text{Ga}_{1-x}\text{Mn}_x\text{As}$ films . . . . .	83
4.4.2	He-ion irradiated $\text{Ga}_{1-x}\text{Mn}_x\text{As}$ films . . . . .	94
4.4.3	Samples with localized charge carriers . . . . .	100
<b>5</b>	<b>Electronic noise measurements on <math>\text{HfO}_x</math> and <math>\text{Y}_2\text{O}_3</math> resistive switching memory devices</b>	<b>113</b>
5.1	Resistive switching memory devices . . . . .	113
5.2	Previous noise studies . . . . .	116
5.3	Experimental realization and results . . . . .	119
5.3.1	Experimental setup . . . . .	119
5.3.2	Measurements on hafnium oxide based RRAM devices . . . . .	121
5.3.3	First results on $\text{Y}_2\text{O}_3$ and outlook . . . . .	129
<b>6</b>	<b>Resistance Fluctuations in Strongly Correlated Electron Systems</b>	<b>135</b>
6.1	The heavy fermion compound $\text{YbRh}_2\text{Si}_2$ . . . . .	136
6.1.1	Introduction . . . . .	136
6.1.2	Kondo effect and crystal electric field . . . . .	137
6.1.3	Nature of quantum criticality in $\text{YbRh}_2\text{Si}_2$ . . . . .	139
6.2	Sample geometry optimization and preparation . . . . .	143
6.3	Fluctuation spectroscopy results . . . . .	148
<b>7</b>	<b>Conclusion and Outlook</b>	<b>155</b>
	<b>Deutsche Zusammenfassung</b>	<b>159</b>

<b>Bibliography</b>	<b>165</b>
<b>Acknowledgements</b>	<b>189</b>
<b>Curriculum Vitae</b>	<b>191</b>





# 1 Introduction

At first glance, electronic noise often appears to be a nuisance, that is, an unwanted signal mixed in with the desired signal, limiting the resolution of a scientific measurement. For instance, a major obstacle towards the discovery of the Higgs boson, an elementary particle in the Standard Model of particle physics, was to discern the particle signal from the background noise in the experimental data [1]. In general, it is true that voltage or current fluctuations impose practical limits on the performance of electronic circuits or measuring devices. Therefore, scientists across different research areas aim for a reduction of the different sources of electronic noise interfering with the measurement. In order to successfully improve the minimum detectable value of the desired quantity, however, it is crucial to understand the origin and the relevant mechanisms for the emergence of electronic noise.

However, researchers have learned to understand that noise is not always a nuisance. Instead, electronic fluctuations in materials and devices contain fundamental information about the system's inherent dynamics near equilibrium, which is not present in the mean quantity (e.g., the electric resistance) itself. In other words, electronic noise can be viewed as a true measurement signal. Although electronic noise is a random process, its statistical properties may be independent of time and thus a careful analysis can provide valuable information, as for example the microscopic behavior of charge carriers and their coupling to lattice defects, electronic traps and magnetic structures [2].

In condensed matter physics, noise (or fluctuation) spectroscopy constitutes a technique which has been successfully established during the past decades and applied to a wide range of materials such as metals, semiconductors, semimetals, low-dimensional materials, superconductors, and insulators. In general, electronic noise in the aforementioned materials may originate from various sources such as defect motion, capture and emission processes of charge carriers by electronic traps, magnetic domain or spin fluctuations, charge carriers crossing an energy barrier or current redistribution within inhomogeneous materials.

It is the focus of the present thesis work to further develop the noise spectroscopy technique, to address open questions in condensed matter physics where fluctuation spectroscopy studies may provide an instructive contribution, and to investigate novel materials and devices of current interest which, for a variety of reasons, have not yet been investigated in terms of their noise properties. These aspects are detailed in the following.

A central topic treated in this thesis is the systematic investigation of the archetypal diluted magnetic semiconductors (DMSs)  $\text{Ga}_{1-x}\text{Mn}_x\text{As}$  and  $\text{Ga}_{1-x}\text{Mn}_x\text{P}$  in order to contribute to

the current debate on the percolation of magnetic polarons and the origin of spontaneous magnetization in these materials. In detail, there exists no theoretical consensus on the precise mechanism of ferromagnetic order and the electronic structure in these compounds, since disorder and interactions appear to play an important role and thus complicate the understanding. As some theoretical studies suggest that the ferromagnetic transition in DMSs with localized charge carriers is a percolation transition [3, 4], it is desirable to find experimental evidence for this phenomenon and to study the correlation between magnetic percolation and electronic transport properties. In the past, fluctuation spectroscopy has been proven to be a well-suited technique to detect electronic phase separation and percolation transitions [5, 6]. The combination of noise measurements with (magneto-)resistance and anomalous Hall effect studies on more than ten thin-film specimens of  $\text{Ga}_{1-x}\text{Mn}_x\text{As}$  and  $\text{Ga}_{1-x}\text{Mn}_x\text{P}$  with different manganese contents  $x$  and other variations in terms of fabrication techniques and post-growth treatments provides a unique opportunity for new insights about charge carrier dynamics and the physics of crystalline defects.

Besides the aforementioned magnetic semiconductors, which have attracted considerable interest with regard to possible applications in the field of spintronics, a different approach towards novel data storage realizations is given by so-called resistive random-access memories (RRAMs), that is, metal-insulator-metal devices based on transition-metal oxides such as  $\text{HfO}_2$ , which exhibit an unusual resistive switching behavior due to oxygen deficient conducting filaments in the oxide layer. More precisely, the rupture and re-formation of these filaments caused by the electric field and Joule heating driven motion of mobile anions leads to the physical switching. In the scope of this thesis, the focus lies on the establishment of noise measurements on RRAM devices in collaboration with the group of Prof. Dr. L. Alff from the Technical University Darmstadt in order to study the fundamental transport and switching processes. It will be pointed out which technical difficulties such as proper electric grounding have to be overcome in order to realize fluctuation spectroscopy measurements on the experimental setup in Darmstadt. In particular, thanks to defect engineering by means of a sophisticated oxide molecular beam epitaxy setup in Darmstadt, a first comparative noise study between oxygen deficient  $\text{HfO}_x$  and stoichiometric  $\text{HfO}_2$  will be presented in this work. Finally, first investigations on  $\text{Y}_2\text{O}_3$  based RRAM devices will be discussed and the results will be compared with the ones on hafnium oxide.

Generally, the application of fluctuation spectroscopy to both extremely metallic and highly insulating materials is very challenging, in many cases to such an extent that is not possible to discern the intrinsic fluctuations from the background noise of the experimental setup. In this thesis, both extremes will be considered. Firstly, the establishment of dielectric polarization noise measurements on highly insulating materials in the laboratory of Prof. Dr. S. Nair at the Indian Institute of Science Education and Research (IISER) in Pune (India) will be presented. It will be shown that this technique is highly suitable to complement standard dielectric spectroscopy experiments and, in particular, to study the relationship between fluctuations

---

and dissipation in condensed matter systems. On the other hand, it will be discussed that tailoring the geometry of single crystal platelets by means of focused ion beam etching makes it possible to investigate the noise properties of low-resistive heavy fermion materials for the first time—here, we will consider the compound  $\text{YbRh}_2\text{Si}_2$ —and hence allows to study a variety of intriguing compounds such as Kondo systems. This new path has been taken in the course of an internal collaboration with the groups of Prof. Dr. C. Krellner and Prof. Dr. M. Huth at the Goethe University Frankfurt, and together with Dr. M. Brando and Dr. A. Steppke from the Max Planck Institute for Chemical Physics of Solids in Dresden.

This thesis is organized as follows. An introduction to electronic noise in condensed matter is given in chapter 2. Besides the basic theoretical framework required for the understanding and analysis of electronic noise in solids, the focus is also put on resistance fluctuations in percolating systems, and the theory of dielectric polarization fluctuations. The experimental realization of noise measurements is discussed in chapter 3. This part is of major importance, since the different material systems mentioned above require the use of disparate measurement techniques. In particular, the realization of dielectric polarization noise measurements is highlighted in the final part of this chapter. Chapter 4 is devoted to resistance noise measurements of the diluted magnetic semiconductors  $\text{Ga}_{1-x}\text{Mn}_x\text{As}$  and  $\text{Ga}_{1-x}\text{Mn}_x\text{P}$ , which is the most extensive research project presented in this thesis work. The application of fluctuation spectroscopy to RRAM devices based on hafnium oxide and yttrium oxide is presented in chapter 5. Chapter 6 includes a discussion of electronic noise in strongly correlated systems, particularly in the heavy fermion compound  $\text{YbRh}_2\text{Si}_2$ . Here, the emphasis lies on the optimization of the sample geometry and a first temperature-dependent noise dataset including approaches for its interpretation and proposals for future research. Finally, conclusions drawn from this thesis work are delineated in chapter 7 and an outlook to future projects is given.



## 2 Electronic Noise in Solids

Despite being frequently regarded as a nuisance even by many physicists, electronic noise can provide meaningful information about the low-frequency dynamics of electronic processes in condensed matter, such as trapping and detrapping of single electrons from a deep donor (DX-type) center in the semiconductor heterostructure  $\text{Al}_x\text{Ga}_{1-x}\text{As}/\text{GaAs}$  [7, 8], the critical slowing down of charge carrier dynamics at the Mott metal-insulator transition in organic charge transfer salts [9, 10] or a magnetically driven electronic phase separation in the ferromagnetic semimetal  $\text{EuB}_6$  [5]. In the present chapter, an introduction to electronic fluctuations with a focus on solid-state materials will be given. The chapter begins with a description of fluctuations in the time domain, which is followed by the definitions of the autocorrelation function and the noise power spectral density. Subsequently, the most common types of electronic noise will be presented. These introductory sections on noise and fluctuations are mainly based on the books by S. Kogan and R. Müller [11, 12], as well as on previous dissertations from the group of Prof. Dr. J. Müller in Frankfurt [13, 14]. Finally, in view of the work presented in the subsequent chapters, two specific topics will be discussed, namely electronic noise in percolating systems and dielectric polarization fluctuations. The former will be relevant for the investigation of the diluted magnetic semiconductors  $\text{Ga}_{1-x}\text{Mn}_x\text{As}$  and  $\text{Ga}_{1-x}\text{Mn}_x\text{P}$  by means of fluctuation spectroscopy as presented in chapter 4. Regarding dielectric polarization noise, in collaboration with the group of Prof. Dr. S. Nair from the Indian Institute of Science Education and Research (IISER) in Pune (India), an experimental setup has been designed and successfully tested. The experimental realization and first results will be presented in chapter 3.

### 2.1 Fluctuations in the time domain

In general, every measured physical quantity  $x$  is subject to random fluctuations and hence is a function of time  $t$ , even though in most cases a temporal mean  $\bar{x}$  can be defined. In condensed matter physics, this variable  $x$  may correspond to the time-dependent voltage drop across a sample, originating from resistance fluctuations inside the material which are probed by a constant applied current. Despite the non-predictability and non-reproducibility of  $x(t)$ , statistical analysis is possible and meaningful. An exemplary time-dependent signal  $x(t)$  is shown in Fig. 2.1.1 (a) together with its mean value  $\bar{x}$  (red line). The calculated probability distribution  $P(x)$  is shown in Fig. 2.1.1 (b) by means of a histogram and can be described by

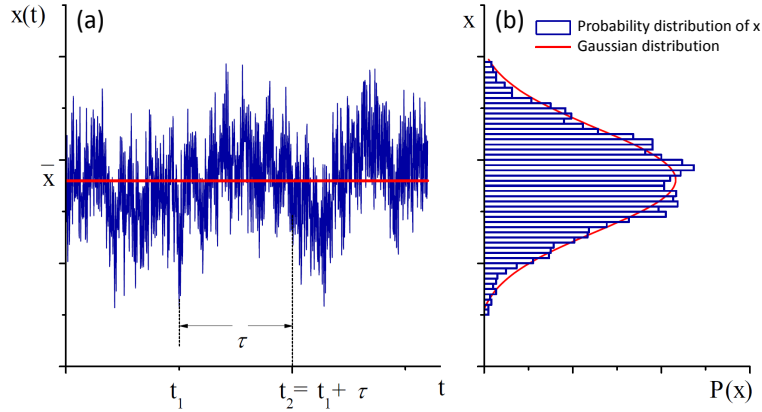


Figure 2.1.1: (a) Exemplary time evolution of a physical quantity  $x(t)$ . Red line indicates the mean value  $\bar{x}$ . (b) Histogram of  $x(t)$ , fitted by a normal (Gaussian) distribution (red curve). From [14].

a Gaussian distribution as indicated by the red curve.

In contrast to the random quantity  $x(t)$  itself, the statistical characteristics of a random process are nonrandom quantities. A corresponding averaging of the random quantity can be carried out in two different ways, either by averaging over time or over an ensemble of a large number of identical systems.

Considering the time-averaging approach, it is assumed that  $N$  discrete measurement points  $x(t) = (x(t_1), \dots, x(t_N))$  are recorded in a real experiment. This time series is equally spaced, whereby  $\Delta t = t_{i+1} - t_i$  ( $1 < i < N-1$ ) is the distance in time between two adjacent measurement points  $x(t_i)$  and  $x(t_{i+1})$ . For a total measuring duration of  $T = N \cdot \Delta t$ , the mean value equals:

$$\bar{x} = \frac{1}{T} \sum_{i=1}^N x(t_i) \cdot \Delta t. \quad (2.1)$$

Alternatively, averaging can be executed over an ensemble of a large number  $N$  of identical systems at a fixed time  $t$ , i.e.,  $(x_1(t), \dots, x_N(t))$ . The mean value in this case can be written as follows:

$$\langle x \rangle = \frac{1}{N} \sum_{i=1}^N x_i(t). \quad (2.2)$$

An alternative way to calculate the ensemble average  $\langle x \rangle$  is given by considering the probability distribution  $P(x, t)$ :

$$\langle x \rangle = \int_{-\infty}^{\infty} x \cdot P(x, t) dx. \quad (2.3)$$

Importantly, if both averaging procedures yield identical mean values, i.e.,  $\bar{x} = \langle x \rangle$ , the random process is considered ergodic. Since this relation is applicable for the majority of

random processes in physics, ergodicity will henceforth be assumed. Moreover, if  $\langle x \rangle$  is independent of the time  $t$ , a random process is considered stationary.

In order to consider the fluctuations of the random variable  $x(t)$ , it is useful to calculate the deviation of its mean value  $\bar{x}$  as

$$\delta x(t) = x(t) - \bar{x}, \quad (2.4)$$

which itself is again a random quantity. By definition, the time and the ensemble average of  $\delta x(t)$  equal zero. In addition to that, the average fluctuation squared,  $\overline{\delta x^2(t)}$ , which corresponds to the variance  $\sigma^2$  and hence to the so-called second-order central moment  $m_2$ , is a measure for the power contained in the fluctuation. It can be calculated after

$$\sigma^2 = m_2 = \overline{\delta x^2(t)} = \frac{1}{T} \sum_{i=1}^N (x(t_i) - \bar{x})^2 \cdot \Delta t. \quad (2.5)$$

Further information about the probability distribution  $P(x, t)$  can be obtained by calculating so-called higher moments. A generalization of Eq. (2.3) yields the  $r$ -th order central moment:

$$m_r = \langle x^r \rangle = \int_{-\infty}^{\infty} x^r \cdot P(x, t) dx. \quad (2.6)$$

In most cases, the fluctuations follow a Gaussian distribution, i.e.,

$$P(x) = \frac{1}{\sqrt{2\pi\sigma^2}} \exp\left(-\frac{(x - \bar{x})^2}{2\sigma^2}\right), \quad (2.7)$$

cf. the example depicted in Fig. 2.1.1. Deviations from the Gaussian distribution, which are usually observed for systems in which individual fluctuation processes (so-called *fluctuators*) are interacting with each other, can be further analyzed by calculating correlation functions and power spectral densities of higher order, cf. Sec. 2.5. In all other systems, which do follow a Gaussian distribution, the first- and second-order central moments, i.e., the mean value and the variance, contain the entire information of the signal.

## 2.2 Autocorrelation function

As mentioned before, the deviation of the random quantity from its mean value,  $\delta x(t) = x(t) - \bar{x}$ , is also random. Although the exact temporal evolution of the function  $\delta x(t)$  is not predictable, the knowledge of the function value at a time  $t_1$  allows for probability statements about the value at a time  $t_2$ . The so-called autocorrelation function provides a measure of the memory of an electronic process, i.e., how fluctuations evolve in time on average. It is nonrandom and, in the case of condensed matter physics, can be related to the dynamics of electronic processes in solids. In order to describe the autocorrelation function correctly, we

focus on a general discussion of correlations at first.

Given two random variables  $x$  and  $y$ , a statistical relationship between these two can exist, i.e., knowledge of the value of one quantity also yields (statistical) information about the value of the second random quantity and vice versa. In the case of this mutual dependence, a correlation between the two quantities exists. In general, a correlation occurs when the fluctuations of two physical quantities have the same origin. In most cases, two random variables exhibit a partial correlation, since there usually exist common, but also independent origins of the fluctuations. When these two quantities are fully correlated, a linear relationship between them exists.

In order to quantify the correlation of two quantities, we first need to define the covariance of the random variables  $x$  and  $y$ :

$$\text{cov}(x, y) = E[(x - E(x)) \cdot (y - E(y))]. \quad (2.8)$$

Here,  $E(x) = \sum_i x_i \cdot P(x = x_i)$  denotes the expected value of  $x$ , with the probability distribution  $P(x)$ . In probability theory, covariance is a measure of how changes in one random variable  $x$  are associated with changes in a second variable  $y$ . The so-called correlation coefficient can be viewed as the normalized version of the covariance, assuming values only in the interval  $[-1, 1]$ . More precisely, the correlation coefficient is the covariance of two variables  $x$  and  $y$  divided by the product of their standard deviations  $\sigma_x$  and  $\sigma_y$ . The correlation coefficient  $\rho_{x,y}$  of random variables  $x$  and  $y$  can be written as

$$\rho_{x,y} = \frac{\text{cov}(x, y)}{\sqrt{\sigma_x^2 \sigma_y^2}}. \quad (2.9)$$

While  $\rho_{x,y} = \pm 1$  indicates perfect linear association,  $\rho_{x,y} = 0$  implies that there is no correlation. In other words, two variables  $x$  and  $y$  are considered correlated if  $\rho_{x,y} \neq 0$ .

A description of the correlation between two random variables  $\delta x(t) = x(t) - \bar{x}$  and  $\delta y(t + \tau) = y(t + \tau) - \bar{y}$  as a function of the distance in time  $\tau$ , under the assumption of ergodic and stationary processes, is given by the correlation function  $\Psi_{xy}(\tau)$ , which is defined as [12]

$$\Psi_{xy}(\tau) = \overline{\delta x(t) \delta y(t + \tau)} = \lim_{T \rightarrow \infty} \frac{1}{T} \int_{-T/2}^{T/2} \delta x(t) \delta y(t + \tau) dt. \quad (2.10)$$

An important requirement is that time averaging is carried out for a sufficiently long time interval  $T$ .

An autocorrelation is the correlation of a signal  $\delta x(t)$  with a delayed copy of itself  $\delta x(t + \tau)$  as a function of the delay  $\tau$ . In other words, the autocorrelation function is a special case of the



correlation function and can be written as

$$\Psi_{xx}(\tau) = \lim_{T \rightarrow \infty} \frac{1}{T} \int_{-T/2}^{T/2} \delta x(t) \delta x(t + \tau) dt. \quad (2.11)$$

Importantly, for zero delay  $\tau = 0$  the autocorrelation function corresponds to the variance  $\sigma^2$ :

$$\Psi_{xx}(0) = \overline{\delta x^2} = \sigma^2. \quad (2.12)$$

For fluctuation processes,  $\Psi_{xx}(\tau)$  usually is a monotonic decreasing function, implying that the correlation decreases with increasing distances in time. In general, it is  $\Psi_{xx}(\tau \rightarrow \infty) = 0$ .

## 2.3 Power spectral density

In order to thoroughly analyze fluctuation processes it is common to transform the time-dependent signal  $\delta x(t)$  into the frequency domain. We will define the power spectral density (PSD)  $S_x(f)$ , which is a measure for the power contained in a fluctuation process within a frequency band of 1 Hz at a particular frequency  $f$ . In general, the Fourier transform  $\mathcal{F}(f)$  of a signal  $\delta x(t)$  is calculated as

$$\mathcal{F}(f) = \int_{t_1}^{t_2} \delta x(t) e^{-2\pi i f t} dt, \quad (2.13)$$

where  $t_1 = -\infty$ ,  $t_2 = \infty$  and  $i^2 = -1$ . In order to calculate the PSD  $S_x(f)$  of a signal measured during a time interval  $T$ , we consider the Fourier transform  $\mathcal{F}(f)$  using  $t_1 = -T/2$  and  $t_2 = T/2$ . We now define the PSD as [11]

$$S_x(f) = 2 \lim_{T \rightarrow \infty} \frac{|\mathcal{F}(f)|^2}{T}. \quad (2.14)$$

In other words, the PSD describes how much power is associated with different parts of the frequency spectrum. The total power  $P$  of the fluctuation process, which corresponds to the variance  $\overline{\delta x^2(t)}$ , can be obtained by integrating the PSD over the entire frequency range, i.e.,

$$P = \overline{\delta x^2(t)} = \int_0^{\infty} S_x(f) df. \quad (2.15)$$

We can also define the spectral weight in a particular frequency interval  $[f_1, f_2]$  by

$$SW = \int_{f_1}^{f_2} S_x(f) df. \quad (2.16)$$

The PSD and the autocorrelation function can be related via the Wiener-Khinchin theorem.

For this purpose, we first calculate the Fourier transform of the autocorrelation function:

$$\zeta(f) = \int_{-\infty}^{\infty} \Psi_{xx}(\tau) e^{-2\pi i f \cdot \tau} d\tau. \quad (2.17)$$

The back-transformation is given by:

$$\Psi_{xx}(\tau) = \int_{-\infty}^{\infty} \zeta(f) e^{2\pi i f \cdot \tau} df. \quad (2.18)$$

For setting  $\tau = 0$  in Eq. (2.18), the comparison of this equation with Eq. (2.15) clarifies that  $\Psi_{xx}(0) = P$  and thus  $\zeta(f)$  can be viewed as a power spectral density. For stationary processes, the autocorrelation function is symmetric, i.e.,  $\Psi_{xx}(\tau) = \Psi_{xx}(-\tau)$ . Therefore,  $\zeta(f)$  must be a real and even function, implying that  $\zeta(f) = \zeta(-f)$ . Considering only positive frequencies, it is  $S_x(f) = 2\zeta(f)$ . Finally, the Wiener-Khinchin theorem can be written as follows [12]:

$$S_x(f) = 2 \int_{-\infty}^{\infty} \Psi_{xx}(\tau) e^{-2\pi i f \cdot \tau} d\tau, \quad (2.19)$$

$$\Psi_{xx}(\tau) = \frac{1}{2} \int_{-\infty}^{\infty} S_x(f) e^{2\pi i f \cdot \tau} df. \quad (2.20)$$

Due to the symmetry of the two functions, the Wiener-Khinchin equations can be modified as follows:

$$S_x(f) = 4 \int_0^{\infty} \Psi_{xx}(\tau) \cos(2\pi f \cdot \tau) d\tau, \quad (2.21)$$

$$\Psi_{xx}(\tau) = \int_0^{\infty} S_x(f) \cos(2\pi f \cdot \tau) df. \quad (2.22)$$

If the fluctuating entity is a voltage fluctuation, units of  $S_V(f)$  are  $V^2/\text{Hz}$ . In analogy to the Wiener-Khinchin equations described above, a spectral function, the so-called cross spectrum  $S_{xy}(f)$ , can also be deduced from the general correlation function  $\Psi_{xy}(\tau)$ . The cross spectrum  $S_{xy}(f)$  indicates the frequency-dependent correlation of two quantities. It can be written as

$$S_{xy}(f) = 2 \int_{-\infty}^{\infty} \Psi_{xy}(\tau) e^{-2\pi i f \cdot \tau} d\tau. \quad (2.23)$$

The real part of  $S_{xy}(f)$  is highly relevant for the addition of individual noise spectra. The spectrum of the sum of two fluctuation processes is given by

$$S(f) = S_x(f) + S_y(f) + 2\text{Re}[S_{xy}(f)]. \quad (2.24)$$

This has important consequences for experiments. Since noise is an additive quantity, care has to be taken in order to minimize the influence of external noise sources, even in the case of independent fluctuation processes, where  $S_{xy}(f) = 0$ .

## 2.4 Types of noise

In general, the observed electronic noise in condensed matter may be composed of various contributions of different origin. Figure 2.4.1 shows a typical noise spectrum, which can be divided into three characteristic regimes. At low frequencies, the power spectral density decreases as  $S_x(f) \propto 1/f$ , which is why this behavior is called  $1/f$  noise. At higher frequencies, the PSD is independent of the frequency and thus exhibits a flat behavior (white noise). In addition, a high-frequency cutoff is required in order to obtain a finite value for the noise power as calculated after Eq. (2.15). Finally, a nonzero mean value of the fluctuating signal leads to a delta function at  $f = 0$ . In this section, we will start with a discussion of frequency-independent types of noise, i.e., thermal and shot noise, which are frequently encountered and rather well understood. This will be followed by an introduction to frequency-dependent noise phenomena, namely generation-recombination and  $1/f$  noise.

### 2.4.1 Thermal noise

Thermal noise, also named Johnson-Nyquist noise after the two physicists who were the first to study it quantitatively [15, 16], results from the random thermal agitation of charge carriers in thermal equilibrium at finite temperatures  $T > 0$  and can be observed in any type of electrically conducting medium. The voltage power spectral density behaves as

$$S_V(f) = S_V = 4k_B TR, \quad (2.25)$$

where  $k_B$  denotes the Boltzmann constant and  $R$  the resistance. The index  $V$  in the PSD  $S_V$  indicates that the voltage is the relevant fluctuating quantity. Regardless of any applied voltage, thermal noise emerges without showing any frequency dependence, which is why it is also called "white" noise. Strictly speaking, this frequency independence is only observed in the "classical" frequency regime, since, as derived by Nyquist by applying a blackbody radiation formalism [16], the thermal noise spectrum is a function of the quantum mean energy

$$\langle E(\omega) \rangle = \frac{\hbar\omega}{\exp\left(\frac{\hbar\omega}{k_B T}\right) - 1}. \quad (2.26)$$

For  $\hbar\omega \ll k_B T$ , Eq. (2.26) becomes the classical energy  $k_B T$ . At room temperature the noise spectrum may be considered as "white" up to frequencies in the THz range [17], whereas towards higher frequencies and lower temperatures the quantum-mechanical correction needs to be considered. This correction is suggested to prevent a divergence of the noise power, which is calculated by Eq. (2.15). On the other hand, there is an ongoing debate about the zero-point term in the thermal noise of a resistor, which originates from a quantum-theoretical treatment and would yield an infinite ground-state energy of a (weakly-damped) linear harmonic oscillator, contradicting basic results of quantum mechanics [18, 19]. For typ-

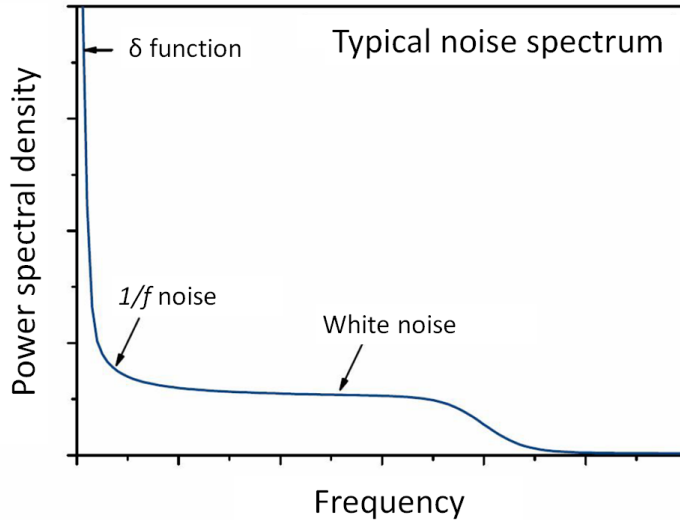


Figure 2.4.1: Power spectral density  $S_x(f)$  as a function of frequency  $f$  for a typical noise signal. After [14].

ical applications, however, these quantum-mechanical corrections do not need to be taken into consideration.

From Eq. (2.25) it is possible to estimate the value of the observable voltage fluctuations by calculating the mean square voltage noise

$$\overline{V^2} = 4k_B TR\Delta f, \quad (2.27)$$

where  $\Delta f$  represents the frequency bandwidth of the measurement. For example, the root mean square (rms) voltage  $V_{\text{rms}}$  measured at the terminals of a  $1\text{ k}\Omega$  resistor in a  $1\text{ MHz}$  frequency bandwidth is  $V_{\text{rms}} = 4\text{ }\mu\text{V}$ . Therefore, matching the frequency bandwidth of the experiment with the frequency domain of the desired signal is an obvious way to improve the signal-to-noise ratio of the experiment, which is defined as

$$\text{SNR} = \frac{P_{\text{signal}}}{P_{\text{noise}}}, \quad (2.28)$$

where  $P_{\text{signal}}$  is the power of a signal (meaningful information) and  $P_{\text{noise}}$  the power of background noise (unwanted signal) as calculated after Eq. (2.15). If the accuracy of an experiment is limited by thermal noise, the signal-to-noise ratio can be improved by applying a larger driving current  $I$ , since, as can be seen from Eq. (2.25), the magnitude of the thermal noise is independent of  $I$ .

In Section 2.7 it will be discussed in further detail that Eq. (2.25) is a formulation of the fluctuation-dissipation theorem. Besides representing a lower limit for the noise level of resistors, thermal noise allows for a precise and non-invasive measurement of the absolute

temperature in ultra-low temperature experiments [20, 21], since, in contrast to standard resistance thermometers, no electrical current needs to be applied, which would heat up the experimental setup.

### 2.4.2 Shot noise

In contrast to thermal noise, the so-called shot noise is a non-equilibrium type of noise, which was discovered by W. Schottky in 1918 [22]. It originates in the discreteness of electric charge. In detail, this type of noise results from the fact that the electric current is not continuous, but is rather composed of the sum of discrete pulses in time, each corresponding to the transfer of a charge carrier through the conductor. The current power spectral density  $S_I$  can be calculated as:

$$S_I(f) = S_I = 2qI_0. \quad (2.29)$$

Here,  $q$  is the charge of the carriers and  $I_0$  the average current. In analogy to thermal noise, shot noise is characterized by a white noise spectrum up to a certain cutoff frequency, which is related to quantum corrections [2]. In general,  $q$  corresponds to the elementary charge  $e$ , but yet there are examples where  $q \neq e$ , as, for instance, the shot noise measured at a tunnel junction between a superconductor and a normal metal [23, 24]. Since the charge in a superconductor cooled below its critical temperature flows in the form of Cooper pairs, it follows  $q = 2e$ . Moreover, shot noise provides a way to measure the quasiparticle charge in the fractional quantum Hall effect [25]. In general, shot noise can only be observed at low temperatures, at high frequencies and for small currents; otherwise thermal noise or  $1/f$  noise come to dominate the measured noise spectrum.

### 2.4.3 Generation-recombination noise

So far, we have considered frequency-independent Gaussian noise. Figure 2.4.2 gives an example of non-Gaussian random telegraph signals, whereby the measured voltage switches between two (or several) discrete values. In this case, the time-dependent Hall voltage  $\Delta V_H$  measured at an  $\text{Al}_x\text{Ga}_{1-x}\text{As}/\text{GaAs}$  heterostructure is depicted for various temperatures [8]. This type of noise has been observed in many different systems such as p-n junctions, metal-oxide-semiconductor field-effect transistors (MOSFETs), metal-insulator-metal (MIM) tunnel junctions, and semiconducting as well as metallic microstructures [11].

In a simple picture, the characteristic random telegraph signal in a semiconductor can be explained by the excitation of electrons into the conduction band and the associated creation of electron-hole pairs, which will recombine after a certain time. Since these generation and recombination processes are random, the number of charge carriers fluctuates around some mean value. This leads to fluctuations of the resistance in the semiconductor. In general, the generation-recombination noise depends on the properties of the semiconductor, such as the

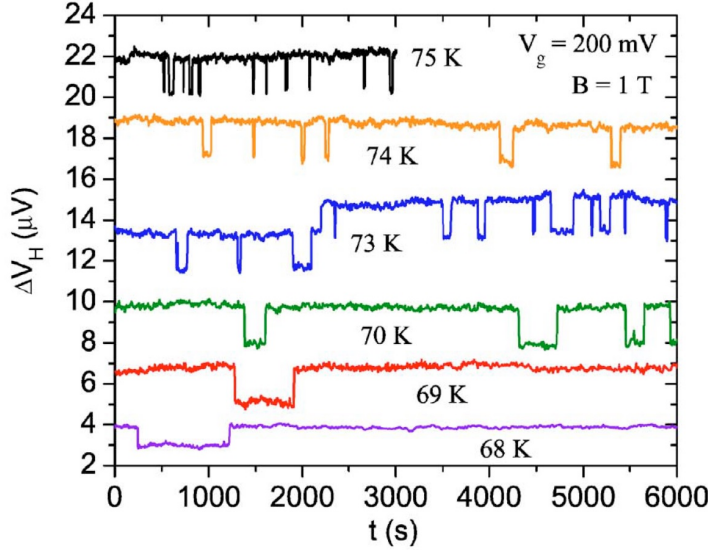


Figure 2.4.2: Exemplary random telegraph signals of an  $\text{Al}_x\text{Ga}_{1-x}\text{As}/\text{GaAs}$  heterostructure. The measured Hall voltage  $\Delta V_H$  is plotted against time for different temperatures. Content reprinted from Ref. [8] with permission of the American Physical Society.

type of trapping or recombination centers and whether a unipolar or a bipolar conduction occurs. In the case of the measurements of the semiconductor heterostructure shown in Fig. 2.4.2, the random telegraph signal can be explained by capture and emission processes of single electrons by deep donor (DX-type) centers [26]. Since the random telegraph noise is of non-Gaussian type, the system cannot be fully described by the lowest-order correlation function given in Eq. (2.11) and 2.22. This may be due to a small number of independent fluctuation processes which couple more strongly to the resistivity than others, or if the single processes (fluctuators) cannot be considered as independent. In this case, higher-order correlation functions have to be utilized, which are experimentally accessible by measuring the so-called second spectrum, cf. Sec. 2.5. A theoretical treatment of two-level fluctuation processes was carried out by S. Machlup in Ref. [27]. The obtained frequency-dependent PSD of a random telegraph signal caused by switching events between two states with voltage amplitude  $\Delta V$  and characteristic lifetimes  $\tau_1$  and  $\tau_2$ , cf. the schematic illustrations in Fig. 2.4.3 (a) and (b), follows a Lorentzian spectrum:

$$S_V(f) = \frac{4(\Delta V)^2}{\tau_1 + \tau_2} \frac{1}{(1/\tau_c)^2 + (2\pi f)^2}, \quad (2.30)$$

where  $1/\tau_c = 1/\tau_1 + 1/\tau_2$ . As can be seen in Fig. 2.4.3 (c), the spectrum is flat for low frequencies and decreases like  $S_V \propto 1/f^2$  towards high frequencies. The corner frequency  $f_c = 1/(2\pi\tau_c)$  is related to the characteristic time constants of the system. Statistical investigations of lifetimes in the different states can provide valuable information on the dynamics and

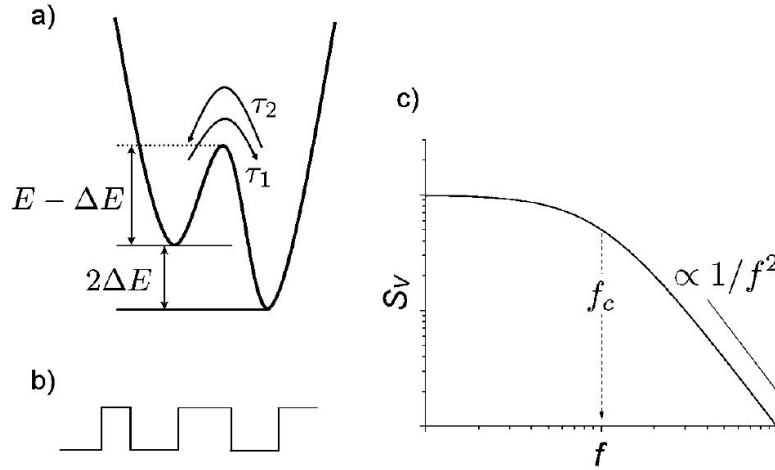


Figure 2.4.3: Two-level fluctuation process. (a) Schematic asymmetrical double-well potential with characteristic energies and time constants. (b) Random telegraph signal in the time domain. (c) Corresponding Lorentzian spectrum in frequency space. Content reprinted from Ref. [28] with permission of John Wiley and Sons.

the energy scales of the switching processes as well as the related electronic properties [2]. Fundamental microscopic variables such as the energy differences between two states, the volume of the fluctuating quantity and its intrinsic nature can be inferred. Random telegraph noise is usually observed in small samples, where the number of fluctuators is significantly reduced. However, in rare cases, mostly related to strongly inhomogeneous materials, random telegraph signals are observed in macroscopic volumes [29, 30, 31]. Very recently, random telegraph noise has been studied extensively in so-called resistive random-access memory (RRAM) devices [32, 33], which is also a topic of the present work, cf. chapter 5.

To summarize, a purely Lorentzian-type random telegraph signal can be explained by an electronic switching process, i.e., trapping and detrapping events of a single electron. In the following, we will address the question of how the noise characteristics change for a superposition of many two-level fluctuation processes. It will be shown that this superposition results in a  $1/f$ -type behavior. However, before considering theoretical approaches, we will start with a phenomenological description of  $1/f$  noise.

#### 2.4.4 $1/f$ noise

The term  $1/f$  noise refers to fluctuations of a physical quantity  $x$  with a PSD  $S_x$  following a  $1/f^\alpha$  law, where the so-called frequency exponent  $\alpha$  is typically equal or close to 1 and corresponds to the slope of the noise spectrum in a log-log plot, i.e.,

$$\alpha = -\frac{\partial \log(S_x)}{\partial \log(f)}. \quad (2.31)$$

Sometimes, this type of noise is also referred to as flicker or excess noise. The first experimental observation of  $1/f$  noise was made in a thermionic tube and reported by J. Johnson in 1925 [34]. A striking aspect of  $1/f$  noise is its ubiquitous nature. Over the last decades, it has been observed in a vast number of systems. Examples beyond the borders of solid state physics are studies of earthquakes and thunderstorms [35], the time dependence of the water level of the river Nile [36], melody and loudness fluctuations in music and speech [37], the light intensity of quasars in astrophysics [38], fluctuations of traffic currents on expressways [39], the distribution of prime numbers [40] or fluctuations of the human heartbeat frequency [41].

The best studied and documented examples of  $1/f$  fluctuations can be found in solid state physics. Here,  $1/f$ -type noise has been observed for a wide variety of materials and systems, such as semiconductors, metals, magnetic thin films, superconductors, spin glasses, heterogeneous conductors, tunnel junctions, electronic devices, magnetic sensors and CMR perovskites [2]. In all these systems it is assumed that resistance fluctuations  $\delta R(t)$  are the cause of  $1/f$  noise. The application of a current  $I$  leads to a fluctuating voltage drop  $\delta V(t) = I\delta R(t)$  across the investigated sample, which itself is related to the intrinsic resistance fluctuations. In other words, the applied current is not the origin of the fluctuations, but rather serves as a probe which reveals the present  $1/f$  fluctuations above the white noise. In general, an increase of the current density facilitates the detection of  $1/f$ -type voltage fluctuations. This intrinsic nature of flicker noise was demonstrated experimentally in Refs. [42, 43], where fluctuations in the mean-square Johnson-noise voltage exhibit  $1/f$ -type noise spectra. Therefore, the authors conclude that  $1/f$  noise in metal and semiconductor films is an equilibrium process, ruling out any contribution of the driving current to the resistance fluctuations. However, as pointed out in a more recent review by G. Zhigal'skii [44], there exists a considerable variety of systems, in which nonequilibrium  $1/f$  fluctuations coexist with equilibrium flicker noise.

Due to the ubiquity of  $1/f$  fluctuations the question arises, whether a universal theory exists. Since flicker noise can be observed in such different complex systems, it seems very unlikely that  $1/f$  fluctuations share a common origin. In fact, experiments indicate that the origins are quite different among the considered systems. Instead, it is now widely accepted that the  $1/f$  spectrum is rather a common mathematical feature, which can be phenomenologically modelled. In the following, selected fundamental properties of flicker noise will be discussed in order to achieve a better understanding of its ubiquity and scale-invariance.

The typical frequency range, in which most of the experiments are performed, is between  $10^{-3}$  and  $10^4$  Hz. In 1974, M. Caloyannides reported on experimentally observed  $1/f$ -type resistance fluctuations in an operational amplifier down to frequencies of about  $0.5 \mu\text{Hz}$  [45]. The resulting noise power spectrum is shown in Fig. 2.4.4. Note that the measurement duration of a single spectrum amounts to several days. Interestingly, no evidence for a low-frequency cutoff has been found. However, this leads to a fundamental paradox with regard



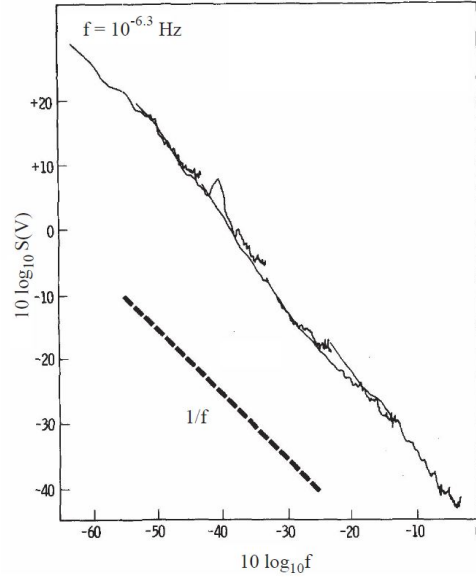


Figure 2.4.4: PSD of an operational amplifier as a function of frequency. Dashed line denotes a perfect  $1/f$  behavior. The lowest frequency corresponds to  $f = 10^{-6.3} \text{ Hz} \approx 0.5 \mu\text{Hz}$ . Content reprinted from Ref. [45] with permission of AIP Publishing LLC.

to the power contained in the noise signal. In analogy to Eq. (2.15), we consider the average power  $P$  in a particular frequency interval  $[f_1, f_2]$ , where we assume that  $f_2 = a \cdot f_1$  and  $\alpha = 1$ :

$$P = \int_{f_1}^{f_2} S_x(f) df = \int_{f_1}^{f_2} \frac{c}{f} df = c \ln\left(\frac{f_2}{f_1}\right) = c \ln(a). \quad (2.32)$$

Therefore, the power contained in the  $1/f$  spectrum is independent of the selected frequencies, but it only depends on the width of the frequency interval. In other words,  $1/f$  noise can be considered timescale-invariant. Furthermore, from Eq. (2.32) it can be concluded that the power  $P$  diverges at the upper (lower) limit if  $\alpha < 1$  ( $\alpha > 1$ ) and at both limits logarithmically in the case of  $\alpha = 1$ . Since a logarithmic divergence is the slowest possible divergence, the  $1/f$  spectrum can be viewed as the energetically most favorable way for the distribution of energy over an extended frequency range. Or, in other words,  $1/f$  noise can be considered as a satisfactory compromise between white noise  $S_x(f) \propto 1/f^0$  and so-called random walk<sup>1</sup> noise  $S_x(f) \propto 1/f^2$ , which may be a possible explanation for the ubiquity of  $1/f$  fluctuations in nature. While—at least in the classical case—an infinite power is obtained for white noise when integrating from some finite frequency towards infinity, in the case of a  $1/f^2$  spectrum the integration of  $S_x(f)$  between a finite frequency down to zero frequency yields an infinite value for  $P$ . As a consequence, due to the divergence at high frequencies, a time signal  $w(t)$

<sup>1</sup>An important example for a random walk is the Brownian movement of small particles immersed in a fluid, which has been statistically analyzed by A. Einstein in 1905 [46, 47].

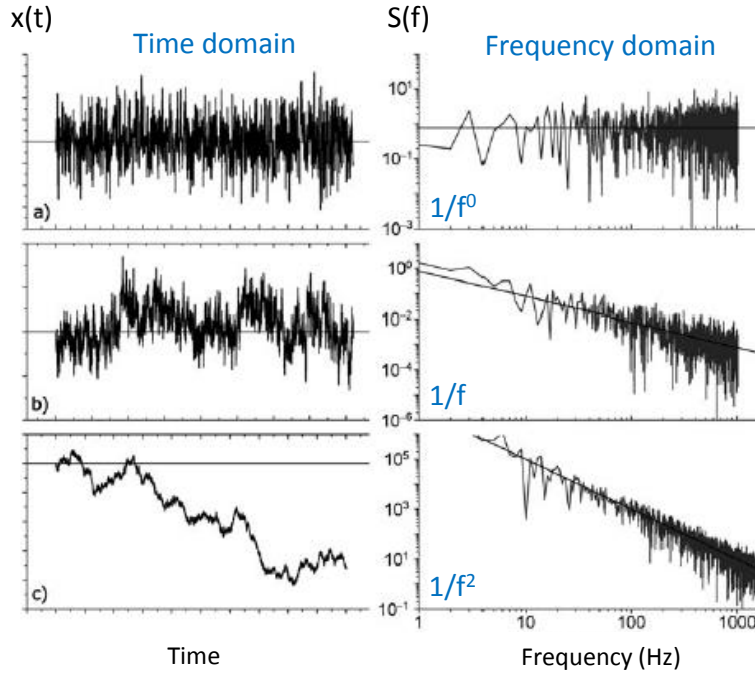


Figure 2.4.5: Time trains of different noise signals  $x(t)$  (left) and the corresponding power spectra  $S_x(f)$  in the frequency domain (right). (a) White noise with no correlations in time. (b)  $1/f$  noise. (c)  $1/f^2$  (random walk) noise. After Ref. [28] with permission of John Wiley and Sons.

exhibiting white noise is infinitely choppy, i.e., the instantaneous value of  $w(t)$  is undefined, whereas the mean value of the signal converges. In contrast to that, a random walk signal  $B(t)$  has a well-defined value at each point, but wanders ever farther from its initial value when considering longer and longer timescales, i.e., it does not have a well-defined mean value over long times. Interestingly, the integral of the white noise signal  $w(t)$  corresponds to a random walk or Brownian motion  $B(t)$ :

$$B(t) = \int w(t) dt. \quad (2.33)$$

This integration brings in a factor of  $1/f$  in the Fourier transform, which corresponds to a factor  $1/f^2$  in its square, that is, the power spectrum. Importantly,  $1/f$  noise is a special case of fractionally integrated white noise [38]. As can be seen in Fig. 2.4.5, the time signal  $x(t)$  in panel (b) looks "in between" the other two in its variability. It has neither a well-defined long-term mean value, nor a well-defined value at a particular point. While white noise does not exhibit any correlations in time,  $1/f$  noise shows long-range correlations in space and time. It remains an open problem to explain such long-term memory correlations down to frequencies in the  $\mu\text{Hz}$  range as observed by M. Caloyannides [45]. In practice, the patience

of the experimentalist usually dictates the existence of a low frequency limit. In this context, an extreme example can illustrate why the divergence in the noise power for  $f \rightarrow 0$  does not constitute a problem [48]. Assuming that the time span which is required for light to pass through the diameter of a proton ( $\sim 2$  fm) constitutes an upper cutoff frequency, and the age of the universe corresponds to a lower cutoff frequency, the relevant frequency range includes 40 decades. Therefore, a  $1/f$  spectrum in the entire possible frequency interval contains only 40 times more energy than it is contained in a single decade [2].

### Hooge Model

As mentioned before, resistance fluctuations  $\delta R(t)$  of a solid can be observed by applying an external current  $I$  and measuring the voltage fluctuations  $\delta V(t) = I\delta R(t)$ . Empirically, it was found by F. Hooge that the voltage noise PSD is proportional to the square of the voltage itself, i.e.,  $S_V \propto V^2$ , and thus in the case of ohmic behavior ( $V = R \cdot I$ ) it is  $S_V \propto I^2$  [49, 50]. Moreover, we can consider the normalized noise magnitude  $S_x(f)/x^2$ , where  $x$  indicates the current  $I$ , the voltage  $V$ , the resistance  $R$  or the conductance  $G$ . The following relation applies [51]:

$$\frac{S_I(f)}{I^2} = \frac{S_V(f)}{V^2} = \frac{S_R(f)}{R^2} = \frac{S_G(f)}{G^2} = \frac{C_{1/f}}{f}. \quad (2.34)$$

Here,  $C_{1/f}$  is a quantity which is a measure for the relative noise of the considered sample and does not depend on the measuring conditions. From the comparison of  $1/f$ -noise measurements of various materials it was concluded that a normalization with respect to the number of free charge carriers  $N_c$  in a sample is required. Therefore, the so-called Hooge law can be written as

$$S_V(f) = \frac{\gamma_H \cdot V^2}{n\Omega f^\alpha}. \quad (2.35)$$

Here,  $n$  denotes the charge carrier density and  $\Omega$  the "noisy" sample volume, i.e.,  $n\Omega = N_c$  yields the total amount of charge carriers in the material causing the observed  $1/f$  noise. The material-specific and temperature-dependent Hooge parameter  $\gamma_H$  allows for comparing the noise level of various systems and covers a range of  $\gamma_H = 10^{-6}$ – $10^7$  for different materials [2], although originally it was wrongly assumed to be a constant,  $\gamma_H = 2 \cdot 10^{-3}$  [49].

As pointed out above, there exists a considerable variety of systems in which nonequilibrium  $1/f$  noise coexists with equilibrium flicker noise [44], leading to deviations from  $S_V \propto V^2$ . Generally, the Hooge formula breaks down at very high currents at which either the entire sample is heated or the charge carriers become hot [11]. Moreover, an ohmic relationship between  $I$  and  $V$  does not imply the validity of the Hooge formula. For various disordered conductors, such as island films and granular composites, a scaling of  $S_V \propto V^\beta$  with  $\beta$  varying from 1 to 4 has been observed [44, 52].

Despite its simplicity, the Hooge formula generally explains experimental results very well.

However, it should be noted that the factor  $1/N_c$  suggests that independent fluctuations are occurring on each of the mobile charge carriers, which is not consistent with experimental results demonstrating the persistence of  $1/f$  noise down to frequencies in the  $\mu\text{Hz}$  range, cf. Fig. 2.4.4. In fact, any fluctuations tied to individual free charge carriers cannot persist for times longer than the carrier transit time in a sample. Since this transit time and often also the diffusion time are in the microsecond to millisecond range, a  $1/f$  spectrum would be required to flatten out below characteristic frequencies well within the observed range [53]. Therefore, the assumption that  $1/f$  noise is composed of independent fluctuation processes of individual mobile charge carriers is an oversimplification in many cases. Furthermore, the noise in metallic films can vary by two orders of magnitude or even more as a function of temperature and substrate material, whereby the number of free charge carriers does not change significantly. The problem is that Hooge assumed that the mechanism of  $1/f$  noise is always of bulk type, although surface effects play a crucial role in many systems [54].

The fact that the noise level is inversely proportional to the volume  $\Omega$  of the sample has important consequences for experimental studies and applications. Firstly, the optimization of the sample geometry is crucial, in particular for materials with a low Hooge constant  $\gamma_H$ , in order to raise the  $1/f$ -type fluctuations above the background noise. In other words, it is advantageous to investigate samples with reduced lateral sizes such as thin films. In terms of applications, as for example micro- and nanoelectronics,  $1/f$  noise can cause a significant degradation of the signal-to-noise ratio for small devices in low-frequency applications.

A further aspect which has been heavily debated in the literature of semiconductors is whether  $1/f$  fluctuations are caused by fluctuations in the number of free charge carriers  $\delta N/N$  or by fluctuations in their mobility  $\delta\mu/\mu$ . Since the Drude model suggests that the number of charge carriers  $N$  and their mobility  $\mu$  govern the resistance  $R$  [55], it seems legitimate to assume that  $\delta R/R = \delta N/N + \delta\mu/\mu$ . A definite conclusion has not been reached and it is presumed that this problem strongly depends on the physics of the respective material. For semiconductors it is well established that trapping and detrapping processes of charge carriers constitute a major contribution to  $1/f$  noise. These capture and emission events affect both the carrier number and their mobility. A sophisticated experiment to distinguish the contributions of  $\delta N/N$  and  $\delta\mu/\mu$  is the measurement of both the  $1/f$  voltage fluctuations on standard probes and those on the Hall voltage, see Refs. [56, 57, 58]. However, as until today such experimental approaches have not lead to any unambiguous conclusion [2]. Despite the presented obscurities and the complexity of flicker noise, there exist a variety of theoretical approaches for the description of  $1/f$  noise, which will be presented in the following.

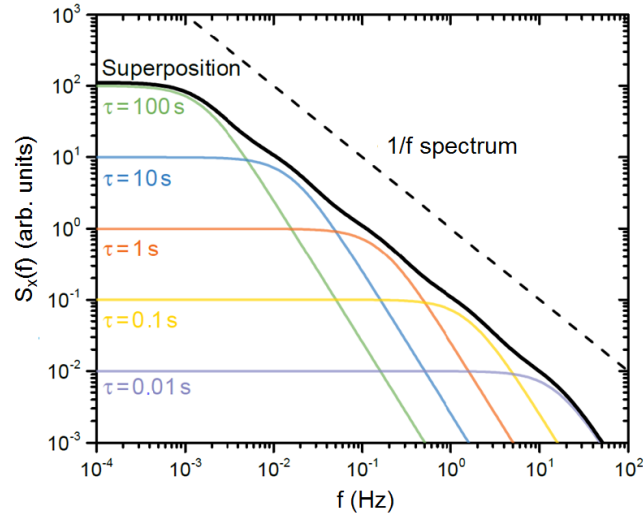


Figure 2.4.6: Superposition of various Lorentzian spectra with different relaxation times yielding a  $1/f$  spectrum. After [13].

### Theoretical description of flicker noise

A possible theoretical description of flicker noise is based on the assumption of a superposition of random and independent fluctuation processes, which couple to the resistance. A simple model for such a process is given by a two-level system with a characteristic relaxation time  $\tau$ —also referred to as *fluctuator*. In case that the kinetics of fluctuation processes is characterized by a single relaxation time  $\tau$ , the autocorrelation function  $\Psi_{xx}(t)$  of the fluctuating variable  $x(t)$  is exponential:

$$\Psi_{xx}(t) = \overline{\delta x^2(t)} e^{-|t|/\tau}. \quad (2.36)$$

The application of the Wiener-Khinchin theorem (Eq. (2.21)) yields a Lorentzian function for the power spectral density  $S_x(f)$ :

$$S_x(f) = 4 \int_0^{\infty} \Psi_{xx}(t) \cos(2\pi f \cdot t) dt = \overline{\delta x^2(t)} \frac{4\tau}{1 + \omega^2 \tau^2}, \quad (2.37)$$

where  $\omega = 2\pi f$ . For more complex processes with a distribution of relaxation times  $p_x(\tau)$  related to independent two-level processes the PSD has to be averaged over this weight function and equals:

$$S_x(f) = \int_0^{\infty} p_x(\tau) \frac{4\tau}{1 + \omega^2 \tau^2} d\tau. \quad (2.38)$$

Therefore, the kinetics is nonexponential, i.e., the correlation function does not decrease exponentially as a function of time  $|t|$ . Assuming a distribution  $p_x(\tau) \propto 1/\tau$ , between two

relaxation times  $\tau_1$  and  $\tau_2$ , the integration of the Lorentzian yields:

$$S_x(f) \propto \frac{1}{f} \quad (2.39)$$

for  $1/\tau_2 \ll f \ll 1/\tau_1$ . An example for the superposition of Lorentzian spectra yielding a  $1/f$  spectrum is shown in Fig. 2.4.6. Following the works of F. Du Pré [59] and A. Van Der Ziel [60], we now consider thermally-activated processes following an Arrhenius law (cf. Fig. 2.4.3),

$$\tau = \tau_0 e^{E/k_B T}, \quad (2.40)$$

where  $E$  is the activation energy and  $1/\tau_0$  is the frequency of attempts to surmount the activation barrier  $E$ , corresponding to typical inverse phonon frequencies. Moreover, the distribution of activation energies  $D(E)$  is assumed to be constant in a broad enough interval. From  $p_x(\tau) d\tau = D(E) dE$  and the assumption of a constant  $D(E)$  it follows that

$$p_x(\tau) = \frac{D(E)}{(d\tau/dE)} = k_B T \frac{D(E)}{\tau} = \frac{C}{\tau}, \quad (2.41)$$

where  $C$  is a constant factor. Therefore, the distribution  $p_x(\tau)$  has the required form. Although no assumptions about the exact physical origin of the individual fluctuators were made, it could be shown how  $1/f$  fluctuations are mathematically built from a superposition of these two-level processes.

One successful model of flicker noise based on this concept has been developed by A. McWhorter for semiconductors [61]. In this model, the  $1/f$  noise is related to fluctuations of the number of charge carriers at the semiconductor-oxide interface. Tunneling exchange of mobile charge carriers between the conduction channel near the surface and traps located inside the oxide layer covering the surface lead to resistance fluctuations. In detail, a constant distribution of tunneling distances leads to the required distribution of relaxation times  $p_x(\tau) \propto 1/\tau$ . The McWhorter model is widely used to interpret the flicker noise in electronic devices such as MOSFETs.

In general, the distribution of activation energies  $D(E, T)$  may also depend on the temperature  $T$ . This is the case when the concentration of defects, which are involved in trapping and detrapping processes of charge carriers and thus create the noise, is not fixed, but increases with  $T$ , or the fluctuating quantity itself is temperature-dependent. An extension of the previously discussed model taking into account a temperature-dependent distribution of activation energies has been developed by P. Dutta, P. Dimon and P. Horn and will be presented in the following [62].

### Dutta-Dimon-Horn Model

Assuming a temperature dependence of  $D(E, T)$  and combining Eq. (2.40), Eq. (2.38) and the fact that  $p_x(\tau) d\tau = D(E) dE$ , the PSD can be written as follows:

$$\begin{aligned} S_x(f, T) &= 4 \int_0^\infty \frac{\tau_0 e^{E/k_B T}}{1 + \omega^2 \tau_0^2 e^{2E/k_B T}} D(E, T) dE \\ &= \frac{2}{\omega} \int_0^\infty \frac{D(E, T)}{\cosh[(E - E_\omega)/k_B T]} dE. \end{aligned} \quad (2.42)$$

Here, it is  $E_\omega = -k_B T \ln(\omega \tau_0)$ , whereby—due to the large logarithmic factor—the values of  $E_\omega$  are comparable with typical activation energies in solids ( $E_\omega = 0.1\text{--}1$  eV) and  $\tau_0$  represents the attempt time, usually between  $10^{-14}$  and  $10^{-11}$  s. The function  $1/\cosh[(E - E_\omega)/k_B T]$  exhibits a peak of width  $\sim k_B T$  with a maximum at  $E = E_\omega$ . If the width of  $D(E, T)$  is considerably smaller than  $k_B T$ , the PSD reduces to a Lorentzian, cf. Eq. (2.37). Considering the case that the width of the distribution  $D(E, T)$  is far greater than  $k_B T$ , the solution of the integral in Eq. (2.42) is given by [62]:

$$S_x(f, T) \propto \frac{k_B T}{2\pi f} D(E_\omega, T). \quad (2.43)$$

Since the energy  $E_\omega$  depends on the frequency  $\omega$  only logarithmically, any not too strong energy dependence of  $D(E_\omega, T)$  results in only a small deviation of the PSD  $S_x(f)$  from the  $1/f$  behavior. In other words, a flat distribution of activation energies leads to perfect  $1/f$  noise with a frequency exponent of  $\alpha = 1$  and to a linear temperature dependence of the noise, whereas for a non-constant  $D(E_\omega, T)$  usually  $1/f^\alpha$  spectra with  $0.8 < \alpha < 1.4$  are observed. While for  $\alpha < 1$  higher energetic fluctuators come to dominate the noise characteristics, for  $\alpha > 1$  lower energetic processes are present.

If the distribution  $D(E_\omega, T)$  does not depend on  $T$  explicitly, but instead only through the temperature dependence of  $E_\omega$ , both the deviation of the temperature dependence of the PSD from a linear behavior and the deviation of the frequency exponent  $\alpha$  from 1 are related to the function  $D(E_\omega)$  and thus are connected by a simple relation within the phenomenological model of Dutta, Dimon, and Horn (DDH) [62]:

$$\alpha(f, T) = -\frac{\partial \ln(S_x(f, T))}{\partial \ln(f)} = 1 - \frac{1}{\ln(2\pi f \tau_0)} \left[ \frac{\partial \ln(S_x(f, T))}{\partial \ln(T)} - 1 \right]. \quad (2.44)$$

This equation is a central result of the DDH model and allows for a comparison of the calculated values of  $\alpha$  with the experimentally determined temperature-dependent frequency exponent in order to verify if the assumptions of the model are fulfilled. Although a good agreement is obtained in many cases, a constant shift of the predicted course of  $\alpha(T)$  may occur [63], which can be explained by an additional temperature dependence of the PSD. If changes of the number of thermally-activated switching events (excitation of defect states)

or of the coupling of fluctuations to the resistivity occur as a function of temperature, the introduction of a temperature-dependent function  $g(T) = a \cdot T^b$  is required. In this case, the PSD equals:

$$S_x(f, T) = 4 \int_0^\infty g(T) \frac{\tau_0 e^{E/k_B T}}{1 + \omega^2 \tau_0^2 e^{2E/k_B T}} D(E) dE. \quad (2.45)$$

Thus the predicted temperature-dependence of the frequency exponent  $\alpha$  is given by:

$$\alpha(f, T) = -\frac{\partial \ln(S_x(f, T))}{\partial \ln(f)} = 1 - \frac{1}{\ln(2\pi f \tau_0)} \left[ \frac{\partial \ln(S_x(f, T))}{\partial \ln(T)} - \frac{\partial \ln(g(T))}{\partial \ln(T)} - 1 \right]. \quad (2.46)$$

If the model calculation and experimental results agree, the distribution of activation energies for fluctuations in the experimentally accessible frequency and temperature window can be calculated via

$$D(E) \propto \frac{2\pi f S_x(f, T)}{k_B T g(T)}. \quad (2.47)$$

Deviations between calculated and experimentally determined frequency exponents can indicate an explicit temperature dependence of the energy distribution  $D(E, T)$ .

The DDH model has been particularly applied to  $1/f$  noise in metals, as for instance Bi, Ag, Ni, Au, and Cu [64, 62]. For some of the investigated films, a maximum in the distribution  $D(E)$  has been found, which could be related to known activation energies for the generation and motion of defects [2, 11]. Different effective scattering cross-sections between the accessible sites have a strong influence on the coupling to the resistivity and hence on the noise properties. Further studies have confirmed that  $1/f$  noise in metals can generally be attributed to the motion of defects and impurities [65], although it may be challenging to identify the defects which produce resistivity fluctuations. Besides the mentioned change of the anisotropic cross-section of an impurity, a second mechanism of resistance fluctuations in metals is given by the change of the interference pattern created by multiple scattering of electrons at the impurities [11].

## 2.5 Second spectrum

In this section, a brief discussion of non-Gaussian fluctuations and the so-called second spectrum will be presented. An example of non-Gaussian fluctuations is given by the generation-recombination noise, which has already been presented in Sec. 2.4.3. Apart from that, a variety of systems exist in which Gaussian  $1/f$  noise can be observed in a broad temperature range, but deviations from Gaussian behavior in the form of a time dependence of the  $1/f$  spectrum itself, so-called spectral wandering, are observed in a particular temperature region. In other words, a spectrum recorded at a time  $t_0$  yields different results from a spectrum acquired at  $t_1 = t_0 + \Delta t$ . Spectral wandering is observed for example in the vicinity of the critical point of organic charge-transfer salts [9], in colossal magnetoresistive materials



(e.g., manganites) with large-scale magnetic inhomogeneities [66], around the metal-insulator transition in doped silicon due to a glassy freezing of the electronic system [67] or in spin glasses [68, 69].

In general, for non-interacting fluctuators the probability distribution of the random quantity can be described by a Gaussian distribution (Eq. (2.7)). Therefore, the first-order and second-order central moments (mean value and variance) contain the entire information of the signal, cf. Sec. 2.1. However, for many systems the assumption of independent two-level fluctuators is not valid and higher-order central moments need to be calculated. In order to gain access to the fourth-order central moment, it is common to determine the so-called second spectrum  $S^{(2)}(f_2, f, T)$ , which is the power spectrum of the fluctuations of  $S_x(f, T)$  with time, that is, the Fourier transform of the autocorrelation function of the time series of  $S_x(f)$ , whereby an additional frequency  $f_2$  related to the time over which  $S_x(f)$  fluctuates is introduced. In detail, the second spectrum  $S^{(2)}(f_2, f)$  is calculated by dividing the first spectra  $S_x(f)$  into octaves and digitalizing the data by summing up the points of the first spectra within the octaves. Subsequently, a spectral analysis of these data is performed for each octave individually. Thereby, the frequency  $f_2 = 1/T_1$  can be introduced, where  $T_1$  is the measuring time for the first spectra. In general,  $S^{(2)}(f_2, f)$  probes a fourth-order noise statistics and thus possible deviations from Gaussian behavior. If the fluctuations are uncorrelated and hence caused by non-interacting fluctuators, the second spectrum is independent of the frequency  $f_2$  and thus can be considered as white noise. In contrast, for interacting (correlated) fluctuators,  $S^{(2)}(f_2, f)$  exhibits a  $1/f_2^\beta$  behavior, where  $\beta$  denotes the corresponding frequency exponent. In general, the magnitude of  $S^{(2)}(f_2, f)$  provides information about how much spectral wandering occurs, while its dependence on  $f_2$  indicates how the memory of the spectral shape decays in time. The most successful theoretical models for non-Gaussian fluctuations are the so-called droplet model and the hierarchical model [68, 69].

Further details about the experimental acquisition and analysis of the second spectrum can be found in Refs. [70, 71], as the focus of the present work will be rather placed on the investigation of Gaussian  $1/f$  fluctuations and random telegraph noise in selected condensed matter systems. In the following section, the emphasis will be laid on electronic noise in disordered conductors and percolating systems.

## 2.6 Electronic noise in percolating systems

In general, a great number of materials can be viewed as disordered conductors, which contain randomly distributed clusters with differing conductances. One example is given by dielectric materials, in which electrical conductivity may occur between metallic grains that have been introduced before hardening and form continuous chains between the electrodes attached to both ends of the sample. A further example are semiconductors in which charge

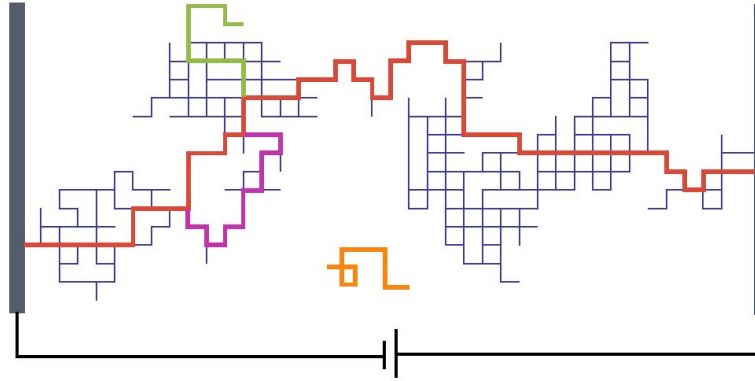


Figure 2.6.1: Exemplary random resistor network in the form of a square lattice just slightly above the percolation threshold ( $p > p_c$ ). Only unbroken bonds are shown. Prominent parts of the network are marked by colors. Red: the backbone, a subset of the infinite cluster, where all bonds have been removed which are not necessary for maintaining the connectivity of the structure throughout the lattice; green: conducting path, which does not contribute to the conductance, a so-called dead end; purple: a segment which may contribute to the electronic transport, a so-called shunt; orange: an isolated cluster. From [73].

transport at low temperatures is dominated by hopping conductivity, that is, tunneling of charge carriers between randomly distributed impurity centers.

### 2.6.1 Percolation in random resistor networks

By varying the proportions of insulating and conductive components in disordered mixtures, a certain type of metal-insulator transition can be induced. A simple approach in order to understand the electrical conductivity of such compounds is given by the model of a random resistor network which exhibits the percolation phenomenon. The term "percolation" was coined by S. Broadbent and J. Hammersley in 1957 [72] in connection with the percolation of gases and liquids through porous filters. An example for a two-dimensional random resistor network (RRN) in the form of a square lattice is depicted in Fig. 2.6.1.

The conductivity of the network can be measured via two electrodes attached to the edges of the RRN. A fraction of the conductors is randomly broken, corresponding to zero conductivity at this part of the network. Let  $p$  be the fraction of unbroken bonds (indicated by blue lines in Fig. 2.6.1). Obviously, as  $p$  decreases from 1, the resistance of the RRN increases. At a certain threshold  $p_c$ , which depends on the type and the dimension of the lattice, the resistance  $R(p)$  abruptly becomes infinite. For the depicted square lattice in two dimensions it is  $p_c = 1/2$ . Starting from  $p = 0$ , where  $R(p = 0) = \infty$ , we consider a successive increase of  $p$ . At  $p \ll 1$ , almost all conducting bonds are isolated, implying that there is no conductance through the entire network between the electrodes. As  $p$  increases, isolated clusters consisting of a few

adjacent conducting bonds can form (denoted by the orange colored bonds in Fig. 2.6.1) and their number will steadily increase for higher values of  $p$ . It should be emphasized that for  $p \ll p_c$ , even for an infinitely large random resistor network, all clusters consist of a finite number of sites. Only at the percolation threshold  $p = p_c$  does a so-called infinite cluster appear which threads the entire RRN. The situation depicted in Fig. 2.6.1 is just slightly above the threshold  $p_c$ , where the red colored path connects both electrodes at the edges. This path is called the "backbone" of the network, which is a subset of the infinite cluster and is formed by removing all dead ends and other bonds which are not necessary for maintaining the connectivity of the structure throughout the lattice. The fraction  $P_\infty(p)$  of all bonds that belong to the infinite cluster is given by

$$P_\infty(p) \propto (p - p_c)^\beta, \quad (2.48)$$

where  $\beta$  denotes a critical index depending on the type of lattice. Calculated values for the exponent  $\beta$  for two and three dimensions are given in Tab. 2.6.1.

In general, the total resistance of the RRN can be calculated after:

$$R = \frac{1}{I^2} \sum_m r_m i_m^2 = \frac{1}{I^2} \sum_m r_m^{-1} v_m^2, \quad (2.49)$$

where  $i_m$  denotes the current passing through the resistor  $r_m$ ,  $v_m$  corresponds to the respective voltage across  $r_m$  and  $I$  is the total current flowing through the lattice. The conductance  $G = 1/R$  of the lattice is determined only by the infinite cluster and tends to zero upon approaching the percolation threshold according to a power law:

$$G \propto (p - p_c)^t. \quad (2.50)$$

Since only a part of the infinite cluster, the above mentioned backbone, is involved in the conduction of the current, the exponent  $t$  is significantly greater than  $\beta$ . This can be seen in Tab. 2.6.1. This table also contains other relevant critical exponents for percolation processes in two and three dimensions.

## 2.6.2 Resistance fluctuations in lattice percolation systems

Resistance fluctuations can provide valuable information about percolation processes in disordered systems. The theory of electronic noise in lattice percolation systems was developed by R. Rammal *et al.* in 1985 [75]. The fluctuations  $\delta R(t)$  of the entire lattice resistance  $R$  are assumed to be produced by the fluctuations  $\delta r_m(t)$  of the individual resistances  $r_m$ .

In order to calculate  $\delta R(t)$ , Eq. (2.49) needs to be linearized. Therefore, we consider the fact that the Joule power is extremal in the variations  $\delta i_m$  of the currents at given resistances  $r_m$ .

Table 2.6.1: Critical exponents and fractal dimensions for percolation in two and three dimensions after [74, 11] and references therein.

Quantity	Scaling	Exponent	$d = 2$	$d = 3$
Order parameter	$P_\infty(p) \propto (p - p_c)^\beta$	$\beta$	5/36	0.42
Correlation length	$\xi(p) \propto  p - p_c ^{-\nu}$	$\nu$	4/3	0.88
Cluster mass	$M(r) \propto r^{d_f}$	$d_f$	91/48	2.52
Backbone mass	$M_B(r) \propto r^{d_B}$	$d_B$	1.62	1.86
Chemical path	$l(r) \propto r^{d_{\min}}$	$d_{\min}$	1.13	1.37
Random Walk	$\langle r^2(t) \rangle \propto t^{2/d_w}$	$d_w$	2.87	3.80
Conductivity	$\sigma_{dc}(p) \propto (p_c - p)^t$	$t$	1.30	1.99
Superconductivity	$\sigma_S \propto (p - p_c)^{-s}$	$s$	1.30	0.74
PSD [75]	$S_R/R^2 \propto (p - p_c)^{-\kappa}$	$\kappa$	1.34	2.33

Hence we obtain that

$$\delta R(t) = \frac{1}{l^2} \sum_m \delta r_m(t) i_m^2. \quad (2.51)$$

In disordered percolating systems the microscopic correlation lengths (e.g., the mean free-path of charge carriers) are usually smaller than the dimensions of clusters of which the heterogeneous conductor is composed. Therefore, the fluctuations in different bonds of the network can be considered as uncorrelated. Furthermore, the resistances  $r_m$  are assumed to be identical for all conducting bonds, i.e.,  $r_m = r$ . Thus the normalized power spectral density  $S_R(f)/R^2$  of the fluctuations of the entire lattice resistance equals

$$\frac{S_R(f)}{R^2} = \frac{s_r(f)}{r^2} \frac{\sum_m i_m^4}{\left(\sum_m i_m^2\right)^2}, \quad (2.52)$$

where  $s_r(f)$  is the PSD of fractional fluctuations of the resistance  $r$ . As  $p$  approaches the percolation threshold  $p_c$ , the total PSD diverges as

$$\frac{S_R(f)}{R^2} \propto (p - p_c)^{-\kappa}, \quad (2.53)$$

with  $\kappa$  denoting another critical exponent, cf. Tab. 2.6.1.

In a disordered system, the current density is strongly inhomogeneous, especially in the vicinity of the metal-insulator transition. The most significant contribution to the resistance and thus to the resistance noise comes from so-called "bottlenecks" which connect large parts of the infinite cluster. Here, the current density is higher than in other parts of the network. The contribution of such a region to the resistance is proportional to the local electric field squared [11]. Importantly, the contribution to the resistance noise is even stronger, since it is proportional to the fourth power of the local field. As for  $p \gg p_c$  the number of current paths in the system is high, the uncorrelated contributions of the individual resistances  $r_m$

to the fluctuations of the total resistance cancel one another and the total noise magnitude is relatively low. As the system approaches  $p_c$ , the number of effective current paths decreases and the effect of their cancellation becomes smaller, which is why a considerable increase of the flicker noise magnitude is expected in the vicinity of the percolation threshold (cf. Monte Carlo results by R. Rammal *et al.* [75]).

Since  $p$  and  $p_c$  are not easily accessible in experiments, the combination of Eq. (2.50) and Eq. (2.53) can be considered in order to find a scaling behavior of  $S_R(f)/R^2$  and  $R$ :

$$\frac{S_R(f)}{R^2} \propto R^w, \quad (2.54)$$

with  $w = \kappa/t$ . Therefore, the exponent  $w$  can be directly obtained from the measured quantities  $S_R(f)/R^2$  and  $R$ .

A great number of experimental studies have demonstrated a strongly enhanced  $1/f$  noise magnitude for disordered conductors with percolative transitions. Examples include various manganite systems such as  $\text{La}_{2/3}\text{Ca}_{1/3}\text{MnO}_3$  [76] or  $\text{La}_{5/8-x}\text{Pr}_x\text{Ca}_{3/8}\text{MnO}_3$  [6, 77], and the ferromagnetic semimetal  $\text{EuB}_6$ , which has been intensively studied in the group of Prof. Dr. J. Müller at the Goethe University in Frankfurt [5, 78, 79]. Furthermore, evidence for percolative-type superconductivity in the layered organic Mott system  $\kappa\text{-(BEDT-TTF)}_2\text{Cu[N(CN)}_2\text{]Cl}$  was also provided by means of fluctuation spectroscopy [80]. In the following, we will give a review of the work on  $\text{EuB}_6$ .

### 2.6.3 Percolation of magnetic polarons in $\text{EuB}_6$

Exemplary noise data reported by P. Das *et al.* on  $\text{EuB}_6$  are shown in Fig. 2.6.2. In panel (a), a strong divergence of the normalized noise magnitude  $S_R/R^2$  evaluated at 1 Hz can be seen in the vicinity of the ferromagnetic transition temperature. The inset shows an exemplary  $1/f$  noise spectrum. Figure 2.6.2 (b) shows a log-log plot of the same data highlighting a steplike increase of the PSD below  $T^* = 35$  K, which coincides with a minimum in the resistivity and marks the onset of magnetic polaron formation, and a power-law divergence below  $T_{c1}$  following  $S_R/R^2 \propto T^{-6}$  (solid line). Finally, Fig. 2.6.2 (c) demonstrates the expected scaling behavior after Eq. (2.54),  $S_R/R^2 \propto R^w$ , in the percolation regime with  $w \approx -2.1$  as determined from a linear fit.

In this case, a percolation of magnetic polarons is deduced from the experimental data. These magnetic clusters are considered as entities of a more conducting and magnetically ordered phase, which is embedded in a paramagnetic and poorly conducting background. Let  $p$  be the portion of the metallic phase in a less conducting background, the portion of which is given by  $q$ . The magnetic polarons form a continuous conduction path through the sample at  $T_{c1}$ , which corresponds to the percolation threshold  $p_c$ . This is accompanied by a considerable drop of the resistance at  $p_c$  and a delocalization of charge carriers. Moreover, the noise

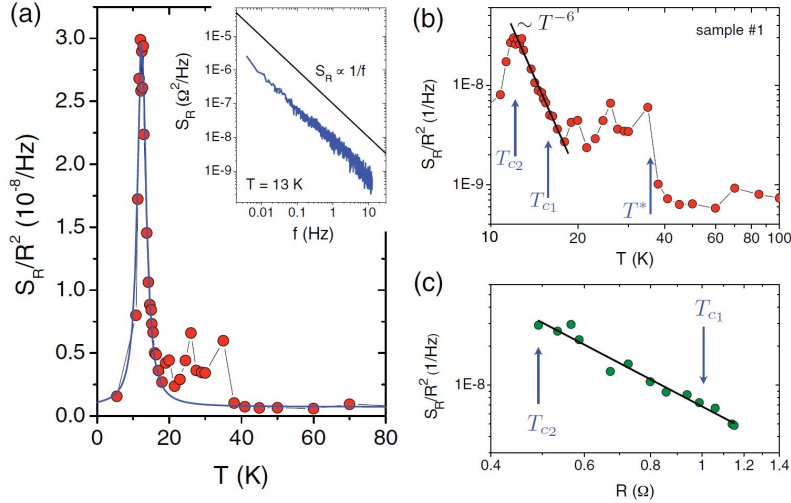


Figure 2.6.2: Resistance noise measurements on  $\text{EuB}_6$ . (a) Normalized PSD  $S_R(1\text{ Hz})/R^2$  against temperature  $T$ . In the vicinity of the ferromagnetic transition temperature, a strong enhancement of the  $1/f$  noise magnitude can be observed. Inset shows a typical spectrum at 13 K. (b) Log-log plot of the same data emphasizing a steplike increase of the noise level below 35 K and a power-law divergence following  $S_R/R^2 \propto T^{-6}$  (solid line). (c) Scaling  $S_R/R^2 \propto R^w$  in the percolation regime with  $w \approx -2.1$  as determined from a linear fit. Content reprinted from Ref. [5] with permission of the American Physical Society.

measurements indicate a percolation threshold  $q_c$  for the less conducting regions at  $T_{c2}$ , which implies that the resistance and its fluctuations are sensitive to different parts of the conducting network. This magnetically driven electronic phase separation is schematically depicted in Fig. 2.6.3. At  $T^* = 35$  K, magnetic polarons are suggested to form, which coincides with the steplike increase in the noise magnitude. Upon decreasing the temperature, these magnetic clusters grow in size and start to overlap until an infinite cluster is formed and spontaneous magnetization occurs. In addition, the number of magnetic polarons also increases towards lower temperatures. This special case of a two-component percolation scenario as suggested by P. Das *et al.* for  $\text{EuB}_6$  is not discussed for other compounds such as manganites [6], since in many cases the two percolation thresholds  $p_c$  and  $q_c$  are equal [81, 82].

It should be mentioned that, besides the above discussed standard discrete percolation network model, further approaches exist such as the continuum random void and inverted random void models. As pointed out by A. Tremblay *et al.*, the percolation transport exponents for a discrete lattice model and a continuum system can differ significantly [83]. Both for the manganites, where an exponent of  $w = 2.9 \pm 0.5$  was found [6], and for  $\text{EuB}_6$ , with a determined (negative) exponent of  $w = -2.1 \pm 0.3$ , the absolute values of the experimentally obtained exponent  $w$  are in good agreement with continuum three-dimensional random void and inverted random void models, which yield scaling exponents  $w = 2.1$  and 2.4, respec-

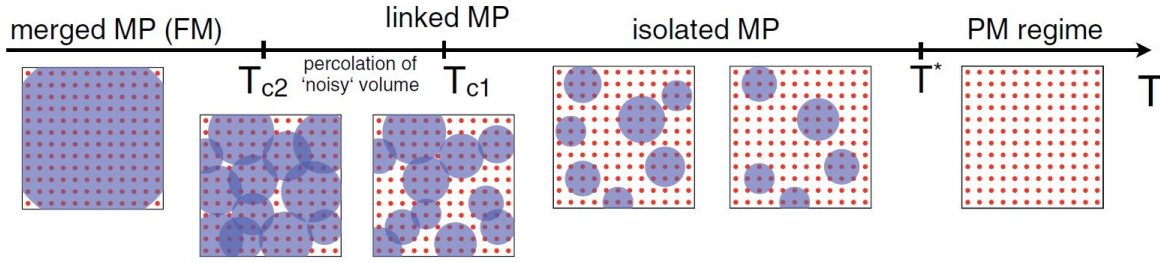


Figure 2.6.3: Schematic diagram of magnetic polaron percolation in  $\text{EuB}_6$ . Upon decreasing the temperature, highly conducting magnetically ordered clusters in a paramagnetic and poorly conducting background start to form, which grow in size towards even lower temperatures. At low enough temperatures, they start to overlap until an infinite cluster is formed and spontaneous magnetization occurs. Content reprinted from Ref. [5] with permission of the American Physical Society.

tively [83]. In the case of  $\text{EuB}_6$ , the negative sign of the exponent  $w$  has been explained by the above-mentioned assumption that the resistance and its fluctuations are sensitive to different parts of the conducting network [5].

To summarize, it was shown that resistance noise spectroscopy can serve as a means to detect percolative transitions and that it allows for an extraction of the relevant percolation exponents, which can be compared to theoretical simulations of different percolation network models.

## 2.7 Dielectric polarization fluctuations

So far, the main focus has been on electronic noise in metals and semiconductors. Experimentally, the study of fluctuation processes in insulators may be challenging. One method to investigate insulating materials is given by dielectric polarization noise measurements. Here, the polarization noise of a sample is measured as current or voltage fluctuations produced within a capacitance cell. The study of dielectric polarization noise enables conclusions to be drawn regarding equilibrium structural dynamics in insulators of current interest such as (relaxor) ferroelectrics, prototype glass formers, liquid crystals and proteins [84, 85, 86].

### 2.7.1 Fluctuation-dissipation theorem

In general, the measurements of dielectric polarization noise are strongly related to dielectric spectroscopy experiments via the fluctuation-dissipation theorem (FDT). The FDT is a general result of statistical thermodynamics which quantifies the relation between the fluctuations in a system at thermal equilibrium and the response of the system to external perturbations. In other words, fluctuations and dissipation are caused by the same mechanism, namely the

interaction of a physical variable with a heat bath. As indicated in Sec. 2.4.1, the Johnson-Nyquist formula (Eq. (2.25)) is a special formulation of the FDT. Another example is the Brownian motion of particles, where fluctuations of the particle at rest can be related to the dissipative frictional force which acts against external perturbations of the system in a particular direction [46, 47]. More generally, the FDT can be written as

$$S_x(\omega) = \frac{2k_B T}{\omega} \chi''(\omega), \quad (2.55)$$

where  $S_x(\omega)$  is the PSD of the measured quantity  $x(t)$ ,  $\omega = 2\pi f$  represents the angular frequency and  $\chi''(\omega)$  denotes the imaginary part of the complex frequency-dependent susceptibility  $\chi(\omega)$ , the linear response function of a system [87].

In order to investigate the dielectric polarization noise of a sample, we now consider the Johnson-Nyquist formula for an electrical network with impedance  $Z(\omega)$ :

$$S_V(\omega) = 4k_B T \operatorname{Re}[Z(\omega)]. \quad (2.56)$$

Here,  $\operatorname{Re}[Z(\omega)]$  is the real part of the impedance producing the noise signal. By modeling the sample as a parallel circuit of a capacitance  $C$  and a resistance  $R$ , we obtain [11, 12, 86, 88]

$$S_V(\omega) = 4k_B T \frac{R(\omega)}{1 + [\omega R(\omega)C(\omega)]^2}. \quad (2.57)$$

In general, one can now measure  $Z$  and  $S_V$  of the sample independently and check the validity of the FDT. There is considerable interest in studying FDT violations experimentally, e.g., for spin glasses, structural glasses, relaxor ferroelectrics, and other nonequilibrium systems [86, 89, 85]. There exist a number of theoretical studies indicating FDT violations in the aforementioned systems, and dielectric polarization noise measurements appear to be a promising tool to prove these predictions. However, to date, the number of published experimental studies is still relatively low. Several publications focus on a supercooled liquid, glycerol, but obtain contradicting results: While indications for a weak FDT violation were reported by T. Grigera and N. Israeloff [89], no violation was observed by J. Schindele *et al.* [86]. A further work by K. O'Brien is devoted to dielectric noise spectroscopy of relaxor ferroelectrics [90]. Finally, several publications deal with a nanometer-scale probing of dielectric fluctuations by means of atomic force microscopy [91, 92, 93].

### 2.7.2 Dielectric spectroscopy

In order to prove the validity of the FDT, the impedance  $Z$  has to be determined by dielectric spectroscopy measuring  $R$  and  $C$ . This method allows for conclusions to be drawn about the dielectric properties of a material as a function of frequency, and is based on the interaction of an external field with the electric dipole moment of the sample. By measuring the impedance



$Z(\omega)$  as a function of frequency, the permittivity or dielectric function

$$\epsilon(\omega) = \epsilon'(\omega) - i\epsilon''(\omega) \quad (2.58)$$

can be determined via  $\epsilon(\omega) = 1/[i\omega Z(\omega) \cdot C_0]$ , where  $C_0$  denotes the capacitance of the empty capacitor in which the sample is placed.

Generally speaking, the permittivity connects the macroscopic electric polarization  $\vec{P}$  in a material and the external electric field  $\vec{E}$ , which causes the polarization, i.e., the alignment of permanent electric dipoles (e.g., molecules) inside the sample:

$$\vec{P}(\omega) = \epsilon_0(\epsilon(\omega) - 1)\vec{E}(\omega), \quad (2.59)$$

where  $\epsilon_0$  denotes the vacuum permittivity. Therefore,  $\epsilon(\omega)$  is a measure for the response of a material to an applied electric field. With the electric susceptibility  $\chi(\omega) = \epsilon(\omega) - 1$  the polarization can also be written as

$$\vec{P}(\omega) = \epsilon_0\chi(\omega)\vec{E}(\omega). \quad (2.60)$$

Usually, instead of  $\chi(\omega)$  the permittivity  $\epsilon(\omega)$  is preferably presented as a result of dielectric spectroscopy measurements. Importantly, the real part

$$\epsilon'(\omega) = C(\omega)/C_0 \quad (2.61)$$

is a measure for the polarization, while the imaginary part

$$\epsilon''(\omega) = 1/[\omega R(\omega)C_0] \quad (2.62)$$

can be related to the dissipation of energy. The typical frequency range investigated by dielectric spectroscopy is from below 1 Hz up to several MHz. The main phenomena contributing to  $\epsilon(\omega)$  are dipolar relaxation, atomic polarization, electronic polarization and ionic relaxation, whereby each effect dominates at a different frequency range. Figure 2.7.1 (a) schematically shows two processes that can lead to dielectric relaxation: molecular reorientation and hopping of particles in a double-well potential. Generally, as can be seen in Fig. 2.7.1 (b)–(d), these processes result in a maximum in  $\epsilon''(\omega, T)$  and a steplike feature in  $\epsilon'(\omega, T)$ , both as a function of frequency and temperature. At high frequencies and low temperatures, the underlying relaxation processes cannot follow the AC (alternating current) electric field anymore, which leads to a decrease of  $\epsilon'$ . The peak in  $\epsilon''$  can be related to a maximum absorption of field energy when the AC-field frequency matches the reorientation frequency of the dipoles [94].

A simple model allowing to extract information about molecular dynamics from the dielectric

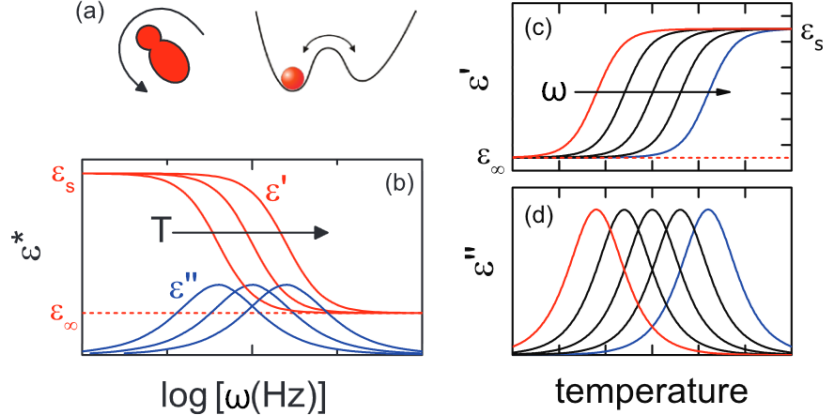


Figure 2.7.1: (a) Schematic representation of two possible processes leading to dielectric relaxation: molecular reorientation and hopping of charged particles in a double-well potential. (b) Schematic frequency dependence of the real and imaginary part of the dielectric function  $\epsilon(\omega)$  for different temperatures. [(c) and (d)] Temperature dependence of (c)  $\epsilon'$  and (d)  $\epsilon''$  at different frequencies. After Ref. [94] with permission of IOP Publishing.

function was introduced by P. Debye [95]. Within this model, it is assumed that the dipolar molecules in a dielectric material do not interact with each other and that the temporal change of the polarization is proportional to the polarization itself:

$$\frac{d\vec{P}(t)}{dt} \propto \vec{P}(t). \quad (2.63)$$

We consider a sample which has been polarized by an external field. After removing the field, the polarization decays exponentially with the characteristic relaxation time  $\tau_D$  after Eq. (2.63). In addition, we assume a nonzero static equilibrium polarization  $\vec{P}_s$  and a contribution  $\vec{P}_\infty$ , which is able to follow the external field instantaneously. Therefore, the time-dependent polarization equals:

$$\frac{d\vec{P}(t)}{dt} = \frac{\vec{P}(t) - \vec{P}_s + \vec{P}_\infty}{\tau_D}. \quad (2.64)$$

A Laplace transform yields the real part of the dielectric permittivity

$$\epsilon' = \epsilon_\infty + \frac{\epsilon_s - \epsilon_\infty}{1 + \omega^2 \tau_D^2}, \quad (2.65)$$

and the imaginary part, which equals

$$\epsilon'' = \frac{(\epsilon_s - \epsilon_\infty) \omega \tau_D}{1 + \omega^2 \tau_D^2}. \quad (2.66)$$

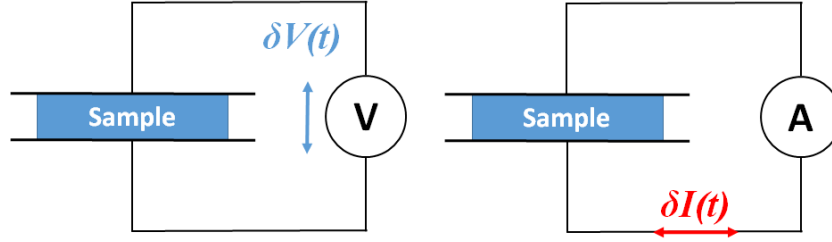


Figure 2.7.2: Two possible setups for the revelation of dielectric polarization noise. The left sketch indicates the measurement of voltage fluctuations  $\delta V(t)$  by means of a voltmeter, whereas the right circuit illustrates the measurement of current fluctuations  $\delta I(t)$  with an ammeter.

Here,  $\epsilon_\infty$  is the permittivity at the high frequency limit and  $\epsilon_s$  represents the static, low frequency permittivity. These quantities are also schematically depicted in Fig. 2.7.1 (b) and (c). Generally, the relaxation time  $\tau_D$  can be obtained from the characteristic maximum in  $\epsilon''(\omega)$  at  $\omega = 1/\tau_D$ .

### 2.7.3 Dielectric polarization noise in selected model systems

After the introduction of the complex permittivity  $\epsilon(\omega)$ , by exploiting Eq. (2.61) and Eq. (2.62), Eq. (2.57) can be rewritten as follows:

$$S_V(\omega) = 4k_B T \frac{\epsilon''(\omega)}{\omega C_0 (\epsilon'(\omega)^2 + \epsilon''(\omega)^2)}. \quad (2.67)$$

Therefore, the determination of the dielectric function  $\epsilon(\omega)$  (or the impedance  $Z(\omega)$ ) allows for a prediction of the thermal polarization noise  $S_V(\omega)$  by means of the FDT. In addition,  $S_V(\omega)$  can be determined experimentally by measuring the voltage fluctuations of the sample-filled capacitor. It should be emphasized that, in contrast to standard dielectric measurements, no externally applied electric field is required in order to investigate the structural dynamics of materials by means of noise spectroscopy.

Apart from voltage fluctuations, the investigation of the current noise  $S_I(\omega)$  is also possible. Here, the current noise PSD equals [96]

$$S_I(\omega) = 4k_B T \frac{1}{R(\omega)} = 4k_B T \omega C_0 \epsilon''(\omega). \quad (2.68)$$

The measurement principle for both voltage and current noise measurements is shown in Fig. 2.7.2. Polarization fluctuations inside the sample can be revealed by measuring either a fluctuating current  $\delta I(t)$  with an ammeter, whose internal resistance should ideally be close to zero, or by measuring voltage fluctuations  $\delta V(t)$  by means of a voltmeter with a very high internal resistance.

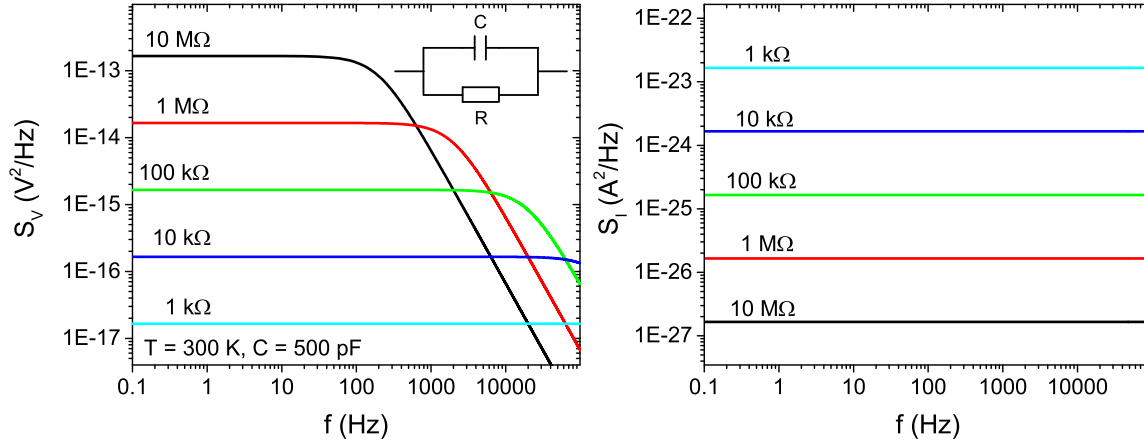


Figure 2.7.3: Calculated voltage noise (left) and current noise (right) spectra for an RC parallel circuit after Eq. (2.57) and Eq. (2.68) at  $T = 300$  K and for a constant  $C = 500$  pF. The circuit is schematically depicted in the inset of the left panel.

We now consider the voltage and current power spectral density of a sample, which can be modeled as a parallel circuit of a resistor and a capacitor. By substituting typical values for  $R$  and  $C$  into Eq. (2.57) and Eq. (2.68) and assuming that  $R$  and  $C$  are frequency-independent, typical noise spectra as shown in Fig. 2.7.3 are obtained. A constant value of  $C = 500$  pF is assumed for the capacitance, while the resistance varies between  $1$  k $\Omega$  and  $1$  M $\Omega$ . Moreover, it is  $T = 300$  K. The left panel of Fig. 2.7.3 illustrates the voltage PSD  $S_V(f)$ , which exhibits a flat behavior at low frequencies and a  $1/f^2$ -type decrease at higher  $f$ . At low  $f$ , the PSD is proportional to the resistance  $R$  as expected after the Johnson-Nyquist formula (Eq. (2.25)), while at higher frequencies the low-pass behavior of the resistor-capacitor circuit (schematically depicted in the inset of the left panel) comes to dominate. Here, the cutoff frequency shifts as  $f_{\text{cutoff}} = 1/(2\pi RC)$  with increasing resistance towards lower frequencies. In contrast to that, the current noise PSD, which is depicted in the right panel of Fig. 2.7.3, displays an entirely constant behavior, since it is independent of frequency and capacitance after Eq. (2.68). In this case, the PSD decreases towards higher resistances, which is intuitively clear, since a higher resistance in such an electrical circuit leads to a smaller current.

In the following, we put the focus on the expected noise behavior of a sample which exhibits a Debye relaxation behavior (cf. Sec. 2.7.2). This can be calculated by exploiting Eq. (2.67) and Eq. (2.68). Here, we insert the Debye relaxation equations (Eq. (2.65) and (2.66)) for  $\epsilon'$  and  $\epsilon''$  and utilize the following exemplary values for the respective parameters, which were chosen in analogy to the calculation in Ref. [96]:  $\epsilon_\infty = 2$ ,  $\epsilon_s = 20$ ,  $C_0 = 10$  pF and  $\tau_D = 1$  ms. Fig. 2.7.4 shows the results of the calculation for three different relaxation processes. In all three panels, the voltage noise PSD  $S_V$  (black curve) and the current noise PSD  $S_I$  (blue curve) are plotted against  $\omega\tau_D$ . In addition to that, the imaginary part  $\epsilon''(\omega)$  of the permittivity is plotted in red color. For reasons of simplicity, the ordinate axis of  $\epsilon''(\omega)$  is not shown. However, one

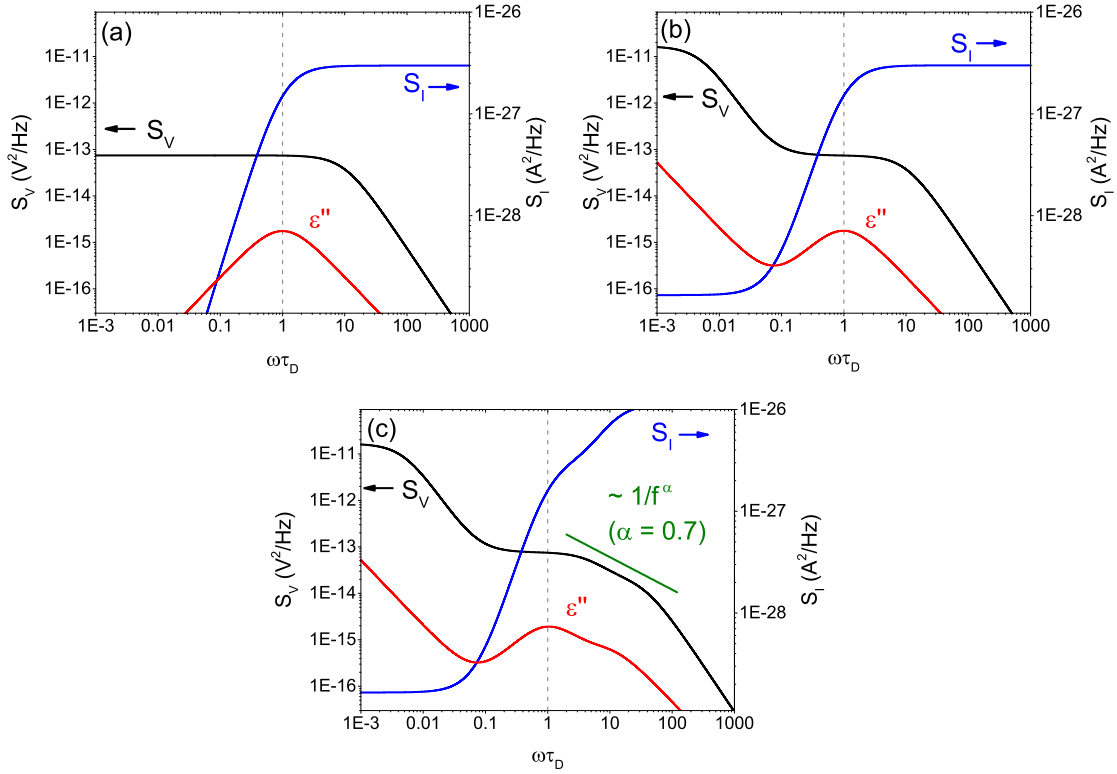


Figure 2.7.4: Calculated  $S_V$ ,  $S_I$  and  $\epsilon''$  against  $\omega\tau_D$  for a sample describable by the Debye relaxation model. (a) Standard Debye relaxation with a peak in  $\epsilon''$  at  $\omega\tau_D = 1$ , indicated by a dashed vertical line. (b) Extended Debye relaxation with an additional contribution of ionic conduction. (c) A second relaxation process is added in order to obtain an asymmetric shape of the peak in  $\epsilon''$ .

decade of the right axis representing  $S_I$  also corresponds to one decade of  $\epsilon''(\omega)$ .

Fig. 2.7.4 (a) shows the calculation for a sample following a standard Debye relaxation behavior and exhibiting a symmetric peak in  $\epsilon''$  at  $\omega\tau_D = 1$  (indicated by a dashed vertical line). At small frequencies, the voltage noise PSD shows a flat behavior, before a  $1/f^2$ -type decrease sets in around the relaxation frequency, i.e., at  $\omega\tau_D = 1$ . In contrast to that,  $S_I$  increases at low frequencies and is proportional to  $f^2$ , and flattens out in the vicinity of the maximum in  $\epsilon''$ .

In the following, the simple Debye relaxation behavior is extended and a contribution of ionic conduction is added in order to obtain a behavior of  $\epsilon''(\omega)$  as it is commonly observed in dielectric spectroscopy experiments. For this purpose, we can write the imaginary part of the dielectric function as

$$\epsilon''(\omega\tau_D) = \epsilon''_{\text{Debye}}(\omega\tau_D) + \frac{0.1}{\omega\tau_D}, \quad (2.69)$$

which implies an increase of  $\epsilon''$  at low values of  $\omega\tau_D$ , cf. Fig. 2.7.4 (b), and has a strong impact on the noise behavior. In the case of  $S_V$ , the noise spectrum remains unaltered at high

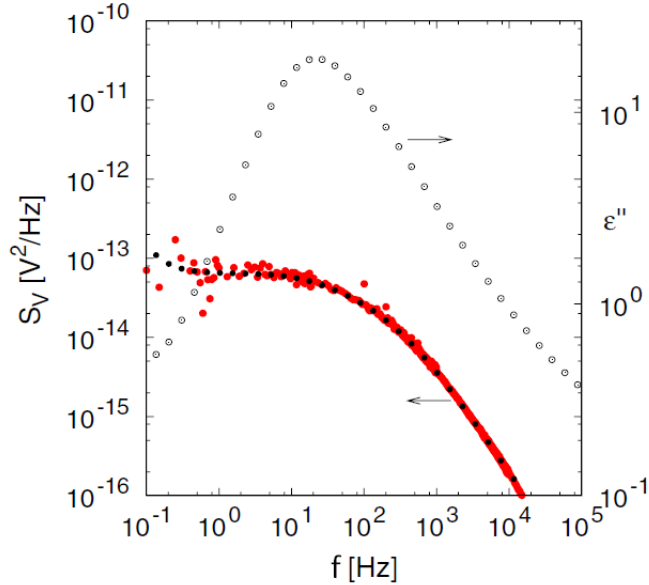


Figure 2.7.5: Dielectric polarization noise measurements on glycerol at 205 K. Imaginary part  $\epsilon''$  (open black circles, right axis) is plotted against the frequency  $f$ . In addition, red circles indicate the directly measured voltage noise  $S_V$ , and the black filled circles are related to a prediction based on the dielectric permittivity measurement by exploiting the FDT. Content reprinted from Ref. [86] with permission of the American Physical Society.

frequencies, whereas for small  $\omega\tau_D$  a new feature is observed. After a narrow plateau around  $\omega\tau_D = 1$  a second  $1/f^2$ -like increase occurs for decreasing  $\omega$  and is followed by another plateau at very low frequencies. A similar modification is observed for  $S_I$ , which displays a flat behavior at the lowest and highest frequencies, and an increase proportional to  $f^2$  in the intermediate frequency range.

Finally, a second relaxation process is added to the extended Debye relaxation process depicted in Fig. 2.7.4 (b) in order to obtain an asymmetric peak in  $\epsilon''$ . This, of course, has a strong impact on the noise spectra, which are shown in Fig. 2.7.4 (c). For frequencies just above  $\omega\tau_D = 1$ , the voltage noise PSD  $S_V$  exhibits a  $1/f^\alpha$  behavior with  $\alpha = 0.7$  (indicated by the green line). In addition, instead of a constant behavior at high frequencies,  $S_I$  displays a further increase with a smaller slope than the one for  $\omega\tau_D < 1$ .

To summarize, the most important observation is that any modification of the imaginary part  $\epsilon''$  of the dielectric function leads to drastic changes in both the voltage noise and current noise spectra. These theoretical calculations provide a first idea for the interpretation of dielectric polarization noise measurements. Figure 2.7.5 shows the validity of these theoretical considerations. Here, the imaginary part  $\epsilon''$  (open black circles) is plotted as a function of frequency  $f$  as obtained from measurements on glycerol at 205 K [86]. The application of the FDT allows a prediction of the voltage noise power spectral density  $S_V$  from the mea-

sured dielectric function. Here, the experimental data (red circles) and the calculated noise spectrum (black filled circles) lie on top of each other almost perfectly. Thus, in this case the validity of the FDT is verified.

As part of the present work, an experimental setup for dielectric polarization noise measurements on pressed pellet samples has been designed and successfully tested in the laboratory of Prof. Dr. S. Nair at IISER Pune (India). After a detailed discussion of experimental techniques with regard to electronic transport measurements at low temperatures and, in particular, different ways of measuring resistance noise, the experimental realization of dielectric polarization noise measurements will be a substantial part of the following chapter.





# 3 Experimental Realization of Electronic Transport and Noise Measurements

The focus of the present chapter lies on the introduction of the relevant experimental techniques and setups, particularly with regard to fluctuation spectroscopy measurements and electronic transport studies at low temperatures. First, the utilized cryostats and their operation principle will be described. Subsequently, the most important experimental details of fluctuation spectroscopy measurements will be presented. Finally, the last part of the chapter is devoted to the design and realization of a novel experimental setup for the measurement of dielectric polarization noise.

## 3.1 Cryostats and low-temperature physics

A major part of the measurements presented in this thesis work were carried out at low temperatures in a so-called cryostat. A cryostat is a highly insulated container which is used to maintain low temperatures of samples or devices mounted within the cryostat. In general, there exist various types of cryostats, each of which having advantages and disadvantages compared to the others. In the present work, three types of cryostats have been utilized: a helium-4 bath cryostat, a continuous helium-flow cryostat with variable temperature insert (VTI) and a closed-cycle refrigerator.

Bath cryostats and continuous-flow cryostats contain large supplies of cryogenic liquids, in many cases helium-4, the boiling point of which is 4.2 K. In general, a cryostat is vacuum-insulated in order to reduce the heat load due to conduction and convection. In addition to that, in most cryostats the radiation load is reduced by the use of a so-called multi-layer superinsulation consisting of many thin layers of low emissivity materials. The helium vapour which boils away from the bath effectively cools the thermal shields around the outside of the bath. In order to access temperatures between 4.2 K and 300 K, the cooling power originating from the cryogenic liquid can be countered by heating power provided by a heater near the mounted sample, which is usually operated by a proportional-integral-derivative (PID) temperature controller. The difference between bath and continuous-flow cryostats lies in the thermal coupling of the sample to the coolant. In the case of a helium-4 bath cryostat, the sample is commonly mounted in an internal vacuum chamber (IVC) which is surrounded by the helium reservoir. The sample is thermally coupled to the surrounding

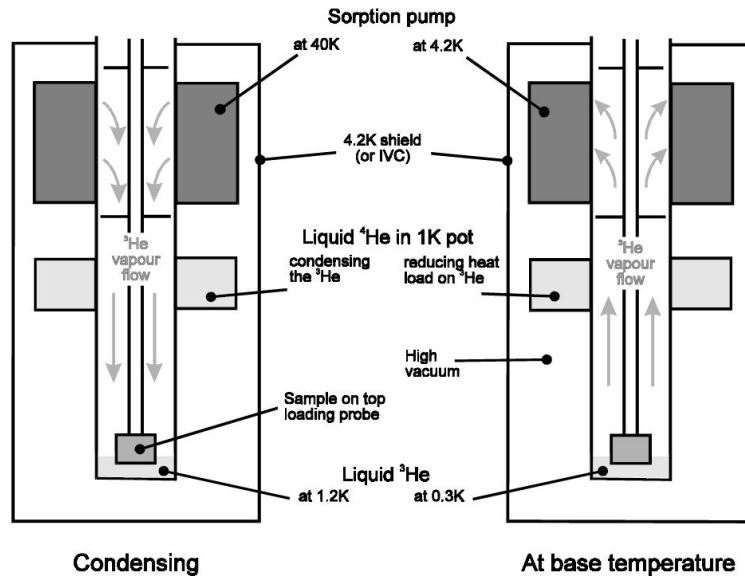


Figure 3.1.1: Operating principle of a sorption pumped helium-3 system during the condensing procedure (left) and at base temperature (right). From [97].

He bath by means of a small amount of introduced helium exchange gas. In this regard, it should be noted that an excessive amount of exchange gas restricts the accessible temperature range, since the available heating power is limited. Furthermore, the boil-off rate of the helium bath will increase. Despite a very good temperature stability of such a bath cryostat, the operation at temperatures far above 4.2 K turns out to be difficult due to the ever-present cooling power, even if the majority of He exchange gas has been removed. In the case of the bath cryostat utilized in the present work (HelioxVL, Oxford Instruments), temperatures up to 150 K can be reached in a convenient way. In addition, a further advantage of the present HelioxVL cryostat is an internal helium-3 circuit, which allows for cooling procedures down to about 300 mK. More precisely, the sorption pumped helium-3 system is capable of maintaining these ultra-low temperatures for a limited time. The operating principle of such a helium-3 system is schematically depicted in Fig. 3.1.1.

The sorption pump will absorb gas when cooled below a particular temperature (typically 40 K), which is done by drawing liquid helium from the main bath through a heat exchanger. In addition, a heater is fitted to the sorption pump in order to control its temperature precisely. The so-called 1 K pot, which is fed from the main helium bath through a needle valve, is utilized to condense the helium-3 gas while the sorption pump is warmed above 40 K, where it will not absorb any helium-3. Consequently, the condensed helium-3 runs down from the reservoir through the 1 K pot to the sample and the helium-3 pot and reduces their temperature down to the temperature of the 1 K pot, which will be about 1.2 K. After most of the gas has condensed into the insert, the needle valve of the 1 K pot is closed and the sorb is

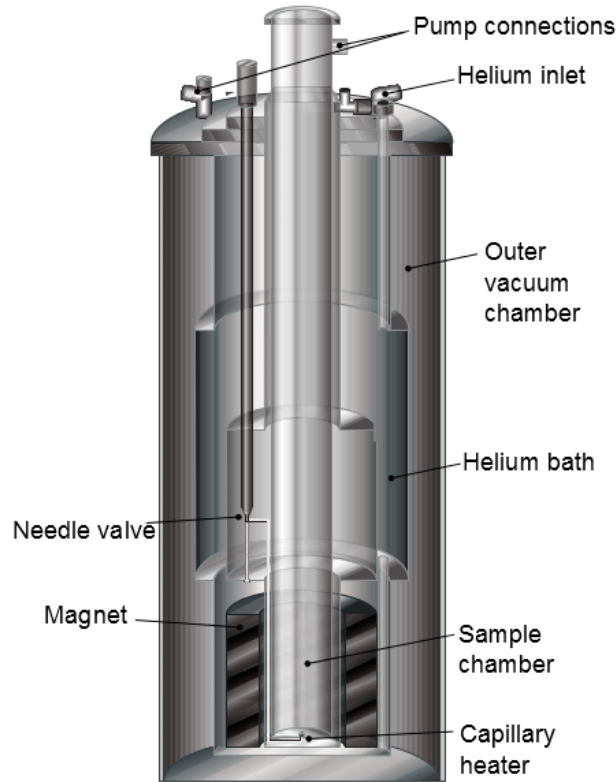


Figure 3.1.2: Schematic representation of a continuous flow cryostat. After [98].

now cooled in order to reduce the vapour pressure above the condensed helium-3. Thus the sample temperature drops down to the base temperature of 300 mK as soon as the limiting pressure has been reached. This situation, as depicted in the right panel of Fig. 3.1.1, can be maintained for several hours. However, this time span gets reduced significantly in case a small heating power is introduced in order to achieve temperatures between 0.3 K and 1.2 K. A major part of the electronic transport measurements discussed in the present work has been carried out in a continuous flow cryostat with a VTI system (VTI 51/30, Oxford Instruments). The temperature range of such a VTI system usually spans from 1.5 K to 300 K. The advantage in comparison with bath cryostats is that the sample temperature can be controlled continuously at any point in this given range. A schematic representation of such a continuous flow cryostat is shown in Fig. 3.1.2.

In contrast to the above described bath cryostat, the sample is directly exposed to a helium-4 gas flow in a separately insulated chamber. Liquid helium is fed from the main He bath through a capillary and a needle valve. In order to prevent the presence of liquid helium inside the sample chamber, it is vaporized by means of a heater located at the end of the capillary (vaporizer). The gas flows past the sample and out of the exhaust port of the insert to a pump located outside the cryostat. The gas flow can be controlled by the needle valve opening and

by the pressure inside the sample chamber. Furthermore, the sample temperature can be controlled by the heater located at the end of the capillary which determines the helium gas temperature and by an additional heater on the sample holder. Therefore, temperatures up to 300 K can be reached very quickly. However, the temperature stability is not as high as that of a bath cryostat. The lowest accessible temperature is about 1.5 K. Considering the vapor pressure curve of helium, a reduction of the pressure inside the sample chamber allows for operating the cryostat down to 1.5 K without exposing the sample to liquid helium.

Both cryostats described above are equipped with a superconducting magnet system allowing for the application of external magnetic fields up to 12 T/14 T.

In contrast to the previously described cryostats, a so-called closed cycle refrigerator (CCR) does not operate with cryogenic liquids. Instead, it uses helium gas from a compressor to produce low temperatures based on the Gifford-McMahon thermodynamic cycle [99]. Room temperature helium gas is first compressed and then supplied to the CCR. The compressed helium is cooled by expansion and then returns to the compressor to repeat the cycle. In general, objects may be cooled by attaching them to a metallic coldplate inside a vacuum chamber which is thermally coupled to the helium vapor chamber. The accessible temperature range is usually between 5 K and 300 K. In some CCR systems, sensitive measurements may be perturbed by mechanical vibrations, which are transmitted directly from the cold head to the sample. Therefore, special care has to be taken in order to minimize these vibrations. Alternatively, CCR systems in which the vibrations of the cold head are isolated from the sample by using helium exchange gas and rubber bellows can be utilized. In the laboratory of Prof. Dr. S. Nair at IISER Pune, a CCR system is used for dielectric measurements. As will be described in Sec. 3.3, the dielectric polarization noise technique has been established in this setup as part of the present thesis work.

## 3.2 Fluctuation spectroscopy

### 3.2.1 Analysis of noise spectra

As discussed in Sec. 2.4.4, the application of a current  $I$  allows for measuring a fluctuating voltage drop  $\delta V(t) = I\delta R(t)$  which is related to the intrinsic resistance fluctuations  $\delta R(t)$  of a sample. In many cases, a  $1/f^\alpha$ -type spectrum is observed, where  $\alpha$  denotes the frequency exponent. A typical noise spectrum, which was obtained for a thin film sample of the magnetic semiconductor  $\text{Ga}_{1-x}\text{Mn}_x\text{As}$ , is shown in Fig. 3.2.1 (green curve). In this log-log plot, the slope of a linear fit to the data (red line) directly yields the frequency exponent  $\alpha = 1.35$ . Moreover, it is common to consider the value of  $S_V$  at a frequency of 1 Hz, which is also indicated in the diagram. In general, both  $\alpha$  and  $S_V(1 \text{ Hz})$  are a function of temperature.

After Hooge's law (Eq. (2.35)), and under the assumption of an ohmic behavior  $V = R \cdot I$ ,

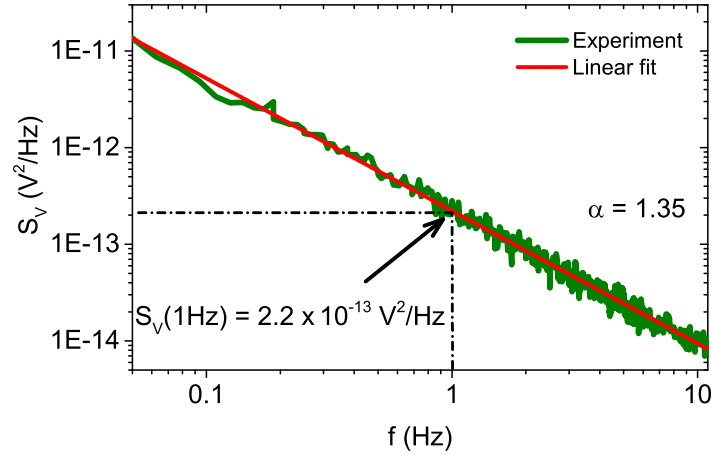


Figure 3.2.1: Typical  $1/f^\alpha$ -type noise spectrum in a log-log plot. Red line represents a linear fit to the experimental data yielding a frequency exponent of  $\alpha = 1.35$ . The value for  $S_V$  evaluated at 1 Hz is also given in the diagram.

the voltage noise PSD is proportional to  $V^2$  and thus also to  $I^2$ . This scaling behavior of  $S_V$  allows to distinguish between parasitic noise contributions related to the experimental setup or measuring instruments and the actual signal originating from the sample. This is clarified in Fig. 3.2.2 (a), where exemplary current-dependent noise spectra are shown. For  $I = 0$ , a white noise background of the experimental setup is observed. For low applied currents, a  $1/f$ -type spectrum emerges at lower frequencies from the background noise. The frequency range in which  $1/f$  noise occurs becomes broader for higher currents. As shown in the inset of Fig. 3.2.2 (b), the PSD evaluated at 1 Hz and the square of the current exhibit a linear relationship (red line indicates a linear fit to the data), proving the validity of Hooge's law. It is common to normalize the voltage noise PSD  $S_V$  with respect to the square of the current in order to obtain the resistance noise PSD  $S_R$ , i.e.,

$$S_R = \frac{S_V}{I^2}. \quad (3.1)$$

Since, in contrast to  $S_V$ , this quantity is independent of the current  $I$ , plotting  $S_R$  against the frequency  $f$  for different currents should lead to multiple  $1/f$  spectra lying on top of each other. As can be seen in the main panel of Fig. 3.2.2 (b), this is the case for the respective frequency ranges in which  $1/f$  fluctuations originating from the sample occur. In addition, the normalized resistance noise PSD  $S_R/R^2$  can be calculated in order to eliminate the resistance dependence of  $S_R$ .

As discussed in Sec. 2.4.4,  $1/f$  fluctuations in solids can be modeled by a superposition of various thermally-activated two-level fluctuation processes, each one represented by a Lorentzian spectrum with a characteristic corner frequency  $f_c$ . The PSD  $S(f)$  of a single

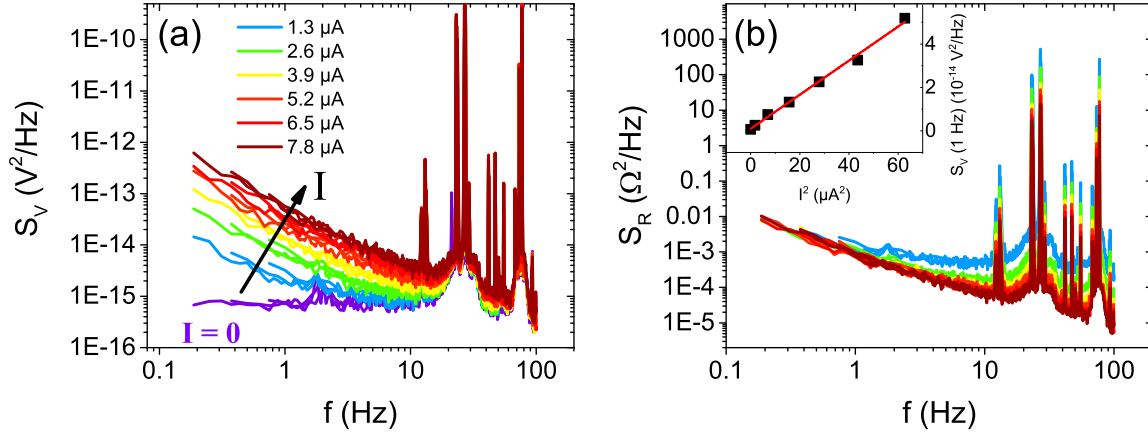


Figure 3.2.2: Exemplary current-dependence of noise spectra obtained from measurements of a semiconducting CoSb<sub>3</sub> film (cf. Ref. [29]). (a)  $1/f$  spectra for different  $I$  and a white noise spectrum for  $I = 0$ . (b) Plot of  $S_R$  against  $f$ . Inset:  $S_V$  at 1 Hz against  $I^2$ . Linear fit (red line) indicates the validity of  $S_V \propto I^2$ .

two-level process can be written as

$$S(f) = \frac{1}{4\pi^3} \cdot \frac{1}{\tau_1 + \tau_2} \cdot \frac{1}{f^2 + f_c^2} \quad (3.2)$$

where  $\tau_1$  and  $\tau_2$  denote the characteristic lifetimes of the respective states, which are related to the corner frequency via  $f_c = 1/(2\pi) \cdot (1/\tau_1 + 1/\tau_2)$ . The corresponding activation energy of a thermally-activated process can be obtained from an Arrhenius plot of  $\ln(f_c)$  against the temperature  $T$  (see Eq. (2.40)).

In some cases, one or a few two-level processes come to dominate the noise spectrum. Therefore, as depicted in Fig. 3.2.3, a superposition of a pure  $1/f$  behavior and a Lorentzian spectrum is observed in the experiment. The normalized resistance noise PSD for this superposition can be written as

$$\frac{S_R(f)}{R^2} \cdot f = \frac{A}{f^{(\alpha-1)}} + \frac{B}{4\pi^3} \frac{f}{f^2 + f_c^2}. \quad (3.3)$$

Here,  $A$  and  $B$  denote fit parameters which indicate the magnitude of the  $1/f$  and the Lorentzian spectrum, respectively. More specifically, the magnitude of the Lorentzian spectrum equals  $B = (\Delta R/R)^2 \cdot 1/(\tau_1 + \tau_2)$ , where  $\Delta R$  is the strength of the resistance fluctuations caused by the underlying two-level process. Thus  $\Delta R/R$  is a measure for the coupling between the fluctuator and the total resistance.

Statements about the individual characteristic lifetimes  $\tau_1$  and  $\tau_2$  are only possible in the case of  $\tau_1 = \tau_2$  or  $\tau_1 \gg \tau_2$  [100]. In order to examine whether one of these conditions applies, an Arrhenius representation of both  $S(f_c) \cdot f_c^2$  and  $f_c$  has to be considered. If the slopes and

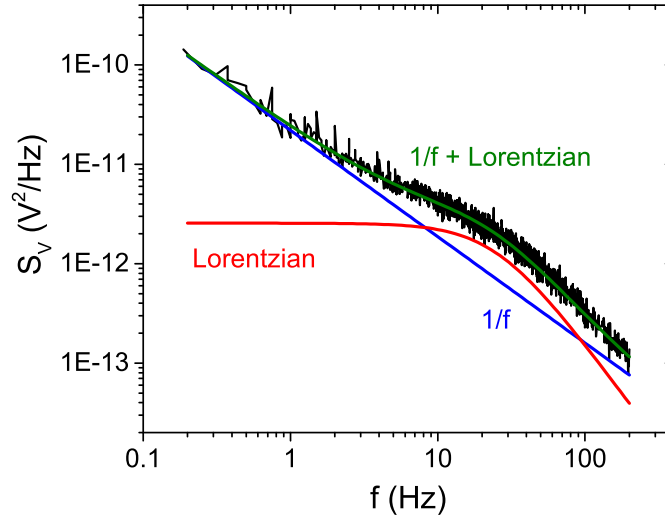


Figure 3.2.3: Exemplary experimentally acquired spectrum (black curve) can be described as a superposition of a Lorentzian (red curve) and a  $1/f$  (blue curve) spectrum.

thus the activation energies are equal, then the lifetimes  $\tau_1$  and  $\tau_2$  are comparable. In the case of  $\tau_1 \gg \tau_2$ , the two slopes are expected to be considerably different, which allows for a determination of the lifetimes from  $f_c$ . An exemplary analysis of the characteristic lifetimes in the case of thermoelectric  $\text{Yb}_2\text{Co}_4\text{Sb}_{12}$  skutterudite thin films can be found in Ref. [29]. Note that the  $\text{Yb}_2\text{Co}_4\text{Sb}_{12}$  system was investigated together with S. Heinz during the course of the present thesis work. An extensive discussion of the performed electronic transport measurements can be found in Ref. [101].

### 3.2.2 Parasitic sources of noise

In the previous section, it was clarified that measurements of  $S_V$  for various currents allow to discriminate between the background noise and the signal originating from the sample. Considering the noise spectra in Fig. 3.2.2 (a), it may be interesting to ask (i) whether the background noise for  $I = 0$  can be reduced and (ii) what the origin of the discrete peaks at higher frequencies is.

In most cases, the measured voltage fluctuations  $\delta V(t)$  are amplified by a preamplifier and then are fed into a spectrum analyzer, which calculates the power spectral density by means of a fast Fourier transform (FFT). Generally, the noise measurements are limited by the inherent noise of the preamplifier, which in most cases is of a  $1/f$ -type nature, and the thermal noise. The magnitude of the preamplifier noise is a function of the source resistance and the frequency. Therefore, the choice of an appropriate preamplifier can decide about the success of an experiment, since it strongly influences the magnitude of the noise background. This fact is clarified in Fig. 3.2.4, where the noise contours of two different preamplifiers (models SR560 and SR554, Stanford Research Systems) are depicted. Here, the so-called noise figure

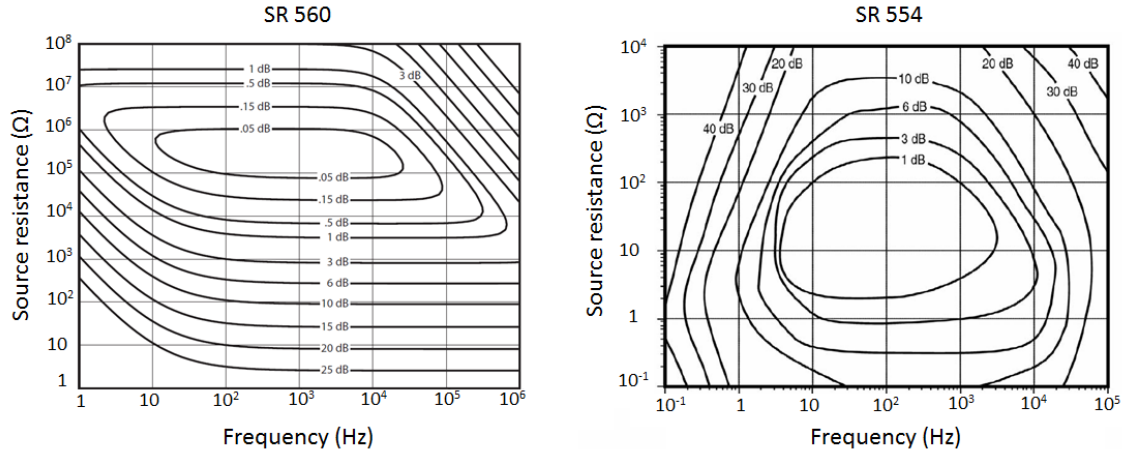


Figure 3.2.4: Contour plot of the noise figure (NF) as a function of frequency and the source resistance for two exemplary preamplifiers. After [102] and [103].

(NF) is plotted as a function of frequency and the source resistance. This quantity is generally defined as

$$\text{NF} = 10 \log \left( \frac{\text{SNR}_{\text{in}}}{\text{SNR}_{\text{out}}} \right), \quad (3.4)$$

where  $\text{SNR}_{\text{in}}$  and  $\text{SNR}_{\text{out}}$  denote the input and output signal-to-noise ratios, respectively (cf. (Eq. 2.28)). In the case of an amplifier with a gain  $g$ , the noise figure can be written as

$$\text{NF} = 10 \log \left( \frac{P_a + gP_{\text{in}}}{gP_{\text{in}}} \right), \quad (3.5)$$

where  $P_a$  is the additive noise power of the preamplifier and  $gP_{\text{in}}$  corresponds to the amplified input noise power. Therefore, the sum  $P_a + gP_{\text{in}}$  corresponds to the output noise power. A low noise figure implies that the output noise is dominated by the (thermal) noise of the source, while high NF values indicate that the output noise of the amplifier is dominated by its own noise. As can be seen in Fig. 3.2.4, the contour plots of NF for the two preamplifiers appear very differently. While the SR560 preamplifier exhibits the lowest NF values for source resistances between  $10^5$  and  $10^6 \Omega$  and frequencies in the range between 10 and  $10^4$  Hz, the SR554 is more suitable for lower resistances between 1 and  $100 \Omega$  and frequencies ranging from 10 to  $10^3$  Hz. Another important consequence of the preamplifier noise contours is that an AC method for measuring low-frequency resistance noise spectra will in most cases show an improved sensitivity over DC (direct current) methods by avoiding preamplifier  $1/f$  noise. This will be discussed in Sec. 3.2.3 in greater detail.

Besides the noise of the utilized preamplifier, there exists a myriad of other possible origins of parasitic noise. Capacitive contributions from coaxial cables or from sample contacts of inferior quality can constitute a parasitic noise source. In addition, temperature fluctuations  $\delta T$  inside the cryostat can lead to resistance fluctuations  $\delta R$  of the sample [13]. In general,



ground loops should also be prevented, mechanical vibrations arising from vacuum pumps should be reduced and unused electronic instruments should be switched off in order to improve the quality of the measurements. Another noteworthy aspect is the influence of the electric power grid. The peaks in the noise spectra shown in Fig. 3.2.2 arise due to the fact that the measurement instruments are connected to the power grid which provides an AC current with a frequency of  $f = 50 \text{ Hz}$ , which itself may also weakly fluctuate. As long as not all instruments are operated in battery mode and are decoupled from the power grid, peaks will be present in the noise spectra at the power line frequency and multiples of it. Furthermore, in the case of an additional AC voltage with a different frequency  $f_{AC}$ , as it is used in AC lock-in measurements (cf. Sec. 3.2.3), the emergence of beats with a frequency  $f = |n \cdot 50 \text{ Hz} - f_{AC}|$  leads to further peaks in the noise spectra.

### 3.2.3 Four-terminal DC and AC noise spectroscopy

At first glance, the easiest manner of how to measure a resistance of a sample is the so-called two-terminal sensing method. A current  $I$  is applied between two contacts of a sample and the voltage  $V$  is measured simultaneously with the same electrodes. Thus the resistance can be determined via  $R = V/I$ . However, the calculated resistance includes the resistance of the leads and the contacts, leading to significant errors in particular for low-resistive samples. A considerable improvement can be achieved by separating the current and voltage electrodes, which is referred to as four-point measurement. In the following, we will consider modifications of the standard four-point measurement technique for the purpose of investigating the fluctuations in the resistance  $R$ .

The standard DC four-probe method for measuring resistance fluctuations is depicted in Fig. 3.2.5 (a). A constant current provided by a current source is applied through the current leads of a sample with a fluctuating resistance  $R(t) = \bar{R} + \delta R(t)$ , where  $\bar{R}$  denotes the time average of  $R$  and  $\delta R(t)$  corresponds to the pure fluctuations. In order to amplify the voltage fluctuations  $\delta V(t) = V(t) - \bar{V}$ , the average voltage is removed by a blocking capacitor  $C$  inside the preamplifier, which acts as a high-pass filter. Therefore, the power spectrum  $S_V(f, I)$  of the voltage fluctuations at the preamplifier output yields:

$$S_V(f, I) = g^2 \left[ S_V^0(f) + I^2 S_R(f) \right], \quad (3.6)$$

where  $g$  is the preamplifier gain,  $S_R(f)$  denotes the resistance noise PSD and  $S_V^0(f)$  is the power spectrum of the background noise, which is composed of the preamplifier noise and the thermal noise.

However, there exist several drawbacks of this DC technique. First, measurements are limited to  $f_{\min} \sim 1/R_i C$ , where  $R_i$  is the input resistance of the preamplifier. Moreover, as discussed in Sec. 3.2.2, typical preamplifiers exhibit a high noise figure when operated in a

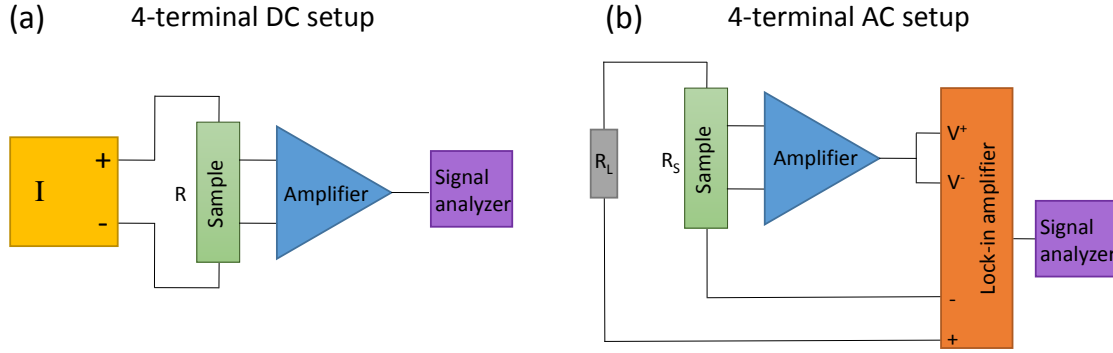


Figure 3.2.5: Four-terminal setup for resistance noise measurements. (a) A constant DC current is supplied by a current source, the fluctuating voltage drop across the sample is amplified and then fed into a signal analyzer in order to calculate the noise spectrum. (b) An AC voltage applied to a voltage divider circuit ( $R_L \gg R_S$ ) leads to an AC current through the sample resistance  $R_S$ . After amplification and further processing of the emerging voltage fluctuations (see main text), the PSD is calculated by a spectrum analyzer.

DC setup. Thus the preamplifier  $1/f$  noise greatly exceeds the thermal noise, which especially complicates noise measurements of metals or other materials with a low Hooge parameter  $\gamma_H$ . Therefore, an AC method for measuring low-frequency resistance fluctuation spectra was proposed by J. Scofield in 1987 [104]. A schematic diagram of the four-terminal AC noise spectroscopy setup, which is a preliminary step towards the setup of J. Scofield, is illustrated in Fig. 3.2.5 (b). Here, the operating frequency of the preamplifier is shifted from zero (DC) up to a carrier frequency of  $f_0 \sim 10^2\text{--}10^3$  Hz. With an AC current  $I = I_0 \sin(2\pi f_0 t)$ , the resistance fluctuations modulate the carrier to produce noise sidebands. After amplification the carrier is demodulated by a lock-in amplifier in order to reveal the desired low-frequency resistance fluctuations.

In detail, an alternating voltage  $V_{\text{out}}$  is applied to a voltage divider circuit, where the load resistance  $R_L$  is much greater than the resistance of the sample  $R_S$ . Thus the voltage drop  $V_S$  across the sample, which can be written as

$$V_S = \frac{R_S}{R_L + R_S + r} V_{\text{out}}, \quad (3.7)$$

is considerably smaller than the output voltage  $V_{\text{out}}$ . Here,  $r$  denotes the contact resistance. The fluctuations  $\delta V_S$  of the voltage drop across the sample equal

$$\delta V_S(R_S, R_L, r) = \frac{\partial V_S}{\partial R_S} \delta R_S + \frac{\partial V_S}{\partial R_L} \delta R_L + \frac{\partial V_S}{\partial r} \delta r. \quad (3.8)$$

Moreover, the current  $I$  is given by

$$I = \frac{V_{\text{out}}}{R_S + R_L + r}. \quad (3.9)$$

Therefore, Eq. (3.8) can be rewritten as:

$$\delta V_S(R_S, R_L, r) = I \cdot \frac{R_L + r}{R_S + R_L + r} \left[ \delta R_S - \frac{R_S}{R_L + r} (\delta R_L + \delta r) \right]. \quad (3.10)$$

Assuming that  $R_L \gg R_S$ , the voltage fluctuations across the sample correspond to

$$\delta V_S = I \delta R_S, \quad (3.11)$$

since the fluctuations  $\delta r$  of the contact resistance as well as the fluctuations  $\delta R_L$  of the load resistance are negligible [14].

Therefore, the four-terminal AC noise spectroscopy setup allows for precise measurements of the voltage noise PSD. In the experiment, a correction of the voltage noise PSD  $S_V^{\text{meas}}$  calculated by the signal analyzer is required, since the preamplifier gain  $g$  and the sensitivity (sens) of the lock-in amplifier have to be considered:

$$S_V = S_V^{\text{meas}} \cdot \frac{1}{g^2} \frac{(\text{sens})^2}{(10 \text{ V})^2}. \quad (3.12)$$

The resulting  $S_V$  can be further processed and analyzed, for instance by calculating the resistance noise PSD  $S_R$ . It should be noted that  $S_R$  is expected to be independent of the ratio  $R_L/R_S$  between the load and the sample resistance in case the contact noise has been fully eliminated [104].

In contrast to the four-terminal DC noise spectroscopy technique, where a high-pass filter inside the preamplifier can be utilized in order to suppress the average voltage  $\bar{V}$ , the four-point AC technique is limited by the lock-in sensitivity, which depends on the magnitude of  $\bar{V}$ . In addition to that, the major obstacle of both four-point techniques is that they suffer from the fluctuations in external sources, such as the bath temperature. These obstacles can be overcome by the five-terminal AC noise spectroscopy setup presented in the following.

### 3.2.4 Five-terminal AC noise spectroscopy

According to the work of J. Scofield [104], the sample can be placed in a bridge circuit in order to suppress the constant voltage offset as shown in Fig. 3.2.6 (a). This bridge-type design makes the output of the circuit insensitive to fluctuations in external sources, such as the voltage source, the bath temperature, or the applied magnetic field. Furthermore, the suppression of the mean voltage  $\bar{V}$  allows to increase the sensitivity of the lock-in amplifier. Another important aspect is that a nonzero average voltage typically leads to a  $1/f^2$ -type noise

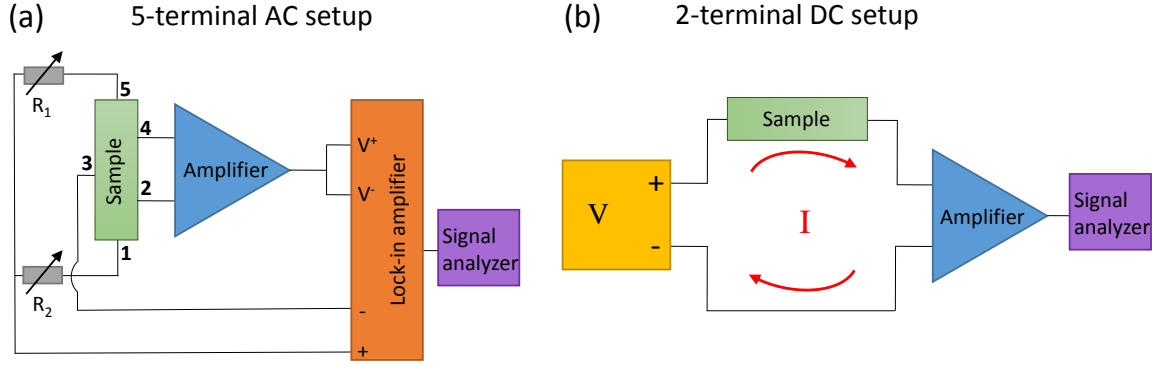


Figure 3.2.6: (a) Five-terminal AC setup for measuring resistance fluctuations. The sample is placed in a bridge circuit in order to suppress the mean voltage  $\bar{V}$  and to minimize external perturbations (b) Two-point DC setup for the measurement of current fluctuations  $\delta I(t)$  in high-resistive samples.

behavior at low frequencies [14], even though this contribution is usually overshadowed by the desired  $1/f$  spectrum originating from the sample. Nevertheless, this  $1/f^2$  contribution is eliminated by the present bridge circuit. Considering the setup illustrated in Fig. 3.2.6 (a), an increase of the applied AC voltage  $V_{\text{out}}$  leads to an increase of the magnitude of the voltage fluctuations, but not to an increase of the average voltage. As for the AC four-probe measurement, large ballast resistors  $R_1$  and  $R_2$  reduce the effect of fluctuations in the current contact resistances. Two opposing currents flow through the sample<sup>1</sup> and are mainly determined by the voltage drops across the ballast resistors. In the case of a perfectly symmetric and homogeneous sample the magnitude of the load resistors should be equal, i.e.,  $R_1 = R_2$ . However,  $R_1$  and  $R_2$  are typically precisely adjustable resistors in order to allow for minor corrections due to a possible weak asymmetry of the contact arrangement or inhomogeneities in the sample. It should be emphasized that a too strong asymmetry leads to difficulties in the normalization of the voltage noise with respect to the current, cf. Ref. [13]. Apart from that, the further processing of the balanced voltage signal is the same as for the four-terminal AC noise setup. Ultimately, the PSD of the lock-in amplifier's output is given by

$$S_V(f, I) = g_{\text{total}}^2 \left[ S_V^0(f_0) + \frac{1}{2} I_0^2 S_R(f) \cos^2(\delta) \right], \quad (3.13)$$

where  $g_{\text{total}}$  includes the total gain composed of the preamplifier gain and the lock-in gain, which is defined to be the ratio of the DC output voltage to the root mean square (rms) voltage at the input, and  $\delta$  is the detection phase angle relative to the excitation current  $I = I_0 \sin(2\pi f_0 t)$ . The validity of Eq. (3.13) is limited to  $f < f_0/2$ . In comparison to the

<sup>1</sup>Considering the numbering of contacts in Fig. 3.2.6 (a), these currents  $I_1$  and  $I_2$  flow between contact No. 1 and 3, and between No. 5 and 3, respectively.

four-terminal DC noise setup (cf. Eq. (3.6)), the major improvement lies in the floor noise  $S_V^0(f_0)$ , which is not a function of  $f$  anymore. If  $f_0$  is chosen to be in the eye of the contour plot of the preamplifier's noise figure (see Fig. 3.2.4), then the floor noise is mainly defined by the thermal noise originating from the sample, i.e.,  $S_V^0(f_0) = 4k_B TR_S$ .

Even though the preamplifier is operated in an optimal frequency range, its inherent fluctuations may still be an obstacle for precise noise measurements. In order to completely eliminate the preamplifier noise, a so-called cross correlation technique may be employed. Here, the properties of the cross spectrum  $S_{xy}(f)$  (Eq. (2.23)) are exploited. In detail, the noise of the sample is measured through two different noise channels with two preamplifiers which are identical in construction. It is assumed that the signal in the first channel  $x = s + a$  is composed of the signal  $s$  originating from the sample and the amplifier noise  $a$ . In the same way, the signal of the other channel corresponds to  $y = s + b$ , where  $b$  is the signal of the second amplifier, which is uncorrelated with  $a$ . Therefore, the cross-correlation spectrum  $S_{xy}$  after averaging  $N$  time blocks yields [105]

$$S_{xy}(f, N) = \frac{1}{N} \sum_{i=1}^N [S_{ss,i}(f) + S_{as,i}(f) + S_{sb,i}(f) + S_{ab,i}(f)]. \quad (3.14)$$

The first term  $S_{ss,i}(f)$  corresponds to the signal of the sample, while all other parts have both a real and an imaginary component whose average values are zero if  $a$ ,  $b$  and  $s$  are uncorrelated. Thus  $S_{xy}(f, N)$  equals the pure sample signal for a sufficient amount of averages  $N$  [105]. At first glance, the combination of the five-terminal AC noise technique with the cross correlation method appears to be the best way of measuring the noise of a specimen. However, stray capacitances may complicate the analysis for high-resistive samples. Therefore, DC noise measurements are recommended for sample resistances higher than 10 k $\Omega$  [104]. Besides four-point DC resistance noise measurements, a two-terminal current fluctuation method is especially suitable for highly insulating samples and will be presented in the following.

### 3.2.5 Two-terminal DC noise spectroscopy

After Eq. (2.34), the normalized resistance noise PSD  $S_R(f)/R^2$  is equivalent to the normalized PSD of the current fluctuations  $S_I(f)/I^2$ . The experimental setup for the measurement of current fluctuations is depicted in Fig. 3.2.6 (b). Here, a constant DC voltage  $V$  is supplied by a voltage source. Thus a current  $I$  through the sample and the current amplifier, which are connected in series, is induced. Via an internal resistance  $R_{\text{int}}$  inside the amplifier, the current is transformed to a voltage, which can be further processed and analyzed. The gain of the preamplifier is given by the resistance  $R_{\text{int}}$  and hence has the units  $[R_{\text{int}}] = \text{V/A}$ . In order to achieve a high gain, a high resistance  $R_{\text{int}}$  has to be chosen. However, as soon as the resistance  $R$  of the sample is of the same order as  $R_{\text{int}}$ , the choice of  $R_{\text{int}}$  has a strong effect on the current

Table 3.2.1: Minimum recommended source resistance values for the Model 428 current amplifier from Keithley Instruments. Adapted from Ref. [106]

Gain [V/A]	Minimum source resistance
$10^3$	1 k $\Omega$
$10^4$	10 k $\Omega$
$10^5$	100 k $\Omega$
$10^6$	1 M $\Omega$
$10^7$	10 M $\Omega$
$10^8$	100 M $\Omega$
$10^9$	1 G $\Omega$
$10^{10}$	10 G $\Omega$

I. In addition to that, the desired current fluctuations of the sample may be overshadowed by the preamplifier noise. Therefore, a table of minimum recommended source resistance values is typically given for current preamplifiers. An exemplary overview for the current amplifier (Model 428, Keithley Instruments [106]) utilized in this work is given in Tab. 3.2.1. In this case, the investigated sample is required to exhibit a resistance of at least  $R = 1$  k $\Omega$ .

Regarding the choice of an appropriate current preamplifier, it should be considered that normally a low-pass filter is included in this type of amplifier. Therefore, it should be ensured that the cutoff frequency lies beyond the frequency range of interest for the noise spectrum to be measured. Furthermore, a current suppression function is helpful in order to remove the average current  $\bar{I}$  and thus to amplify only the fluctuations. These two conditions are met by the aforementioned Model 428 amplifier from Keithley Instruments.

Besides its suitability for measuring highly insulating samples, another obvious benefit of the two-point current noise technique is the applicability to samples or devices which have less than four electrical contacts. A relevant example is given by HfO<sub>x</sub> and TaO<sub>x</sub> resistive random-access memory (RRAM) devices [32, 33]. Noise studies on HfO<sub>x</sub> and novel Y<sub>2</sub>O<sub>3</sub> systems are presented in chapter 5.

### 3.3 Dielectric polarization noise measurements

The focus of the present section is the experimental realization of dielectric polarization noise measurements on pressed pellet samples, which is mainly based on a setup by J. Schindele *et al.* [86, 88] for polarization noise measurements on liquid glycerol.

#### 3.3.1 Electrical circuit and operational amplifier

The experimental setup of J. Schindele *et al.* is illustrated schematically in Fig. 3.3.1. Here, the fluctuating voltage across the sample-filled capacitor located in a cryostat is measured by two preamplifiers in parallel. The application of the cross correlation method as presented

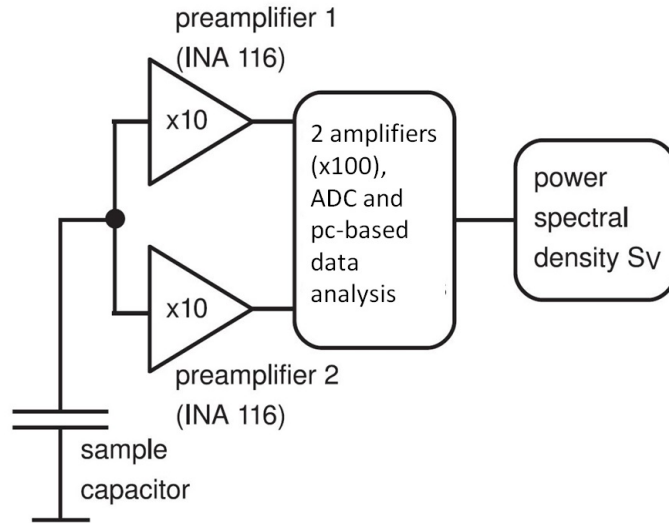


Figure 3.3.1: Experimental setup for the measurement of dielectric polarization noise in liquid glycerol. Voltage fluctuations across the sample-filled capacitor are read out by two preamplifiers in parallel. Application of the cross-correlation method and Fourier transform yield the noise spectra. Content reprinted from Ref. [86] with permission of the American Physical Society.

in Sec. 3.2.4 allows to strongly reduce the contribution of the uncorrelated noise of the two preamplifiers. The fluctuating signal is further amplified outside the cryostat and then digitized using an analog-to-digital converter. Finally, the Fourier transform yields the voltage noise PSD  $S_V(f)$ .

The difficulty about the measurements of polarization noise lies in the fact that the fluctuations of the dipolar molecules inside the material cause voltage fluctuations in the  $\mu\text{V}$  range which are measured across a highly insulating sample with a resistance of order  $\text{M}\Omega$  or  $\text{G}\Omega$ . Importantly, the input impedance of a measuring instrument has to be considerably higher than the sample resistance. Otherwise, only the Johnson-Nyquist noise of the input impedance will be measured. The input impedance of an SR560 voltage preamplifier (Stanford Research Systems), which is generally used for standard resistance noise measurements, is only  $100\text{ M}\Omega$ . Consequently, a special operational amplifier has to be utilized. Figure 3.3.2 (a) illustrates the measurement circuit in more detail. Here, one electrode of the capacitor is connected with the noninverting input of the operational amplifier, which has an input resistance of  $10^{14}\ \Omega$  or even more. The second input line of the operational amplifier and the other electrode of the capacitor are grounded.

In detail, the input stage of the operational amplifier is based on junction gate field-effect transistors (JFETs), which, in principle, have a purely capacitive input impedance and hence an infinitely large resistance. The inverting input is connected to the output via a feedback resistance  $R_2$ . Due to the large input resistance, no current can flow through the input, which is why the current passing through  $R_2$  must equal the current through  $R_1$ . It can be shown

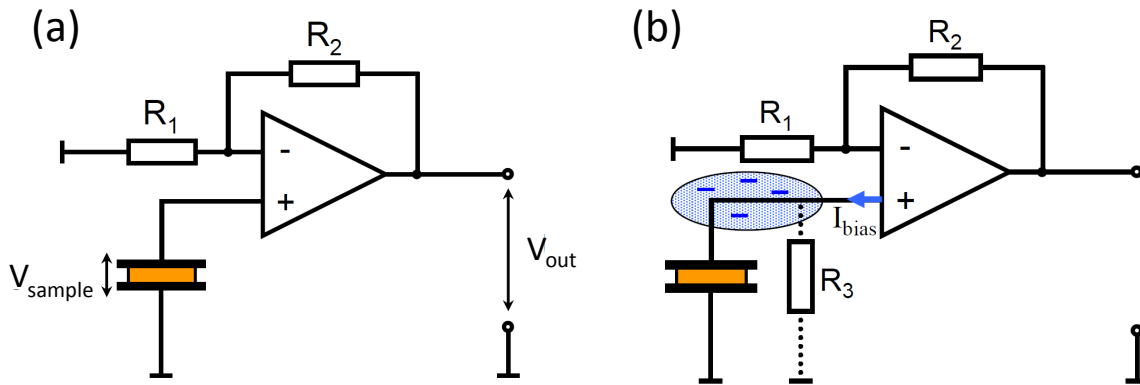


Figure 3.3.2: (a) Schematic illustration of the use of an operational amplifier for dielectric polarization noise measurements. (b) For very high sample resistances, the input bias current of the operational amplifier cannot discharge and the amplifier goes into saturation due to the emerging charge accumulation. After [88].

that the gain  $g$  is defined by the ratio of  $R_2$  to  $R_1$ , i.e.,  $g = 1 + R_2/R_1$  [88]. For polarization noise measurements, the main purpose of the operational amplifier is not the amplification itself, but rather it is used as a buffer amplifier, that is, to transfer the voltage fluctuations at the sample-filled capacitor to a second circuit with a considerably lower impedance level. Therefore, in the work of J. Schindele *et al.*, the gain of the operational amplifier was only chosen as  $g = 10$  and the signal was further amplified outside the cryostat by a factor of 100 (cf. Fig. 3.3.1) [86, 88]. Another reason for the choice of a low gain will be discussed in the following.

Since the assumption of an infinite input impedance of the operational amplifier is an idealization, a finite leakage current originating from the JFET at the amplifier input is expected to flow through the input. In certain cases, the sample resistance may be so high that the leakage current cannot discharge and charge accumulation between the noninverting input and the sample occurs, cf. Fig. 3.3.2 (b). Therefore, the inputs would eventually float to a potential which exceeds the common-mode range and the operational amplifier would saturate. A common strategy would be to connect an additional resistor  $R_3$ , whose resistance is smaller than the sample resistance in order to enable the electric charge to run off. However, since the smaller resistance  $R_3$  dominates the parallel circuit with the sample, the operational amplifier would mainly amplify the voltage noise of  $R_3$ . As it is not possible to prevent charge accumulation, the choice of an operational amplifier with a low input bias current is crucial. Moreover, operating the amplifier with a lower gain allows greater potential differences between the inputs before it runs into saturation. Following the example of J. Schindele *et al.* [88, 86], in the course of this work an ultra-low input bias current instrumentation ampli-



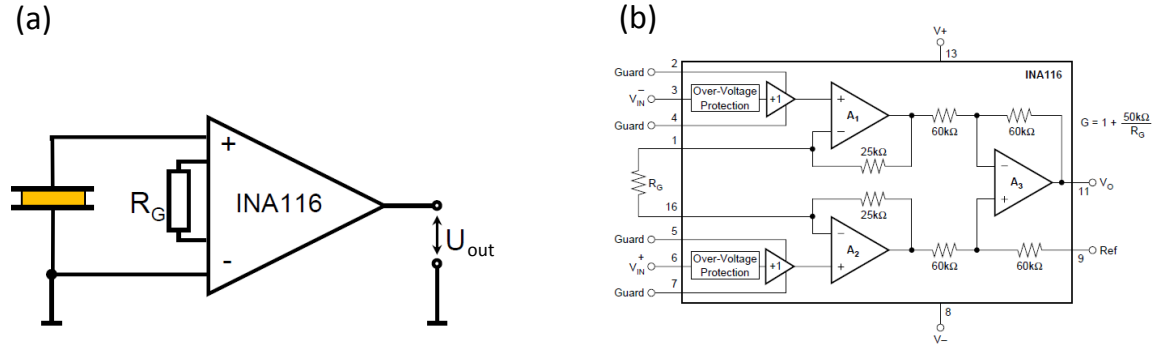


Figure 3.3.3: (a) Schematic diagram of the circuit consisting of the sample-filled capacitor and the utilized operational amplifier INA 116 (Burr-Brown/Texas Instruments). The gain is set by connecting a single external resistor  $R_G$ . (b) Connections and circuit diagram of the INA 116 instrumentation amplifier. After [88] and [107].

fier (INA116, Burr-Brown/Texas Instruments) was chosen, since special guarding techniques yield input bias currents of only 3 fA at room temperature [107]. As can be seen in Fig. 3.3.3 (b), the internal circuitry of the INA116 consists of three operational amplifiers, which is typical for instrumentation amplifiers. In this case, the gain  $g$  can be set by a single external resistor  $R_G$  and thus is calculated after  $g = 1 + (50\text{ k}\Omega/R_G)$ , where 50 k $\Omega$  corresponds to the sum of the two feedback resistors connected to the operational amplifiers  $A_1$  and  $A_2$ . The connection of the INA116 amplifier to the sample-filled capacitor is illustrated in Fig. 3.3.3 (a).

The supply voltage of 18 V is provided by two 9 V batteries in order to prevent perturbations related to the 50 Hz AC power line hum. A further criterion for an appropriate operational amplifier is a low inherent noise, which is composed of thermal noise originating from the resistors included in such an amplifier and a frequency-dependent  $1/f$  contribution. The thermal noise can be reduced by cooling the operational amplifier. In the case of the INA116 instrumentation amplifier, the integrated circuit is specified down to 230 K [107]. However, it was shown that the amplifier is still functional at 200 K [88]. Apart from the reduction of the thermal noise, there is another advantage of placing the amplifier inside the cryostat in the vicinity of the sample-filled capacitor, namely that a short cable length between the noninverting input of the INA116 and the sample guarantees a low parasitic stray capacitance.

### 3.3.2 Experimental realization in a closed cycle refrigerator

Before the realization of polarization noise measurements in a cryostat, the INA116 instrumentation amplifier was tested by measuring the voltage fluctuations of an RC circuit with variable  $R$  and  $C$ . The results are shown in Fig. 3.3.4.

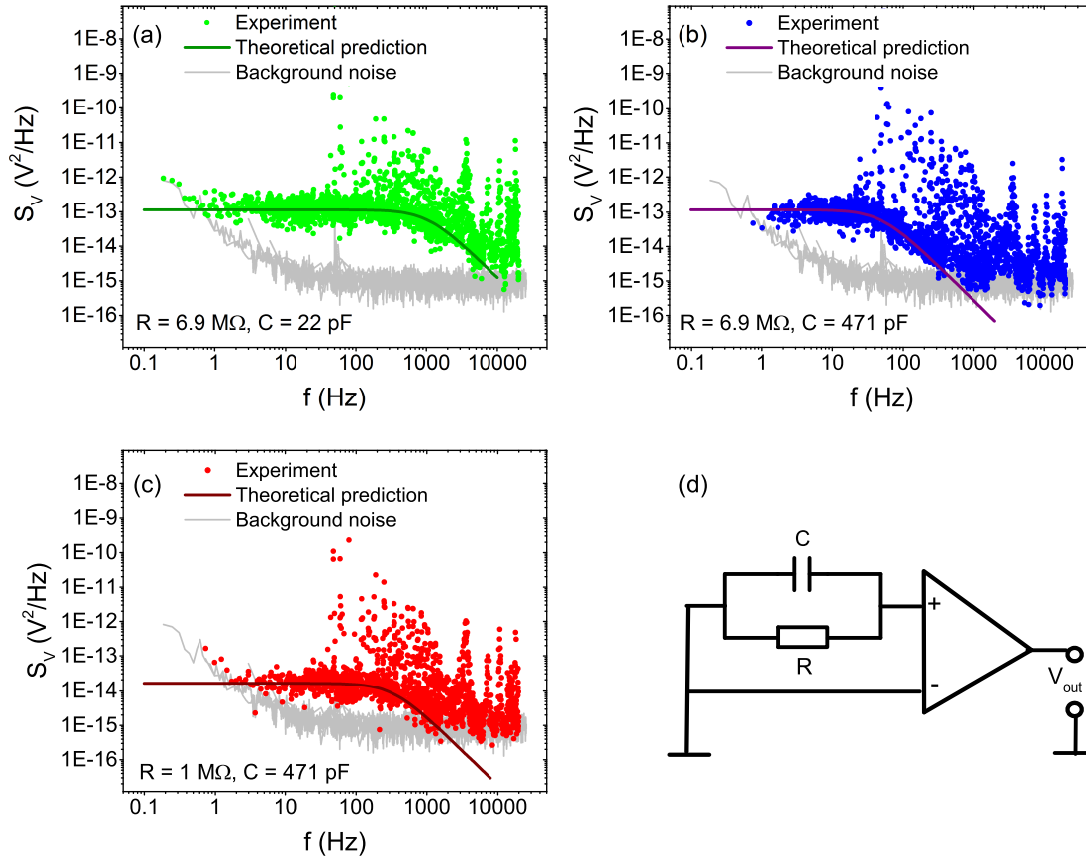


Figure 3.3.4: [(a)–(c)] Experimentally determined voltage noise PSD of an RC parallel circuit for different values of  $R$  and  $C$  (filled circles). Gray curves represent the background noise which is mainly dominated by the INA116 instrumentation amplifier. Solid lines correspond to the theoretical prediction calculated with Eq. (2.57). (d) Schematic diagram of the RC circuit.

Diagram (a) shows the measured PSD for  $R = 6.9 \text{ M}\Omega$  and  $C = 22 \text{ pF}$  (filled circles) and the corresponding theoretical prediction after Eq. (2.57) (solid line). The background noise of the experimental setup, which is mainly dominated by the INA116 amplifier, is represented by the gray curve. In order to determine the background correctly, it is required to short-circuit the inputs of the instrumentation amplifier. As demonstrated in Ref. [107], the noise characteristics of the INA116 depend on the gain factor, which has been set to  $g \approx 10$  in all experiments presented here.

A good agreement between theory and experiment can be observed in a broad frequency range between 0.5 Hz and 5000 Hz. Below 0.5 Hz, the  $1/f$  contribution of the background noise reaches the level of the experimental data. As a result, a weak increase of the measured data points can be observed at very low frequencies. For the results shown in Fig. 3.3.4 (b), a higher capacitance of  $C = 471 \text{ pF}$  is utilized. As a consequence, the cutoff frequency at which the spectrum changes from a flat behavior to a  $1/f^2$ -type noise is considerably lower. The

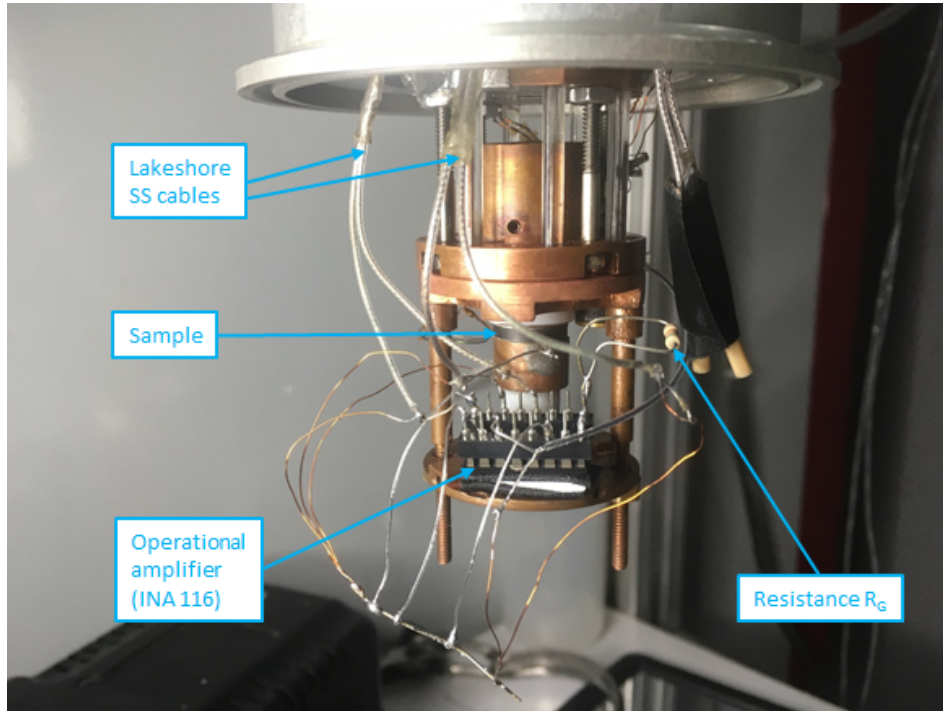


Figure 3.3.5: Photograph of the experimental setup for dielectric polarization noise measurements in the group of Prof. Dr. S. Nair at IISER, Pune. See main text for details.

experimentally determined spectrum shows a good concordance with the calculated curve. This is also the case in Fig. 3.3.4 (c), where the resistance  $R = 1 \text{ M}\Omega$  is chosen to be smaller than before. A schematic picture of the measurement circuit is shown in Fig. 3.3.4 (d). The fluctuating voltage signal is amplified by a factor of 10 by means of the operational amplifier, then passes through an SR560 (Stanford Research Instruments) preamplifier with a gain of 100 and is further processed in a signal analyzer (SR785, Stanford Research Instruments). Since the signal analyzer is connected to the electricity grid, all spectra shown in panels (a)–(c) display a high number of peaks at multiples of 50 Hz. These discrete features can be simply removed by hand after the experiment.

The results obtained from the measurements on different RC parallel circuits demonstrate the functionality of the measurement setup and especially the INA116 amplifier. In the next step, this circuit was realized in a closed cycle refrigerator (CCR) in the laboratory of Prof. Dr. S. Nair at IISER, Pune. A photograph of the experimental setup for polarization noise measurements is shown in Fig. 3.3.5.

In general, the present CCR is utilized for dielectric spectroscopy measurements of pressed pellet samples. More precisely, polycrystalline specimens are synthesized by the standard solid state reaction technique. Stoichiometric amounts of the starting materials are thoroughly mixed and treated at high temperatures with possible intermediate grinding procedures. Subsequently, the fine and homogeneous mixture is pelletized. Finally, the so-produced

disks are heated in a furnace again. Exemplary fabrication procedures are described in more detail in Refs. [108] and [109]. The temperature-dependent dielectric properties of the pressed pellets are then studied by placing them between the two copper electrodes shown in Fig. 3.3.5. In order to perform polarization noise measurements, the standard dielectric spectroscopy setup had to be modified accordingly. For dielectric spectroscopy, four stainless steel coaxial cables (Type SS, Lake Shore) are available inside the cryostat. In the case of polarization noise measurements, two of these cables can be used for the battery supply of the operational amplifier, which is placed on its back onto a copper plate in the vicinity of the sample. The use of a circuit board for the INA116 amplifier is not recommended, since the conductivity of the board may be similar to—or even higher than—the conductivity of the highly insulating sample and thus additional leakage currents can occur. A resistor with  $R_G = 5 \text{ k}\Omega$  is soldered to the instrumentation amplifier in order to achieve a gain  $g$  of about 10, since  $g = 1 + (50 \text{ k}\Omega/R_G)$ . One of the copper electrodes is connected to the noninverting input of the amplifier by an additional short stainless steel coaxial cable. In contrast to that, the inverting input and the second copper electrode are grounded. Moreover, the output of the INA116 is connected with the third available Lake Shore SS cable, which is connected to an SR560 preamplifier outside the cryostat. The fourth Lake Shore SS cable is connected to the common ground of the setup. Care has to be taken in order to prevent any ground loops in the circuit.

#### 3.3.3 First results on pressed pellet samples

Within the scope of this work, first measurements on various samples were performed. This was done by generating a vacuum, running the compressor of the CCR and operating the cryostat only at room temperature, in order to check for possible effects of mechanical vibrations. First results on two different materials,  $\text{KH}_2\text{PO}_4$  and  $\text{Ca}_3\text{NaRuO}_6$ , are illustrated in Fig. 3.3.6.

At first, before changing the setup to the polarization noise configuration, dielectric spectroscopy was performed in order to calculate a prediction for the polarization noise from the permittivity after Eq. (2.67). Figure 3.3.6 (a) shows a noise measurement (orange data points) on potassium dihydrogen phosphate, which is an optical material widely used for frequency conversion and optoelectronic switching in laser systems. Importantly, a structural phase transition leads to ferroelectricity below  $T_C = 123 \text{ K}$  [110]. As can be seen in the diagram, the measured noise spectrum of  $\text{KH}_2\text{PO}_4$  at room temperature lies far above the background noise (gray curve) in the entire frequency range. Moreover, blue data points indicate several predicted values for  $S_V$  as calculated from the dielectric function. The agreement with the experimentally acquired data points is very good between 10 Hz and 10000 Hz, but smaller deviations can be observed towards lower frequencies. This may be explained by the fact that the background noise starts to increase very strongly below 10 Hz, causing the orange curve

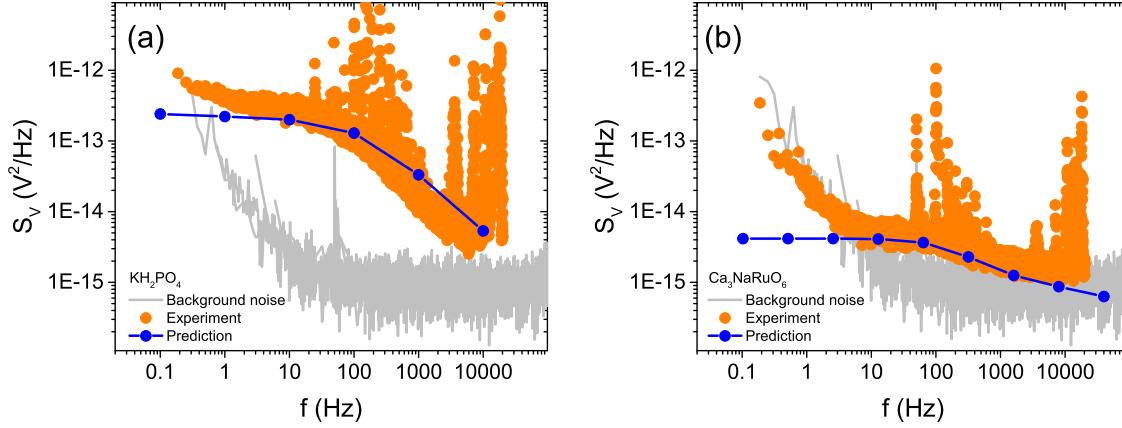


Figure 3.3.6: First dielectric polarization noise spectroscopy results on samples of two different materials, (a)  $\text{KH}_2\text{PO}_4$  and (b)  $\text{Ca}_3\text{NaRuO}_6$ , with entirely different magnitude of the voltage PSD (orange data points). Blue data points represent the theoretical prediction of  $S_V$  as calculated from dielectric spectroscopy measurements (blue lines are a guide for the eye). The gray curve indicates the background noise of the experimental setup. All curves were obtained at  $T = 300$  K.

to deviate from the expected constant behavior. In comparison, the measured noise spectrum for the ruthanate compound  $\text{Ca}_3\text{NaRuO}_6$ , which shows antiferromagnetic behavior below 87 K [111], is located much closer to the background noise, cf. Fig. 3.3.6 (b). In other words, the noise magnitude for  $\text{Ca}_3\text{NaRuO}_6$  is considerably smaller than for the  $\text{KH}_2\text{PO}_4$  sample. Only between 10 Hz and about 1000 Hz it is possible to clearly differentiate between the real signal and the background. In this frequency range, the agreement with the predicted values is as good as in the case of  $\text{KH}_2\text{PO}_4$ . At this point, it should be emphasized that proper grounding is an essential prerequisite for carrying out dielectric polarization noise measurements. Since, in contrast to the work by J. Schindele *et al.* [86, 88], the setup in the group of Prof. Dr. S. Nair has not been designed for these kind of measurements from scratch, it was crucial to properly shield the experimental setup from external perturbations.

The results illustrated in Fig. 3.3.6 clearly demonstrate the functionality of the designed experimental setup at room temperature. An intriguing future project would be to measure the dielectric polarization noise of relaxor ferroelectrics and to study possible deviations from the fluctuation-dissipation theorem. For this purpose, a number of extensions and improvements of the setup are necessary. First of all, the instrumentation amplifier should be operated at lower temperatures in order to decrease the background noise, which is presented in Fig. 3.3.6. In addition to that, the use of a second amplifier and the application of the cross-correlation method as described in Sec. 3.2.4 would allow to further reduce the noise background. The smoothness of the measured noise spectra could be improved by increasing the number of averages during one measurement run and a complete decoupling of all electronic instruments from the power grid. Finally, in order to allow for an easier switching

between dielectric spectroscopy and polarization noise measurements, a new sample holder should be designed—at least in the longer term. Apart from that, a new setup for the measurement of polarization noise in organic charge-transfer salts will be realized in the group of Prof. Dr. J. Müller at the Goethe University in Frankfurt. Since the desired compounds are mainly available as very small single crystals, the design of a completely different sample holder will be required for this purpose, which, however, is not a part of the present work. Instead, the following chapter will concentrate on the application of standard resistance noise measurements on magnetic semiconductors, which constitute the most extensively studied material system in this thesis.

## 4 Magnetic Semiconductors $\text{Ga}_{1-x}\text{Mn}_x\text{As}$ and $\text{Ga}_{1-x}\text{Mn}_x\text{P}$ Studied by Noise Spectroscopy

Diluted magnetic semiconductors (DMSs) combine the benefits of semiconducting and magnetic materials and thus represent highly promising candidates for future spintronics applications. The fundamental idea behind this class of materials is the introduction of local magnetic moments into well-understood non-magnetic semiconductors in order to induce ferromagnetic behavior. The ultimate objective is to fabricate or manipulate a compound in such a way that its Curie temperature exceeds room temperature and essential semiconducting properties as, for instance, sensitivity to doping or electric fields created by gate charges are present and allow for the design of functional spintronic devices. H. Ohno and collaborators were the first to report a long-range ferromagnetic order in transition metal doped III-V semiconductors such as  $\text{In}_{1-x}\text{Mn}_x\text{As}$  [112, 113] and  $\text{Ga}_{1-x}\text{Mn}_x\text{As}$  [114, 115]. Due to the formation of undesirable ferromagnetic MnAs clusters for higher Mn doping concentrations, the Mn solubility in GaAs is severely restricted. Therefore, incorporating a sufficiently high concentration in order to increase the ferromagnetic transition temperature is highly challenging and requires the use of special growth techniques. So far, the highest achieved Curie temperature for  $\text{Ga}_{1-x}\text{Mn}_x\text{As}$  is around 190 K [116].

Although  $\text{Ga}_{1-x}\text{Mn}_x\text{As}$  has been extensively studied for more than two decades, the theoretical description of the electronic structure and the development of spontaneous magnetism is still neither consistent nor complete. While the mean-field Zener model assumes extended hole states with the Fermi energy located within the valence band, the so-called impurity-band model proposes localized hole states in a separate impurity band detached from the valence band [117]. In the context of the impurity-band model, A. Kaminski and S. Das Sarma [3, 4] have developed an analytic polaron percolation theory for the ferromagnetism in DMSs in the limit of strong charge carrier localization. This model describes the emergence and percolation of so-called bound magnetic polarons as an origin of spontaneous magnetization. Since fluctuation spectroscopy is a method which is sensitive to electric inhomogeneities on the nano- and micrometer scale and has been proven to be a versatile tool for the identification of magnetically driven percolation, cf. studies on perovskite manganites [6] or the ferromagnetic semimetal  $\text{EuB}_6$  [5], this technique has been applied in order to detect possible electronic phase separation in  $\text{Ga}_{1-x}\text{Mn}_x\text{As}$  and the related compound  $\text{Ga}_{1-x}\text{Mn}_x\text{P}$ .

In this chapter a detailed description of the III-V DMSs  $\text{Ga}_{1-x}\text{Mn}_x\text{As}$  and  $\text{Ga}_{1-x}\text{Mn}_x\text{P}$  is given,

followed by a presentation of the major results on electronic transport as well as fluctuation spectroscopy studies. It should be noted that this chapter makes no claim to completeness, but only the most important properties of Ga<sub>1-x</sub>Mn<sub>x</sub>As and Ga<sub>1-x</sub>Mn<sub>x</sub>P will be introduced. For a more detailed description of the theoretical background refer to Refs. [118, 119, 120, 121, 122]. This chapter is also based on Refs. [123, 124, 125, 126, 127].

First of all, we will focus on the basic properties of these compounds and the growth of thin films by means of molecular beam epitaxy or ion implantation combined with pulsed laser melting followed by various post-growth treatments. Subsequently, the origin of ferromagnetism and the corresponding theoretical models will be discussed. Furthermore, an overview of the metal-insulator transition in Ga<sub>1-x</sub>Mn<sub>x</sub>As will be given, followed by a short discussion of fundamental magnetotransport properties such as the magnetoresistance and the (anomalous) Hall effect. After a brief overview of all investigated compounds and their most important parameters, we will describe substantial steps of defining Hall bar patterns by optical lithography and the electric contacting of the films. Finally, the presentation of the results is divided into three subsections: We will discuss measurements on metallic Ga<sub>1-x</sub>Mn<sub>x</sub>As films ( $x > 2\%$ ), He-ion irradiated samples with  $x = 6\%$  and films with localized charge carriers, i.e., Ga<sub>1-x</sub>Mn<sub>x</sub>As with  $x < 2\%$  as well as two Ga<sub>1-x</sub>Mn<sub>x</sub>P samples. A major part of the results discussed in the course of this chapter has been published in Refs. [128] and [129].

## 4.1 Basic properties and fabrication

### 4.1.1 Crystal structure and defects

GaAs is a III-V semiconductor with a direct band gap of about 1.42 eV at room temperature, and is widely used in industry, e.g., for microwave-frequency integrated circuits, laser diodes or solar cells. In the case of Ga<sub>1-x</sub>Mn<sub>x</sub>As and Ga<sub>1-x</sub>Mn<sub>x</sub>P, a fraction of Ga atoms in GaAs is substituted by magnetic Mn ions. As in other diluted magnetic semiconductors Mn provides both a local magnetic moment and one hole, i.e., it acts as an acceptor. The impurity binding energy of Mn is of intermediate strength,  $E_a^0 = 0.11$  eV [130, 131, 132, 133]. The electron configuration of isolated Mn atoms is [Ar] 3d<sup>5</sup>4s<sup>2</sup>, implying that due to the half-filled 3d shell the resulting spin is  $S = 5/2$ . In the case of Ga and As, the electron configurations are [Ar] 3d<sup>10</sup>4s<sup>2</sup>4p<sup>1</sup> and [Ar] 3d<sup>10</sup>4s<sup>2</sup>4p<sup>3</sup>, respectively. Due to the missing valence 4p electron, the substitution of a Ga atom by Mn leads to the formation of a hole. Substitutional Mn in GaAs can be in a  $A^0(d^5 + \text{hole})$  or  $A^-(d^5)$  state, depending on the doping concentration [120, 134, 135]. Here,  $A^0(d^5 + \text{hole})$  indicates the state in which the Mn impurity is electrically neutral with respect to the GaAs background and hence corresponds to a Mn<sup>3+</sup> state with a moderately bound hole, while  $A^-(d^5)$  is the negatively charged Mn<sup>2+</sup> center. It should be noted that the presence of divalent (Mn<sup>2+</sup>) or trivalent (Mn<sup>3+</sup>) states has not yet been



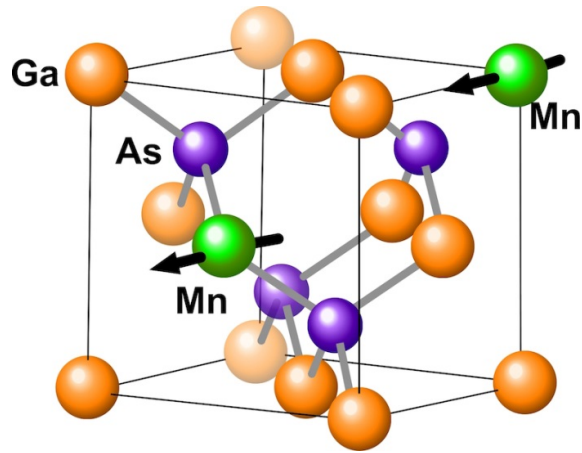


Figure 4.1.1: Schematic zincblende crystal structure of  $\text{Ga}_{1-x}\text{Mn}_x\text{As}$ . A fraction of Ga atoms is substituted by magnetic Mn ions. From [137].

conclusively determined, and also the degree of localization of the Mn  $3d$  states remains under debate [136]. A detailed review of the possible electronic states of substitutional Mn in GaAs can be found in Ref. [134]. Like their host lattice GaAs, both  $\text{Ga}_{1-x}\text{Mn}_x\text{As}$  and  $\text{Ga}_{1-x}\text{Mn}_x\text{P}$  crystallize in the zincblende structure, which is composed of two interpenetrating face-centered cubic sublattices. The individual sublattices are shifted by  $1/4$  of the space diagonal with respect to each other. The unit cell is shown schematically in Fig. 4.1.1 for  $\text{Ga}_{1-x}\text{Mn}_x\text{As}$ . From this point on, we will first of all focus on  $\text{Ga}_{1-x}\text{Mn}_x\text{As}$ , before discussing major differences and commonalities between  $\text{Ga}_{1-x}\text{Mn}_x\text{As}$  and  $\text{Ga}_{1-x}\text{Mn}_x\text{P}$  further below. Apart from substitutional Mn ( $\text{Mn}_{\text{Ga}}$ ), a variety of point defects such as Mn interstitials ( $\text{Mn}_{\text{I}}$ ) [138] or As antisites ( $\text{As}_{\text{Ga}}$ ) [139, 140] can be present in  $\text{Ga}_{1-x}\text{Mn}_x\text{As}$  due to non-equilibrium growth conditions at low temperatures as it will be explained further below. These defects have an important influence on the electronic and magnetic properties of the respective compound. Importantly, interstitial Mn atoms serve as double donors, i.e., two electrons are provided, which results in a compensation of the holes provided by substitutional Mn atoms. Since the ferromagnetic order in  $\text{Ga}_{1-x}\text{Mn}_x\text{As}$  is mediated by itinerant holes, a high concentration of Mn interstitials leads to a strong decrease of the Curie temperature  $T_{\text{C}}$ . In addition, due to an antiferromagnetic coupling between neighboring  $\text{Mn}_{\text{I}}$  and  $\text{Mn}_{\text{Ga}}$  via the superexchange interaction, the saturation magnetization can be reduced [141]. Arsenic antisites ( $\text{As}_{\text{Ga}}$ ) correspond to As atoms occupying Ga sites and also act as double donors with each As defect capturing two holes in  $\text{Ga}_{1-x}\text{Mn}_x\text{As}$ . In contrast to Mn interstitials, which are weakly bound and can be removed by post-growth annealing at temperatures slightly below the growth temperatures,  $\text{As}_{\text{Ga}}$  defects are very stable and higher temperatures for the post-growth annealing process would be required. However, such high annealing temperatures above  $250^\circ\text{C}$  would lead to the formation of MnAs clusters. These are metallic clusters with hexagonal symmetry, whereby MnAs is a ferromagnet with a Curie temperature of

330 K. Therefore, it is crucial to avoid the presence of MnAs clusters, since their high Curie temperature can lead to incorrect conclusions about the magnetic properties of  $\text{Ga}_{1-x}\text{Mn}_x\text{As}$ . Apart from the above-mentioned ones, there exist also other types of defects, such as Ga vacancies or As interstitials, the concentrations of which are usually small enough in order to be neglected.

Because of the various aforementioned defects, a complete and consistent description of the electronic band structure is highly challenging. Although the binding energies of defects which also occur in GaAs are well known, it is clear that heavily doped semiconductors experience band gap renormalization, which is accompanied by a shift of the respective impurity binding energies. Much of the perceived difference between electronic transport results and those obtained by hot photoluminescence and infrared spectroscopy resulted from the misconception, that  $\text{Ga}_{1-x}\text{Mn}_x\text{As}$  binding energies could just be transferred from the GaAs material system.

#### 4.1.2 Low-temperature molecular beam epitaxy

At first glance, molecular beam epitaxy (MBE) seems to be a highly suitable method for the growth of  $\text{Ga}_{1-x}\text{Mn}_x\text{As}$  films. However, the standard MBE technique has to be modified in order to allow for growing homogeneous single-phase  $\text{Ga}_{1-x}\text{Mn}_x\text{As}$ . In general, the major obstacle is the limited solubility of Mn in GaAs, since high doping concentrations lead to the formation of a second ferromagnetic phase, namely MnAs clusters. This solubility limit can be circumvented by growing the films at much lower temperatures between 200 and 270 °C and employing the so-called low-temperature molecular beam epitaxy (LT-MBE), whereby the provided thermal energy is not sufficient for the formation of the second phase [114]. A schematic phase diagram which shows the relation between the utilized growth parameters and the properties of  $\text{Ga}_{1-x}\text{Mn}_x\text{As}$  is shown in Fig. 4.1.2. Generally, the Curie temperature is proportional to the Mn content of the compound, since a stronger doping leads to an increase of the carrier concentration. The highest achieved Curie temperature for  $\text{Ga}_{1-x}\text{Mn}_x\text{As}$  to date is about 190 K with maximum Mn contents of approximately 10 % [142, 116].

It should be noted that lower growth temperatures generally lead to samples of lower quality, which is reflected in the transport properties, in particular in a very low carrier mobility even in the best  $\text{Ga}_{1-x}\text{Mn}_x\text{As}$  samples with relatively small defect densities. Typical mobilities in metallic  $\text{Ga}_{1-x}\text{Mn}_x\text{As}$  compounds are only about 1–50  $\text{cm}^2/\text{Vs}$ , corresponding to a carrier mean free path of 0.1–1 nm [121]. This is due to the unintentional formation of a large number of point defects such as  $\text{Mn}_\text{I}$  or  $\text{As}_{\text{Ga}}$ . These defects can be partially removed by performing a post-growth annealing procedure at temperatures slightly below the growth temperature. In detail, the weakly bound interstitial Mn ions diffuse towards the film surface, where they are passivated by oxidation or by binding with surplus As atoms [143].

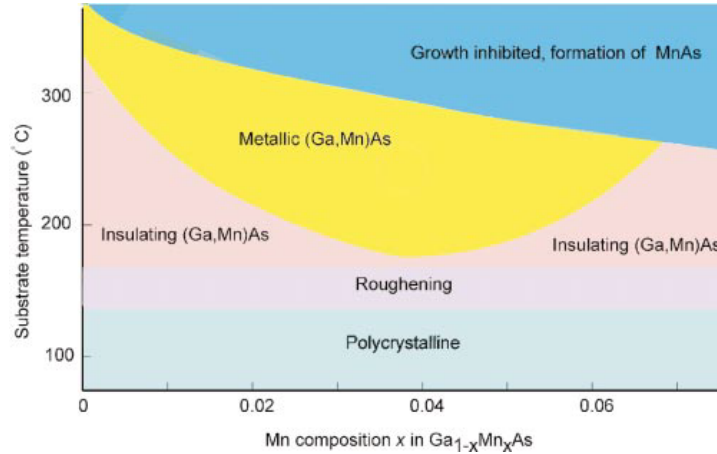


Figure 4.1.2: Schematic phase diagram showing the relation between growth parameters (Mn content and growth temperature) and the properties of  $\text{Ga}_{1-x}\text{Mn}_x\text{As}$  grown by molecular beam epitaxy. This parameter space was obtained by H. Ohno *et al.* in 1998 from studies on  $\text{Ga}_{1-x}\text{Mn}_x\text{As}$  films with thicknesses of 150–200 nm. From [115]. Reprinted with permission from AAAS.

### 4.1.3 He-ion irradiation

As mentioned earlier, the charge carrier concentration and thus the Curie temperature of  $\text{Ga}_{1-x}\text{Mn}_x\text{As}$  can be controlled by varying the Mn doping and by performing thermal annealing. An alternative method to tune the Curie temperature without changing the Mn content is given by the irradiation with high-energy particles (ions), which leads to the introduction of donor-like defects into the system and thereby to a compensation of holes in combination with a decrease of  $T_C$  [144, 145]. This standard industry method, which allows for a fine tunability and reproducibility, is widely used for conventional III-V semiconductors and has been successfully applied to  $\text{Ga}_{1-x}\text{Mn}_x\text{As}$  [144, 145, 146] and  $\text{Ga}_{1-x}\text{Mn}_x\text{P}$  [147]. Other approaches for controlling the Curie temperature are, for instance, the compensation of holes by exposing the samples to a hydrogen plasma followed by postannealing [148, 149] or the electrical gating of a  $\text{Ga}_{1-x}\text{Mn}_x\text{As}$  metal-insulator-semiconductor structure [150]. A great advantage of ion irradiation compared to the addition of hydrogen to the epilayer is that no additional material is incorporated in the  $\text{Ga}_{1-x}\text{Mn}_x\text{As}$  sample, since the projectile ions are fast enough to cross the  $\text{Ga}_{1-x}\text{Mn}_x\text{As}$  layer. Instead, these particles are implanted only in the nonmagnetic substrate. Typical ion species utilized for the irradiation procedure are  $\text{He}^+$ ,  $\text{Ne}^+$ ,  $\text{Ar}^+$  and  $\text{Li}^+$ . With the help of simulations, e.g., by using the Stopping and Range of Ions in Matter (SRIM) code [151], conclusions about the intentionally generated defects and their distribution can be drawn. It is well established that most of the introduced defects correspond to vacancies or interstitials and that they reside in the As sublattice. Although the irradiation process produces a similar amount of defects in the Ga sublattice, the induced vacancies tend to recombine immediately with the interstitials since they have op-

posite charge [145]. Rutherford backscattering spectroscopy in channeling geometry shows that no measurable increase of Mn interstitials occurs even for high irradiation doses [146]. To summarize, the irradiation of DMS films leads to a significant increase in disorder associated with a change in the electronic and magnetic properties of the respective sample.

### 4.1.4 Ion implantation and pulsed laser melting

So far, we have only considered  $\text{Ga}_{1-x}\text{Mn}_x\text{As}$  films grown by LT-MBE and possibly modified by various post-growth treatments such as thermal annealing or ion irradiation. As an alternative approach to the widely used LT-MBE, ion implantation combined with pulsed laser melting can be applied to GaAs films grown by MBE [152, 153, 154]. This technique is widely being used in order to incorporate foreign ions into a host material. By operating far from thermal equilibrium, ion implantation offers the possibility of exceeding the solubility limit of Mn in GaAs. Apart from fundamental research, this method finds its application in semiconductor device fabrication. In the case of  $\text{Ga}_{1-x}\text{Mn}_x\text{As}$ , Mn ions are electrostatically accelerated to a high energy and impacted into an epitaxial GaAs film. Inside the target, the ions undergo collisions with the lattice atoms and lose energy due to inelastic processes, namely excitation and ionization of atoms, as well as elastic collisions with nuclei leading to atomic displacements. This can lead to a significant lattice damage and even to amorphization [153]. Therefore, subsequent high-temperature annealing is usually required in order to enforce recrystallization. In detail, fast thermal treatments such as rapid thermal annealing (RTA), flash lamp annealing (FLA) and pulsed laser melting (PLM) are commonly applied in order to ensure that dopants occupy only substitutional sites and broken bonds get repaired, whereas the diffusion of dopants and formation of extended defects are prevented. In the case of  $\text{Ga}_{1-x}\text{Mn}_x\text{As}$ , attempts to apply RTA failed due to the formation of secondary phases such as MnAs [155] and MnGa [156]. Similar problems were also encountered for FLA [157], which is why PLM has emerged to be the most suitable method. While for RTA and FLA the recrystallization process takes place through solid phase epitaxy, in the case of PLM, the semiconductor surface melts and subsequently regrows via liquid phase epitaxy. The major advantages of the latter method are a higher solidification speed, which overcomes the diffusion speed of impurities, and a shorter annealing duration in order to prevent the diffusion of Mn dopants out of their substitutional positions [153]. The essential steps of ion implantation combined with PLM are depicted schematically in Fig. 4.1.3. At the end, this process leads to epitaxial films of hyperdoped semiconductors. It was found that, compared to  $\text{Ga}_{1-x}\text{Mn}_x\text{As}$  grown by LT-MBE, the basic structural, electronic and magnetic properties of films fabricated by ion implantation and PLM are essentially the same. Strikingly, the fraction of Mn atoms occupying interstitial sites is considerably smaller in films fabricated by the latter method, as inferred from particle-induced X-ray emission (PIXE) experiments [152]. This is also supported by the observation of a smaller difference in the lattice constants of

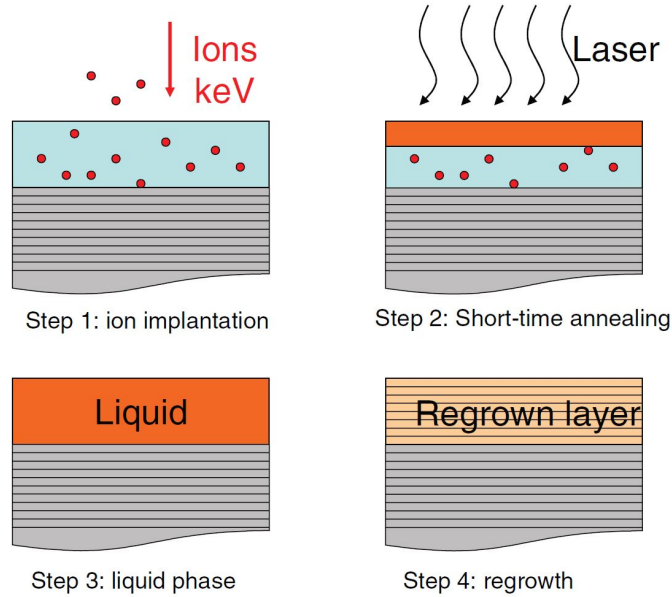


Figure 4.1.3: The process of ion implantation followed by pulsed laser melting. In the first step, ion implantation introduces a large amount of dopants. Subsequently, pulsed laser melting induces the recrystallization of the host via liquid phase epitaxy. Content reprinted from Ref. [153] with permission of IOP Publishing.

$\text{Ga}_{1-x}\text{Mn}_x\text{As}$  and the GaAs substrate in X-ray diffraction (XRD) studies [158], which is usually attributed to the high quantity of point defects in LT-MBE grown  $\text{Ga}_{1-x}\text{Mn}_x\text{As}$  [159, 160]. After this review of basic properties and the fabrication of  $\text{Ga}_{1-x}\text{Mn}_x\text{As}$ , the following section will be devoted to a discussion of current models explaining the origin of ferromagnetism and the band structure in  $\text{Ga}_{1-x}\text{Mn}_x\text{As}$  and related compounds such as  $\text{Ga}_{1-x}\text{Mn}_x\text{P}$ .

## 4.2 Ferromagnetism and Electronic Transport in $\text{Ga}_{1-x}\text{Mn}_x\text{As}$ and $\text{Ga}_{1-x}\text{Mn}_x\text{P}$

### 4.2.1 Theoretical models

It is well established that magnetism in  $\text{Ga}_{1-x}\text{Mn}_x\text{As}$  and related (III,Mn)V compounds originates from local Mn moments. However, since the doping concentration is generally very low, the average distance between substitutional Mn atoms is too large for a direct exchange interaction. The reason, why a ferromagnetic order can still emerge in  $\text{Ga}_{1-x}\text{Mn}_x\text{As}$ , can be found in the itinerant holes provided by the Mn dopants. In experiments it was demonstrated that ferromagnetism is mediated by these charge carriers and thus the magnetic properties, in particular the Curie temperature, strongly depend on the hole concentration. In detail, an antiferromagnetic coupling between the hole spin and the localized Mn spin leads to a long-range ferromagnetic coupling between neighboring Mn spins.

The most successful theory for Ga<sub>1-x</sub>Mn<sub>x</sub>As is the so-called mean field *p-d* Zener model, proposed by T. Dietl *et al.* [161]. It should be noted that this model has been developed according to the spirit of second-principles methods, i.e., in contrast to first-principle calculations it makes use of experimental information on the host band structure, the ground state of magnetic impurities and the coupling between these two subsystems [162]. This theory is based on the original model of Zener [163], and it could be demonstrated that it is equivalent to the Ruderman-Kittel-Kasuya-Yoshida (RKKY) model in the case of Ga<sub>1-x</sub>Mn<sub>x</sub>As [164, 165, 166]. We will start with a short review of the RKKY interaction, which can be described as follows: The introduction of magnetic impurities into a metal generally leads to a shielding of these spins by itinerant carriers, which results in a spin polarization of the carriers around the impurity. The spin of a second impurity located in the vicinity of the first impurity is aligned in order to minimize the exchange energy. Therefore, an indirect exchange interaction is induced between the localized spins  $\vec{S}_i$  and  $\vec{S}_j$ , which can be described by the following RKKY Hamiltonian [167]:

$$\mathcal{H}_{\text{RKKY}} = - \sum_{i,j} J_{ij}^{(\text{RKKY})}(R_{ij}, k_F) \vec{S}_i \vec{S}_j. \quad (4.1)$$

Here, the exchange integral  $J_{ij}^{(\text{RKKY})}(R_{ij}, k_F)$  depends on the distance  $R_{ij}$  between adjacent impurity atoms—in the concrete case of Ga<sub>1-x</sub>Mn<sub>x</sub>As this is the distance between two Mn<sub>Ga</sub> atoms—and the magnitude of the Fermi wave vector  $k_F = (3\pi^2 p)^{1/3}$ , where  $p$  is the hole concentration and the Fermi surface is assumed to be spherical. In detail,  $J_{ij}^{(\text{RKKY})}(R_{ij}, k_F)$  is proportional to the density of states for holes at the Fermi energy  $D(E_F)$  and to the exchange constant  $J_{pd}$  for the interaction between *p*-like hole states and localized *d*-electrons of the substitutional Mn:

$$J_{ij}^{(\text{RKKY})}(R_{ij}, k_F) = \frac{D(E_F) J_{pd}^2 k_F^3}{(2\pi)^3} F(2k_F R_{ij}). \quad (4.2)$$

The function  $F(2k_F R_{ij})$  is defined as

$$F(2k_F R_{ij}) = \frac{\sin(2k_F R_{ij}) - 2k_F R_{ij} \cos(2k_F R_{ij})}{(2k_F R_{ij})^4}. \quad (4.3)$$

Figure 4.2.1 depicts the course of  $J_{ij}^{(\text{RKKY})}$  as a function of  $k_F R_{ij}$ . It can be seen that the RKKY exchange constant shows a damped oscillatory behavior, whereby the sign switches between positive (ferromagnetic coupling) and negative (antiferromagnetic coupling) with increasing distance  $R_{ij}$ . This should lead to oscillations of the electron spin polarization around the localized spins. However, since the mean distance between charge carriers in Ga<sub>1-x</sub>Mn<sub>x</sub>As is greater than that between localized impurity spins, the oscillating character of the RKKY interaction does not become apparent in Ga<sub>1-x</sub>Mn<sub>x</sub>As and the exchange interaction is only ferromagnetic [168]. In detail, for typical Mn concentrations in Ga<sub>1-x</sub>Mn<sub>x</sub>As, the RKKY

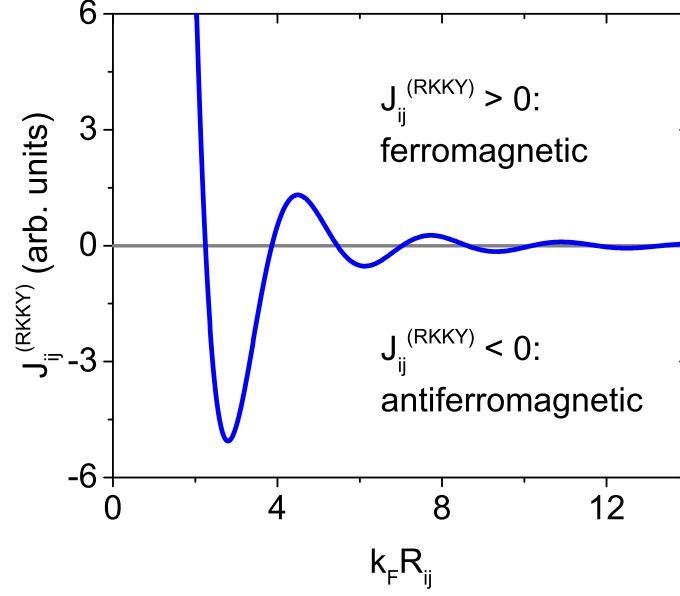


Figure 4.2.1: RKKY exchange coupling constant  $J_{ij}^{(\text{RKKY})}$  as a function of  $k_F R_{ij}$ . For positive values of  $J_{ij}^{(\text{RKKY})}$  the coupling between spins is ferromagnetic, while for negative values it is antiferromagnetic.

exchange constant can only assume values located left of the first root of the function, i.e.,  $k_F R_{ij} = 2.25$ . In other systems with higher carrier densities these so-called Friedel oscillations of the spin polarization might lead to a spin-glass ground state. Despite the experimentally observable long-range ferromagnetic order in  $\text{Ga}_{1-x}\text{Mn}_x\text{As}$  it is important to note that there can exist a local antiferromagnetic coupling between two Mn spins, because the Mn atoms are randomly distributed in the GaAs host and thus the distance of adjacent dopants is not constant [127].

In the case of  $\text{Ga}_{1-x}\text{Mn}_x\text{As}$ , a mean-field approximation of the original Zener model [163] is equivalent to the RKKY picture discussed above, although it takes account of neither the itinerant character of the magnetic charge carriers nor the Friedel oscillations of the spin polarization. This mean-field approximation was initially proposed by T. Dietl *et al.* [161] and extended in Refs. [169, 168, 170].

In terms of the Zener model of the carrier-mediated ferromagnetic interactions the equilibrium magnetization, and thus the Curie temperature, can be determined by the minimum of the Ginzburg-Landau free energy functional  $F[\vec{M}(\vec{r})]$  of the system, where  $\vec{M}(\vec{r})$  is the local magnetization of the localized spins [171]. Several aspects as spin-orbit coupling, disorder, carrier correlation and antiferromagnetic interactions can be added to this rather versatile scheme in a controlled way. The free energy is obtained by diagonalizing the following Hamiltonian:

$$\mathcal{H} = \mathcal{H}_{pd} + \mathcal{H}_{\text{KL}} + \mathcal{H}_{\text{str}}. \quad (4.4)$$

The first term  $\mathcal{H}_{pd}$  represents the  $p$ - $d$  exchange interaction caused by the hybridization of  $p$ -like valence states and local Mn  $d$  shells. In the mean-field approximation it is assumed that the holes are located in an effective field which is proportional to the magnetization  $\vec{M}(\vec{r})$  of the localized spins. Since the ferromagnetic order is mediated by itinerant holes, it is crucial to consider the valence band structure of the holes and thus  $\mathcal{H}_{KL}$  represents the  $6 \times 6$  Kohn-Luttinger-Hamiltonian taking into account the first six valence bands of pure undoped GaAs. Finally, the lattice strain generated by the lattice mismatch of the Ga<sub>1-x</sub>Mn<sub>x</sub>As film and the substrate is considered by means of  $\mathcal{H}_{str}$ . Although the strain has no significant effect on the Curie temperature, it induces a considerable perpendicular magnetic anisotropy [168]. The mean-field Zener model yields results for various parameters such as the Curie temperature or magnetic anisotropies, which are in reasonable agreement with experimental studies on Ga<sub>1-x</sub>Mn<sub>x</sub>As. Finally, the mean field theory predicts the following relation between the Curie temperature  $T_C$ , the hole density  $p$  and the effective Mn concentration  $x_{eff}$ :

$$T_C \propto x_{eff} \cdot p^{1/3}, \quad (4.5)$$

whereby  $x_{eff} = x_{sub} - x_i$  is the difference between the density of substitutional Mn  $x_{sub}$  and the concentration of Mn located at interstitial positions  $x_i$  [161]. Although some experiments have shown a reasonable agreement with this predicted behavior [172], this topic is still controversially debated in the literature. In general, the experimental determination of  $p$  is quite challenging, in particular because of the presence of point defects and the occurrence of the anomalous Hall effect, which is usually observed in ferromagnets. Moreover, the extraction of reliable values for  $x_{eff}$  from magnetization data is difficult [173].

Not only the relation for the Curie temperature as a function of  $x_{eff}$  and  $p$  is questionable, but also the general validity of the mean-field Zener model with respect to Ga<sub>1-x</sub>Mn<sub>x</sub>As. As early as in 2000, T. Dietl *et al.* pointed out possible limitations of this mean-field model, since charge carriers can be close to the localization boundary and a disorder-driven static phase separation might occur. In this case, one regime would be populated by charge carriers in extended states and the other phase would contain singly-occupied impurity-like states [161]. Since it has been observed experimentally that Ga<sub>1-x</sub>Mn<sub>x</sub>As films can reside in the vicinity of the metal-insulator transition boundary [174, 175], both disorder and carrier-carrier correlations are assumed to play an important role in this system [162, 176].

Furthermore, there exist entirely opposite models to the widely held view that ferromagnetism is mediated by a Fermi sea of itinerant holes located in the valence band [117]. In the Zener model the Fermi energy is assumed to lie within the extended states derived from the GaAs host lattice. A main result of this picture is that the Curie temperature increases monotonically with both the effective Mn concentration  $x_{eff}$  and the hole density  $p$ . In contrast to that, experimental studies by M. Dobrowolska *et al.* suggest that the Fermi energy is



always located within a separate impurity band up to rather high nominal Mn doping levels [173]. This is supported by electronic-structure calculations using tight binding [177] and first principles methods [178]. In their work, M. Dobrowolska *et al.* observe a non-monotonic variation of the Curie temperature, which stands in contradiction to the Zener model. Interestingly, this work supports the results by S. Erwin and A. Petukhov [179], who show that in the context of the impurity-band model partial compensation by Mn interstitials promotes ferromagnetic order below the metal-insulator transition. In this picture, the Mn interstitials are needed to achieve an optimal location of the Fermi level within the impurity band in order to maximize  $T_C$ . An appropriate control of the Mn interstitial concentration, co-doping with donor ions or modulation doping are suggested for optimizing the location of the Fermi energy within the impurity band [173]. For instance, co-doping of  $\text{Ga}_{1-x}\text{Mn}_x\text{As}$  layers with Si results in an increase of  $T_C$ , although Si acts as a donor in  $\text{Ga}_{1-x}\text{Mn}_x\text{As}$  [180]. This unexpected result is ascribed to an increase in the hole mobility due to changes in the relative occupancy of the impurity band associated with compensation by Si donors. Finally, it should be noted that the work by M. Dobrowolska *et al.* strictly concentrates on compounds with relatively small Curie temperatures, which are located on the insulating side of the metal-insulator transition. Apart from doubts about the interpretation of infrared absorption measurements which support the impurity-band model [181], this constitutes one of the main points of criticism with regard to the general validity of this theory.

This long-standing controversy about the origin of ferromagnetism and the precise electronic structure in  $\text{Ga}_{1-x}\text{Mn}_x\text{As}$ , sometimes named the "Battle of the bands" after an article by N. Samarth [117], is still not fully resolved and it is possible that there is an overinterpretation of these two pictures discussed above. For instance, a work by T. Jungwirth *et al.* indicates the presence of an impurity band only in low-doped insulating  $\text{Ga}_{1-x}\text{Mn}_x\text{As}$  films ( $x < 1\%$ ), whereas for metallic compounds with  $x > 2\%$  there is evidence that the impurity band has merged with the valence band [175]. These observations are schematically depicted in Fig. 4.2.2. Therefore, both the Zener model and the impurity-band picture are applicable for the respective Mn concentration ranges. Note that signatures of ferromagnetism are usually being detected in  $\text{Ga}_{1-x}\text{Mn}_x\text{As}$  layers with Mn contents higher than  $x = 0.5\text{--}1.5\%$ , whereas samples with lower Mn doping are found to be paramagnetic [154, 182].

#### 4.2.2 Percolation of bound magnetic polarons

An intriguing concept in order to explain the origin of ferromagnetism in  $\text{Ga}_{1-x}\text{Mn}_x\text{As}$  within the impurity-band model is the percolation of bound magnetic polarons, which was first proposed by A. Kaminski and S. Das Sarma [3, 4]. The fundamental prerequisite is that the hole density  $p$  is considerably lower than the concentration of magnetically active impurities. Furthermore, an inhomogeneous distribution of magnetic impurities is assumed. The spins of the localized charge carriers can polarize the surrounding magnetic impurities within a

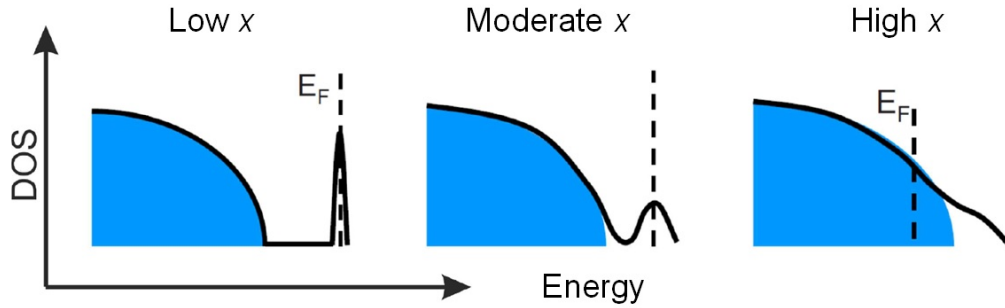


Figure 4.2.2: Schematic diagrams of the density of states (DOS) as a function of energy  $E$  for  $\text{Ga}_{1-x}\text{Mn}_x\text{As}$  with different Mn doping concentrations  $x$ . For low-doped insulating  $\text{Ga}_{1-x}\text{Mn}_x\text{As}$  (left diagram) an impurity band is detached from the valence band, whereas for high-doped metallic compounds the valence and impurity bands become merged (right diagram). Blue areas indicate delocalized states, white areas represent localized states. Content reprinted from Ref. [175] with permission of the American Physical Society.

certain radius, in which the antiferromagnetic coupling is stronger than thermal fluctuations, leading to the emergence of bound magnetic polarons, which grow in size for decreasing temperatures [183]. Although the direct exchange interaction of the localized holes is antiferromagnetic, the interaction between bound magnetic polarons may be ferromagnetic at large enough densities of magnetic impurities [184]. The volume of the individual magnetic polarons increases logarithmically as the temperature is decreased and polaron clusters are formed [183]. At the ferromagnetic transition temperature, an infinite cluster spanning the whole sample is formed and spontaneous magnetization occurs. The quantitative theory of this transition was first presented in Ref. [3] and further developed in Ref. [121], whereas Ref. [4] focuses on the relationship between polaron percolation and electronic transport properties. A typical situation of charge transport close the Curie temperature  $T_C$  is depicted in Fig. 4.2.3. In this temperature range, charge transport occurs by means of nearest-neighbor hopping and the resistivity of such a system increases exponentially with decreasing temperature. Figure 4.2.3 shows a nearly infinite cluster of magnetic polarons and three conceivable hopping scenarios, namely: (a) forbidden hopping onto an already occupied site due to on-site repulsion, (b) hopping to a free site, which may be located outside the infinite cluster, and (c) the unlikely case of hopping to already polarized regions.

In general, for compounds in which a percolative transition is expected, the shape of the temperature-dependent magnetization curve  $M(T)$  is predicted to be concave [3]. This is in good agreement with experimental magnetization data for  $\text{Ge}_{1-x}\text{Mn}_x$  [185] and low- $T_C$  III-V magnetic semiconductors [113, 186]. The crossover from a Brillouin-function-like magnetization curve to a concave one for decreasing charge carrier concentration or increasing localization is very robust, and experiments show that the curves change smoothly with

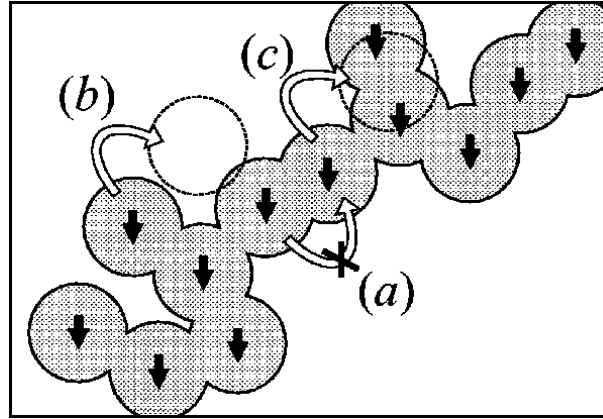


Figure 4.2.3: Conceivable hopping mechanisms in an almost infinite cluster of magnetic polarons in  $\text{Ga}_{1-x}\text{Mn}_x\text{As}$  in the vicinity of the Curie temperature  $T_C$ . The spins of localized holes are indicated by black arrows, the regions with magnetic impurities polarized by these spins are dotted. Three situations are indicated: (a) A hole is not allowed to hop onto a site already taken by another hole because of on-site repulsion. (b) Hopping to a free site, which might be located outside the region polarized by other holes. (c) Hopping to already polarized regions is very unlikely around  $T_C$ . Content reprinted from Ref. [4] with permission of the American Physical Society.

disorder strength [176]. In contrast to the Zener model [161], quantitative predictions of the polaron model are not to be expected, since the calculated values for the Curie temperature deviate about one order of magnitude from experimental results [3].

### 4.2.3 Metal-insulator transition and magnetotransport

As previously discussed, a metal-insulator transition (MIT) occurs in  $\text{Ga}_{1-x}\text{Mn}_x\text{As}$  as a function of Mn doping. More generally, this is sometimes also called a metal-nonmetal transition, where the term "nonmetal" can indicate a semiconductor or an insulator. At first, we recall that the insulating behavior of a specific material generally arises from electronic band theory, since there is a forbidden region in energy, the so-called band gap, between a completely filled valence band and an empty conduction band. However, there also exist other types of insulators. In the case of Mott insulators a gap opens due to electron-electron interactions [187, 188]. For a doped semiconductor it is conceivable that these interactions result in a splitting of the impurity band into an upper Hubbard band and a lower Hubbard band (the actual impurity band). For stronger doping, the distance between the impurities decreases and both Hubbard bands broaden until they overlap. In the case of  $\text{Ga}_{1-x}\text{Mn}_x\text{As}$  one has to consider the merging of the impurity band with the valence band. Theoretical studies, which also include disorder effects, predict an MIT for  $x = 1\%$  in  $\text{Ga}_{1-x}\text{Mn}_x\text{As}$  which is in good agreement with experimental results [189, 190].

Another example is the so-called Anderson insulator, in which a random variation of the lattice potential (disorder) can lead to electron localization and hence to an insulating behavior [191]. In general, disorder can be realized by impurities or defects in semiconductors. A high disorder and/or reduced overlap of wave functions between neighboring sites lead to regions with localized states appearing at the band edges. The energy  $E_m$  which separates these localized states from delocalized ones is called mobility edge. In the case of an increasing degree of disorder and/or an ever decreasing overlap of wave functions, the localized regions expand until they extend over the entire band. In this case, charge carrier transport can only take place via hopping, whereby carriers hop from one impurity to another. To summarize, by varying the doping and the degree of disorder the electronic states in an impurity band may be localized or delocalized. The change of these parameters can make the Fermi level cross from a region with localized states to a region with delocalized states, which results in either an insulating or a metallic behavior of the system. This model constitutes another example for an MIT. It should be mentioned, that the Anderson transition is a quantum phase transition which is only well-defined at zero temperature. At finite temperatures a crossover region exists, where the true ground state of the system is not distinguishable.

In doped semiconductors, both charge correlation effects and disorder are usually present and have to be considered to describe the MIT [192], which also appears to be true for  $\text{Ga}_{1-x}\text{Mn}_x\text{As}$ . Such a disorder-induced MIT in the presence of interactions is called Mott-Anderson transition. A. Richardella *et al.* studied the nature of electronic states in  $\text{Ga}_{1-x}\text{Mn}_x\text{As}$  samples close to this MIT ( $x = 1.5$  to  $5\%$ ) by employing scanning tunneling microscopy [193, 194]. Their findings suggest that spatial heterogeneity and electronic correlations have to be considered for a better understanding of the origin of magnetism in highly-doped magnetic semiconductors. As pointed out by L. Bergqvist *et al.*, the wide range of experimentally reported ordering temperatures is attributable to the fact that the distribution of magnetic impurities and thus the disorder in the samples critically depend on how the films are prepared [195]. Temperature-dependent electronic transport measurements can provide valuable information about the position of  $\text{Ga}_{1-x}\text{Mn}_x\text{As}$  films with respect to the MIT. In detail, the resistivity  $\rho(T)$  shows a different behavior for metallic and insulating samples. Metallic samples with high Mn contents generally behave like normal semiconductors at temperatures far above  $T_C$ , as the resistivity increases with decreasing temperatures. In the vicinity of the ferromagnetic transition temperature a characteristic maximum in  $\rho(T)$  can be observed, which is followed by a decrease in resistivity and hence a metallic behavior towards even lower temperatures. The maximum in  $\rho(T)$  is usually explained as being due to an increase in scattering caused by spin fluctuations near  $T_C$  [142, 174], but there also exist other possible explanations [176, 196]. Moreover, the temperature derivative of the resistance displays a peak at  $T_C$ , which is expected to have the same functional form as that of the specific heat [197]. However, experimental studies which tried to determine critical exponents generated imprecise and contradictory results, cf. Ref. [198] and references therein. Once again disorder-

der seems to play an important role in this case. For rather insulating samples, where  $\rho(T)$  increases very strongly for  $T \rightarrow 0$ , this peak becomes considerably less pronounced [174]. Apart from studies of  $\rho(T)$  at zero magnetic field, it is also instructive to study the magnetoresistance  $\Delta R/R$  of  $\text{Ga}_{1-x}\text{Mn}_x\text{As}$ . This quantity is defined as follows:

$$\frac{\Delta R}{R} = \frac{R(B) - R(0)}{R(0)}. \quad (4.6)$$

In the case of  $\text{Ga}_{1-x}\text{Mn}_x\text{As}$ , the magnetoresistance is typically negative, which can be explained by a reduction of spin-disorder scattering [174, 199, 200]. As discussed further below in more detail, under certain circumstances a positive anisotropic magnetoresistance (AMR) effect can be observed in the ferromagnetic phase of  $\text{Ga}_{1-x}\text{Mn}_x\text{As}$ .

Finally, it should be emphasized that the participation of free charge carriers in the magnetism leads to a large anomalous Hall effect contribution [200]. The total Hall resistivity  $\rho_{xy}$  is given by the sum of two contributions, namely the ordinary Hall effect  $\rho^{\text{NH}}$  and the anomalous Hall effect  $\rho^{\text{AH}}$ , which are proportional to the magnetic field  $B$  and the magnetization  $M$ , respectively:

$$\rho_{xy} = \rho^{\text{NH}} + \rho^{\text{AH}} = R_0 B + R_A M. \quad (4.7)$$

Here,  $R_0$  and  $R_A$  indicate the normal and anomalous Hall constant, respectively. Considering Eq. (4.7), the Hall resistivity does not only contain information on the charge carrier concentration  $p$  via  $R_0 = 1/pe$ , but also on the magnetism of the sample. However, the analysis is complicated by the dependence of the anomalous Hall constant  $R_A$  on the resistance  $\rho$ , which on the other hand depends on the magnetic field  $B$ . In general, it is

$$R_A(\rho(B)) = \sum_i C_i \cdot \rho^{\beta_i}(B), \quad (4.8)$$

where a summation over all relevant contributions to the anomalous Hall effect is performed. The coefficients  $C_i$  are weighting factors for the corresponding contributions and  $\beta_i$  represents the respective scaling exponent. In reality, generally two contributions are relevant, namely skew scattering [201, 202] and a side-jump mechanism [203], where  $R_A \propto \rho(B)$  and  $R_A \propto \rho^2(B)$ , respectively. While the skew scattering mechanism is based on an asymmetric Mott scattering of charge carriers at magnetic impurities, the side-jump process originates from a discontinuous sideways displacement of the center of mass of charge carrier wave packets by a central potential in the presence of spin-orbit interaction. Besides these two contributions, a further noteworthy contribution is based on the theory of the so-called Berry phase, which is a geometric phase acquired by a quantum system which is adiabatically transported round a closed circuit in the parameter space of the respective Hamiltonian [204, 205].

#### 4.2.4 Related compounds

Apart from the archetypal compound Ga<sub>1-x</sub>Mn<sub>x</sub>As, there exists a plethora of other DMSs studied in the literature, as for example (In,Mn)As, (III,Mn)Sb, (III,Mn)P and (III,Mn)N [206]. In this study, we decided to compare the electronic transport and particularly the resistance noise behavior of Ga<sub>1-x</sub>Mn<sub>x</sub>As to Ga<sub>1-x</sub>Mn<sub>x</sub>P, since the charge carriers in the latter compound are of a much more localized nature than in Ga<sub>1-x</sub>Mn<sub>x</sub>As and a percolation of bound magnetic polarons is more likely to be observed. In detail, Mn-doped GaP exhibits a larger hole binding energy of about 0.4 eV [207, 208]. Due to its shorter bond length, it is expected to have a stronger *p-d* hybridization. Experiments have not yet established unambiguously the nature of magnetic interactions in Ga<sub>1-x</sub>Mn<sub>x</sub>P. However, a comparative study of Ga<sub>1-x</sub>Mn<sub>x</sub>P and Ga<sub>1-x</sub>Mn<sub>x</sub>As also suggests a carrier-mediated mechanism for ferromagnetism in Ga<sub>1-x</sub>Mn<sub>x</sub>P [208]. In the work by M. Scarpulla *et al.*, indications for a percolative transition of magnetic polarons are discussed [208]. As no resistance noise measurements of insulating Ga<sub>1-x</sub>Mn<sub>x</sub>As films with  $x < 1$  % could be performed within the frame of this work, cf. discussion in Sec. 4.4.3, two Ga<sub>1-x</sub>Mn<sub>x</sub>P films with different Mn content were investigated instead.

In analogy to the Ga<sub>1-x</sub>Mn<sub>x</sub>As films described in section 4.1.4, GaP wafers are grown by standard MBE techniques, followed by the implantation of Mn ions into the GaP matrix. Subsequently, rapid thermal [209] or pulsed laser annealing [208, 153] are applied in order to recrystallize the samples.

### 4.3 Investigated samples

Electronic transport measurements have been performed on a total of nine Ga<sub>1-x</sub>Mn<sub>x</sub>As thin film samples and two Ga<sub>1-x</sub>Mn<sub>x</sub>P samples, see Table 4.3.1 for an overview. For all films, the corresponding Curie temperatures were determined by magnetization measurements. It should be emphasized that extensive studies on all present samples, including magnetization measurements and standard thin film characterization techniques, have been published and can be found in Refs. [146, 210, 154, 153, 211]. The samples in this work were prepared in two different ways. Metallic Ga<sub>1-x</sub>Mn<sub>x</sub>As samples with  $x = 4$  % and  $x = 7$  % were grown by low-temperature molecular beam epitaxy (LT-MBE) on semi-insulating GaAs(001) substrates in a Mod Gen II MBE system with the lowest possible As<sub>2</sub>-partial pressure of about  $2 \times 10^{-6}$  mbar at the Physikalisch-Technische Bundesanstalt (PTB) in Braunschweig [210]. After the growth of a 100 nm high-temperature (HT) GaAs buffer layer at  $T_g = 560$  °C, the temperature was decreased to 270 °C for the  $x = 4$  % samples and to 225 °C for the  $x = 7$  % samples for the subsequent LT Ga<sub>1-x</sub>Mn<sub>x</sub>As growth. Post-growth annealing at 200 °C (18 hours in ambient atmosphere) was performed for two of the samples in order to enhance  $T_C$ . The total Mn concentration  $x$  was calculated from the molecular flux ratio of Mn and Ga measured in the MBE at the position of the wafer and compared with reflection

Table 4.3.1: Overview of the investigated thin film samples and related parameters, including: information about the manganese content  $x$ , whether samples were grown by low-temperature molecular beam epitaxy (LT-MBE) or ion implantation combined with pulsed laser melting (II+PLM), the institute where samples have been fabricated, which kind of post-treatment was given, and the values of the film thickness  $d$  as well as the Curie temperature  $T_C$  determined by magnetization measurements.

Mn content $x$	Fabrication	Source	Post-treatment	Thickness	$T_C$
<b>Ga<sub>1-x</sub>Mn<sub>x</sub>As</b>					
7.0 ± 1.0 %	LT-MBE	PTB	as-grown	25 nm	60 K
7.0 ± 1.0 %	LT-MBE	PTB	annealed at 200°C (18 h)	25 nm	122 K
6.0 ± 0.3 %	LT-MBE	UoN	annealed at 190°C (48 h)	25 nm	125 K
6.0 ± 0.3 %	LT-MBE	UoN	He-ion irradiated (low dose)	25 nm	75 K
6.0 ± 0.3 %	LT-MBE	UoN	He-ion irradiated (high dose)	25 nm	50 K
4.0 ± 1.0 %	LT-MBE	PTB	as-grown	25 nm	70 K
4.0 ± 1.0 %	LT-MBE	PTB	annealed at 200°C (18 h)	25 nm	110 K
1.8 ± 0.2 %	II+PLM	HZDR	as-grown	60 nm	60 K
1.2 ± 0.1 %	II+PLM	HZDR	as-grown	60 nm	31 K
<b>Ga<sub>1-x</sub>Mn<sub>x</sub>P</b>					
7.5 ± 0.8 %	II+PLM	HZDR	as-grown	65 nm	65 K
3.5 ± 0.4 %	II+PLM	HZDR	as-grown	34 nm	45 K

high-energy electron diffraction (RHEED) and energy-dispersive X-ray spectroscopy (EDX) measurements. Moreover, three Ga<sub>1-x</sub>Mn<sub>x</sub>As samples with a nominal Mn concentration of  $x = 6\%$  were grown by LT-MBE on semi-insulating GaAs(001) using a Veeco Mod III MBE system at the University of Nottingham (UoN) [146, 212]. In this case, thermal annealing was performed at 190 °C for 48 hours in ambient atmosphere and the Mn content was determined from the Mn/Ga flux ratio. Two of the films were irradiated with different doses of He-ions after growth. As described above, this particular method allows to control the hole concentration and thus the electronic as well as the magnetic properties without changing the Mn content of a sample. The He-ion energy was chosen as 4 keV. The fluences were  $2.5 \times 10^{13} \text{ cm}^{-2}$  and  $3.5 \times 10^{13} \text{ cm}^{-2}$  for the two irradiated samples. A better measure for the effect of irradiation on material properties than the fluence is the so-called displacement per atom (DPA), i.e., the number of times that an atom in the target is displaced during irradiation. This allows for a comparison with data reported in the literature, in which other ion species and energies are used. For the two irradiated samples, the DPA was  $1.60 \times 10^{-3}$  and  $2.24 \times 10^{-3}$ , respectively [146]. During ion irradiation, the films were tilted by 7° to avoid channeling. Figure 4.3.1 shows the magnetic properties of various He-ion irradiated thin film samples from Ref. [146]. The temperature-dependent magnetization  $M(T)$  measured at a small field of 20 Oe after cooling in field is depicted in Fig. 4.3.1 (a), while (b) shows the magnetic hysteresis for various ion fluences measured at  $T = 5 \text{ K}$ . Clearly, the Curie

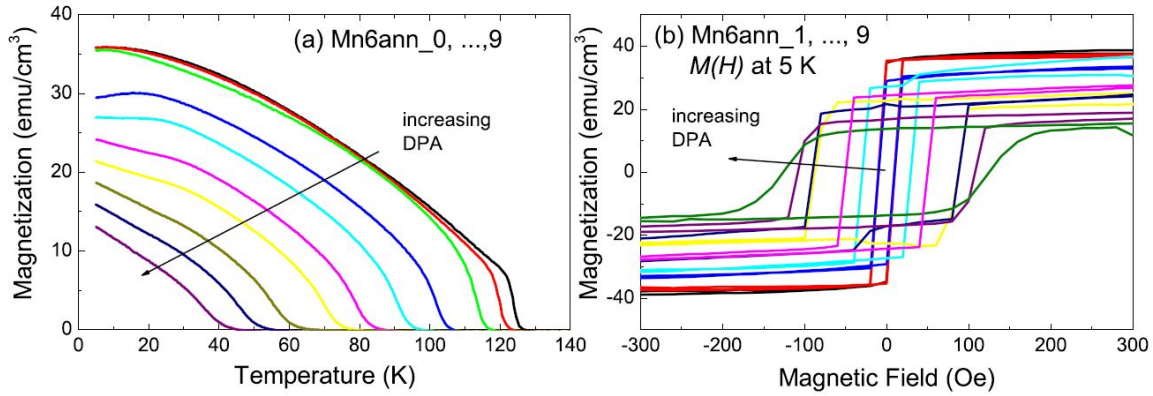


Figure 4.3.1: Magnetic properties of He-ion irradiated thin films studied in Ref. [146]. (a) Temperature-dependent magnetization  $M(T)$ . (b) Field-dependent magnetization  $M(H)$  measurements. In the nomenclature of S. Zhou *et al.*, Mn6ann\_0 denotes the unirradiated film, while Mn6ann\_6 and Mn6ann\_8 indicate the samples irradiated with ion fluences of  $2.5 \times 10^{13} \text{ cm}^{-2}$  and  $3.5 \times 10^{13} \text{ cm}^{-2}$ , respectively. Content reprinted from Ref. [146] with permission of the American Physical Society.

temperature  $T_C$  and the remanent magnetization  $M_r$  decrease for an increasing DPA, while the coercive field  $H_c$  increases. In the nomenclature of S. Zhou *et al.*, Mn6ann\_0 denotes the unirradiated sample, while Mn6ann\_6 and Mn6ann\_8 indicate the films irradiated with ion fluences of  $2.5 \times 10^{13} \text{ cm}^{-2}$  and  $3.5 \times 10^{13} \text{ cm}^{-2}$ , respectively. The  $M(T)$  data are consistent with the values for  $T_C$  shown in Table 4.3.1.

The irradiation parameters result in defects distributed roughly uniformly in the whole  $\text{Ga}_{1-x}\text{Mn}_x\text{As}$  layer as confirmed by simulations using the SRIM (Stopping and Range of Ions in Matter) code [151]. No measurable increase of Mn interstitials was observed by Rutherford backscattering spectroscopy (RBS) [146]. Previous studies show that also the sheet concentration of substitutional Mn atoms remains constant [147], which is why we conclude that the main effect of He-ion irradiation is to introduce deep traps and thereby compensate the holes. It is well established that these defects reside in the As sublattice and most of them are primary defects related to vacancies and interstitials [145, 213]. In our case, atomic force microscopy (AFM) and RBS measurements do not show any indications of irradiation induced surface reconstruction. The crystal quality is comparable with the unirradiated samples. Further details can be found in Ref. [146]. Finally, two  $\text{Ga}_{1-x}\text{Mn}_x\text{As}$  samples with low Mn contents of 1.8 % and 1.2 % as well as two  $\text{Ga}_{1-x}\text{Mn}_x\text{P}$  samples with  $x = 3.5 \%$  and  $x = 7.5 \%$  were fabricated by ion implantation combined with pulsed laser melting at the Helmholtz-Zentrum Dresden-Rossendorf (HZDR) [154, 153]. As mentioned earlier, ion implantation is a common materials engineering technique for introducing foreign ions into a host material. In this case, Mn ions are implanted into GaAs or GaP wafers. The subsequent laser pulse drives a rapid liquid-phase epitaxial growth. The implantation energy was set to 100 keV for



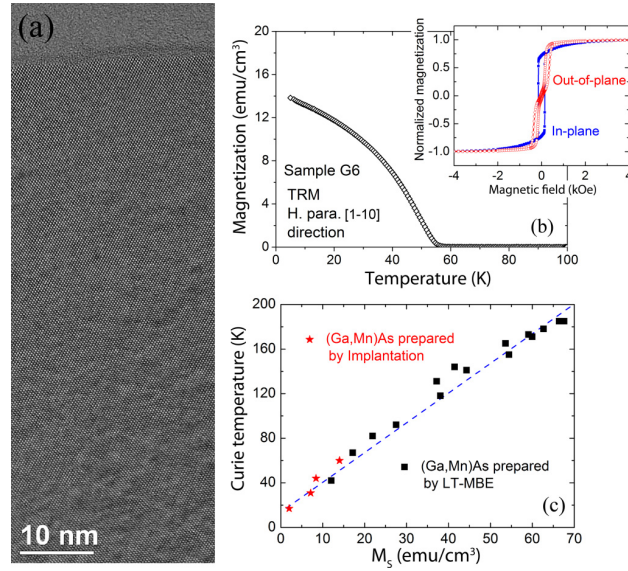


Figure 4.3.2: (a) Cross-sectional TEM image of the  $\text{Ga}_{1-x}\text{Mn}_x\text{As}$  film with  $x = 1.8\%$  indicating a high crystalline quality and excluding the presence of lattice defects or other crystalline phases. (b) Magnetization as a function of temperature showing ferromagnetism below  $T_C = 60$  K. Inset: Character of the magnetic anisotropy. (c) Curie temperature as a function of the spontaneous magnetization  $M_S$ , following the trend observed for optimized  $\text{Ga}_{1-x}\text{Mn}_x\text{As}$  films grown by LT-MBE. Reprinted from Ref. [154] with permission of the American Physical Society.

GaAs [154] and 50 keV for GaP [211, 153]. The wafer normal was tilted by  $7^\circ$  with respect to the ion beam to avoid a channeling effect. A coherent XeCl laser (with 308 nm wavelength and 28 ns duration) was employed to recrystallize the samples, and the energy densities were optimized to achieve high crystalline quality and the highest Curie temperature. The optimal laser energy density is  $0.30 \text{ J/cm}^2$  for  $\text{Ga}_{1-x}\text{Mn}_x\text{As}$  and  $0.45 \text{ J/cm}^2$  for  $\text{Ga}_{1-x}\text{Mn}_x\text{P}$ . The Mn concentration was determined by secondary ion mass spectroscopy. In contrast to films grown by LT-MBE, neither Mn interstitials nor As antisites are observed in samples prepared by ion implantation combined with pulsed laser melting [154, 214]. Transmission electron microscopy (TEM) studies prove the high crystalline quality of the films and exclude the presence of any extended lattice defects, amorphous inclusions and precipitates of other crystalline phases [154]. An exemplary high-resolution TEM image for the  $\text{Ga}_{1-x}\text{Mn}_x\text{As}$  layer with  $x = 1.8\%$  is shown in Fig. 4.3.2 (a). Moreover, a typical temperature-dependent magnetization  $M(T)$  measurement is depicted in Fig. 4.3.2 (b), together with an out-of-plane and an in-plane field-dependent magnetization  $M(H)$  measurement in the inset, indicating the character of magnetic anisotropy. Finally, the magnitude of the Curie temperature is shown in Fig. 4.3.2 (c) for given spontaneous magnetization  $M_S$ , proving the trend established in optimized  $\text{Ga}_{1-x}\text{Mn}_x\text{As}$  samples fabricated by LT-MBE [212].

For some selected films, an array of  $50 \times 50 \mu\text{m}^2$  Hall bars was defined by photolithography

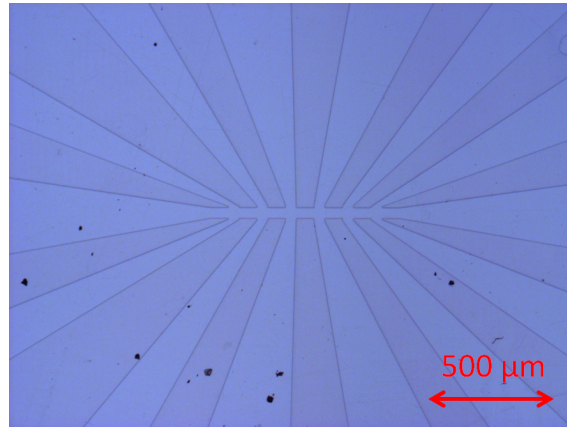


Figure 4.3.3: Microscope image of a typical Hall-bar structure with six adjacent Hall crosses defined by photolithography followed by wet chemical etching. Each Hall cross has an area of about  $50 \times 50 \mu\text{m}^2$ .

followed by wet chemical etching. The quality of Hall effect measurements thereby improves significantly due to a well-defined contact geometry and the resistance noise magnitude increases due to smaller sample volumes according to Hooge's law [49, 50]. In the following, a brief description of the sample preparation procedure will be given. A more detailed instruction can be found in Ref. [215].

At first, the  $\text{Ga}_{1-x}\text{Mn}_x\text{As}$  samples are cut to a size of about  $5 \times 5 \text{ mm}^2$  by first making a slight scratch along the desired edge, then flipping the film over and applying pressure by rolling a glass rod on the back side. Care has to be taken in order to prevent any surface damage, and a surface cleaning procedure using acetone and isopropanol is applied in order to remove debris or dust. Subsequently, the sample is spincoated with the photoresist Allresist AR-U4060. In the following step, the patterning by means of optical lithography is carried out. In detail, the exposure with ultraviolet light emitted by a mercury vapor lamp (desired intensity:  $60 \text{ mJ/cm}^2$ ) leads to photochemical reactions in well-defined regions of the resist, which are not protected by a photomask. Therefore, the solubility of these regions will be enhanced. In the subsequent step, this part of the photoresist will get removed from the film surface in a resist development procedure (developer solution: AR 300-26). After this step, the Hall-bar structure is clearly visible. Moreover, all described steps including the development procedure are still reversible, whereas the subsequent wet chemical etching constitutes an irreversible step, since the etching solution destroys the parts of the  $\text{Ga}_{1-x}\text{Mn}_x\text{As}$  film which are not protected by photoresist. In the case of  $\text{Ga}_{1-x}\text{Mn}_x\text{As}$ , a dilute solution of  $\text{H}_2\text{SO}_4:\text{H}_2\text{O}_2:\text{H}_2\text{O}$  (1:8:40) can be applied and allows for a good control of the etching depth, which can be determined by atomic force microscopy. A typical Hall-bar structure is shown in Fig. 4.3.3.

Finally, together with J. Teschabai-Oglu, within the scope of Ref. [215] all  $\text{Ga}_{1-x}\text{Mn}_x\text{As}$  films fabricated at the PTB in Braunschweig were successfully micro-structured under the use of

instructions above. Moreover, the two weakly doped  $\text{Ga}_{1-x}\text{Mn}_x\text{As}$  films with  $x = 1.8\%$  and  $x = 1.2\%$  have been patterned. No micro-structuring has been carried out neither for the three LT-MBE grown  $x = 6\%$  layers nor for the  $\text{Ga}_{1-x}\text{Mn}_x\text{P}$  films. In the latter case, entirely different etching solutions would be required, cf. Ref. [216, 217]. For all samples, electrical contacts were prepared by soldering In-Sn alloy on top of the films. In each case, the diameter of the utilized gold wires is  $25\ \mu\text{m}$ . After contacting, the sample can be attached to the sample holder by means of GE varnish. Finally, the gold wires connected to the thin film are soldered to the pins of the sample holder.

## 4.4 Results

This section comprises the most important results of electronic transport measurements on  $\text{Ga}_{1-x}\text{Mn}_x\text{As}$  and  $\text{Ga}_{1-x}\text{Mn}_x\text{P}$  thin film samples, which have been performed in the laboratory of Prof. Dr. J. Müller at the Goethe University in Frankfurt. It is divided into three parts. First of all, measurements on metallic  $\text{Ga}_{1-x}\text{Mn}_x\text{As}$  films fabricated at the PTB in Braunschweig will be presented. A major part of these results has already been discussed in Ref. [215]. However, an advanced analysis will be carried out within the scope of this work and the results will be compared to the findings for rather insulating samples. The second part focuses on He-ion irradiated samples, before the chapter will be concluded with a discussion of results obtained from measurements on  $\text{Ga}_{1-x}\text{Mn}_x\text{As}$  and  $\text{Ga}_{1-x}\text{Mn}_x\text{P}$  films with localized charge carriers.

### 4.4.1 Metallic $\text{Ga}_{1-x}\text{Mn}_x\text{As}$ films

Resistivity curves of as-grown and annealed metallic  $\text{Ga}_{1-x}\text{Mn}_x\text{As}$  samples are depicted in Fig. 4.4.1. The corresponding Curie temperatures as determined from magnetization measurements are indicated by arrows. It can be seen that, as expected for strongly doped films, the resistivity shows an increasing behavior towards decreasing temperatures, followed by a maximum in the vicinity of  $T_C$  and a metallic behavior at even lower temperatures. Furthermore, the resistivity decreases after post-growth annealing and  $T_C$  shifts towards higher temperatures for both the  $x = 4\%$  and the  $x = 7\%$  films. This is due to an out-diffusion of interstitial manganese atoms to the film surface, where they are passivated by oxidation or by binding with surplus As atoms [143, 138]. The reduction of Mn interstitials, which commonly act as double donors in  $\text{Ga}_{1-x}\text{Mn}_x\text{As}$ , leads to an increase of the effective carrier concentration  $p$  and hence to a smaller resistivity. Since  $T_C \propto p$ , the Curie temperature is enhanced after the thermal annealing process.

Here, it is important to note that a comparison between samples with different Mn content is complicated, since the utilized growth parameters were slightly different. While the  $x = 4\%$  films were grown at  $270\ ^\circ\text{C}$ , the substrate temperature during the growth of the  $x = 7\%$  layers

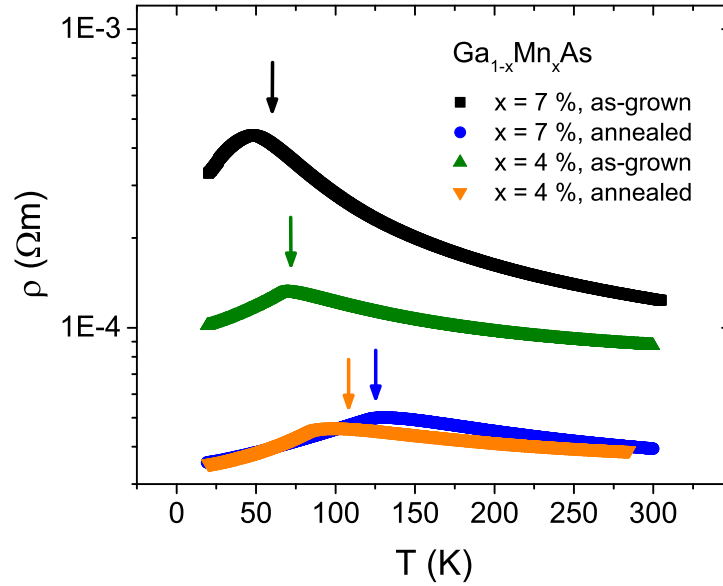


Figure 4.4.1: Temperature-dependent resistivity showing characteristic maxima around  $T_C$  (marked by arrows) for as-grown and annealed metallic  $\text{Ga}_{1-x}\text{Mn}_x\text{As}$  samples with  $x = 4\%$  and  $x = 7\%$ .

was  $225^\circ\text{C}$ . This may account for the fact that the resistivity of the as-grown  $x = 7\%$  film is higher than for the  $x = 4\%$  sample. Moreover, the Curie temperature is higher for the film with the lower Mn content, which is counter-intuitive. In contrast to the as-grown samples, the situation is different for the annealed films. In this case, as expected,  $T_C$  of the sample with  $x = 7\%$  is higher, and the magnitude of resistivity is relatively similar for both films. These observations lead to the hypothesis that an unusually high defect concentration is present in the as-grown  $x = 7\%$  sample. Presumably, these defects are mainly Mn interstitials, since a higher Mn flux rate is utilized during the growth of films with a higher desired Mn doping. Moreover, thermal annealing leads to the out-diffusion of interstitial manganese atoms to the film surface, which explains the consistent results for the annealed samples as opposed to as-grown films.

As discussed in Sec. 4.2.3, the maximum in  $\rho(T)$  can be ascribed to an increase in critical spin disorder scattering caused by thermodynamic magnetization fluctuations near  $T_C$  [142, 174]. Below  $T_C$ , the resistivity exhibits a quadratic dependence on temperature, presumably due to single magnon scattering arising from the ferromagnetically correlated local Mn spins [218].

The temperature-dependent resistivity  $\rho(T)$  was also measured in constant external magnetic fields for all present metallic films. Selected curves for the annealed  $x = 4\%$  sample are depicted in Fig. 4.4.2 for various fields up to 7 T. In this case, magnetic fields were applied perpendicular to the film plane. For increasing magnetic field, the resistivity decreases significantly and the maximum in  $\rho(T)$  is shifted towards higher temperatures. This already

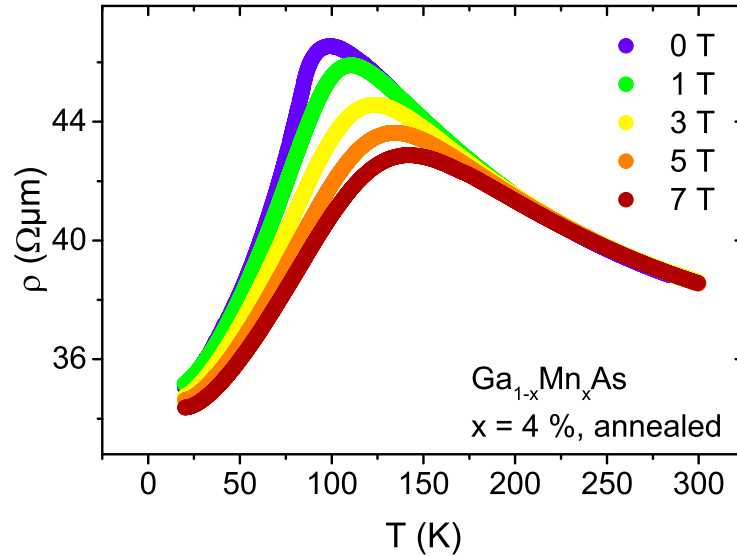


Figure 4.4.2: Resistivity  $\rho(T)$  for various external magnetic fields applied perpendicular to the film plane of the annealed  $x = 4\%$   $\text{Ga}_{1-x}\text{Mn}_x\text{As}$  sample. Higher magnetic fields lead to a decrease of the resistivity and a shift of the maximum in  $\rho(T)$  towards higher temperatures.

indicates a negative magnetoresistance which can be understood as the reduction of scattering due to the alignment of the local magnetic moments by the external magnetic field  $B$  [174]. Three exemplary curves of the magnetoresistance  $\Delta R/R$  are shown in Fig. 4.4.3 for the as-grown  $x = 4\%$   $\text{Ga}_{1-x}\text{Mn}_x\text{As}$  sample. As expected, at 200 K and 90 K, i.e., far above the Curie temperature  $T_C = 70$  K of the film, the magnetoresistance is negative and hence decreases towards higher out-of-plane magnetic fields (green and black curves). It should be mentioned that the highest magnetoresistance of about 15 % at a field of 11 T is observed around the ferromagnetic transition temperature, cf. the inset of Fig. 4.4.3. The magnetoresistance becomes negligible when approaching room temperature and is also small at very low temperatures. For the present samples, the magnetoresistance is considerably larger for the  $x = 7\%$  samples in comparison with the  $x = 4\%$  films, which is related to the higher concentrations of substitutional and interstitial Mn atoms leading to an enhanced scattering of charge carriers. This is also supported by the fact that the magnetoresistance decreases significantly after thermal annealing. In the case of the sample presented in Fig. 4.4.3, compared to temperatures  $T > T_C$ , the magnetoresistance displays a different behavior at 20 K, i.e., at temperatures below  $T_C$  (red curve). While  $\Delta R/R$  still shows a decreasing behavior at higher magnetic fields, at low fields ( $B < 0.5$  T) a positive magnetoresistance can be observed. This observation can be qualitatively explained in terms of the anisotropic magnetoresistance (AMR) effect, whereby the local magnetic moments rotate coherently from their original in-plane direction to the perpendicular direction as it is described within a simple Stoner-Wohlfarth single domain model. Therefore, in the case of an in-plane applied magnetic field, no positive magnetore-

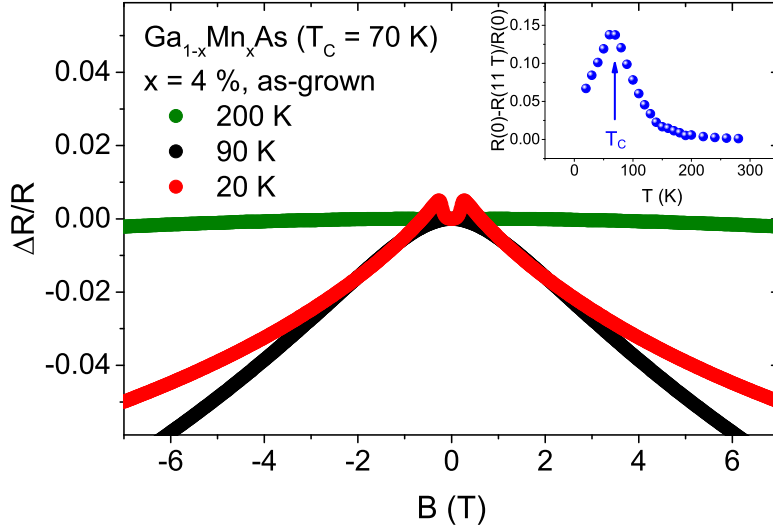


Figure 4.4.3: Magnetoresistance  $\Delta R/R$  of the as-grown  $x = 4\%$   $\text{Ga}_{1-x}\text{Mn}_x\text{As}$  sample measured at three different temperatures, whereby two temperatures are clearly above and the other one below  $T_C = 70$  K. The inset shows the magnetoresistance at a field of  $B = 11$  T for different temperatures with a clear maximum in the vicinity of  $T_C$ .

sistance is observed in the experiment (see Ref. [215]). Finally, it should also be noted that the shape of the negative magnetoresistance changes from a convex behavior at  $T < T_C$  to a rather concave behavior for  $T > T_C$ .

Apart from investigations of the magnetoresistance, we carried out temperature-dependent Hall effect measurements for all present metallic samples in order to determine the hole concentration. However, as described in Sec. 4.2.3, the analysis is complicated due to the occurrence of a strong anomalous Hall effect contribution, which is proportional to the magnetization of the sample. We recall that the Hall resistivity  $\rho_{xy}$  can be written as

$$\rho_{xy} = R_0 B + R_A M, \quad (4.9)$$

where  $R_0 = 1/pe$  contains information on the hole concentration  $p$  and the anomalous Hall constant  $R_A(\rho(B)) = C_1 \cdot \rho(B) + C_2 \cdot \rho^2(B)$  depends on different spin-dependent scattering mechanisms and on the field-dependent resistivity  $\rho(B)$ . Despite the well-defined geometry of the present lithographically patterned thin film samples, the measured signal can still contain a contribution originating from the magnetoresistance. In order to eliminate this contribution, measurements were performed for positive and negative magnetic field sweep directions. Since the Hall voltage  $V_{xy}$  is an antisymmetric function of the magnetic field  $B$ , i.e.,

$$V_{xy}(B) = -V_{xy}(-B), \quad (4.10)$$

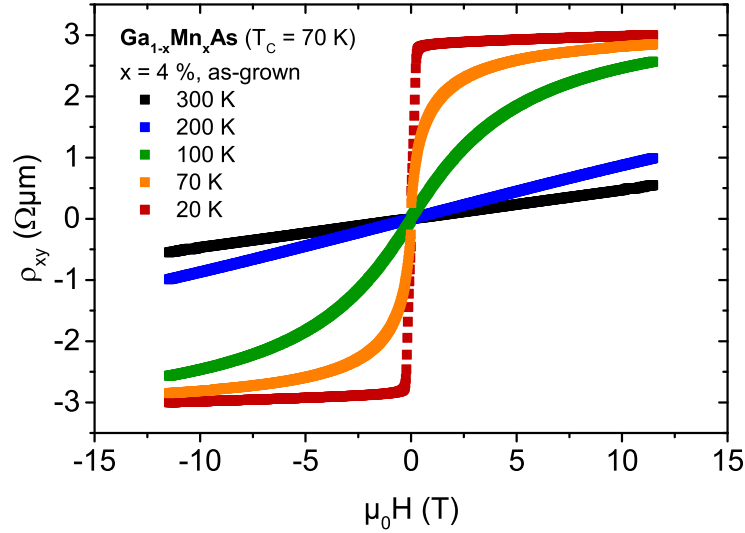


Figure 4.4.4: Temperature-dependent Hall resistivity  $\rho_{xy}$  for the as-grown  $\text{Ga}_{1-x}\text{Mn}_x\text{As}$  sample with  $x = 4\%$ . While only the ordinary, linear Hall effect is observable far above  $T_C$ , below and in the vicinity of the transition temperature a strong anomalous Hall contribution proportional to the magnetization occurs.

contributions from a longitudinal voltage can be eliminated via

$$V_{xy}(B) = \frac{1}{2} (V_{xy}(+B \downarrow) - V_{xy}(-B \uparrow)), \quad (4.11)$$

where  $\uparrow$  denotes a positive and  $\downarrow$  a negative sweep direction. In contrast to the transverse voltage, the longitudinal voltage  $V_{xx}$  is a symmetric function of the magnetic field:

$$V_{xx}(B) = V_{xx}(-B). \quad (4.12)$$

Finally, the Hall resistivity  $\rho_{xy}$  can be calculated from the Hall voltage  $V_{xy}$  via

$$\rho_{xy} = \frac{V_{xy}}{I} \cdot d, \quad (4.13)$$

where  $I$  represents the applied current and  $d$  the film thickness.

Fig. 4.4.4 exemplarily shows the Hall resistivity  $\rho_{xy}(B)$  for magnetic fields between  $-11.5\text{ T}$  and  $11.5\text{ T}$  and various temperatures for the case of the as-grown  $\text{Ga}_{1-x}\text{Mn}_x\text{As}$  sample with  $x = 4\%$ . At high temperatures the Hall resistivity exhibits a linear behavior in the entire field range, while for decreasing temperatures an anomalous Hall contribution becomes more apparent. Although it may seem that at low temperatures the Hall resistivity exhibits a linear behavior at least for high magnetic fields, it should be emphasized that due to the dependence of the anomalous Hall constant  $R_A$  on the magnetoresistance  $\rho(B)$ , which is not negligible and of a non-trivial nature in the case of  $\text{Ga}_{1-x}\text{Mn}_x\text{As}$ , there is still an anomalous Hall contribution

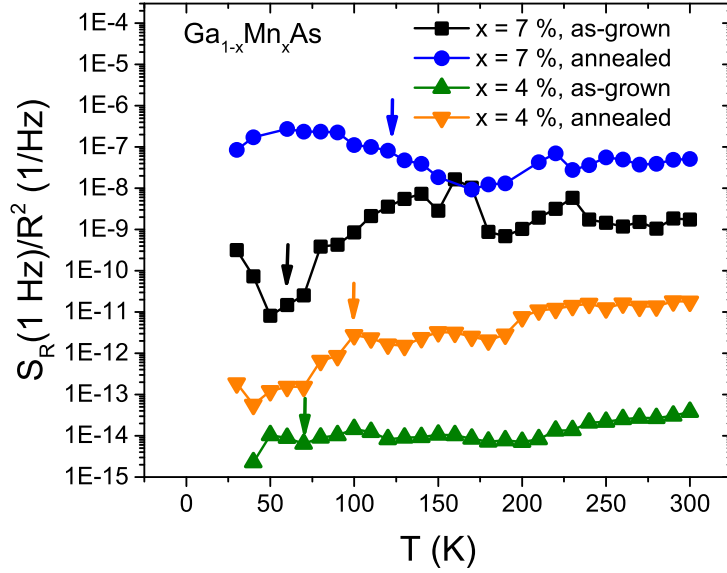


Figure 4.4.5: Temperature-dependent normalized power spectral density  $S_R/R^2$  at 1 Hz. No prominent features can be observed around  $T_C$  (marked by arrows) for as-grown and annealed metallic  $\text{Ga}_{1-x}\text{Mn}_x\text{As}$  samples with  $x = 4\%$  and  $x = 7\%$ . Strikingly, the noise magnitude varies over many orders of magnitude.

which impedes a straightforward calculation of the hole concentration  $p$ . In other words, the anomalous Hall constant should rather be named anomalous Hall coefficient. Moreover, care has to be taken even at room temperature, since, due to paramagnetism, the magnetization in an external magnetic field is non-vanishing even for temperatures far above  $T_C$ . For a detailed description of different approaches for the calculation of the hole concentration in a broad temperature range see Refs. [215, 123]. Within the scope of this work we only focus on the values of  $p$  at room temperature and neglect the magnetization related to paramagnetism. The determined values for  $p(300\text{ K})$  are summarized in Table 4.4.1 for all four samples fabricated at the PTB in Braunschweig. These values are of order  $10^{19}$ – $10^{20}$   $1/\text{cm}^3$ , which is in good agreement with literature [219].

Fig. 4.4.5 shows the normalized power spectral density (PSD) as a function of temperature for all four samples in a semi-logarithmic representation. All measurements were carried out in a five-terminal AC setup, where the sample is placed in a bridge circuit in order to suppress the constant DC voltage offset and to minimize external perturbations, cf. Sec. 3.2.4. Strikingly,  $S_R(1\text{ Hz})/R^2$  varies over many orders of magnitude for the different films and shows, in contrast to the resistivity, no significant features around  $T_C$ . Moreover, a universal behavior of the temperature-dependent noise magnitude cannot be observed for the considered samples. In addition, for externally applied out-of-plane magnetic fields between 0.1 T and 7 T, no significant changes were observed in the temperature-dependent PSD down to about 20 K for all films [215]. Previous noise studies by M. Zhu *et al.* on



Table 4.4.1: Overview of the four epitaxial  $\text{Ga}_{1-x}\text{Mn}_x\text{As}$  layers grown at the PTB in Braunschweig, including: the Mn content  $x$ , the post-growth treatment, the Curie temperature  $T_C$ , the hole concentration  $p$  at 300 K determined from Hall effect measurements and the calculated Hooge constant  $\gamma_H$  at room temperature.

Mn content $x$	Post-growth treatment	$T_C$	$p(300\text{ K})[1/\text{cm}^3]$	$\gamma_H(300\text{ K})$
$7.0 \pm 1.0\%$	as-grown	60 K	$3.7 \times 10^{19}$	$8 \times 10^1$
$7.0 \pm 1.0\%$	annealed at 200°C for 18 h	122 K	$1.3 \times 10^{20}$	$7 \times 10^3$
$4.0 \pm 1.0\%$	as-grown	70 K	$8.0 \times 10^{19}$	$1 \times 10^{-2}$
$4.0 \pm 1.0\%$	annealed at 200°C for 18 h	110 K	$1.2 \times 10^{20}$	$3 \times 10^0$

$\text{Ga}_{1-x}\text{Mn}_x\text{As}$  samples with similar parameters discuss a magnetic field dependence at low temperatures  $T < 10\text{ K}$ , which can be attributed to fluctuating nanoscale magnetic clusters of Mn interstitials [220]. In the present work, no noise measurements below about 20 K could be performed for the  $x = 4\%$  and  $x = 7\%$  films due to a strong frequency dependence of the resistance, which will be discussed in more detail further below. Both Ref. [220] and our study have in common that no indications for electronic phase separation are observed in the resistance noise of metallic  $\text{Ga}_{1-x}\text{Mn}_x\text{As}$  films in the vicinity of the ferromagnetic transition temperature. One reason could be that possible contributions from mixed phases are overshadowed by thermally-activated impurity switching processes. However, more likely, due to the high concentration of Mn substitutional atoms, holes are delocalized and the formation of magnetic polarons is not to be expected for the present metallic samples. The observed  $1/f$ -type noise is likely to be dominated by switching processes related to crystalline defects. In detail, the noise magnitude is significantly higher for the  $x = 7\%$  films than for the  $x = 4\%$  layers, which can be explained by a higher density of substitutional and interstitial Mn atoms, since a higher Mn flux rate is utilized during sample growth for films with higher  $x$ . Moreover,  $S_R(1\text{ Hz})/R^2$  increases considerably after thermal annealing, which is another indication that Mn interstitials have to be involved in the relevant fluctuation processes. However, as thermal annealing reduces the density of Mn interstitials, a lower PSD for annealed samples would be expected, but the opposite is the case. This observation may be related to surface effects, since for two further  $x = 4\%$  films with a higher thickness of  $d = 100\text{ nm}$  and similar values for the utilized growth parameters as well as for  $T_C$ , a slight decrease of  $S_R(1\text{ Hz})/R^2$  is observed after thermal annealing [215]. This observation indicates that the rearrangement of Mn interstitials after thermal annealing related to diffusion processes towards the surface and the subsequent passivation due to oxidation or binding with surplus As atoms show varying effects on the noise properties depending on the film thickness.

Finally, a strong variation of the Hooge parameter  $\gamma_H$  also indicates that the observed  $1/f$ -type noise is dominated by defects. Calculated values of  $\gamma_H$  for the four metallic films are given in Tab. 4.4.1.

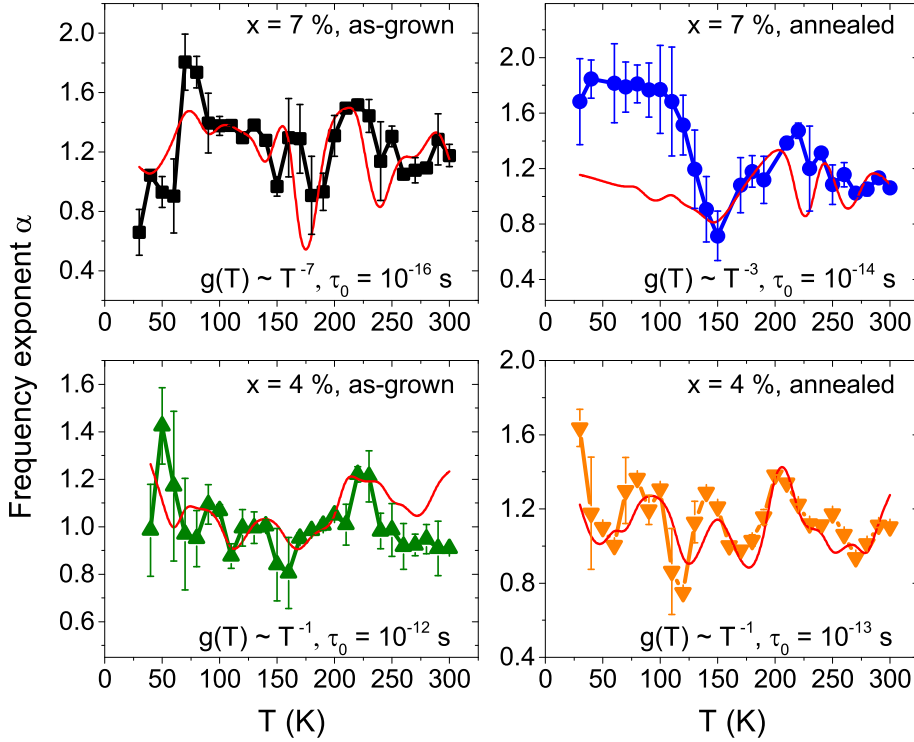


Figure 4.4.6: Application of the phenomenological DDH model (red curves) to the resistance noise data of four metallic  $\text{Ga}_{1-x}\text{Mn}_x\text{As}$  films. A reasonable agreement between calculated and experimentally determined frequency exponents  $\alpha(T)$  can be seen except for the  $x = 7\%$  film at low temperatures. The function  $g(T)$  and the attempt time  $\tau_0$  are indicated in each case.

In order to deduce the characteristic energies of the switching processes contributing to the  $1/f$ -type noise, we apply the phenomenological DDH model, cf. Sec. 2.4.4. An essential requirement for the applicability of this model is to check whether the frequency exponent  $\alpha(T)$  calculated after

$$\alpha(T) = 1 - \frac{1}{\ln(2\pi f \tau_0)} \left[ \frac{\partial \ln\left(\frac{S_R}{R^2}(f, T)\right)}{\partial \ln(T)} - \frac{\partial \ln(g(T))}{\partial \ln(T)} - 1 \right] \quad (4.14)$$

shows a reasonable agreement with the measured values [221]. Here,  $\tau_0$  represents an attempt time, usually between  $10^{-14}$  and  $10^{-11}$  s, which corresponds to typical inverse phonon frequencies. In addition,  $g(T) = a \cdot T^b$  may account for an explicit temperature dependence of the distribution of activation energies  $D(E, T)$ , which can be caused by a change of the number of thermally-activated switching events or of the coupling of fluctuations to the resistance with temperature.

Figure 4.4.6 shows a comparison of calculated values obtained from Eq. (4.14) with experimentally determined frequency exponents  $\alpha(T)$  for all four metallic films. A reasonable

agreement can be seen for all samples except for the annealed  $x = 7\%$  film at temperatures below 150 K. The function  $g(T)$  and the attempt time  $\tau_0$  are indicated in each case. The attempt time  $\tau_0$  is found to be in the typical range except for the as-grown  $x = 7\%$  film. In addition, the exponent  $b$  contained in the function  $g(T)$  is relatively high for this sample. This may be related to the hypothesis put up further above that an unusually high defect concentration is present in this film.

Moreover, for the deviation between model and experiment for the annealed  $x = 7\%$  film at low temperatures different explanations are conceivable. As some of the metallic thin films grown at the PTB in Braunschweig showed a frequency-dependent resistivity at low temperatures, the lock-in AC excitation frequency was reduced from 227 Hz down to 43 Hz or even 17 Hz in order to minimize this effect. Due to the metallic nature of the films, it was not possible to carry out DC noise measurements. The aforementioned frequency dependence of the resistance was previously also observed in the work by M. Zhu *et al.* [220]. However, the origin of the frequency dependence is unknown and may be either related to the electric contacts or to the material itself. Nevertheless, in spite of the reduced excitation frequency it is conceivable that the noise spectra recorded for the annealed  $x = 7\%$  film at low temperatures are erroneous due to the frequency-dependent resistance. Another explanation for the non-applicability of the DDH model below 150 K may be given by the fact that, as will be pointed out further below, Lorentzian contributions can be superimposed on the  $1/f$  spectrum for the  $x = 7\%$  films. Since the noise measurements are limited to a certain frequency window, the unusually high frequency exponent below 100 K may be related to the tails of Lorentzian contributions, whose corner frequencies are below the lowest measured frequency.

In general, the agreement between model and experiment allows for calculating the distribution of activation energies,

$$D(E) \propto \frac{2\pi f}{k_B T} \frac{1}{g(T)} \frac{S_R}{R^2}(f, T), \quad (4.15)$$

where  $E = -k_B T \ln(2\pi f \tau_0)$ .

Figure 4.4.7 displays the distribution of activation energies  $D(E)$  for the present metallic samples. All films show a similar behavior, namely an increase of  $D(E)$  towards higher activation energies and local maxima which can be attributed to specific defects in  $\text{Ga}_{1-x}\text{Mn}_x\text{As}$ . Due to the deviation between calculated and experimentally determined values at low temperatures,  $D(E)$  is only shown at higher activation energies for the annealed film with  $x = 7\%$ . In the case of the  $x = 4\%$  films, four local maxima can be found in  $D(E)$  at about 100 meV, 250 meV, 380 meV and 550 meV for both the as-grown and the annealed version and are indicated by arrows in Fig. 4.4.7. It is plausible to assume that, due to the low growth temperatures utilized during LT-MBE, which are required in order to prevent phase separation within the material, a great variety of defects, such as Mn interstitials and As antisites, exist and contribute to the  $1/f$ -type fluctuations. Although the energies of the local maxima are comparable to typical

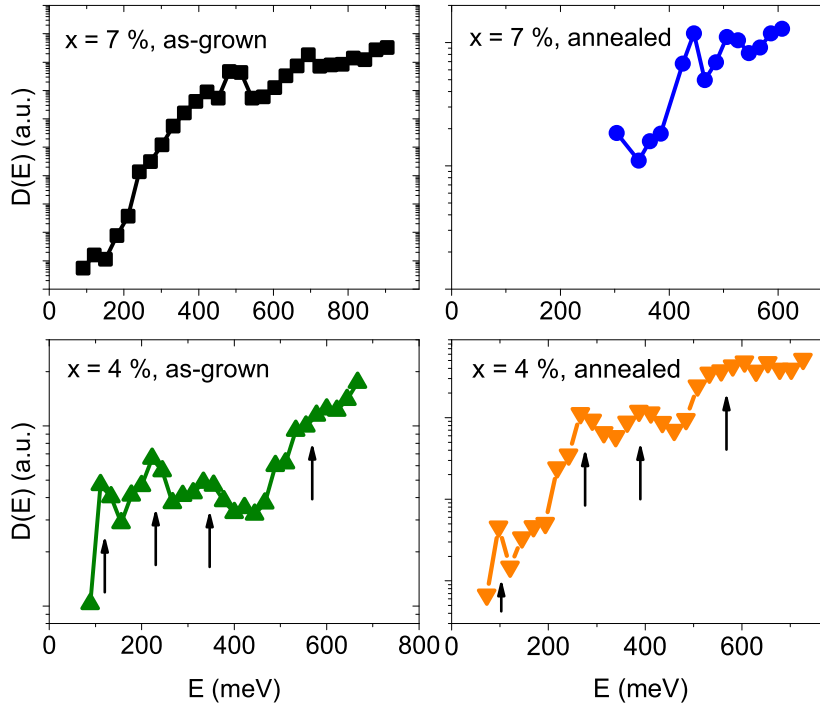


Figure 4.4.7: Calculated distribution of activation energies  $D(E)$ . An increasing behavior towards higher  $E$  and discrete features are observed for all films. Local maxima occurring at similar  $E$  are indicated by arrows for the  $x = 4\%$  layers.

impurity binding energies in GaAs, band gap renormalization in heavily doped semiconductors such as  $\text{Ga}_{1-x}\text{Mn}_x\text{As}$  leads to a shift of the respective binding energies and has to be considered. Therefore, care has to be taken, even though it is tempting to attribute the local maximum at 100 meV to fluctuation processes related to capture and emission processes at substitutional Mn atoms or, for instance, the maximum at 250 meV to As antisites, which are assumed to produce two deep donor levels separated by exactly this energy [222, 223]. Nevertheless, these results indicate that the phenomenological DDH model is suitable for the analysis of switching processes related to defects in (magnetic) semiconductors, although both a small spacing between data points on the temperature axis and a larger number of investigated samples would be necessary in order to carry out a quantitative analysis with a better statistics.

In general,  $1/f$ -type noise is constituted of a superposition of many two-level fluctuation processes with different time constants, each represented by a Lorentzian spectrum. However, in certain cases, a dominating Lorentzian spectrum with a characteristic corner frequency  $f_c$  is superimposed on the  $1/f$ -type signal and can be separated, cf. Fig. 3.2.3. Figure 4.4.8 (a) shows four exemplary spectra between 120 K and 150 K for the as-grown film with  $x = 7\%$ . Here,  $S_R/R^2 \times f$  is plotted against  $f$  and the spectra are shifted with respect to each other for clarity. For individual thermally-activated two-level processes, the corner frequency shifts

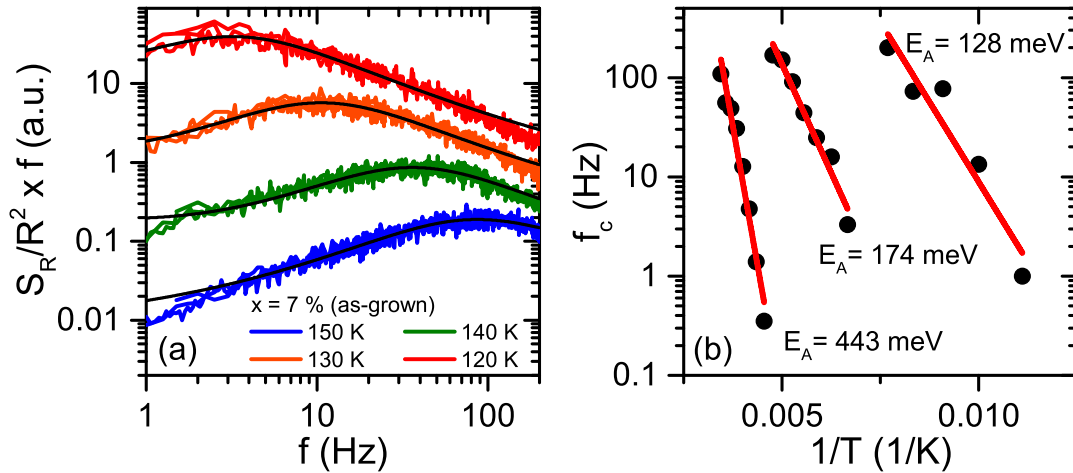


Figure 4.4.8: (a) Plot of  $S_R/R^2 \times f$  against  $f$  showing Lorentzian spectra for the  $x = 7\%$  film (as-grown) for four different temperatures. For better overview, spectra were shifted. (b) Arrhenius plot of the corner frequency  $f_c$  against  $1/T$ . Linear fits yield the activation energies  $E_A$  of the underlying two-level fluctuation processes.

as  $f_c = f_0 \exp(-E_A/k_B T)$ . Therefore, the activation energies  $E_A$  can be determined from an Arrhenius representation as shown in Fig. 4.4.8 (b). In this case, linear fits yield values for  $E_A$  of about 128 meV, 174 meV and 443 meV. For measurements in external magnetic fields between  $B = 0.1$  T and 3 T, similar activation energies around 100 meV and between 400 meV and 600 meV are obtained [129, 215]. The annealed  $x = 7\%$  film yields comparable results, whereas both  $x = 4\%$  samples do not exhibit any Lorentzian spectra. The observation of Lorentzian spectra in the  $x = 7\%$  films can be ascribed to a greater density of electrically active Mn interstitials due to the higher Mn flux rate utilized during the growth procedure, or to the enhanced presence of other crystalline defects, leading to an increased rate of capture and emission processes of charge carriers. Alternatively, spin-dependent scattering from fluctuating nanoscale magnetic clusters is conceivable [220]. However, we detect two-level fluctuations in a much broader range  $50 \text{ K} \leq T \leq 300 \text{ K}$  with higher activation energies than in Ref. [220] and do not observe any magnetic field dependence, which speaks for capture and emission processes of charge carriers causing the random telegraph signal. It should be emphasized that the activation energies of the observed dominating two-level fluctuation processes in  $x = 7\%$  samples strongly resemble the characteristic activation energies in  $D(E)$  for the  $x = 4\%$  films. This is an indication for the common origin of fluctuation processes in all present samples, whereby the occurrence of selected mechanisms is enhanced in the  $x = 7\%$  layers.

Since no signatures of a percolative transition can be identified for conventional metallic  $\text{Ga}_{1-x}\text{Mn}_x\text{As}$  films with high Mn content, we now focus on samples irradiated by He ions, whereby disorder in the film is enhanced by the introduction of deep traps, i.e., the Fermi level is shifted by means of charge carrier compensation in order to change the conductivity

Table 4.4.2: Overview of the three  $\text{Ga}_{1-x}\text{Mn}_x\text{As}$  layers grown at the University of Nottingham, two of which were irradiated by He ions at HZDR Dresden. The following information is given: the Mn content  $x$ , the utilized He-ion fluence, the displacement per atom (DPA), the Curie temperature  $T_C$ , the hole concentration  $p$  at 300 K determined from Hall effect measurements and the calculated Hooge constant  $\gamma_H$  at room temperature. All samples were thermally annealed at 190°C for 48 h after LT-MBE growth.

Mn content $x$	Fluence	DPA	$T_C$	$p(300\text{ K})[1/\text{cm}^3]$	$\gamma_H(300\text{ K})$
$6.0 \pm 0.3\%$	unirradiated	unirradiated	125 K	$9.6 \times 10^{20}$	$8.0 \times 10^3$
$6.0 \pm 0.3\%$	$2.5 \times 10^{13}\text{ cm}^{-2}$	$1.60 \times 10^{-3}$	75 K	$8.0 \times 10^{20}$	$6.3 \times 10^4$
$6.0 \pm 0.3\%$	$3.5 \times 10^{13}\text{ cm}^{-2}$	$2.24 \times 10^{-3}$	50 K	$5.6 \times 10^{20}$	$9.2 \times 10^4$

from metallic to insulating.

#### 4.4.2 He-ion irradiated $\text{Ga}_{1-x}\text{Mn}_x\text{As}$ films

An overview of all three epitaxially grown  $\text{Ga}_{1-x}\text{Mn}_x\text{As}$  samples with a Mn content of 6 % is provided in Tab. 4.4.2. For the sake of simplicity, hereinafter we will refer to the fluence of  $2.5 \times 10^{13}\text{ cm}^{-2}$  as "low dose" and the fluence of  $3.5 \times 10^{13}\text{ cm}^{-2}$  as "high dose" when considering the irradiated samples. The temperature-dependent resistivity data of all three samples is shown in Fig. 4.4.9. The corresponding Curie temperatures determined from magnetization measurements are marked by arrows. Strikingly, the resistivity is changing over many orders of magnitude as a function of He-ion irradiation. First, it is noted that the unirradiated sample exhibits the lowest resistivity in the entire temperature range, whereby the Curie temperature  $T_C = 125\text{ K}$  is relatively high and comparable with the annealed  $x = 7\%$  sample grown at the PTB in Braunschweig. For the sample irradiated with a low He-ion dose, the magnitude of the resistivity increases, while  $T_C$  is suppressed down to 75 K. Finally, the sample irradiated with the high He-ion dose exhibits an even higher resistivity in the entire temperature interval and only shows a weakly pronounced local maximum in the vicinity of  $T_C = 50\text{ K}$ . Therefore, the nature of the films becomes more insulating as a function of He-ion irradiation. These major changes can be explained by an increase of the displacement per atom (DPA) for higher irradiation doses, which results in a decrease of the hole concentration. This is confirmed by Hall effect measurements at room temperature. The calculated hole densities are shown in Tab. 4.4.2 for all three films.

The normalized temperature-dependent resistance noise power spectral density evaluated at 1 Hz is shown in Fig. 4.4.10. The unirradiated sample exhibits the lowest noise level over the entire temperature range. For  $T < 100\text{ K}$ ,  $S_R(1\text{ Hz})/R^2$  is nearly temperature-independent, followed by a slight increase between 100 K and 300 K. Likewise, below 80 K, the film irradiated with a low He-ion dose shows the identical constant noise magnitude, while displaying a much stronger increase of nearly two orders of magnitude towards room temperature. The

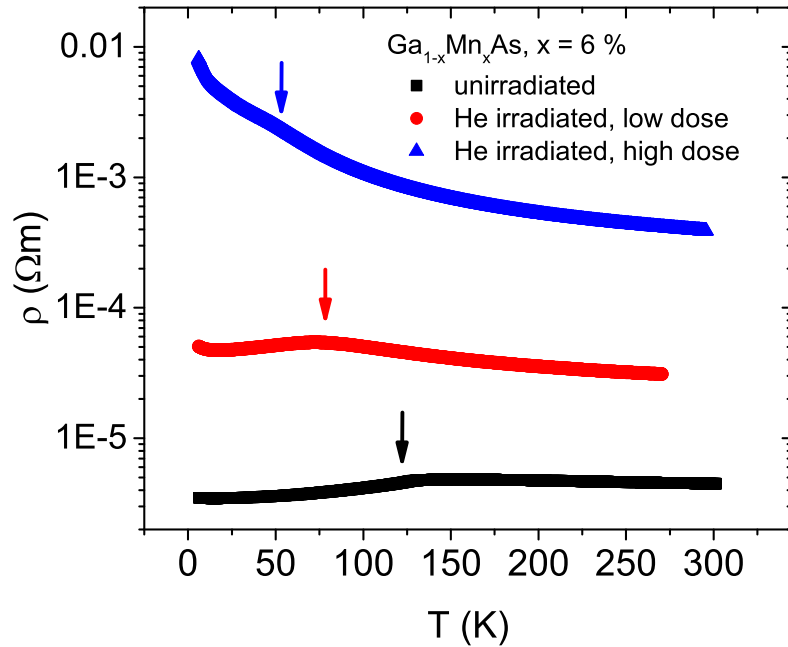


Figure 4.4.9: Temperature-dependent resistivity data of three  $\text{Ga}_{1-x}\text{Mn}_x\text{As}$  layers with a Mn content of  $x = 6\%$  and different He-ion irradiation doses. The introduction of deep traps leads to a reduction of the effective hole density and thus  $\rho$  increases as a function of irradiation dose, while  $T_C$  is reduced.

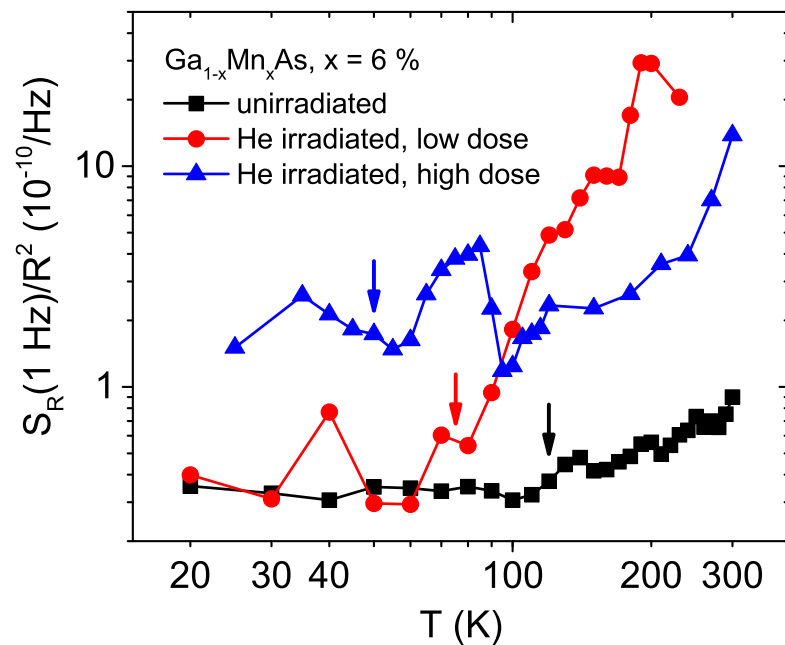


Figure 4.4.10: Normalized noise PSD as a function of temperature for three  $\text{Ga}_{1-x}\text{Mn}_x\text{As}$  films in a logarithmic representation. Arrows indicate the corresponding Curie temperatures. Clear changes in the normalized noise can be observed as a function of He-ion irradiation.

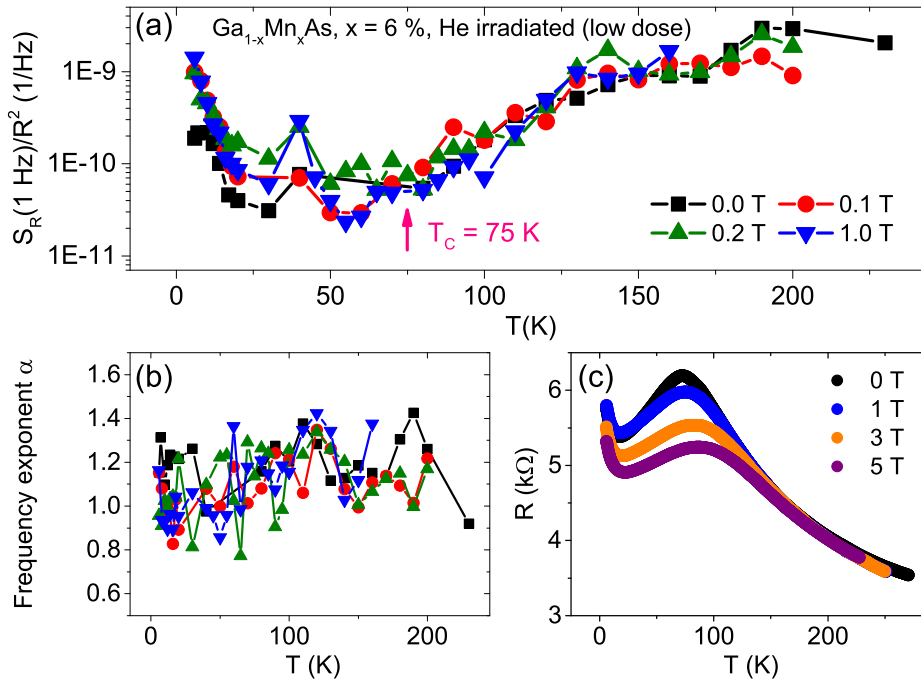


Figure 4.4.11: (a) Semi-logarithmic plot of  $S_R/R^2$  evaluated at 1 Hz against temperature for the film ( $x = 6\%$ ) irradiated with a low He-ion dose for different magnetic fields. (b) Frequency exponent  $\alpha$  versus  $T$  as determined from noise spectra. (c) Resistance  $R(T)$  for various magnetic fields including very low temperatures down to 6 K.

film irradiated with the high dose exhibits the highest noise level of all three samples below 100 K and also displays a characteristic increase for  $T$  approaching room temperature. The large variation in  $S_R(1 \text{ Hz})/R^2$  for the present samples may be explained by the introduction of deep traps into the As sublattice. An exchange of charge carriers between such traps and the rest of the conducting material, resulting in fluctuations of the hole density, can cause the observed  $1/f$ -type noise. As shown in previous studies [146], the irradiation of He ions should not alter the concentration of Mn interstitials. Therefore, the interstitial atoms are not the origin for the variation in the PSD as a function of the irradiation dose, although they might still contribute to the  $1/f$  noise. In addition, the results suggest a crossover between two temperature regimes: A temperature-independent regime below about 100 K and a characteristic increase of the noise magnitude, where the number of activated defects increases towards higher temperatures. The Hooge parameter, given in Tab. 4.4.2 for all three films, is of order  $\gamma_H = 10^3\text{--}10^5$  and thus is comparable to the values obtained for the annealed  $x = 7\%$  film, which can be assumed to be similar to the unirradiated  $x = 6\%$  layer. Furthermore, the values for  $\gamma_H$  are several orders of magnitude larger than for typical "clean" semiconductors, implying a considerable contribution of various crystalline defects to the observed  $1/f$  noise.



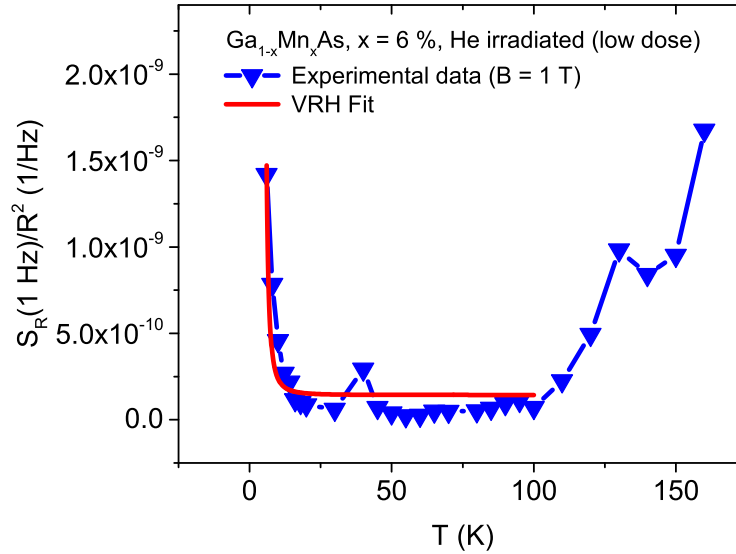


Figure 4.4.12:  $S_R(1 \text{ Hz})/R^2$  as a function of  $T$  for the film ( $x = 6 \%$ ) irradiated with a low He-ion dose and measured in an out-of-plane magnetic field of  $B = 1 \text{ T}$ . The red curve represents a fit to the experimental data after Eq. (4.16), implying an increasing localization of charge carriers.

Now we place the focus on the film irradiated with a low dose and consider the noise behavior in magnetic fields and at very low temperatures. Figure 4.4.11 (a) shows the normalized PSD as a function of temperature for various magnetic fields up to 1 T, while the frequency exponent  $\alpha$  is shown in Fig. 4.4.11 (b). No obvious magnetic field dependence can be observed. For all externally applied out-of-plane fields, apart from the aforementioned decrease of the PSD between 200 and 50 K, a drastic increase can be observed below 20 K. Similarly, the resistance  $R(T)$ , which is shown in Fig. 4.4.11 (c), increases steeply towards very low temperatures and can be fitted by either the Mott variable range hopping (VRH) model, where  $\ln(R) \propto T^{-1/4}$  [224], or assuming a Kondo screening of magnetic moments by localized charge carriers, leading to  $R \propto \ln(T)$  [225]. Both models parametrize the resistance behavior below 10 K equally well (not shown). This kind of analysis has also been carried out successfully in Ref. [215] for a  $x = 4 \%$   $\text{Ga}_{1-x}\text{Mn}_x\text{As}$  sample with a thickness of  $d = 100 \text{ nm}$  from the PTB in Braunschweig. In the case of Mott VRH, theoretical calculations by B. Shklovskii predict a steep increase of the PSD in the hopping regime for doped semiconductors [226]. In detail, the temperature dependence of the PSD in the case of nearest-neighbor hopping (NNH), VRH and the crossover regime between these two different hopping mechanisms can be written as

$$S_R(1 \text{ Hz})/R^2 \propto \exp\left(-B \ln^3(\nu_0/2\pi)\right) \exp\left((T_0/T)^3\right), \quad (4.16)$$

where  $B$  denotes a numerical factor,  $\nu_0$  the charge carrier hopping rate and  $T_0$  the transition temperature. In Fig. 4.4.12, an exemplary fit (red curve) to the experimental data acquired

at an external out-of-plane magnetic field of  $B = 1$  T is depicted. The observed agreement suggests that the increase in  $S_R(1\text{ Hz})/R^2$  towards very low temperatures originates from the increasing localization of charge carriers. Interestingly, as can be seen in Fig. 4.4.11 (a), this increase in  $S_R/R^2$  is more pronounced in the presence of an external magnetic field, since the curve for  $B = 0$  T shows a significantly weaker increase. This resembles the observations by M. Zhu *et al.*, where an increase of the noise magnitude is observed at comparable temperatures and magnetic fields, which can be explained by spin-dependent scattering from nanoscale magnetic clusters that fluctuate between different possible orientations [220]. However, more detailed measurements would be required in order to confirm this hypothesis for the present sample.

Finally, it should be noted that in analogy to the  $x = 7\%$  samples from the PTB in Braunschweig, Lorentzian spectra were observed for the  $x = 6\%$  samples, which, however, occurred markedly less frequently. Consequently, it was not possible to determine the activation energies of the underlying two-level fluctuation processes.

Similar to the films with  $x = 4\%$  and  $x = 7\%$  grown at the PTB, no indications for an electronic phase separation can be observed in the electronic noise for the unirradiated  $x = 6\%$  sample. The same holds for the sample irradiated with a low He-ion dose. However, for the  $\text{Ga}_{1-x}\text{Mn}_x\text{As}$  film irradiated with the high dose, besides a pronounced maximum in  $S_R/R^2$  above  $T_C$ , which, as it follows from an analysis by means of the DDH model, can be explained by impurity switching processes, a weak increase occurs just below the ferromagnetic transition temperature. It is not immediately clear whether this already is a signature of a (weak) percolative transition or if it can be related to the increasing localization of charge carriers in this rather insulating sample. In this case, an analysis by means of the DDH model might shed light on this open question.

Fig. 4.4.13 shows the application of the DDH model on all three samples. In detail, Fig. 4.4.13 (a), (b) and (c) contains the comparison between calculated and experimentally determined values of the frequency exponent  $\alpha$ . A barely acceptable agreement is obtained for the unirradiated sample, while the irradiated samples exhibit a considerably better agreement between theory and experiment. This allows for a calculation of the distribution of activation energies  $D(E)$ , which is depicted in Fig. 4.4.13 (d), (e) and (f). As for the metallic films from the PTB, we observe a monotonic increase of  $D(E)$  for each sample, which we interpret as a superposition of several thermally-activated processes with different energies, that can be attributed to various kinds of defects. The film with a high irradiation dose shows a distinct maximum at  $E \approx 180$  meV, which presumably is caused by the high density of intentionally introduced defects due to the heavy irradiation with ions, causing trapping and detrapping processes of charge carriers with this particular activation energy. An alternative explanation for the strong changes in the electronic noise as a function of irradiation and the maximum at 180 meV in  $D(E)$  could be the spin-dependent scattering from weakly interacting nanoscale magnetic clusters with fluctuating spin orientation, which form after the irradiation

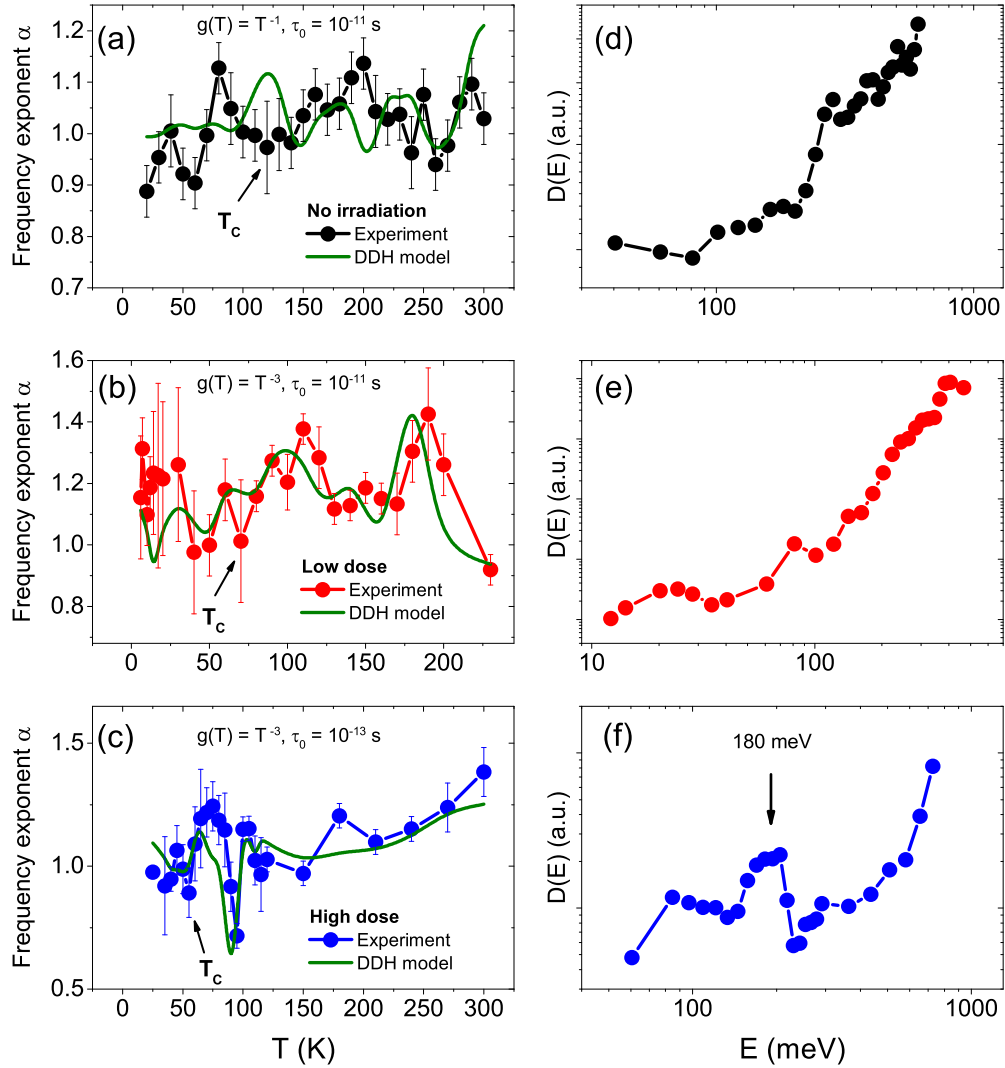


Figure 4.4.13: [(a)-(c)] Comparison between the experimentally determined  $\alpha(T)$  with DDH-model predictions for films with different irradiation doses. The attempt time  $\tau_0$  and the function  $g(T)$  are indicated in each case. [(d)-(f)] Calculated distribution of activation energies  $D(E)$ . A pronounced maximum occurs at  $E = 180$  meV for the sample irradiated with the highest irradiation dose.

procedure due to the increased degree of disorder [145]. However, as mentioned above, we do not observe a systematic magnetic field dependence of the resistance noise. Therefore, capture and emission processes of introduced defects are the most plausible explanation. Finally, the analysis by means of the DDH model suggests that an electronic phase separation in the sample with the highest disorder level is rather improbable, since the agreement between experimentally determined and calculated frequency exponents  $\alpha$  is very good in the entire temperature range. Nevertheless, a percolative transition cannot be entirely ruled out.

To summarize, it was shown that intentionally introduced defects by ion irradiation lead to substantial changes in the resistance noise behavior. On the other hand, it was not possible to unambiguously clarify whether the disorder in the system and hence an increased degree of localization of charge carriers lead to a percolation of bound magnetic polarons, although our results suggest that this is rather not the case. A different approach is to investigate compounds with low Mn contents and will be presented in the following.

### 4.4.3 Samples with localized charge carriers

In order to detect possible signatures of a percolation of bound magnetic polarons in the vicinity of  $T_C$ , two  $\text{Ga}_{1-x}\text{Mn}_x\text{As}$  films with low Mn contents of  $x = 1.8\%$  and  $1.2\%$  were investigated by means of fluctuation spectroscopy. As discussed in Sec. 4.2.1 and 4.2.3, the metal-insulator transition (MIT) is expected to occur for Mn contents between  $1\%$  and  $2\%$ . By performing a careful analysis of electronic transport and magnetic measurements, Y. Yuan *et al.* have shown that the present  $x = 1.2\%$   $\text{Ga}_{1-x}\text{Mn}_x\text{As}$  sample is located right at the edge of the MIT [154]. In detail, electronic transport measurements indicate its insulating character, whereas the sample still exhibits a global ferromagnetic order below  $T_C$ . Therefore, the  $x = 1.8\%$  layer is located on the metallic side, but yet in the vicinity of the MIT. Within the scope of this work, it was not possible to investigate  $\text{Ga}_{1-x}\text{Mn}_x\text{As}$  films with  $x < 1\%$ , since the necessary current for a reliable analysis of  $1/f$ -type noise spectra exceeded the linear regime of the current-voltage characteristic in the relevant temperature range around  $T_C$ . Instead, two  $\text{Ga}_{1-x}\text{Mn}_x\text{P}$  reference samples with  $x = 3.5\%$  and  $7.5\%$  were chosen to be investigated. As discussed in Sec. 4.2.4, the holes in this related compound are of a more localized nature and a percolation of bound magnetic polarons is more likely to be expected. All four samples are listed in Tab. 4.4.3, including the Curie temperature  $T_C$  obtained from magnetization measurements, the hole density  $p$  at room temperature as determined from Hall effect measurements and the Hooge parameter  $\gamma_H$  at 300 K, which was calculated from  $p$  and the respective PSD evaluated at 1 Hz. For the  $x = 7.5\%$  film, no Hall effect data at room temperature could be acquired and thus  $\gamma_H$  cannot be determined.

Measurements of the resistivity  $\rho(T)$  are presented in Fig. 4.4.14 for all four films. Apparently,

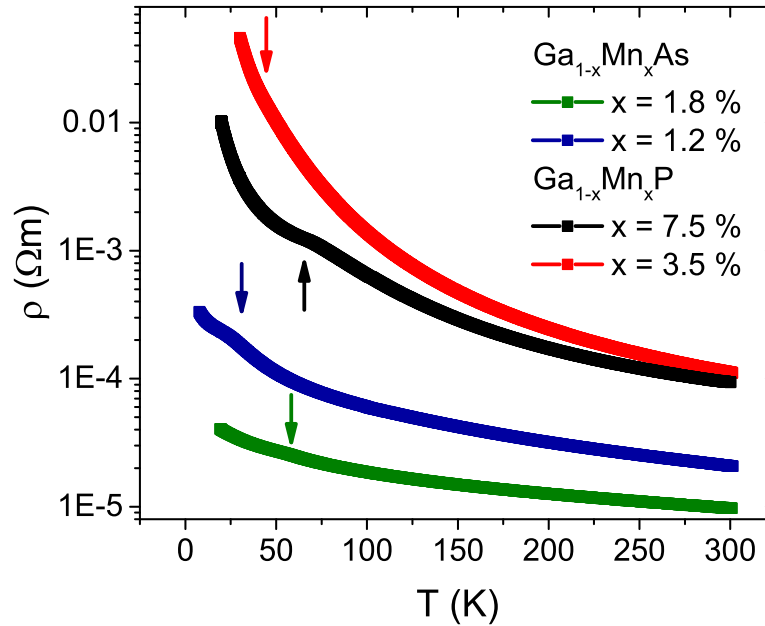


Figure 4.4.14: Resistivity  $\rho(T)$  of four insulating  $\text{Ga}_{1-x}\text{Mn}_x\text{As}$  and  $\text{Ga}_{1-x}\text{Mn}_x\text{P}$  films fabricated by ion implantation combined with pulsed laser melting. Ferromagnetic transition temperatures are indicated by arrows.

all samples show a strongly insulating behavior as compared to the samples with higher Mn contents discussed above. More precisely, only a weak kink can be observed in the vicinity of the respective ferromagnetic transition temperature for the two  $\text{Ga}_{1-x}\text{Mn}_x\text{As}$  samples and the  $x = 7.5\%$   $\text{Ga}_{1-x}\text{Mn}_x\text{P}$  film. In contrast to that, no significant feature around  $T_C$  occurs for the  $\text{Ga}_{1-x}\text{Mn}_x\text{P}$  film with  $x = 3.5\%$ . For both compounds, the magnitude of resistivity increases consistently for lower Mn doping. As can be seen in Tab. 4.4.3, this is accompanied by a decrease of the hole density.

Fig. 4.4.15 shows an Arrhenius plot of the measured resistivity (red data points) of the  $\text{Ga}_{1-x}\text{Mn}_x\text{P}$  film with  $x = 3.5\%$ . The black curve is a fit to a simple phenomenological model [208, 227, 147] assuming that the resistivity behaves as

$$\rho(T) = [\sigma_{\text{free}} \cdot \exp(-\epsilon_1/k_B T) + \sigma_{\text{hop}} \cdot \exp(-\epsilon_3/k_B T)]^{-1}, \quad (4.17)$$

where the first term describes thermally-activated hole transport via the valence band and the second term is attributed to hopping conduction. The activation energies are found to be  $\epsilon_1 = 35.3$  meV and  $\epsilon_3 = 9.3$  meV which is in excellent agreement with previous results on ion-implanted  $\text{Ga}_{1-x}\text{Mn}_x\text{P}$  films by T. Winkler *et al.* [147] and M. Scarpulla *et al.* [208]. In detail, thermally-activated resistivity in the high-temperature range of p-type semiconductors is typically associated with hole transitions between the valence-band and bound-acceptor states. From their electronic transport results being supported by far-infrared photoconduc-

Table 4.4.3: Overview of the  $\text{Ga}_{1-x}\text{Mn}_x\text{As}$  and  $\text{Ga}_{1-x}\text{Mn}_x\text{P}$  layers fabricated by ion implantation combined with pulsed laser melting. The following information is given: the Mn content  $x$ , the Curie temperature  $T_C$ , the hole concentration  $p$  at 300 K determined from Hall effect measurements and the calculated Hooge constant  $\gamma_H$  at room temperature.

Mn content $x$	$T_C$	$p(300\text{ K})[1/\text{cm}^3]$	$\gamma_H(300\text{ K})$
$\text{Ga}_{1-x}\text{Mn}_x\text{As}$			
$1.2 \pm 0.1\%$	31 K	$1.0 \times 10^{20}$	$2 \times 10^0$
$1.8 \pm 0.2\%$	60 K	$2.8 \times 10^{20}$	$5 \times 10^1$
$\text{Ga}_{1-x}\text{Mn}_x\text{P}$			
$3.5 \pm 0.4\%$	45 K	$3.1 \times 10^{20}$	$1 \times 10^4$
$7.5 \pm 0.8\%$	65 K	n/a	n/a

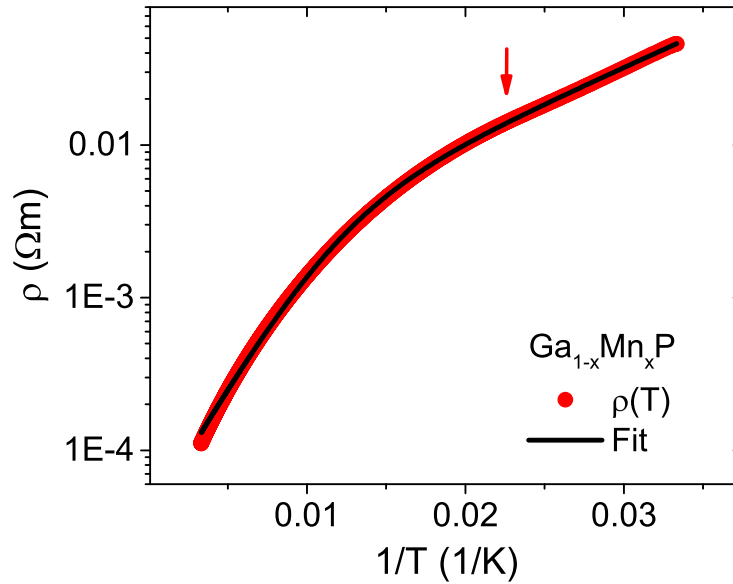


Figure 4.4.15: Resistivity  $\rho(T)$  of the  $\text{Ga}_{1-x}\text{Mn}_x\text{P}$  film with  $x = 3.5\%$  in an Arrhenius representation (red data points). Black line indicates the application of a phenomenological model including both a thermally-activated hole transport via the valence band and hopping conduction at low temperatures. See text for details.

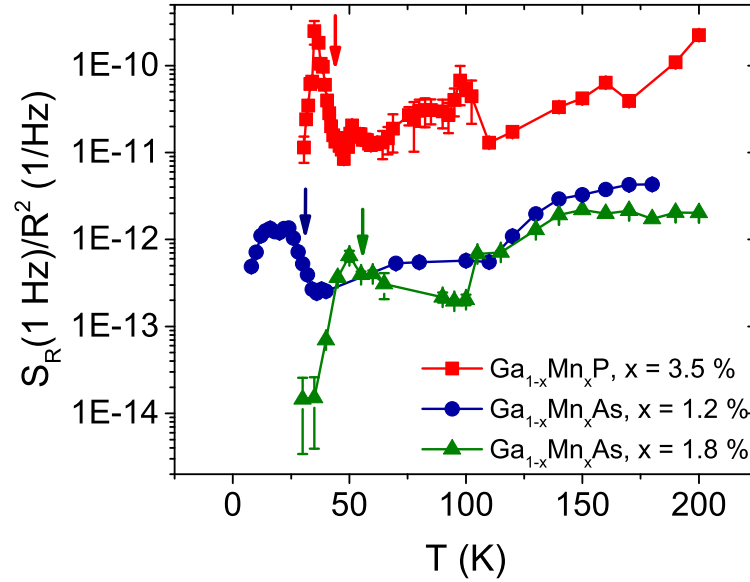


Figure 4.4.16: Temperature-dependent resistance noise power spectral density in a semi-logarithmic representation for the two insulating  $\text{Ga}_{1-x}\text{Mn}_x\text{As}$  samples and the  $\text{Ga}_{1-x}\text{Mn}_x\text{P}$  film with  $x = 3.5\%$ . In contrast to the metallic samples investigated in this work, significant features can be observed around  $T_C$ . Curie temperatures are marked by arrows.

tive spectroscopy measurements, M. Scarpulla *et al.* assign the activation energy of about 30 meV to excitations across a gap between a Mn-derived impurity band and the valence band. Moreover, the fact that the change in slope occurs near  $T_C$  is consistent with the formation of a continuous hopping transport path at a percolative transition of magnetic polarons [208].

The temperature-dependent resistance noise magnitude for the two  $\text{Ga}_{1-x}\text{Mn}_x\text{As}$  films and the  $\text{Ga}_{1-x}\text{Mn}_x\text{P}$  sample with  $x = 3.5\%$  is depicted in Fig. 4.4.16. The noise behavior of the  $\text{Ga}_{1-x}\text{Mn}_x\text{P}$  layer with  $x = 7.5\%$  will be discussed separately further below. As can be seen in Fig. 4.4.16, the noise magnitude for the two insulating  $\text{Ga}_{1-x}\text{Mn}_x\text{As}$  samples is nearly identical above 50 K. This becomes immediately clear since the same fabrication technique has been employed, the Mn content is similar and hence the defect landscape contributing to the  $1/f$ -type noise is comparable. As shown in Tab. 4.4.3, the calculated Hooge parameter at room temperature is also comparable for these two samples. Strikingly, for both  $\text{Ga}_{1-x}\text{Mn}_x\text{As}$  samples the noise magnitude is significantly enhanced in the vicinity of the respective ferromagnetic transition temperature. More precisely, for the  $\text{Ga}_{1-x}\text{Mn}_x\text{As}$  layer with  $x = 1.8\%$  only a weak increase can be observed, followed by a sharp decrease towards lower temperatures. Although, according to the work by Y. Yuan *et al.* [154], this compound is still to be considered as metallic, in the phase diagram it is located very close to the metal-insulator transition and thus weak signatures of electronic phase separation are

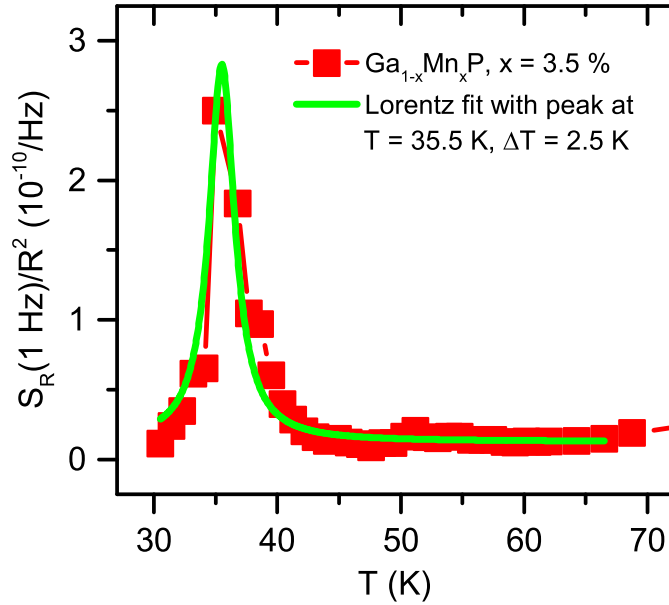


Figure 4.4.17: PSD as a function of temperature  $T$  for the  $\text{Ga}_{1-x}\text{Mn}_x\text{P}$  sample with  $x = 3.5\%$ . The green line represents a Lorentz fit parametrizing a diverging behavior with a peak at  $T = 35.5\text{ K}$  and a width  $\Delta T = 2.5\text{ K}$ .

conceivable. In contrast to that, as discussed in the introduction of the present section, the film with  $x = 1.2\%$  is located right at the edge of the MIT. This is consistent with the fact that for this sample the peak in  $S_R/R^2$  evaluated at 1 Hz is much more pronounced than for the one with  $x = 1.8\%$ . In contrast to samples with even lower Mn doping located far on the insulating side of the MIT, the  $x = 1.2\%$  film still exhibits a global ferromagnetic behavior below  $T_C$ . A percolation of bound magnetic polarons as suggested by A. Kaminski and S. Das Sarma [3, 4] is a conceivable scenario in order to explain the pronounced maximum in the PSD. This hypothesis is supported by noise measurements on the  $\text{Ga}_{1-x}\text{Mn}_x\text{P}$  sample with  $x = 3.5\%$ , where an even more pronounced enhancement of more than one order of magnitude in  $S_R/R^2$  appears in a small temperature interval around the ferromagnetic transition temperature. Apart from that, this sample shows a higher noise magnitude in the entire temperature range as compared to the  $\text{Ga}_{1-x}\text{Mn}_x\text{As}$  films, and also a considerably higher Hooge parameter  $\gamma_H$ , cf. Tab. 4.4.3.

In analogy to previous studies on the ferromagnetic semimetal  $\text{EuB}_6$  [5, 73], the diverging behavior of the resistance noise PSD for the present  $\text{Ga}_{1-x}\text{Mn}_x\text{P}$  film can be described by a Lorentz function with a peak at  $T = 35.5\text{ K}$  and a width  $\Delta T = 2.5\text{ K}$ , cf. Fig. 4.4.17. Therefore, the noise behavior is very similar to the case of  $\text{EuB}_6$ , where this sharp peak in  $S_R/R^2$  was attributed to a magnetic polaron percolation.

Due to the high defect concentration in  $\text{Ga}_{1-x}\text{Mn}_x\text{As}$  and  $\text{Ga}_{1-x}\text{Mn}_x\text{P}$ , it is assumed that the carrier concentration is highly inhomogeneous and as ferromagnetism is mediated by holes,



the ferromagnetic transition will first occur locally within the regions with higher carrier densities upon cooling through  $T_C$ . Towards lower temperatures, these finite-size clusters will grow and merge until the entire sample becomes ferromagnetic via a percolation transition [183]. However, in contrast to  $\text{EuB}_6$ , where the ferromagnetic transition is accompanied by a drastic reduction of the resistivity  $\rho(T)$  and a colossal magnetoresistance effect, the temperature dependence of  $\rho(T)$  is monotonic in the case of  $\text{Ga}_{1-x}\text{Mn}_x\text{As}$  and  $\text{Ga}_{1-x}\text{Mn}_x\text{P}$ . For samples located in the vicinity of the MIT, only a small kink or even no feature is observable in  $\rho(T)$  around the ferromagnetic transition temperature. In general, a ferromagnetic percolation is accompanied by an increase of the electrical conductivity, but, at the same time, this may be compensated by the increase of the resistivity with decreasing temperature due to the semiconducting nature of the material [4]. In the case of localized charge carriers, the decrease in the hopping rate upon cooling may overcome the decrease in the hopping activation energy due to the ferromagnetic transition. To summarize, although no features can be observed in  $\rho(T)$  around  $T_C$  for insulating  $\text{Ga}_{1-x}\text{Mn}_x\text{As}$  and  $\text{Ga}_{1-x}\text{Mn}_x\text{P}$  films, resistance noise, which is highly sensitive to the microscopic current distribution in the sample, exhibits a strong peak. This maximum in  $S_R/R^2$  is more pronounced in the case of the  $\text{Ga}_{1-x}\text{Mn}_x\text{P}$  sample with  $x = 3.5\%$ , which is presumably due to the more localized nature of charge carriers in this system.

A subsequent analysis by means of the phenomenological DDH model provides further evidence for a percolative transition in these DMSs. Figures 4.4.18 (a) and (b) show a comparison between experimentally determined and calculated frequency exponents  $\alpha$  for the  $\text{Ga}_{1-x}\text{Mn}_x\text{As}$  film with  $x = 1.2\%$  and the  $\text{Ga}_{1-x}\text{Mn}_x\text{P}$  sample with  $x = 3.5\%$ . Apparently, there is a good agreement in the entire temperature range for both samples except for the gray shaded areas, where strong deviations can be observed. These areas lie exactly in the temperature range of the ferromagnetic transition in both cases. In these temperature intervals, the DDH model is not applicable, possibly, because the assumptions of this phenomenological approach are not compatible with the nonlinear electronic transport behavior around the percolation threshold.

The deviations between experimentally determined and calculated frequency exponents and the strongly enhanced  $1/f$ -noise magnitude in the vicinity of the percolation threshold  $p_c$  can be understood within the frame of a random resistor network (RRN) model, cf. Sec. 2.6 and Ref. [11]. In detail, the reduced number of effective current paths results in the suppression of cancellation of uncorrelated resistance fluctuations along different paths, which are abundant far away from  $p_c$ . Around  $p_c$ , the current density is strongly inhomogeneous and the most significant contribution to the resistance noise comes from so-called bottlenecks which connect large parts of the infinite cluster. Here, the current density is higher than in other parts of the network. R. Rammal *et al.* have shown that in the vicinity of the percolation threshold  $p_c$ , the PSD diverges as  $S_R/R^2 \propto (p - p_c)^{-\kappa}$ , while the resistance  $R$  behaves as  $R \propto (p - p_c)^{-t}$  [75]. Here,  $\kappa$  and  $t$  denote critical percolation exponents derived from an

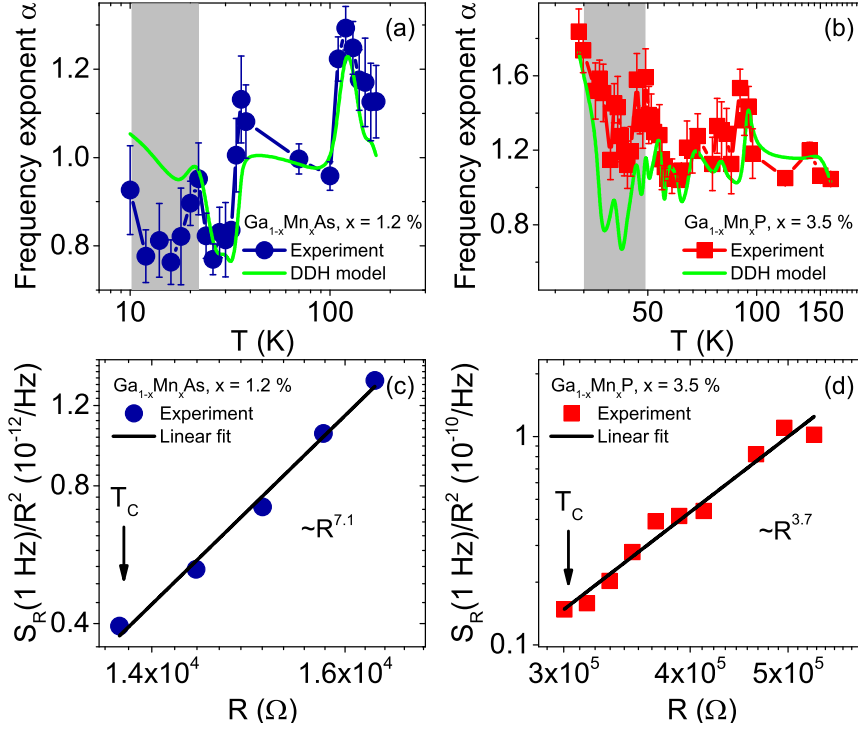


Figure 4.4.18: [(a) and (b)] Comparison between experimentally determined and calculated (DDH model, green lines)  $\alpha$  for the  $\text{Ga}_{1-x}\text{Mn}_x\text{As}$  film with  $x = 1.2\%$  and the  $\text{Ga}_{1-x}\text{Mn}_x\text{P}$  film with  $x = 3.5\%$ . [(c) and (d)] Log-log plot of the PSD against the resistance  $R$  between 24 and 32 K for  $\text{Ga}_{1-x}\text{Mn}_x\text{As}$  and between 35 and 45 K for  $\text{Ga}_{1-x}\text{Mn}_x\text{P}$ . Linear fits yield  $S_R/R^2 \propto R^w$  with  $w = 7.1 \pm 0.3$  for the weakly doped  $\text{Ga}_{1-x}\text{Mn}_x\text{As}$  film and  $w = 3.7 \pm 0.3$  in the case of the  $\text{Ga}_{1-x}\text{Mn}_x\text{P}$  sample.

RRN model, and  $p$  is the fraction of unbroken bonds of an RRN. Since the microscopic details determining  $p$  are generally not accessible in an experiment, it is common to link the PSD and the resistance via  $S_R/R^2 \propto R^w$ , where  $w = \kappa/t$  [228]. The corresponding analysis for the two considered thin film samples is shown in Fig. 4.4.18 (c) and (d). In the case of the  $\text{Ga}_{1-x}\text{Mn}_x\text{P}$  ( $x = 3.5\%$ ) sample we obtain  $w = 3.7 \pm 0.3$ , whereas for the  $\text{Ga}_{1-x}\text{Mn}_x\text{As}$  sample ( $x = 1.2\%$ )  $w = 7.1 \pm 0.3$ . While for the  $\text{Ga}_{1-x}\text{Mn}_x\text{P}$  film this is in fair agreement with typical values for the exponent  $w$ , e.g.,  $w = 2.9 \pm 0.5$  in the case of perovskite manganites [6], the value for the  $\text{Ga}_{1-x}\text{Mn}_x\text{As}$  sample is exceptionally high. As for the manganites, this ratio of critical exponents  $w = \kappa/t$  significantly exceeds  $w = 0.5\text{--}0.8$  for discrete random models and, at least for the  $\text{Ga}_{1-x}\text{Mn}_x\text{P}$  film, instead coincides with theoretical calculations of  $w$  for the continuum percolation model of conducting regions, randomly placed in an insulating matrix (inverted random-void model), cf. Sec. 2.6 and Ref. [83].

No clear systematic changes of shape, position and height of the sharp peak in the temperature-dependent noise magnitude as a function of the applied out-of-plane magnetic field  $B$  can be observed, cf. Fig. 4.4.19. Noise data are shown for the  $\text{Ga}_{1-x}\text{Mn}_x\text{P}$  ( $x = 3.5\%$ ) film for several

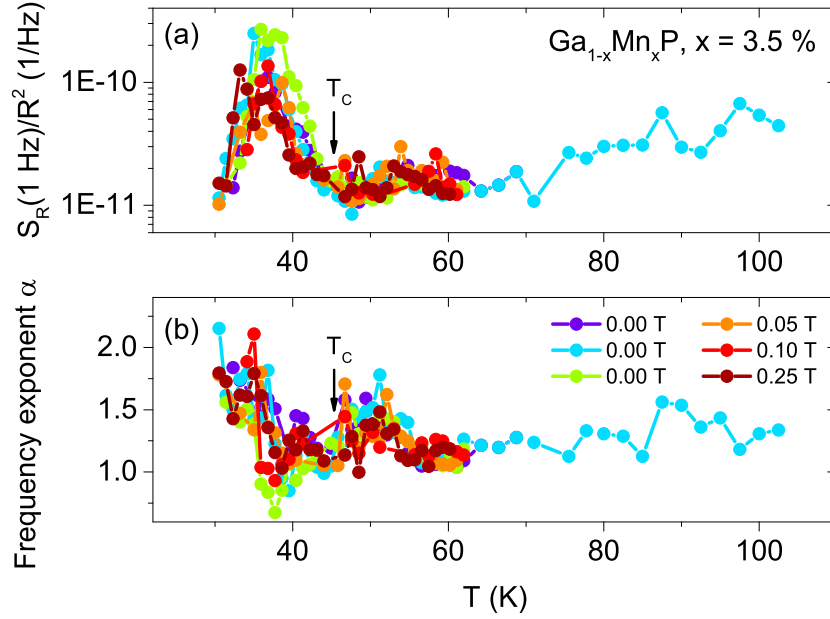


Figure 4.4.19: Noise measurements for the  $\text{Ga}_{1-x}\text{Mn}_x\text{P}$  ( $x = 3.5\%$ ) film carried out in various external out-of-plane magnetic fields  $B$ . No clear systematics can be seen neither for the PSD shown in panel (a) nor for the frequency exponent  $\alpha$  depicted in (b).

magnetic fields up to  $B = 0.25\text{ T}$ , whereby panel (a) depicts the normalized PSD and (b) the frequency exponent  $\alpha$ . It can be assumed that possible changes as a function of the external field are too weak in order to be resolved and, in future studies, the application of an in-plane magnetic field could potentially lead to a stronger effect. For zero magnetic field, three consecutive measurement runs are shown, clarifying that already for repetitive measurements there are minor differences in the characteristics of the sharp peak in the PSD. On the other hand, these results confirm the reproducibility of the noise measurements performed in this work.

In the following, the noise behavior of the  $\text{Ga}_{1-x}\text{Mn}_x\text{P}$  film with a higher Mn doping of  $x = 7.5\%$  will be presented. In contrast to the resistivity  $\rho(T)$  depicted in Fig. 4.4.14, the noise behavior of this sample does not fit into the systematics of all other films. The normalized PSD  $S_R/R^2$  evaluated at 1 Hz is shown in panels (a) and (b) of Fig. 4.4.20 for two different applied currents  $I$ . Commonly, due to the normalization,  $S_R/R^2$  is independent of the current. However, in this case, despite a similar trend, the magnitude of the increase below the ferromagnetic transition temperature is strongly different for  $I = 50\ \mu\text{A}$  and  $I = 30\ \mu\text{A}$ . While for  $I = 50\ \mu\text{A}$  the increase extends over nearly four orders of magnitude between 70 and 50 K, for  $I = 30\ \mu\text{A}$  it is less than one order of magnitude. The explanation is given in Fig. 4.4.20 (c) and (d), where the relation between the voltage noise PSD  $S_V(1\text{ Hz})$  and the applied current  $I$  is depicted for two different temperatures. In these log-log plots, the slope

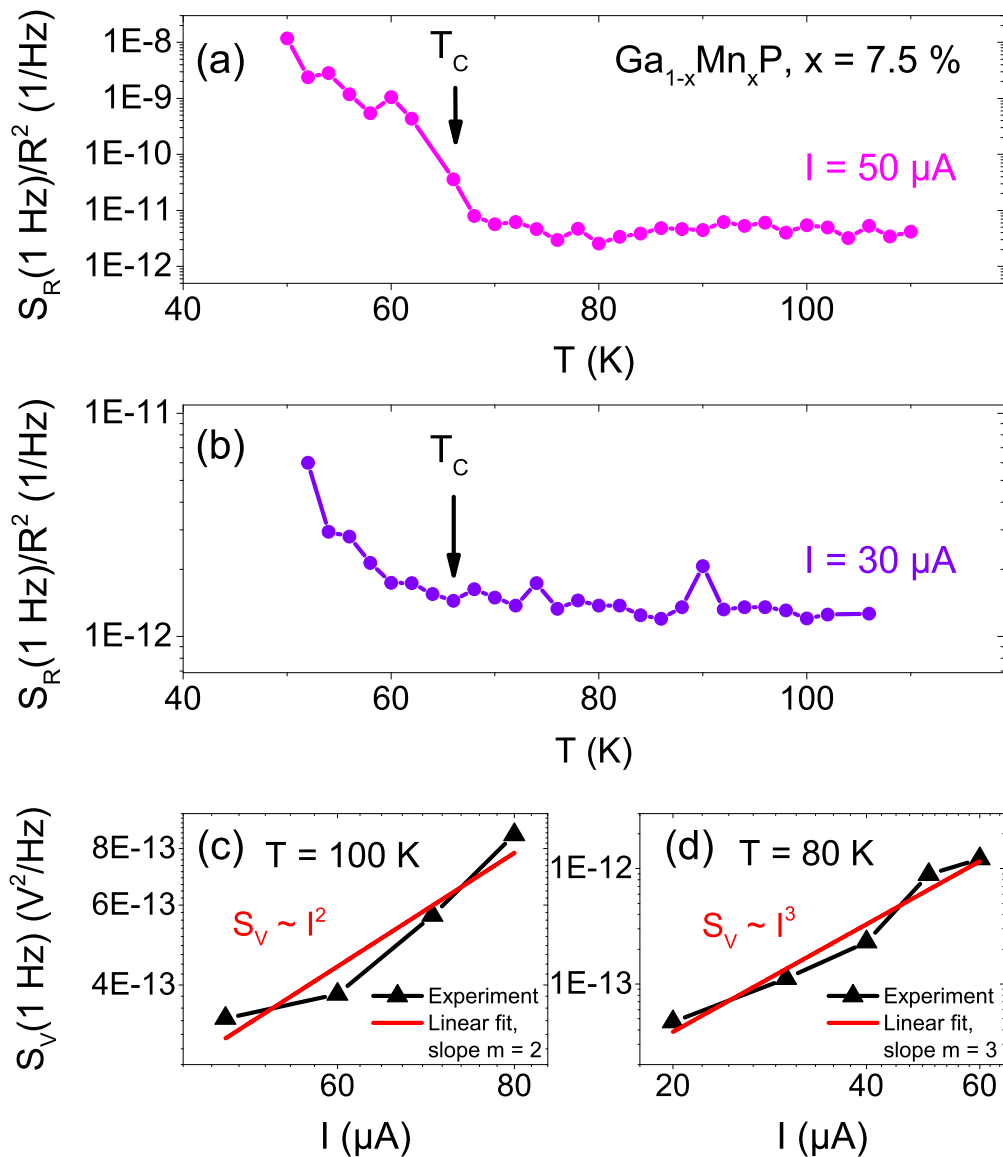


Figure 4.4.20: Noise measurements of the  $\text{Ga}_{1-x}\text{Mn}_x\text{P}$  film with  $x = 7.5\%$ . [(a) and (b)] Normalized PSD at 1 Hz as a function of  $T$  for two different applied currents. Despite a similar trend, the magnitude of the increase below  $T_C$  (marked by arrows) is strongly different. [(c) and (d)]  $S_V(1 \text{ Hz})$  against the current  $I$  for two different temperatures. While at 100 K  $S_V \propto I^2$  as expected after Hooge's law,  $S_V \propto I^3$  at 80 K. Red lines are linear fits to the data, the slope of which yields the scaling exponent  $\beta$  in  $S_V \propto I^\beta$ .

of a linear fit to the experimental data (red lines) yields the scaling exponent  $\beta$  in

$$S_V \propto I^\beta. \quad (4.18)$$

While for  $T = 100$  K it holds that  $\beta = 2$  as expected after Hooge's law, cf. Eq. (2.35), it is  $\beta = 3$  for a lower temperature of  $T = 80$  K. Since this scaling exponent  $\beta$  increases even further towards lower temperatures, an analysis of the noise data is not straightforward. Importantly, despite an Ohmic relationship between the current and voltage, which was checked for every temperature in the respective current range, there is no linear dependence of the noise on  $I^2$  at low temperatures. Although this unusual scaling behavior of the noise magnitude is rarely observed, there exist several examples in the literature, where deviations from Hooge's law were observed. For instance, C. Barone *et al.* observed  $2 < \beta < 3$  in FeTe<sub>0.5</sub>Se<sub>0.5</sub> epitaxial thin films for selected temperatures [229] and ascribe this to nonequilibrium fluctuations. Similarly, noise measurements of Cr films with high defect concentrations and Al/Cu alloy films showed  $S_V \propto I^\beta$  with  $2 < \beta < 4$ , cf. Ref. [44]. In contrast to that, the observation of  $S_V \propto V^\beta$  with  $2 < \beta < 4$  on island Pt films by J. Williams and I. Stone was interpreted by the existence of very intricate current paths in disordered conductors, which affects the noise much more strongly than the mean quantities (e.g., the current-voltage characteristics) [52]. For the present Ga<sub>1-x</sub>Mn<sub>x</sub>P sample ( $x = 7.5$  %) we assume that nonequilibrium fluctuations lead to the observed deviations from Hooge's law at low temperatures. In contrast to equilibrium  $1/f$  fluctuations, nonequilibrium flicker noise arises directly from the passage of current through the sample. In most systems, equilibrium and nonequilibrium noise are assumed to coexist and the nonequilibrium fluctuations become apparent only at high current densities. In general, nonequilibrium  $1/f$  noise contains information about defects and damages in the crystal lattice, and is used to predict electromigration stability of thin films [44]. In the case of the Ga<sub>1-x</sub>Mn<sub>x</sub>P film with  $x = 7.5$  %, scaling exponents  $\beta \gg 3$  were observed at very low temperatures. Within the scope of this work, the details of the underlying physical processes could not be conclusively determined. Importantly, deviations from Hooge's law were not observed for the Ga<sub>1-x</sub>Mn<sub>x</sub>P sample with a lower Mn content of  $x = 3.5$  %. However, due to the more insulating nature of the weaker doped film, the applied current densities were considerably smaller and thus nonequilibrium noise effects may be masked by equilibrium  $1/f$  noise. Moreover, for none of the investigated Ga<sub>1-x</sub>Mn<sub>x</sub>As films nonequilibrium fluctuations were observed. Therefore, this type of flicker noise may be more pronounced for the Ga<sub>1-x</sub>Mn<sub>x</sub>P compound in general.

Due to the dominating nonequilibrium noise effects for the Ga<sub>1-x</sub>Mn<sub>x</sub>P layer with  $x = 7.5$  %, the temperature dependence of the resistance noise magnitude should be assessed critically. With some certainty we can state that, in contrast to metallic Ga<sub>1-x</sub>Mn<sub>x</sub>As films, there is a considerable change in the temperature-dependent behavior of  $S_R/R^2$  in the vicinity of  $T_C$ . Although no distinct peak occurs in the investigated temperature range below  $T_C$ , this

sample can be assigned to the group of films, in which an electronic phase separation is observed. Despite the relatively high Mn content, the degree of charge carrier localization in this  $\text{Ga}_{1-x}\text{Mn}_x\text{P}$  sample is assumed to be still high enough in order to allow for a formation of bound magnetic polarons, which grow in size towards low temperatures until a percolation transition occurs around  $T_C$ . Future investigation towards lower temperatures and considering more  $\text{Ga}_{1-x}\text{Mn}_x\text{P}$  films should lead to a more complete picture.

In general, the percolation of bound magnetic polarons has been proposed within the frame of the impurity-band model [3, 4]. However, an alternative interpretation of our findings is conceivable, which assumes the  $p$ - $d$  Zener model to be applicable also on the insulating side of the metal-insulator transition. In this case, the hole localization length remains much greater than the average distance between the acceptors [162, 230]. Large mesoscopic fluctuations in the local value of the density of states near the MIT are expected to lead to a nano-scale phase separation into ferromagnetic and paramagnetic regions below  $T_C$ . In this respect, the paramagnetic (insulating, hole-poor) regions can persist down to low temperatures, coexisting with ferromagnetic (metallic, hole-rich) bubbles. Since magnetism and transport are strongly related in these DMSs, this leads to a magnetically driven electronic phase separation. There exist experimental indications for this type of phase separation as shown by low energy muon spin rotation measurements by V. Storchak *et al.* [231], although the case of magnetic percolation within the impurity-band model is also discussed. More precisely, the authors come to the conclusion that further theoretical studies are required in order to understand the nature of the decomposition into ferromagnetic and paramagnetic regions. The phase separation into ferromagnetic and paramagnetic regions proposed by T. Dietl within the scope of the  $p$ - $d$  Zener model [230] should persist in a broad temperature range below  $T_C$ , which is not expected to result in such a pronounced and sharp peak in the temperature-dependent noise power spectral density as it was observed in the present thesis work. In addition to that, the analysis by means of the DDH model and the comparison with previous studies lead us to the conclusion that the polaron percolation scenario within the impurity-band model is favored to explain our results for the insulating films. Our results support the view of holes being trapped in localized impurity-band states for weakly doped  $\text{Ga}_{1-x}\text{Mn}_x\text{As}$  and  $\text{Ga}_{1-x}\text{Mn}_x\text{P}$ , whereas for metallic  $\text{Ga}_{1-x}\text{Mn}_x\text{As}$  with higher  $x$ , where no signatures of a percolation mechanism are observed in the electronic noise, the widely-held view of delocalized holes within the valence band mediating ferromagnetism is more appropriate. DC transport and optical studies [175], as well as first-principle calculations [232] corroborate the applicability of the two different models on  $\text{Ga}_{1-x}\text{Mn}_x\text{As}$  for the respective Mn concentration ranges. Finally, it should also be noted that all investigated samples show global ferromagnetism below  $T_C$ , i.e., there are no mixed phases consisting of ferromagnetic clusters and superparamagnetic grains. Yuan *et al.* have shown that these mixed phases exist for  $\text{Ga}_{1-x}\text{Mn}_x\text{As}$  samples with  $x \leq 0.9\%$ , but not for  $x \geq 1.2\%$  [154]. It is desirable to study the resistance noise behavior of such mixed phases in future.

In conclusion, magnetic semiconductors are highly suitable systems to be studied by means of resistance noise spectroscopy. Given the fact that this material system is of high interest for potential spintronics and information technology applications, it may be worthwhile to study further compounds beyond  $\text{Ga}_{1-x}\text{Mn}_x\text{As}$  and  $\text{Ga}_{1-x}\text{Mn}_x\text{P}$  in terms of their noise characteristics. However, there also exist entirely different approaches for the realization of efficient data storage than the use of magnetic materials. A much-heeded candidate for future memory devices is given by oxide-based resistive switching memory devices, which exhibit highly non-linear current-voltage characteristics and a variety of different charge transport mechanisms. Therefore these devices at the same time constitute interesting systems to be studied by means of fluctuation spectroscopy. The realization of noise measurements and first results will be presented in the subsequent chapter.





# 5 Electronic noise measurements on $\text{HfO}_x$ and $\text{Y}_2\text{O}_3$ resistive switching memory devices

The present chapter is devoted to the study of electronic noise in oxide-based resistive switching memory devices fabricated by means of a molecular beam epitaxy setup which allows to control the defect concentration and thus the transport properties of the devices. At first, an introduction to resistive switching devices will be given. In this respect, the relevant physical transport and switching mechanisms will be discussed, and the sample fabrication will be described. This will be followed by an overview of previous noise studies on resistive switching systems. Finally, the technical details and the results of noise measurements on hafnia- and yttria-based RRAM devices performed in the laboratory of Prof. Dr. L. Alff at the Technical University in Darmstadt will be presented.

## 5.1 Resistive switching memory devices

Resistive random access memory (RRAM) devices, also discussed under the notion of memristors, are one of the most promising candidates in order to achieve reliable, fast and high-density non-volatile memories. These devices have attracted great attention because of their simple structure, low power consumption, excellent switching characteristics and their compatibility with complementary metal-oxide-semiconductor (CMOS) technology [233]. In recent years, many transition-metal oxides, as for instance  $\text{HfO}_x$ ,  $\text{TaO}_x$ ,  $\text{TiO}_x$ , and  $\text{WO}_x$ , have been reported to be promising materials for RRAMs. In hafnium oxide based devices, the mechanism of resistive switching is commonly related to oxygen deficient conducting filaments which form in the oxide layer located between two (metallic) electrodes after an electroforming step. More precisely, the rupture and re-formation of a conducting filament due to the electric field and Joule heating driven motion of mobile anions (oxygen ions or vacancies) leads to the physical switching mechanisms. Initially, an as-fabricated RRAM device is in a highly resistive state and no conducting filament exists. During the forming process a conducting path forms in the transition-metal oxide by applying a high voltage, and the device is switched into a low-resistance state (LRS). This is interpreted as a dielectric soft breakdown associated with the migration of oxygen ions towards the anode, leaving

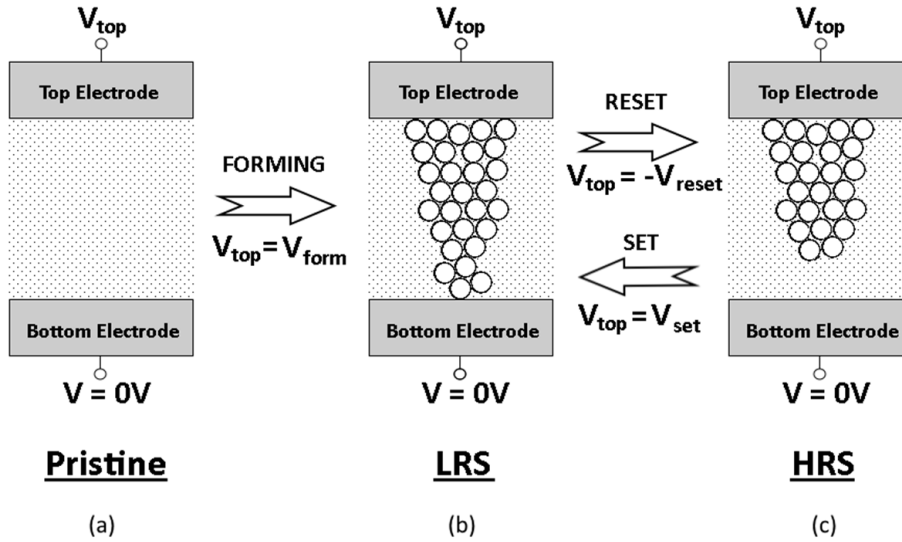


Figure 5.1.1: Bipolar switching mechanism of a typical transition-metal oxide RRAM. (a) Switching layer in pristine state before electroforming process. (b) A conducting filament is formed at the forming voltage  $V_{\text{form}}$ . (c) The filament is ruptured when a reset voltage  $V_{\text{reset}}$  of opposite polarity is applied, here with a negative value, and thereby the HRS is created. Subsequently, the LRS can be reached by applying a positive set voltage  $V_{\text{set}}$ . From [234].

behind the oxygen vacancies in the material to form a conducting filament. By applying a so-called reset voltage, the filament is ruptured and the device can be switched back to the high-resistance state (HRS). Figure 5.1.1 shows a schematic diagram of the described switching mechanism in a typical RRAM device.

In general, there exist a myriad of different switching behaviors in the typical metal-insulator-metal device configurations. With respect to the operating electrical polarity, there are two types of RRAMs. While for unipolar switching the procedure is independent of the polarity of the applied voltage, in the case of bipolar switching the set and reset process occur with opposite voltage polarities. The former case is generally attributed to Joule heating effects, whereas the latter mechanism is related to electrochemical migration. Moreover, simultaneously occurring bipolar switching mechanisms of opposite polarity can be classified as figure-eightwise and counter figure-eightwise [233]. Coexisting switching modes have been observed in stoichiometric  $\text{HfO}_2$  devices using Pt and TiN electrodes.

In order to reduce the electroforming voltages and thus the power consumption, defect engineering has turned out to be a suitable approach. For example, in oxygen deficient  $\text{HfO}_x$  an increased oxygen vacancy formation leads to a significantly reduced forming voltage [235]. This is due to the fact that higher defect concentrations induce structural phase transitions from the most stable monoclinic phase ( $m\text{-HfO}_2$ ) to higher symmetry phases [236], such as the highly oxygen deficient tetragonal phase ( $t\text{-HfO}_x$ ).

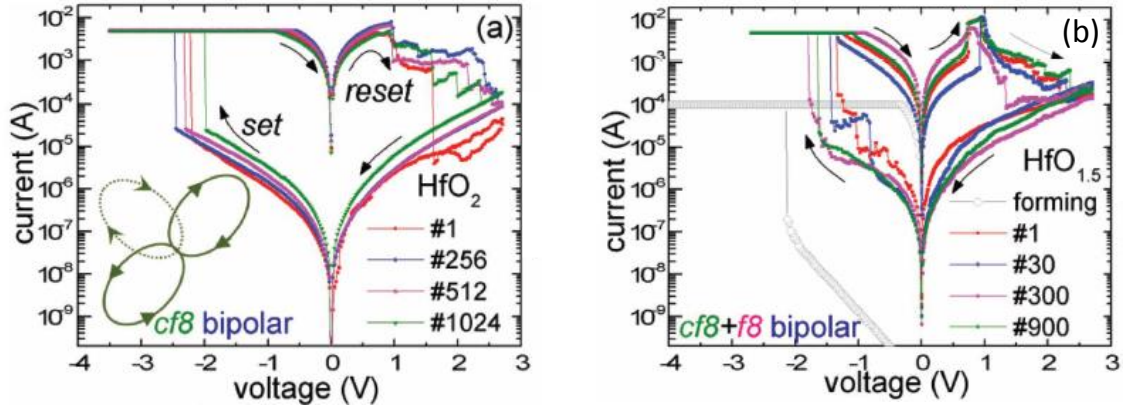


Figure 5.1.2: Comparison of the resistive switching behavior in stoichiometric  $m\text{-HfO}_2$  and oxygen deficient  $t\text{-HfO}_x$ . (a) Counter figure eightwise bipolar resistive switching in  $m\text{-HfO}_2$  after a negative electroforming voltage of  $-7\text{ V}$  (not shown). (b) Counter figure eightwise switching in  $t\text{-HfO}_x$  after a negative electroforming at  $-2.2\text{ V}$ . Here, figure eightwise switching is sometimes superimposed in the same cycle. Content reprinted from Ref. [233] with permission of John Wiley and Sons.

The  $\text{Pt}/\text{HfO}_x/\text{TiN}$  ( $x \leq 2$ ) devices studied in the present work were fabricated by means of an oxide molecular beam epitaxy setup (see Ref. [237] for details) in the group of Prof. Dr. L. Alff at the Technical University in Darmstadt.  $\text{HfO}_x$  thin films with a thickness of about  $20\text{ nm}$  were grown on polycrystalline  $\text{TiN}$  films deposited on  $\text{Si}$  wafers. By changing the hafnium evaporation rate and the oxygen flow rate to the radical source supplying radiofrequency activated oxygen radicals, the stoichiometry of the  $\text{HfO}_x$  films can be controlled. Importantly, the growth temperature of  $320^\circ\text{C}$  is compatible with CMOS technology.

Typical current-voltage characteristics for stoichiometric  $m\text{-HfO}_2$  and oxygen deficient  $t\text{-HfO}_x$  are shown in Fig. 5.1.2. As can be seen in panel (a), a counter figure eightwise bipolar resistive switching behavior is observed in  $m\text{-HfO}_2$  after a negative electroforming voltage of  $-7\text{ V}$  (not shown). In the case of  $t\text{-HfO}_x$ , counter figure eightwise switching occurs after a negative electroforming at  $-2.2\text{ V}$ , cf. Fig. 5.1.2 (b). Note that figure eightwise switching is sometimes superimposed in the same cycle. As can be seen in Fig. 5.1.2, systematic intermediate steps occur in the set process in the case of  $t\text{-HfO}_x$ , whereas the set curves are completely smooth for  $m\text{-HfO}_2$ . These steps are in this case observed as sharp transitions between discrete quantized conductance steps, where the resistance corresponds to multiples of the quantum of conductance  $G_0$ :

$$G_0 = \frac{2e^2}{h} = (12.9\text{ k}\Omega)^{-1}. \quad (5.1)$$

Here,  $e$  denotes the elementary charge and  $h$  the Planck constant. Quantized conduction

occurs when the size of the conducting filament is comparable to the mean free path of the electrons. At this point, the filament acts as a waveguide for electrons, and the charge transport becomes ballistic, that is, scattering-free [238]. Interestingly, there also exist fractional quantum conductance levels like  $0.5 G_0$ . However, to date, no conclusive theoretical explanation has been developed.

In order to enhance the RRAM device performance, it is crucial to identify the dominating physical transport mechanisms and their relation with resistive switching processes. In detail, the reliability of RRAM devices is an important aspect to be improved towards the realization in information technology applications. Particularly, random telegraph noise affects the reliability of these potential memory devices as it could lead to a failure of the readout operation, i.e., an erratic bit detection [239]. Thus the investigation of noise characteristics can provide a pathway to the reduction or elimination of hampering properties. As demonstrated in the previous chapters, fluctuation spectroscopy is a powerful tool in order to investigate the dynamics of charge carriers. Moreover, electronic noise measurements have been proven to be a suitable technique for the characterization of trap-assisted conduction [54, 11, 240], which is suggested to be one of the dominating charge transport mechanisms in the HRS of  $\text{HfO}_x$  [33]. It is desirable to compare the noise characteristics between different resistance states of both the stoichiometric  $m\text{-HfO}_2$  and the oxygen deficient  $t\text{-HfO}_x$  devices. In particular, studying the dynamics in the vicinity of the quantized conductance steps may provide new insights into the underlying physics. Furthermore, previous studies indicate a percolative nature of the  $1/f$ -type fluctuations in other resistive switching devices [241, 242]. Finally, an investigation of the noise behavior in other materials such as  $\text{Y}_2\text{O}_3$  [243, 244, 245, 246] is of great interest in order to find commonalities and differences in respect of the resistive switching and charge transport processes. Therefore, the remaining part of the present chapter will deal with previous noise studies and new measurements performed within the framework of this thesis at the Technical University of Darmstadt.

## 5.2 Previous noise studies

This section provides a general review about noise measurements on resistive switching devices. The focus is put on the much-heeded studies by S. Yu *et al.* and W. Yi *et al.* on  $\text{HfO}_2$  and  $\text{TaO}_x$  devices, respectively [33, 32]. Moreover, it should be noted that several publications by F. Puglisi *et al.* deal with the analysis of random telegraph signals in resistive random access memories in the time domain [239, 247, 248, 249, 250].

Figure 5.2.1 shows the main results by S. Yu *et al.* on a  $\text{HfO}_2$  device for different resistance states [33]. All measurements were performed in a two-terminal DC current noise configuration as described in Sec. 3.2.5. In panel (a), the normalized current noise PSD  $S_I/I^2$  is plotted against the frequency. While in the LRS the low-frequency noise exhibits a  $1/f^\alpha$

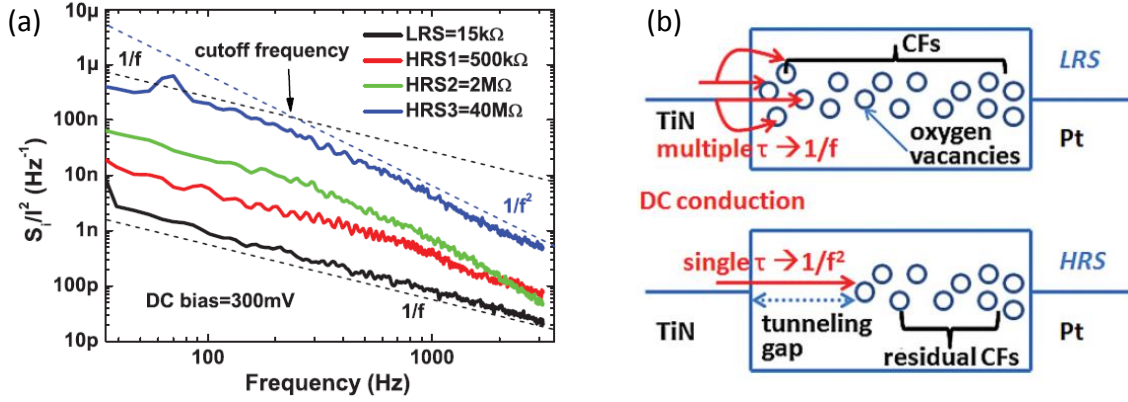


Figure 5.2.1: (a) Normalized current noise PSD as obtained from measurements on a HfO<sub>2</sub> device for different resistance states. From LRS to HRS, the frequency exponent  $\alpha$  changes from 1 to 2 at a certain cutoff frequency, while the noise magnitude increases. (b) Conduction process in the LRS and HRS: In the LRS the electrons have multiple tunneling paths with various relaxation times, which results in  $1/f$ -type noise, while in the HRS the shortest path causes a cutoff frequency in the noise behavior. Content reprinted from Ref. [33] with permission of the American Physical Society.

behavior with a frequency exponent of  $\alpha = 1$ , the slope changes from 1 to 2 at a certain cutoff frequency in the HRS. The explanation for this observation is schematically illustrated in Fig. 5.2.1 (b). In the LRS, the conducting filament connects both electrodes, while in the HRS, the filament is ruptured near one electrode. Here, no oxygen vacancies are present and the conduction of charge carriers can only happen via tunneling processes across a large gap. Therefore, multiple electrode-to-trap tunneling processes and thus relaxation times exist in the LRS, which results in a pure  $1/f$ -type behavior. Under the assumption of a high enough trap density of the conducting filament, the trap-to-trap hopping rate is much larger than the electrode-to-trap tunneling rate, which is why the observed low-frequency noise is mainly dominated by electrode-to-trap tunneling processes. In contrast to that, the noise characteristics in the HRS are strongly affected by the shortest possible tunneling distance between the electrode and the nearest trap, causing a minimum relaxation time  $\tau_{\min}$ . Therefore,  $f_c = 1/\tau_{\min}$  corresponds to the cutoff frequency of the associated Lorentzian. Tunneling processes between the electrode and traps located farther away produce Lorentzian spectra with lower cutoff frequencies. Consequently, the superposition of various Lorentzian spectra leads to a perfect  $1/f$  noise at frequencies below  $f_c$ , while the course of the PSD above  $f_c$  is determined by the  $1/f^2$  tail of the Lorentzian associated with the shortest tunneling distance. In conclusion, the cutoff frequency  $f_c$  between  $1/f$  and  $1/f^2$  noise in the HRS is an indicator for the spatial tunneling gap between the electrode and the ruptured filament. S. Yu *et al.* find this distance to lie between 1.5 nm and 2.0 nm in their devices [33]. Finally, it should be

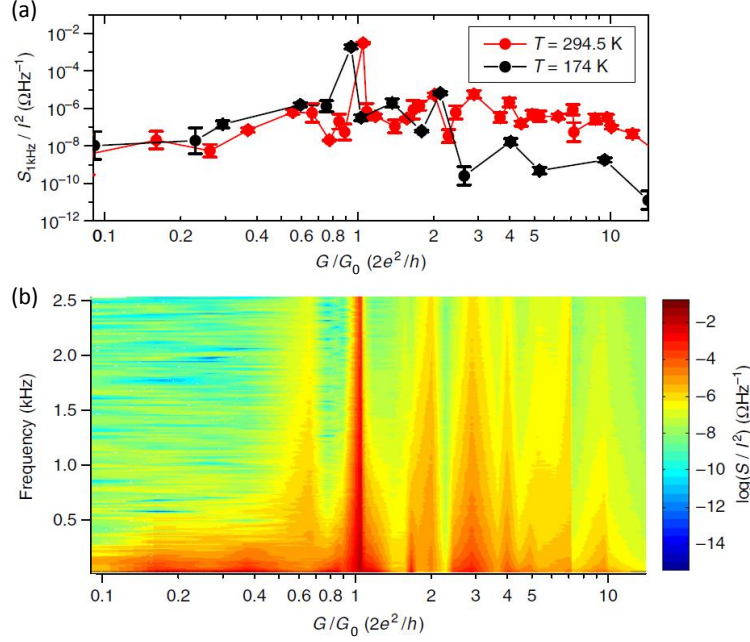


Figure 5.2.2: (a) Normalized noise PSD  $S_R = S_V/I^2$  at 1 kHz for a  $\text{TaO}_x$  RRAM device as a function of  $G_0$ -normalized conductance for two temperatures with clear features at integer multiples of the conductance quantum. (b) Two-dimensional color plot showing  $S_R$  as a function of  $G/G_0$  and frequency  $f$  at  $T = 295\text{ K}$ . After [32].

emphasized that this model was inspired by the McWhorter model, cf. Sec. 2.4.4, which was initially developed to explain the noise behavior in the drain current of field-effect transistors. The main difference to the McWhorter model is that the tunneling path of the electrons into or out of the RRAM material is along with the current flowing direction, whereas the tunneling processes in field-effect transistors are perpendicular to the current direction.

The studies by W. Yi *et al.* yield similar results on  $\text{TaO}_x$  based RRAM devices: Lower conductance states exhibit larger normalized noise magnitudes and a  $1/f^2$  behavior, while metallic states show a pure  $1/f$  functional dependence [32]. In addition to that, it was shown that there is a pronounced maximum in the noise at the conductance quantum  $G_0$ , where a characteristic Lorentzian spectrum is observed, and several minor peaks at integer multiples of  $G_0$ . This can be seen in Fig. 5.2.2 (a), where the normalized noise PSD  $S_R = S_V/I^2$  evaluated at 1 kHz is plotted against the normalized conductance  $G/G_0$  for two different temperatures. Figure 5.2.2 (b) shows a two-dimensional color plot of  $S_R$  as a function of the conductance and the frequency.

In this publication, the quantized conductance states are regarded as an indication for a quantum point contact (QPC) within the oxide layer. However, the authors state that an enlarged noise behavior at a QPC is very uncommon and has not yet been revealed in any system. On the contrary, shot noise experiments on QPCs in two-dimensional electron gases in GaAs/AlGaAs heterostructures yield a suppression of the noise magnitude at integer mul-

titles of conductance quanta [251]. For the case of TaO<sub>x</sub> RRAM devices, W. Yi *et al.* attribute the enhanced noise magnitude to a thermally-activated atom motion in the conductance channel [32]. In detail, due to high local Joule heating at the QPC, which is the narrowest part of the conductance channel, atomic fluctuations lead to disruptions of the electronic transport and hence to an enhanced noise magnitude. In order to explain the existence of a peak in the noise at a discrete conductance, the oxide layer can be viewed as a random resistor network, cf. Sec. 2.6, where the electronic noise diverges as soon as the concentration of the conducting bonds decreases to a critical value for disconnecting a conducting channel between the electrodes. Finally, it should be mentioned that the stochastic behavior near the point contact regime was modeled using Molecular Dynamics-Langevin simulations, which show a good concordance with the experimental noise data.

In several studies, the charge transport in RRAM devices is described by means of a percolation picture. For instance, in the case of unipolar resistance switching in Pt/NiO/Pt devices [241] and organic nanocomposites of polyimide and phenyl-C61-butyric acid methyl ester (PCBM) [242], the normalized PSD scales as

$$S_R/R^2 \propto R^w, \quad (5.2)$$

where  $w$  denotes a critical exponent, cf. Sec. 2.6.2. In the case of NiO, typical values for the exponent are found to be around  $w \sim 2$ , while for the organic nanocomposite  $w \sim 1$ . While for NiO a filamentary-type switching is observed, the switching mechanism for the organic nanocomposite system is still under debate and it may be related to trapping or detrapping of charges, see Ref. [252] for details. This may be a possible explanation for the different critical exponents  $w$  in these two systems. Indications for a percolative conductivity have also been found for HfO<sub>x</sub> by D. Islamov *et al.* [253]. Here, the experimental RRAM current-voltage characteristics in HfO<sub>x</sub> are found to be in good agreement with theoretical predictions according to the percolation model by B. Shklovskii and A. Efros [254]. However, to date, no systematic noise studies focusing on percolation exist for HfO<sub>x</sub> and Y<sub>2</sub>O<sub>3</sub> based RRAM devices. Therefore, one of the future goals is the investigation of the electronic noise characteristics of HfO<sub>x</sub> and Y<sub>2</sub>O<sub>3</sub> metal-insulator-metal structures in terms of percolation.

## 5.3 Experimental realization and results

### 5.3.1 Experimental setup

The fabrication of RRAM devices by means of the oxide molecular beam epitaxy setup in the group of Prof. Dr. L. Alff at the Technical University in Darmstadt provides the unique opportunity to compare the noise characteristics of stoichiometric *m*-HfO<sub>2</sub> and oxygen deficient *t*-HfO<sub>x</sub> systems. In the present work, a two-terminal DC current noise setup has been real-

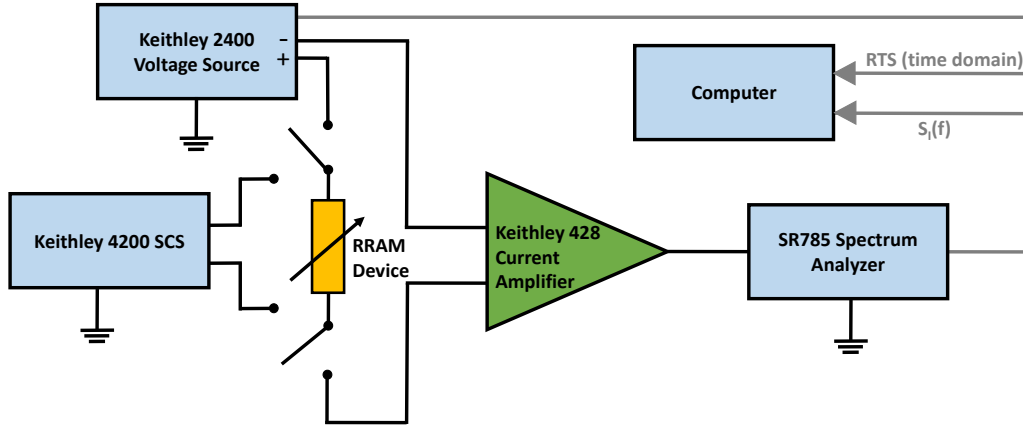


Figure 5.3.1: Schematic illustration of the two-terminal DC current noise setup for RRAM devices established in the laboratory of Prof. Dr. L. Alff at the Technical University Darmstadt. A Keithley 4200 Semiconductor Characterization System (SCS) is used to set the device to the desired resistance state. Subsequently, a Keithley 2400 is used as a voltage source and the emerging current fluctuations are measured in two ways: firstly, the time-dependent random telegraph signal (RTS) is fed into the computer; and secondly, the current fluctuations are amplified by a Keithley 428 current amplifier and then transformed into voltage fluctuations, which are further processed by a signal analyzer (SR785, Stanford Research Instruments).

ized in analogy to the studies by S. Yu *et al.* [33]. A schematic illustration of the experimental setup is shown in Fig. 5.3.1. At first, we focus on fluctuation spectroscopy measurements on hafnia-based RRAMs. In order to set the investigated RRAM device to the desired resistance state, a Keithley 4200 Semiconductor Characterization System (SCS) is utilized. The sample itself is placed inside the chamber of a cryogenic probe station (Model TTPX, Lake Shore). Since every fabricated RRAM chip contains a matrix of  $14 \times 14$  individual devices, and each top contact has a size of  $30 \mu\text{m} \times 30 \mu\text{m}$ , it would be highly unpractical to use permanent contacts as it is the case for other samples investigated in this thesis. Instead of conductive silver paste or soldering, the RRAM samples are contacted by two probe needles which can be precisely approached towards the respective electrodes. Although the endurance of the investigated RRAM devices is relatively high, some samples can degrade with time or may not show the expected behavior, such as the quantized conductance. Therefore, flexibility with regard to the contacting of devices is crucial. After the desired resistance state has been prepared, a Keithley 2400 DC voltage source is utilized in order to apply a small readout voltage. As a consequence, a fluctuating current will flow through the oxide layer, which will be analyzed in two different ways. Firstly, the current fluctuations are amplified by means of a Keithley 428 current amplifier and transformed into voltage fluctuations, which are Fourier transformed by an SR785 (Stanford Research Instruments) signal analyzer. The calculated



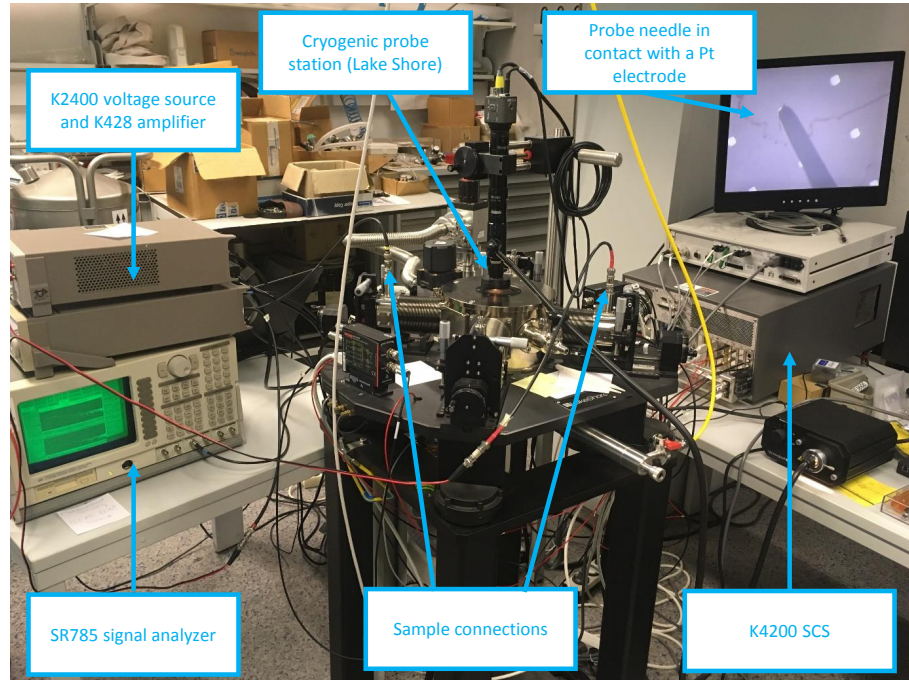


Figure 5.3.2: Photograph of the experimental setup for noise measurements on RRAM devices. The sample chip is located inside the chamber of a cryogenic probe station (Model TTPX, Lake Shore).

current noise PSD  $S_I(f)$  is then fed into a computer. Simultaneously, the time-dependent current  $I(t)$  measured by the Keithley 2400 can also be read out by the computer, which allows for a time-domain analysis of emerging random telegraph noise. A photograph of the experimental setup is shown in Fig. 5.3.2. It should be noted that the computer screen in the top right of the picture shows a microscope image of one of the probe needles, which is in contact with a Pt top electrode. All measurements in this thesis work were performed at room temperature, but in principle the cryogenic probe station allows for measurements down to liquid helium temperatures.

### 5.3.2 Measurements on hafnium oxide based RRAM devices

In order to conduct noise measurements, the respective RRAM device is set to the desired resistance state. The readout voltage was chosen as  $V_r = -0.1$  V for a majority of measurements and the gain of the Keithley 428 current amplifier was set according to Tab. 3.2.1. Since the experimental setup in Darmstadt was not specifically designed for electronic noise measurements, care had to be taken in order to eliminate external perturbations and ensure a proper grounding. Figure 5.3.3 (a) shows three exemplary noise spectra measured on a stoichiometric  $\text{HfO}_2$  memristor. While the black and red curve reflect the true response originating from the sample, the green noise spectrum is an artifact of improper grounding.

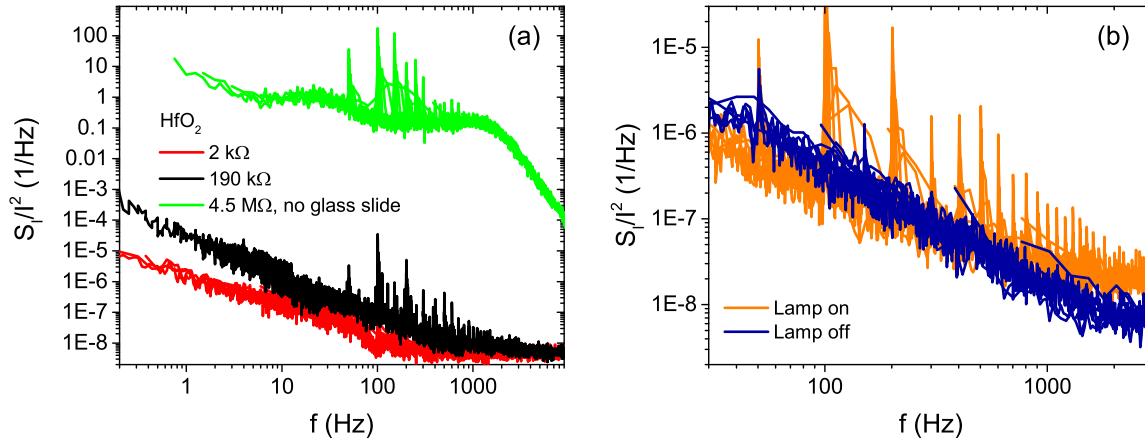


Figure 5.3.3: (a) Three exemplary noise spectra measured on a stoichiometric  $\text{HfO}_2$  RRAM device. Green spectrum is an artifact of improper grounding. (b) Two noise spectra recorded at a similar resistance state of an RRAM device. Orange spectrum exhibits peaks at multiples of 100 Hz due to the power supply of the microscope lamp.

Apparently, the noise magnitude of the green spectrum is many orders of magnitude higher than the true sample signal and, moreover, the shape of the spectrum is abnormal. In detail, we assume that the electric current was not flowing through both probe needles in this case, but rather from one tip to the ground of the setup, since the device was not properly isolated from the metallic sample stage. Although the RRAM devices are typically grown on an insulating substrate, remaining silver paste from the sample growth and preparation process may short-circuit the bottom electrode with the sample stage, leading to erroneous noise spectra. Therefore, the use of a glass slide was crucial in order to isolate the device from the sample stage. Due to the complicated current-voltage characteristics of RRAM devices, it is furthermore not straightforward to apply Hooge's law (Eq. (2.35)) in order to discriminate between fluctuations arising from the sample and electronic noise due to external perturbations.

Fig. 5.3.3 (b) illustrates the possible impact of external perturbations. Here, two noise spectra recorded at similar resistance states of an RRAM device are shown. While the blue spectrum is very smooth in the depicted frequency range, the orange spectrum exhibits a number of peaks at multiples of 100 Hz, which are not present in the other spectrum. It was found that these peaks originate from the power supply of the microscope lamp which is part of the experimental setup in Darmstadt. This simple example clarifies the importance of a thorough review of the experimental setup in terms of external perturbations and parasitic noise sources.

In the following, we concentrate on the investigated current noise in the high resistance state of stoichiometric  $\text{HfO}_2$  and oxygen deficient  $\text{HfO}_x$  based memristor devices. In analogy to the results reported in the literature for stoichiometric  $\text{HfO}_2$ , our measurements demonstrate the presence of pronounced random telegraph noise. Exemplary noise spectra for a  $\text{HfO}_2$

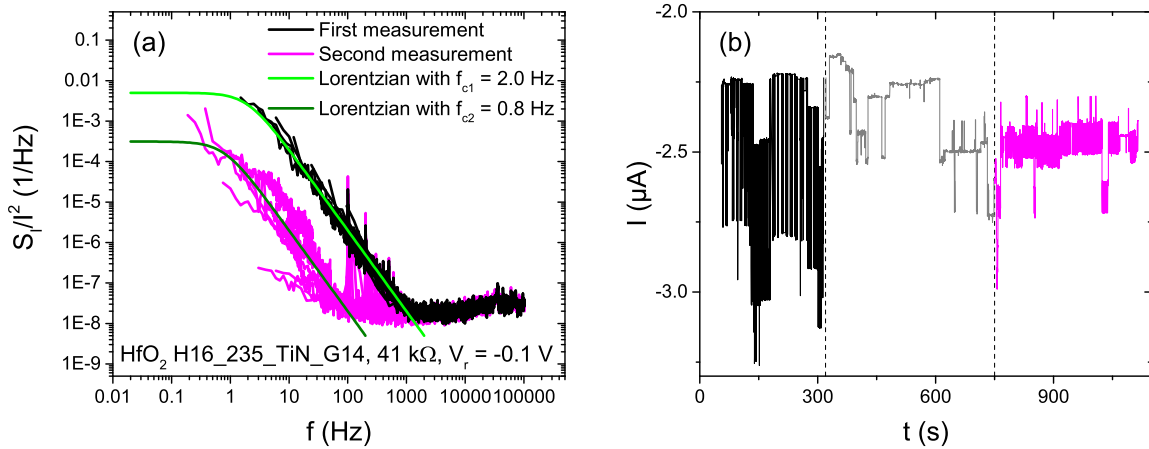


Figure 5.3.4: (a) Two successively measured current noise spectra of a stoichiometric  $\text{HfO}_2$  device at a readout voltage of  $V_r = -0.1$  V and  $R = 41$  k $\Omega$  following a Lorentzian behavior as indicated by green curves. (b) Simultaneously acquired time signal  $I(t)$  verifying the pronounced changes in the random telegraph noise behavior.

device are shown in Fig. 5.3.4 (a). Here, the device was set to a HRS with  $R = 41$  k $\Omega$ , and the noise measurements were performed at a DC bias voltage of  $V_r = -0.1$  V. Interestingly, the two successively measured noise spectra are not lying on top of each other. As indicated by the green curves, both spectra follow a Lorentzian behavior. Here, the corner frequencies were chosen as  $f_{c1} = 2.0$  Hz and  $f_{c2} = 0.8$  Hz, respectively, even though the uncertainty in these values is relatively high due to a lack of data points below  $\sim 1$  Hz. Furthermore, the second measurement (magenta curve) does not yield such a smooth noise spectrum as compared to the first one (black curve). Since the signal analyzer, which calculates the Fast Fourier Transform of the fluctuating time signal, yields different results for the successively measured frequency ranges, we assume that the noise characteristics has changed during the course of the measurement, which can take about 5–20 minutes depending on the number of averages. The non-reproducibility of the first measurement therefore indicates temporal changes in the fluctuating current signal. We now consider the time signal  $I(t)$ , which was recorded simultaneously to the noise measurements, as indicated in Fig. 5.3.1. Figure 5.3.4 (b) shows the time-dependent current for a measuring duration of about 20 min. Firstly, it can be seen that, as expected, a pronounced random telegraph signal occurs during the entire measurement. Data points have been saved every 110 ms, which is a limitation for the resolution of fast switching processes. In future, a fast data acquisition card is planned to be utilized in order to increase the sampling rate. However, this sampling rate is sufficient in order to confirm the results shown in Fig. 5.3.4 (a). Apparently, the characteristics of the random telegraph signal change as indicated by dashed vertical lines. Note that the color coding in both panels was chosen to indicate the concurrent measurements. The intermediate time interval in  $I(t)$  contains only very slow RTN processes (gray curve). As described in

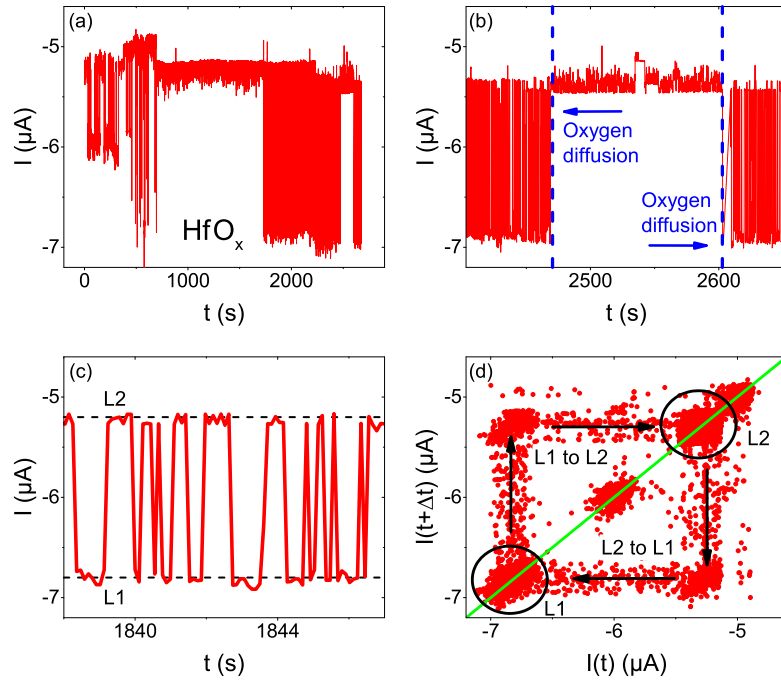


Figure 5.3.5: RTN for an oxygen deficient  $\text{HfO}_x$  device. (a)  $I(t)$  for a measurement time of about 43 min. (b) Magnified view clarifying temporary RTN. (c) Further magnification indicating two levels L1 and L2. (d) Time-lag plot.

more detail further below, the abrupt changes in the RTN characteristics can be related to oxygen diffusion processes. This example is a clear verification that the measured noise spectra originate from the sample, since the determined corner frequencies are comparable to the switching frequencies observed in the time signal. Moreover, it was shown that abrupt changes in the RTN characteristics can complicate the noise measurements by means of a signal analyzer. Nevertheless, a suitable approach for a better understanding of the underlying physical processes causing the observed fluctuations in RRAM devices is the analysis of random telegraph signals in the time domain. As for the stoichiometric devices, a complex random telegraph noise (RTN) behavior was also observed for oxygen deficient  $\text{HfO}_x$ . Figure 5.3.5 (a) shows the current  $I(t)$  for a measurement time of more than 40 min. In analogy to the stoichiometric device, besides conventional RTN, i.e., switching between two or more states, it can be observed that fluctuations suddenly appear and disappear over time. This observation is clarified in Fig. 5.3.5 (b), which shows a magnified view between  $t = 2400$  s and  $t = 2650$  s. This effect is considered temporary RTN, which is one type of anomalous RTN [239]. A further type of anomalous RTN would be mutant RTN, where temporary changes of the RTN stochastic properties occur. For multi-level RTN, F. Puglisi *et al.* apply the Factorial Hidden Markov Model algorithm in order to decompose the signal into many independent two-level signals, which allows to correctly assess the statistical characteristics of every individual defect contributing to the multi-level RTN [239]. However, in the case of

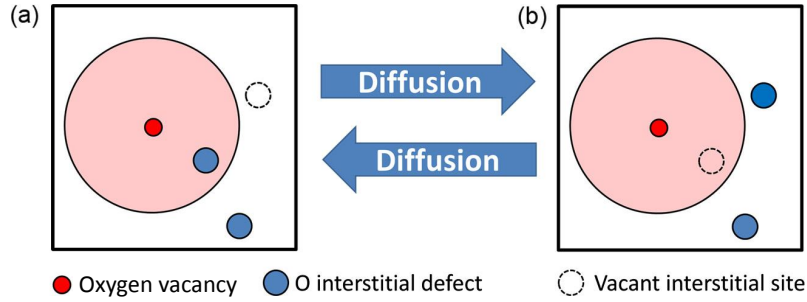


Figure 5.3.6: Oxygen interstitial diffusion scenario as a possible explanation for temporary RTN. See main text for details. After [239] with permission of Elsevier.

anomalous RTN, the signal cannot be described by a superposition of independent two-level RTN fluctuations. Considering the behavior shown in Fig. 5.3.5 (b), the temporary RTN is associated with oxygen interstitial diffusion [255], which is indicated by blue dashed lines and in good agreement with the observations by F. Puglisi *et al.* [239]. In detail, two-level RTN can be considered as a result of the Coulomb interaction between an oxygen vacancy which is involved in trap-assisted tunneling and an oxygen interstitial defect in its proximity. If, due to a diffusion mechanism, the location of the oxygen interstitial changes as a function of time, a corresponding change in the RTN statistical properties is expected. A possible scenario is illustrated in Fig. 5.3.6. In panel (a), an oxygen vacancy is depicted, whereby the light-red region around it corresponds to the zone in which an oxygen interstitial (blue sphere) needs to be located in order to make the Coulomb interaction between these defects relevant. In the depicted scenario, the oxygen vacancy is involved in trap-assisted tunneling conduction and its Coulomb interaction with the adjacent oxygen interstitial inside the light-red region generates the observed RTN. In panel (b), the oxygen interstitial diffuses to another free interstitial site further away from the vacancy defect, which leads to a temporary stopping of the RTN process. A subsequent diffusion back to the first interstitial position as shown in Fig. 5.3.6 (a) will cause a re-appearance of RTN with the original statistical characteristics. In the case of the RTN depicted in Fig. 5.3.5 (b), the main RTN process disappears for more than 100 s.

As can be seen in a further magnification of the RTN trace in Fig. 5.3.5 (c), the switching mainly occurs between two levels L1 and L2, whereby the mean difference in the current between the two states equals  $\Delta I = |I_{L2} - I_{L1}| = 1.6 \mu\text{A}$ . Thus, the RTN between  $t = 1800$  s and  $t = 2400$  s can be viewed as a two-level RTN. However, as suggested by Fig. 5.3.5 (a), the situation in a broader time interval appears to be more complex. For the sake of further analysis, a so-called time-lag plot can be helpful to visualize the different current levels and the transitions between these states, and thus to understand the statistical behavior of telegraphic noise [256, 257, 258]. A time-lag plot can be obtained by plotting points on a two-dimensional graph, where the x- and y-axis are set to the current value at time  $t$  and

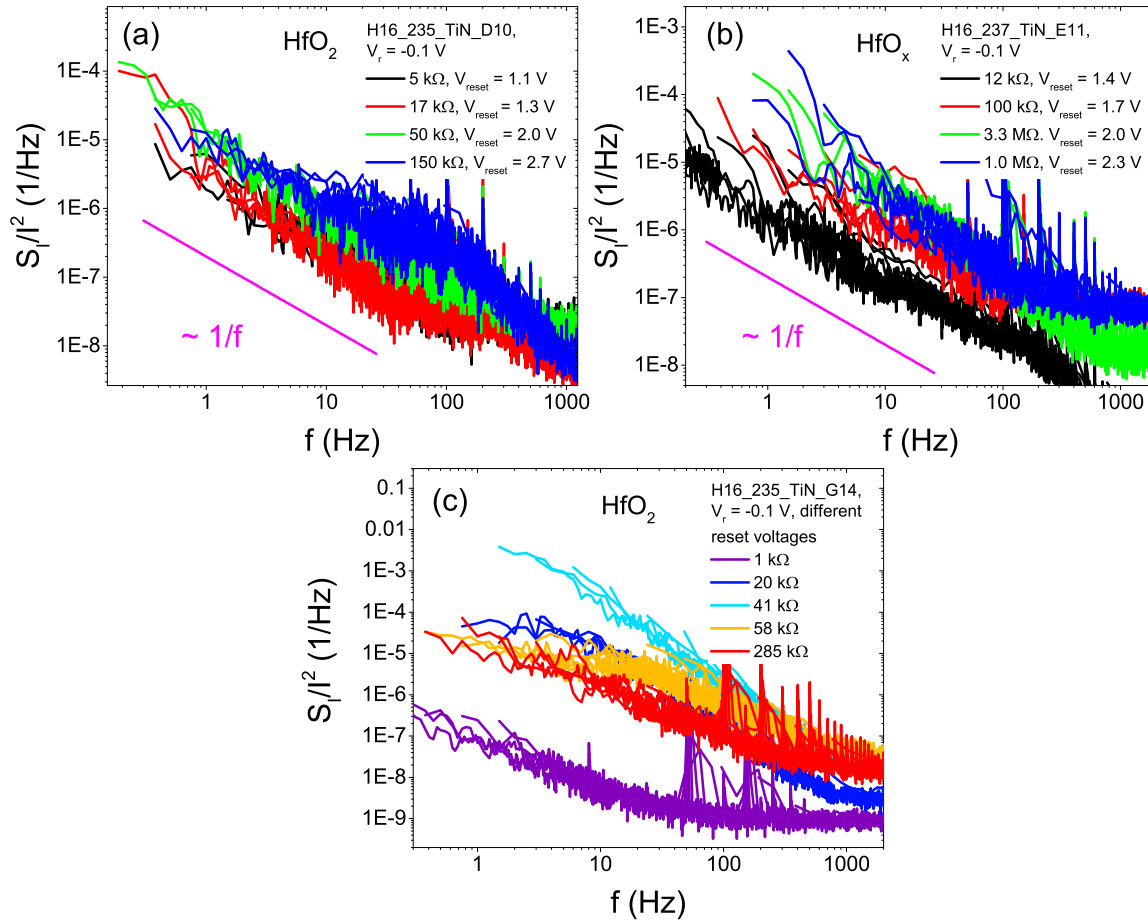


Figure 5.3.7:  $S_I/I^2$  against  $f$  for four reset voltages compared for (a) a stoichiometric  $\text{HfO}_2$  and (b) an oxygen deficient  $\text{HfO}_x$  RRAM sample. (c) Measurements on a further stoichiometric device for various cyclings of the current-voltage characteristics and different reset voltages clarifying the occurrence of Lorentzian spectra.

$t + \Delta t$ . In the present case,  $\Delta t = 110$  ms, which corresponds to the sampling time of the RTN measurement. The clusters circled in black, which are lying on the diagonal (green line), correspond to the two current states L1 and L2. The two further clusters can be attributed to other predominant current levels which occur between  $t = 0$  s and  $t = 700$  s. The non-diagonal points indicate the transition between current levels, that is, the upper data points correspond to the transition from L1 to L2, while the lower points indicate a switching from L2 to L1.

In the scope of this work, no major differences in the noise behavior between stoichiometric  $\text{HfO}_2$  and oxygen deficient  $\text{HfO}_x$  could be revealed. Comparative low-frequency noise spectra are presented in Fig. 5.3.7. As can be seen in diagram (c), pronounced Lorentzian contributions can be observed for nearly all resistance states in the considered stoichiometric  $\text{HfO}_2$  device, which were accessed by cycling the device several times through its current-

voltage characteristics and using different reset voltages between 1.15 V and 2.7 V. Since some parameters, as for example the number of cycles or the compliance current, were changed and, moreover, this particular device occasionally switched spontaneously to different resistance states in between the noise measurements, no analysis in dependence of the reset voltage is performed for this sample.

In many cases, as illustrated in Fig. 5.3.4 (a), the noise behavior changes with time. Therefore, an analysis in terms of the scaling of the noise magnitude with the resistance as presented in Refs. [33, 259, 249] is difficult in this case. However, it was found that the strongest RTN and most abrupt changes in the noise characteristics occur during the first minutes after the preparation of a resistance state, where we assume a larger number of diffusion processes than at a later time. Consequently, after a waiting time of about 5–15 min, the observed noise spectra exhibit weaker or no Lorentzian contributions. Therefore, the spectra shown in Fig. 5.3.7 (a) and (b) for the stoichiometric and oxygen deficient hafnium oxide based RRAMs are more of a  $1/f$ -type nature and only weak Lorentzian contributions are visible. It will be the matter of future studies to investigate this time dependence on a larger number of devices.

As can be seen in Fig. 5.3.7 (a) and (b), the normalized current noise PSD  $S_I/I^2$  increases towards higher resistances. In both cases, the reset voltage was varied in order to increase the rupture length of the conducting filament. While for stoichiometric  $\text{HfO}_2$  devices the set voltage typically corresponds to  $-2.5$  V, it is only  $-2.3$  V for oxygen deficient  $\text{HfO}_x$  memristors. Furthermore, the maximum reset voltages are 2.7 V and 2.3 V for  $\text{HfO}_2$  and  $\text{HfO}_x$ , respectively. Finally, we note that after the electroforming step, each RRAM device is cycled at least 30 times through its current-voltage characteristics in order to stabilize the conducting filament. This topic will be discussed in more detail in Sec. 5.3.3 for the case of yttrium oxide.

As stated before, the noise in the HRS is attributed to the temporary modification of the properties of a trap involved in the trap-assisted tunneling charge transport, which can be due to charge trapping/emission into/from a trap or due to the Coulomb blockade effect [249]. Here, we find that the magnitude of the  $1/f$ -type noise is proportional to the reset voltage and hence the rupture length of the filament, which is in good agreement with the results by F. Puglisi *et al.* on stoichiometric hafnium oxide based devices [249]. For the first time, evidence for this behavior is also found for oxygen deficient  $\text{HfO}_x$  in the present thesis work. However, we suggest further measurements on more devices, including more resistance states and a higher number of averages, since the experimental resolution in Fig. 5.3.7 (b) is still improvable. Due to the limited statistics and resolution, an analysis in terms of percolation is not carried out in the scope of the present work, even though the scaling of  $S_I/I^2 = S_R/R^2$  with the resistance  $R$ , as illustrated in Fig. 5.3.7 (a) and (b), points to a percolating nature of the charge transport.

Since the present chapter mainly focuses on the realization and implementation of first fluctuation spectroscopy measurements on RRAMs at the Technical University Darmstadt, there remain a number of open questions about the noise properties in hafnium oxide based

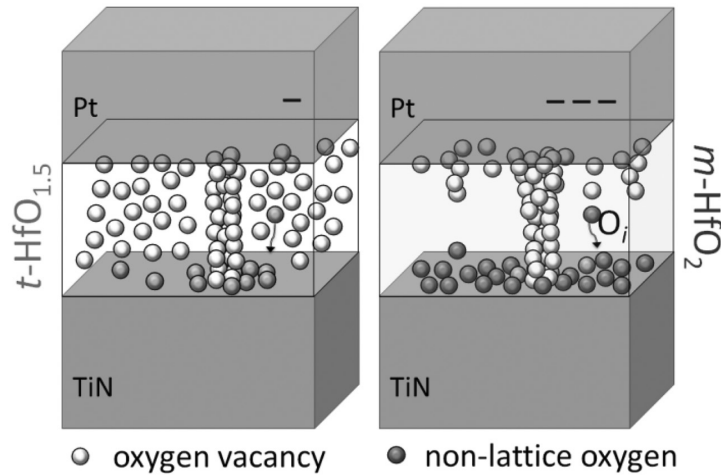


Figure 5.3.8: Schematic illustration of the conducting filament formation in Pt/ $t\text{-HfO}_{1.5}$ /TiN with  $x = 1.5$  (left) and Pt/ $m\text{-HfO}_2$ /TiN (right). Content reprinted from Ref. [233] with permission of John Wiley and Sons.

RRAMs, which will be addressed in future investigations. Firstly, in contrast to the studies by W. Yi *et al.* on  $\text{TaO}_x$  based devices [32], no pronounced enhancement in the noise magnitude is observed in the vicinity of  $G_0$ , cf. Fig. 5.2.2. Since the maximum in the noise PSD is very narrow in the case of  $\text{TaO}_x$ , a higher number of measurements on  $\text{HfO}_x$  based devices would be necessary in order to make conclusive statements. Furthermore, in the work by W. Yi *et al.* the noise spectra at  $G_0$  appear to have a pure Lorentzian nature without any indications for a  $1/f$  behavior. In consideration of the results presented in this chapter, the question arises whether this Lorentzian spectrum would change to a  $1/f$ -type spectrum after a certain time due to diffusion processes or if the physics in hafnium oxide is different than in  $\text{TaO}_x$ . Moreover, comparative noise measurements in the LRS and HRS are planned. However, for the investigation of electronic fluctuations in the LRS, a technique different than the current noise measurements is required to be established, since the magnitude of the resistance is generally too low in order to allow for operating the current amplifier. Instead, voltage noise measurements will have to be realized in the LRS.

In addition, as mentioned before, no clear differences between stoichiometric and oxygen deficient hafnium oxide RRAM devices could be revealed in the present work. However, there are first indications that the observed RTN is more pronounced and occurs more frequently in stoichiometric samples than in oxygen deficient devices. A conceivable explanation is given by the fact that the presence of a large amount of oxygen vacancies in oxygen deficient  $\text{HfO}_x$  implies a higher probability of trapping and detrapping events of charge carriers at various vacancies located in the vicinity of the (ruptured) filament. Furthermore, within the dielectric barrier between the ruptured filament and the electrode, charge transport in the HRS is dominated by trap-assisted tunneling at positively charged oxygen vacancy defects.



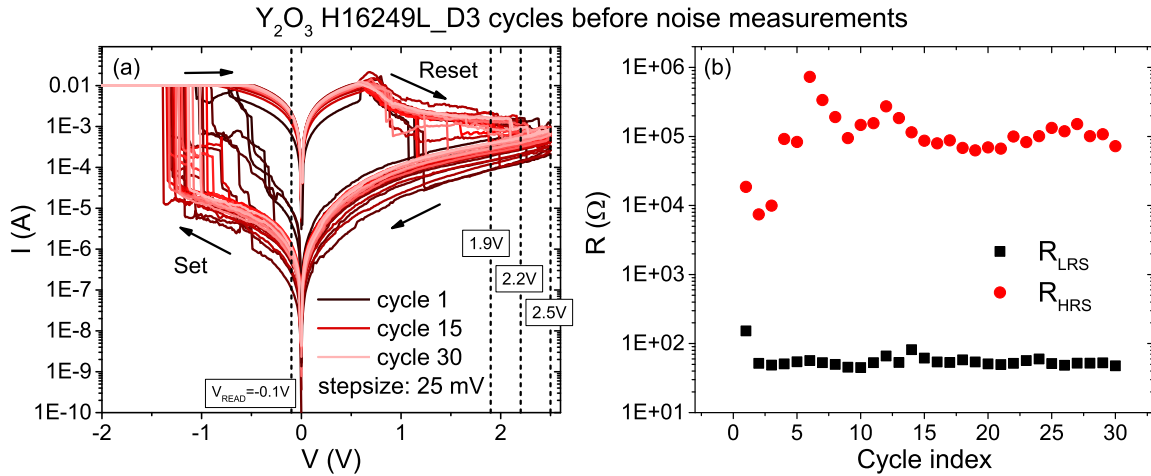


Figure 5.3.9: (a) Resistance switching behavior of a bipolar  $\text{Y}_2\text{O}_3$  RRAM (30 cycles). Three different reset voltages (1.9 V, 2.2 V and 2.5 V) and the readout voltage ( $-0.1$  V) utilized for noise measurements are indicated by vertical dashed lines. (b) Resistance values in the HRS and LRS for 30 successive cycles.

In fact, the observation of two-level random telegraph noise in the HRS is generally ascribed to the random activation and deactivation of an individual oxygen vacancy [258, 260]. Since these processes will be strongly enhanced in oxygen deficient devices, and the respective time constants will be different, the fluctuations in the electric current will appear as a  $1/f$ -type spectrum. In contrast, as indicated in the right illustration of Fig. 5.3.8, only a few oxygen vacancies are located in the proximity of the conducting filament in stoichiometric  $\text{HfO}_2$ . Therefore, the number of possible trapping/detrapping and trap-assisted tunneling processes is drastically reduced and the noise spectrum is likely to contain a dominating Lorentzian contribution as can be seen in Fig. 5.3.7 (c). Further noise measurements on hafnia-based RRAMs are required in order to substantiate the findings of the present study.

### 5.3.3 First results on $\text{Y}_2\text{O}_3$ and outlook

In the previous subsection, the successful implementation of noise measurements on hafnium oxide based RRAM devices was demonstrated. A further material of current interest for the realization of RRAM devices is  $\text{Y}_2\text{O}_3$  [243, 244, 245, 246], the noise properties of which have not yet been reported in the literature. In the group of Prof. Dr. L. Alff at the Technical University Darmstadt, Pt/ $\text{Y}_2\text{O}_3$ /TiN RRAM devices were fabricated in analogy to  $\text{HfO}_2$  based systems by means of an oxide molecular beam epitaxy setup. Exemplary current-voltage curves are presented in Fig. 5.3.9 (a) for a device with bipolar resistance switching behavior. For all bipolar  $\text{Y}_2\text{O}_3$  RRAMs the set voltage was chosen to be  $-2.5$  V, while the maximum utilized reset voltage was 2.5 V. However, as indicated by dashed vertical lines in Fig. 5.3.9 (a), lower reset voltages were also utilized in order to reach intermediate resistance states.

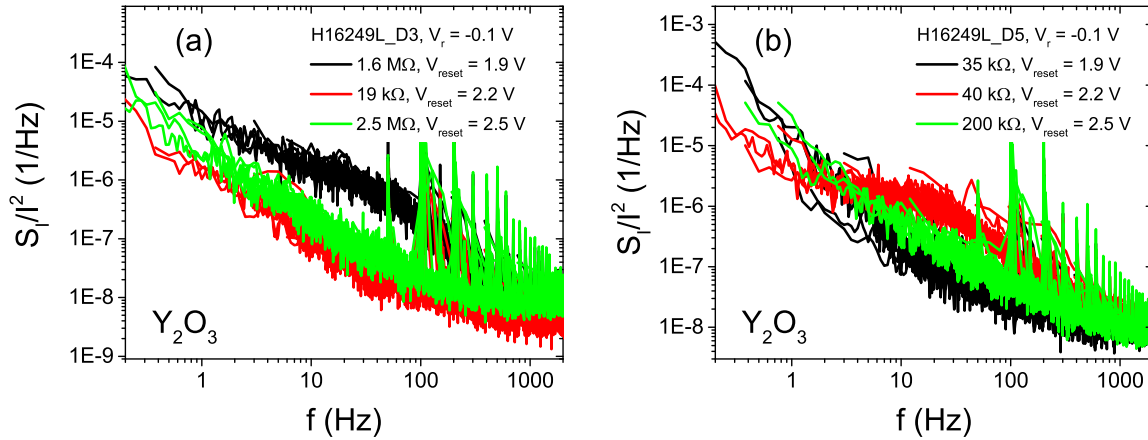


Figure 5.3.10: Normalized current noise PSD against frequency for three different reset voltages measured on two different  $\text{Y}_2\text{O}_3$  RRAM devices.

Finally, the current compliance during the set process was chosen as 10 mA for the bipolar devices. Fig. 5.3.9 (b) illustrates the resistance values in the HRS and in the LRS during the first 30 cycles. It can be seen that, particularly for the HRS, there are considerable variations in the resistance during the first cycles. After 15–20 cycles the conducting filament is assumed to be more stable, which results in less scattered resistance values. Therefore, in view of the implementation of noise measurements, it is advisable to carry out at least 30 cycles after the electroforming step in order to stabilize the filament. In the scope of this thesis work, first noise data on both bipolar and unipolar  $\text{Y}_2\text{O}_3$  RRAM devices was acquired and will be presented in the following.

In Fig. 5.3.10,  $S_I/I^2$  plotted against  $f$  is shown for two different devices as a function of the reset voltage. For the device analyzed in diagram (a), a Lorentzian spectrum is observed for the lowest reset voltage of 1.9 V, while the other spectra are of  $1/f$ -type. By contrast, the device considered in panel (b) yields a Lorentzian-type spectrum at the intermediate reset voltage of 2.2 V, while the other two spectra show a  $1/f$  behavior. In addition, the resistance for the intermediate reset voltage in Fig. 5.3.10 (a) is unexpectedly low, while all other resistances are proportional to the reset voltage. This may be related to instabilities in the conducting filament. Although 30 consecutive cycles through the current-voltage characteristics were performed for the considered sample after the electroforming step and thereby the stability of the resistance values in the HRS has improved significantly (cf. Fig. 5.3.9), the number of cycles prior to the noise measurements will be increased in future studies in order to check for possible improvements.

The occurrence of Lorentzian spectra for both RRAMs and the unexpectedly low resistance for the intermediate reset voltage in panel (a) do not allow to draw unambiguous conclusions. We can only speculate that the scaling of  $S_I/I^2$  with the resistance or reset voltage does not appear to be as strong or systematic as in the case of hafnium oxide based memristors.

Together with the fact that the occurrence of strong RTN or even anomalous RTN in the simultaneously measured time signal  $I(t)$  is considerably more infrequent as compared to hafnia devices, it may be assumed that the current fluctuations in  $Y_2O_3$  have a different origin. This is also supported by results reported in the literature, where several publications affirm that the dominating conduction mechanism in  $Y_2O_3$  is of Schottky type, cf. Refs. [244, 245]. In general, Schottky or thermionic emission is the most commonly observed conduction mechanism in many oxides—especially at relatively high temperature—and is limited by the electrical properties at the electrode-dielectric contact [261]. Here, a crucial parameter is given by the barrier height at the electrode-dielectric interface, which can be overcome by electrons only if enough energy is provided by thermal activation.

While the electric current density  $j_S$  in the case of Schottky emission exhibits an explicit temperature dependence,

$$j_S \propto T^2 \exp\left(A \frac{\sqrt{E}}{T} - B\right), \quad (5.3)$$

there is no temperature dependence of the current density  $j_T$  for the trap-assisted tunneling mechanism:

$$j_T \propto \exp\left(\frac{-A}{E}\right). \quad (5.4)$$

Here,  $A$  and  $B$  are constants and  $E$  represents the electric field [234]. Since trap-assisted tunneling is the main mechanism of electric conduction in hafnium oxide based RRAMs and thus determines the noise characteristics, both the resistance and the noise magnitude exhibit only a weak temperature dependence [33]. On the other hand, as indicated by Eq. (5.3), the resistance and electronic noise in  $Y_2O_3$  are expected to show a strong temperature dependence if Schottky emission is the main conduction mechanism and, unlike in hafnium oxide, the precise microstructure of the conducting filament together with the arrangement of traps are of minor importance. Therefore, future projects will involve comparative temperature-dependent noise measurements on hafnia- and yttria-based RRAMs.

The aforementioned ideas are supported by results on further  $Y_2O_3$  based RRAMs which exhibit a unipolar resistance switching behavior. The current-voltage characteristics of such a device is depicted in 5.3.11 (a) for 11 successive cycles. In contrast to bipolar RRAM devices, the set and reset process both occur at the same polarity for unipolar devices. In the case of unipolar resistance switching, Joule heating is more dominant and leads to a concentration-gradient driven diffusion (according to Fick's law) as well as a temperature gradient driven thermophoresis (Soret effect) [233]. For the present devices which exhibit unipolar switching behavior, the set voltage was chosen as 7 V, while the reset process is performed up to a voltage of 2.5 V. The compliance current during the set process corresponds to  $I = 1$  mA. As for the RRAMs with bipolar switching behavior, it is advisable to carry out a sufficient number of cycles through the current-voltage characteristics in order to stabilize the conducting filament, cf. Fig. 5.3.11 (b).

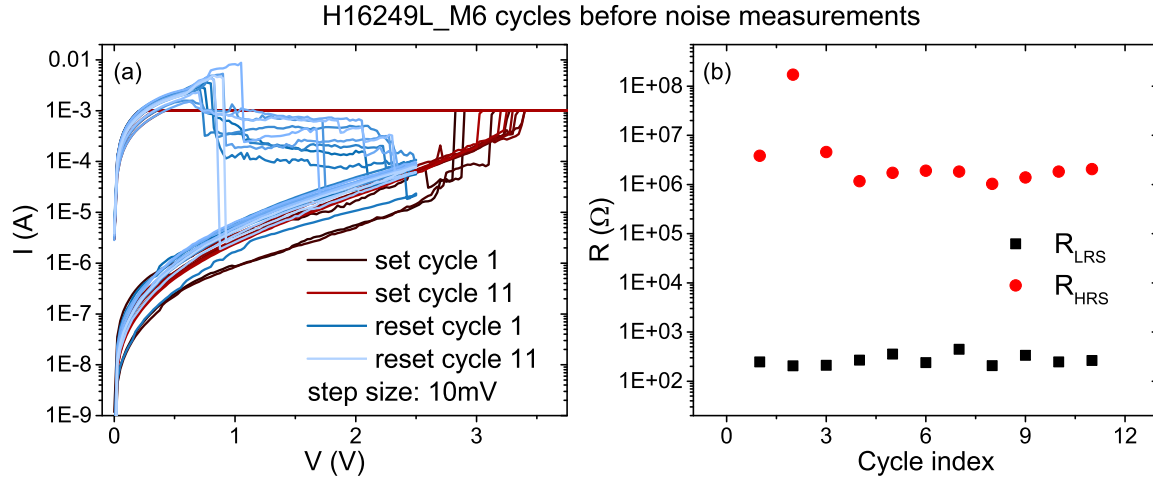


Figure 5.3.11: (a) Current-voltage characteristics of a  $\text{Y}_2\text{O}_3$  RRAM showing unipolar resistance switching (11 cycles). The set voltage corresponds to 7 V, while the reset process is performed up to a voltage of 2.5 V. The compliance current in the set process is 1 mA. (b) Resistance values in the HRS and LRS for 11 successive cycles.

Figure 5.3.12 shows  $1/f$ -type noise spectra with a frequency exponent  $\alpha \approx 1$  at different resistance states, which were achieved by applying different DC readout voltages between 100 mV and 700 mV for two different  $\text{Y}_2\text{O}_3$  devices which exhibit unipolar switching at positive voltages. As observed by V. Maccaronio *et al.* in the case of  $\text{HfO}_2$  RRAMs [262], the current noise PSD  $S_I$  increases as a function of the applied DC readout voltage. By contrast, the normalized current noise PSD  $S_I/I^2$  does not exhibit a significant dependence on the readout voltage (not shown). Due to the agreement with previous results on  $\text{HfO}_2$  [262], the observed noise characteristics in unipolar  $\text{Y}_2\text{O}_3$  devices confirm the assumption that charge transport also happens by means of a conducting filament. However, no clear indications for RTN have been found for any of the resistance states of the two unipolar  $\text{Y}_2\text{O}_3$  devices, which is another indication that a different transport mechanism than trap-assisted tunneling may be present.

Finally, we note that, as for hafnium oxide based devices, future projects will involve the investigation of the noise characteristics in both the HRS and LRS, temperature-dependent measurements of fluctuations in order to gain access to activation energies of the observed two-level processes, and further measurements of the time signal with higher data acquisition rates. In addition, possible device-to-device variations will be studied in future work. In conclusion, the present study has laid a foundation for further noise studies on RRAMs in order to examine the underlying resistance switching processes and the reliability of devices. Since the involved oxide materials are—at least in the HRS—relatively insulating, it was shown that two-terminal current noise spectroscopy is a suitable approach in order to investigate the noise characteristics of RRAM devices. However, as already pointed out

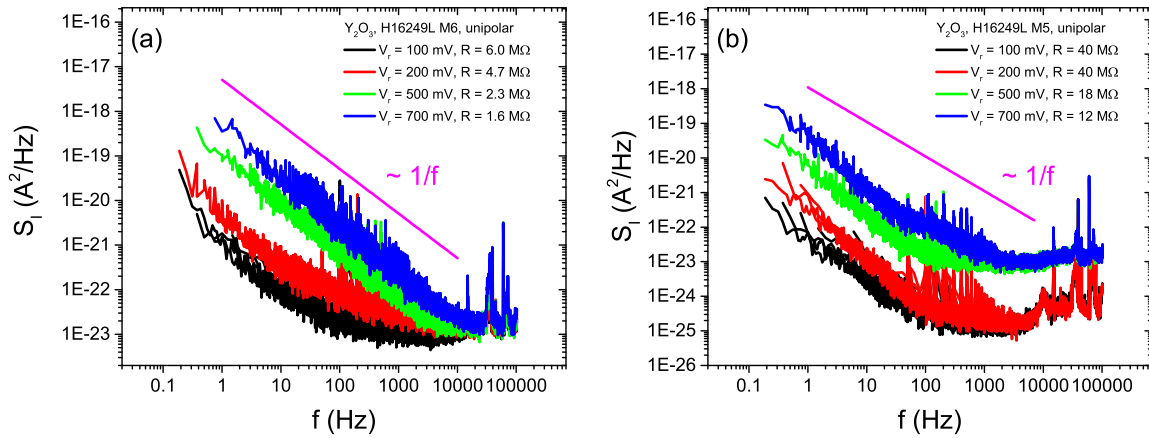


Figure 5.3.12: Current noise PSD plotted against the frequency for two stoichiometric Y<sub>2</sub>O<sub>3</sub> RRAM devices with unipolar switching. The bias voltage  $V_{DC}$  was varied from 100 mV to 700 mV.

in the previous chapters, for some condensed matter systems, entirely different approaches are necessary in order to carry out fluctuation spectroscopy measurements. In the following chapter, we will put the focus on a different class of materials, so-called strongly correlated electron systems, which can exhibit extremely small resistance values, particularly at low temperatures. Consequently, until now, for many of these systems no systematic noise measurements have been carried out, since the  $1/f$  noise magnitude typically scales with the square of the resistance. As will be shown in the following chapter, new approaches for the optimization of the sample geometry allow for a considerable enhancement of the sample resistance and thus for the realization of noise measurements.



## 6 Resistance Fluctuations in Strongly Correlated Electron Systems

In order to calculate the electronic band structure of a material, it is often legitimate to neglect interactions between charge carriers. However, there exist a vast number of materials, so-called strongly correlated electron systems, in which the Coulomb interaction between electrons cannot be treated as being negligibly small. In addition to that, interactions of electrons with local magnetic moments or the atomic lattice can yield an electronic structure which deviates considerably from predictions of non-interacting band calculations. Strongly correlated systems can display a wide range of ground state properties including high-temperature superconductivity [263], multiferroicity [264], unusual metallic and insulating phases [265], and exotic magnetic phenomena such as spin-liquid phases [266].

An intriguing material class in which strong correlations are present are so-called heavy fermion compounds. The term "heavy fermion" was decisively shaped by F. Steglich *et al.* [267] in the context of electronic excitations in  $\text{CeCu}_2\text{Si}_2$  with an electronic density of states 1000 times larger than copper [268]. In general, heavy fermion materials are a subclass of intermetallic compounds, typically containing  $4f$  or  $5f$  elements (e.g., Ce, Yb or U). The term "heavy fermion" comes from the fact that below a characteristic temperature, due to the hybridization of the local  $4f$  or  $5f$  moments with the wave function of the conduction electrons, the latter exhibit an unusually high effective mass, up to several 100 or even 1000 times the mass of a free electron  $m_e$ . At high temperatures, heavy fermion compounds behave like normal metals, implying that the interaction between the  $f$  electrons which possess a local magnetic moment and the conduction electrons is negligible, and the system can be described as a Fermi gas. In contrast, at low temperatures the Fermi liquid theory developed by L. Landau [269] is more appropriate to describe the material properties. As it will be shown further below, the Kondo effect is of major importance in order to understand heavy fermion systems [225].

In this chapter, we will consider the prototypic heavy fermion compound  $\text{YbRh}_2\text{Si}_2$ . This material has been intensively studied over the last fifteen years and has turned out to be an ideal model system for the study of the Kondo effect and quantum criticality. Up until today, there is a lack of experimental studies on the low-frequency noise behavior in heavy fermion systems. The metallic character of these compounds makes fluctuation spectroscopy measurements on clean single crystals extremely difficult. However, the structuring of

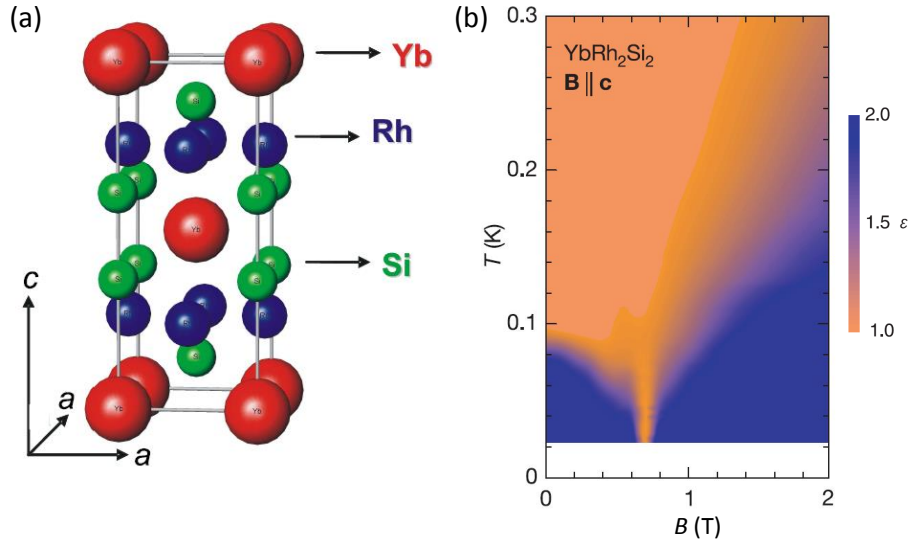


Figure 6.1.1: (a) Tetragonal crystal structure of YbRh<sub>2</sub>Si<sub>2</sub>. From [271]. (b) Temperature-field phase diagram showing the evolution of  $\epsilon$ , the exponent in  $\Delta\rho(T) = [\rho(T) - \rho_0] \propto T^\epsilon$ . After [272] with permission of Springer Nature.

YbRh<sub>2</sub>Si<sub>2</sub> single crystals by means of a focused ion beam allows for a substantial enhancement of the sample resistance. Consequently, it becomes possible to study the intrinsic resistance fluctuations in a heavy fermion system.

The present chapter is devoted to the study of low-frequency charge carrier dynamics in single crystalline YbRh<sub>2</sub>Si<sub>2</sub>. Initially, the most important material properties will be introduced and the current state of research will be presented. Subsequently, the focused ion beam structuring process will be described. Finally, the obtained electronic transport results will be discussed and an outlook to further projects will conclude the chapter.

## 6.1 The heavy fermion compound YbRh<sub>2</sub>Si<sub>2</sub>

### 6.1.1 Introduction

As schematically depicted in Fig. 6.1.1 (a), YbRh<sub>2</sub>Si<sub>2</sub> crystallizes in a tetragonal ThCr<sub>2</sub>Si<sub>2</sub> structure [270]. It is a clean and stoichiometric material that is well characterized. This compound exhibits a weak antiferromagnetic order below a Néel temperature of  $T_N = 70$  mK. Importantly, the application of small magnetic fields which suppress the antiferromagnetic order induces a quantum critical point (QCP). Generally, a phase transition at zero temperature driven by a non-thermal control parameter is considered a quantum phase transition. If the phase transition is continuous, i.e., of second order, a QCP can be observed. The QCP results solely from quantum fluctuations, since thermal fluctuations are cut off for  $T \rightarrow 0$ .



The quantum-critical state is distinct from the phases on both sides, and is expected to exhibit features in its physical properties which are universal [273]. The magnetic field  $B$  is an ideal control parameter for tuning a material as close as possible to a QCP. As indicated in Fig. 6.1.1 (b), the antiferromagnetic order is entirely suppressed at a critical field  $B_c = 0.66$  T, when the field is applied parallel to the crystallographic  $c$  axis [270]. In the case of a magnetic field applied perpendicular to the  $c$  axis,  $B_c = 0.06$  T.

Other tuning parameters than the magnetic field can be the chemical composition or pressure. In general, a large number of  $f$ -electron systems show considerable deviations from the properties of a conventional Landau-Fermi liquid behavior when they are tuned through a QCP. For a zero-field QCP which is tuned by doping or pressure, close to the point at which  $T_N \rightarrow 0$ , the occurrence of spin fluctuations mediating the interactions between the heavy quasiparticles leads to strongly temperature-dependent quasiparticle masses and quasiparticle-quasiparticle scattering cross sections, and thus to deviations from a Landau-Fermi liquid behavior [270, 274, 275]. The controversially discussed scenarios for field-induced QCPs will be presented further below.

A physical quantity which is sensitive to possible deviations from a Landau-Fermi liquid behavior is, for instance, the resistivity  $\Delta\rho(T) = [\rho(T) - \rho_0] \propto T^\epsilon$ , where  $\rho_0$  denotes the temperature-independent residual resistivity and  $\epsilon$  is a characteristic exponent. As shown in Fig. 6.1.1 (b) for the case of YbRh<sub>2</sub>Si<sub>2</sub>, at  $B > B_c$  a field-induced Landau-Fermi liquid state characterized by  $\epsilon = 2$  is found to occur below a certain crossover temperature  $T_0(B)$  which grows linearly as a function of  $B$  (blue region). Strikingly, a non-Fermi liquid behavior, characterized by  $\epsilon = 1$  (orange region), occurs at very low  $T$ , right at the quantum critical point ( $B = B_c$ ) and in an extended field range at higher  $T$ . A further physical quantity sensitive to deviations from Landau-Fermi liquid behavior is the electronic specific heat  $C_{el}(T)$  [270, 274].

### 6.1.2 Kondo effect and crystal electric field

At intermediate temperatures between 10 K and 300 K, the properties of YbRh<sub>2</sub>Si<sub>2</sub> are determined by a competition of crystal electric field excitations and the Kondo interaction [276], whereas the previously described non-Fermi liquid behavior dominates below 10 K. Due to the crystal electric field, the  $4f^{13}$  multiplet of the Yb<sup>3+</sup> ions is split into four doublets at energies corresponding to 0–17–25–43 meV [277]. This splitting of electron orbital states originates from a static electric field produced by a surrounding charge distribution, i.e., the neighboring ions. Besides the crystal field splitting, the Kondo effect plays an important role in YbRh<sub>2</sub>Si<sub>2</sub>. In general, the Kondo interaction describes the antiferromagnetic exchange coupling between a local magnetic moment and the spins of the conduction electrons, where the ground state corresponds to a so-called Kondo singlet (total spin  $S = 0$ ), which is energetically more favorable than the triplet state ( $S = 1$ ). The Kondo temperature  $T_K$  indicates the energy difference between the singlet and the triplet states. At low temperatures  $T \ll T_K$ , only the

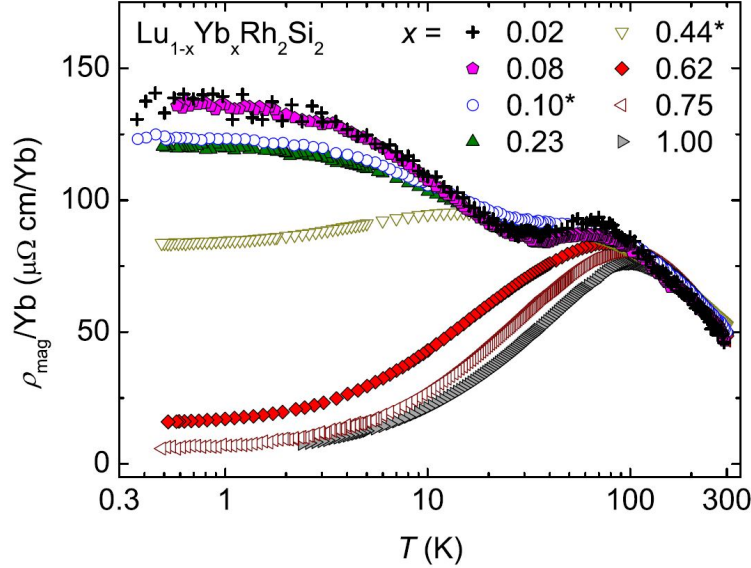


Figure 6.1.2: Plot of the magnetic contribution  $\rho_{\text{mag}}(T)$  to the resistivity of  $\text{Lu}_{1-x}\text{Yb}_x\text{Rh}_2\text{Si}_2$  clarifying the evolution from a diluted to a dense Kondo system. Content reprinted from Ref. [276] with permission of the American Physical Society.

singlet state will be occupied and excitations in the meV range are possible, whereas at higher temperatures singlet and triplet states will be equally occupied. In other words, a screening of the local magnetic moments occurs at low temperatures. Originally, an anomalous increase in the resistance of metals was observed at low temperatures and ascribed to the presence of magnetic impurities, which serve as scattering centers for the conduction electrons. J. Kondo was the first to describe this unusual temperature dependence theoretically [225]. In the case of  $\text{YbRh}_2\text{Si}_2$ , the (single-ion) Kondo temperature below which a formation of composite quasiparticles emerges has been determined as  $T_K \approx 25$  K [276, 278, 279]. However, the exact value is still under debate.

Studies of the electrical resistivity on  $\text{Lu}_{1-x}\text{Yb}_x\text{Rh}_2\text{Si}_2$  have revealed further details about the interplay of Kondo physics and crystal electric field splitting in this heavy fermion compound. Figure 6.1.2 shows the magnetic contribution  $\rho_{\text{mag}}(T)$  to the resistivity, which was calculated by subtracting the data of the nonmagnetic reference compound  $\text{LuRh}_2\text{Si}_2$  and a sample-dependent disorder term [276]. The quantity  $\rho_{\text{mag}}(T)$  shows the evolution from a diluted to a dense Kondo system. Firstly, a logarithmic increase is observed above 100 K for all samples upon cooling. Subsequently, samples with low Yb concentrations ( $x \leq 0.23$ ) display a plateau around 60–100 K, which is followed by a further increase towards low temperatures. Finally,  $\rho_{\text{mag}}(T)$  saturates below 4 K. This behavior can be explained by Kondo scattering off the ground-state doublet of the  $\text{Yb}^{3+}$  ions [225].

In contrast to that, specimens with high Yb doping  $x \geq 0.62$  show a maximum in  $\rho_{\text{mag}}(T)$  between 70 K and 100 K, which is followed by a monotonic decrease towards lower temper-

atures. This decrease can be attributed to the development of coherence due to a higher density of local magnetic moments, which can be viewed as being arranged in a so-called Kondo lattice. More precisely, in this regime, electron waves scattered from individual Kondo ions interfere coherently and form a narrow band of heavy electrons. To summarize, it is widely believed that the plateau or maximum between 70 K and 100 K originates from the onset of coherence between screened magnetic sites, but, however, in the case of  $\text{YbRh}_2\text{Si}_2$ , crystal electric field effects also influence this feature and can shift the maximum to higher temperatures [280, 281].

### 6.1.3 Nature of quantum criticality in $\text{YbRh}_2\text{Si}_2$

In heavy fermion materials, the energy scale of the Kondo effect is typically similar to the RKKY interaction described in Sec. 4.2.1. In contrast to Kondo screening, where the conduction electrons weaken the interaction between adjacent magnetic moments, the RKKY interaction exploits the conduction electrons to strengthen the tendency to magnetic order. Due to the competition of Kondo screening and RKKY interaction, the ground state of a heavy fermion material can usually be shifted between magnetic and nonmagnetic variants by means of various tuning parameters, giving rise to a quantum critical behavior.

Phenomenologically, the interplay of the Kondo and RKKY interaction has been described by S. Doniach [282]. In a mean-field approximation of the periodic Anderson model it was shown that for a one-dimensional system of coupled localized spins there exists a critical value  $\Gamma_c$ , which separates a magnetically ordered ground state from a disordered one. This results from the different relationship between the competing interactions and the hybridization strength  $\Gamma$ , which is a measure for the hybridization between  $4f$  and conduction electrons, and can be generally tuned by external parameters, such as pressure or doping. While the RKKY interaction shows a quadratic dependence of  $\Gamma$ ,

$$T_{\text{RKKY}} \propto N(E_F) |\Gamma|^2, \quad (6.1)$$

the Kondo temperature  $T_K$  follows an exponential behavior,

$$T_K \propto \exp(-1/|\Gamma N(E_F)|), \quad (6.2)$$

where  $N(E_F)$  corresponds to the density of conduction-electron states. Therefore, a magnetically ordered ground state is observed for  $\Gamma < \Gamma_c$ , since the RKKY interaction dominates in this range. In contrast, for  $\Gamma > \Gamma_c$  the Kondo interaction leads to a screening of the local magnetic moments by the conduction electrons and thus to a paramagnetic ground state. The resulting phase diagram is illustrated in Fig. 6.1.3. Here,  $T_K$  and  $T_{\text{RKKY}}$  are plotted against  $\Gamma$  (red and green curve, respectively). The ordered antiferromagnetic (AFM) phase and the Landau-Fermi liquid (LFL) phase are separated by a quantum critical point at  $T = 0$  and

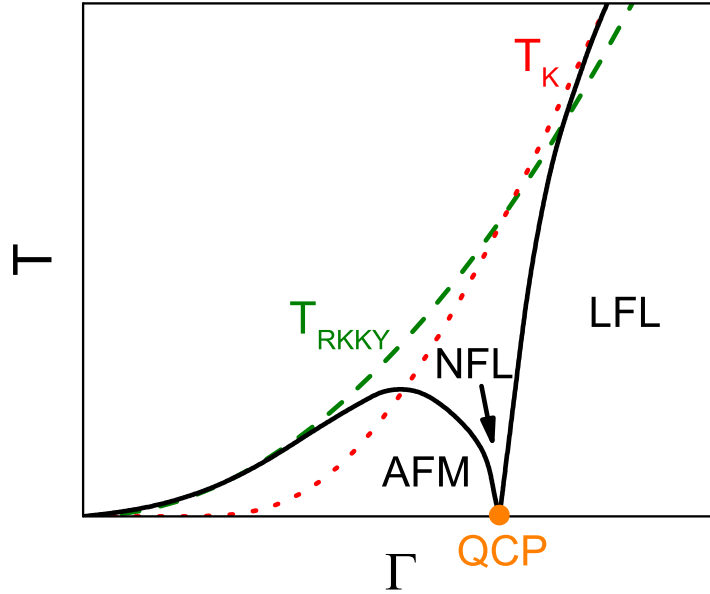


Figure 6.1.3: Phase diagram of heavy fermion systems after S. Doniach [282].  $T_K$  and  $T_{\text{RKKY}}$  are plotted against the hybridization strength  $\Gamma$ . The antiferromagnetic (AFM) and the Landau-Fermi liquid (LFL) phase are separated by a quantum critical point (QCP) at  $T = 0$ . In addition, non-Fermi liquid (NFL) behavior is also indicated.

$\Gamma = \Gamma_c$ , where the critical fluctuations are characterized by the spatial fluctuations of the order parameter. In the vicinity of the QCP, a non-Fermi liquid (NFL) phase is indicated. In case that an external magnetic field leads to a stronger suppression of magnetic order than of the competing Kondo effect, the QCP can be induced by a magnetic field.

Generally, in a Kondo lattice, the interplay between localized spins and itinerant electrons leads to a huge density of states at the Fermi energy, the so-called Kondo resonance [273, 283, 284]. Besides the magnitude of the density of states, the Kondo effect can also affect the momentum dependence of the quasiparticles, i.e., the shape and size of the Fermi surface. Scanning tunneling microscopy (STM) [285] and angle-resolved photoemission spectroscopy (ARPES) [281] studies demonstrate that the large Fermi surface of  $\text{YbRh}_2\text{Si}_2$  does not change its size or shape in a wide temperature range extending from well below to far above the Kondo temperature. This stands in stark contrast to the widely believed evolution from a large Fermi surface, including the  $4f$  degrees of freedom, to a small Fermi surface upon increasing the temperature. However, it is also conceivable that the formation of the large Fermi surface takes place at higher temperatures than the onset of coherence [281].

We now focus on the characteristics of the Fermi surface at very low temperatures. While the heavy quasiparticles stay intact at the QCP in the case of the conventional spin-density wave scenario, they disintegrate in the so-called Kondo-breakdown scenario, which is related to a discontinuous change of the Fermi surface. However, it is not clear whether all antiferro-

magnetic heavy fermion QCPs fall into one of the two aforementioned categories, and even for YbRh<sub>2</sub>Si<sub>2</sub> there exist conflicting views in the literature. On the one hand, the observation of a large Fermi surface in a large temperature range from 1 to 100 K [281] supports a spin-density wave scenario for the QCP in YbRh<sub>2</sub>Si<sub>2</sub>. In general, a spin-density wave corresponds to a spontaneous spatial modulation of the spins of the charge carriers in a system. A spin-density wave picture is typically applied for itinerant *d*-electron based metals and for heavy fermion metals, in which the heavy charge carriers behave like *d* electrons [286]. This concept can be viewed as a quantum generalization of the Ginzburg-Landau-Wilson theory of finite-temperature phase transitions [287, 275]. On the other hand, transport and thermodynamic properties observed in the vicinity of the QCP indicate a Kondo breakdown scenario for the case of YbRh<sub>2</sub>Si<sub>2</sub>, which goes beyond the standard theory of order-parameter fluctuations. For this type of QCP, strong low-dimensional spin fluctuations are assumed to cause a critical destruction of the heavy fermions, i.e., the propagating Kondo singlets [286]. In detail, the Kondo effect is critically destroyed because the local moments are coupled not only to the conduction electrons, but also to the magnetic fluctuations of other local moments. These fluctuations act as a source of dissipation and thus cause a decoherence of the Kondo effect [273].

Hall effect measurements turned out to be of major importance in order to understand the nature of the QCP. Since anomalous contributions are negligible at low temperatures, the Hall coefficient  $R_H$  is directly related to the volume enclosed by the Fermi surface [288, 289]. S. Paschen *et al.* have shown that  $R_H$  displays a crossover linked to the QCP, which sharpens to a discontinuous jump in the extrapolation to zero temperature [288]. Thus the idea of a sudden change of the Fermi surface and a Kondo-breakdown scenario are supported by these Hall effect measurements. However, the assumption that the Hall coefficient  $R_H$  is inversely proportional to the carrier concentration is only valid in the case of a spherical Fermi surface with a single band at the Fermi energy  $E_F$ , which is certainly not the case for YbRh<sub>2</sub>Si<sub>2</sub> as deduced from band-structure calculations and photoemission studies [290]. For this material, theoretical calculations yield multiple bands crossing  $E_F$  with canceling positive and negative contributions to  $R_H$  [289]. In contrast to simple metals, for which the Hall coefficient does not depend on the magnetic field, in more complex materials a change of the Fermi surface topology induced by the external magnetic field may lead to nonlinearities in  $R_H$ . Therefore, it is often useful to calculate the differential Hall coefficient [291]

$$\tilde{R}_H(B) = \partial \rho_H(B) / \partial B. \quad (6.3)$$

Figure 6.1.4 shows the experimentally determined behavior of  $R_H$  as a function of temperature for various YbRh<sub>2</sub>Si<sub>2</sub> single crystals. In this case, the linear-response Hall coefficient  $R_H$  was derived as the slope of linear fits to the Hall resistivity  $\rho_H$  for fields  $B \leq 0.4$  T. A minimum in  $R_H(T)$  can be observed in the same temperature range where the resistivity  $\rho(T)$  displays

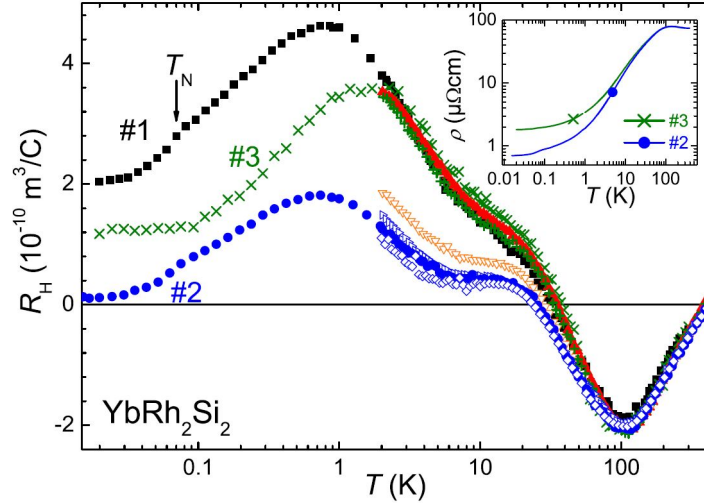


Figure 6.1.4: Temperature dependence of the Hall coefficient  $R_H$  for different  $\text{YbRh}_2\text{Si}_2$  single crystals. Results for samples of the same batch are shown in identical color. Arrow indicates  $T_N$ . Inset: Resistivity of two selected samples. Content reprinted from Ref. [289] with permission of the American Physical Society.

a maximum, i.e., at about 100–120 K. This minimum is ascribed to the anomalous Hall effect arising from skew scattering, since

$$R_H = R_0 + C\rho\chi, \quad (6.4)$$

where  $R_0$  is the normal Hall coefficient,  $C$  is a constant,  $\rho$  the resistivity and  $\chi$  the magnetic susceptibility [292]. Here, the term  $C\rho\chi$  corresponds to the anomalous Hall effect due to intrinsic scattering. An extensive review of the Hall effect in heavy fermion metals can be found in Ref. [291]. After S. Paschen *et al.*, Eq. (6.4) holds between between 7 K and 300 K in the case of  $\text{YbRh}_2\text{Si}_2$  [288]. Furthermore, the intrinsic anomalous contribution is negligible below 1 K. Generally, in addition to that, a further temperature-independent extrinsic anomalous Hall coefficient  $R_{\text{ex}}$  due to skew scattering by residual defects has to be considered, but is negligible for the considered samples. Consequently, the initial-slope Hall coefficient  $R_H$  is found to be free of any anomalous contribution below 1 K, which would typically lead to a flat behavior of  $R_H(T)$ . However, between 70 mK and 7 K, there exists an additional contribution  $\Delta R_H$  which manifests itself in the form of a pronounced maximum in  $R_H(T)$  and does not stem from the anomalous Hall effect, but instead can be attributed to fluctuations of the Fermi surface volume [288].

Below 50 K, a strong sample dependence can be observed. Between 30 K and 40 K, the sign of  $R_H(T)$  changes from negative to positive. As can be seen in Fig. 6.1.4, samples 1 and 3 display a shoulder around 15 K, whereas the Hall coefficient of sample 2 shows a plateau around this temperature range. All samples show a maximum in  $R_H(T)$  around 1 K, which is assigned to

the quantum critical spin fluctuations. At similar temperatures, nuclear magnetic resonance (NMR) measurements revealed antiferromagnetic fluctuations to be present [293]. Finally, all samples show a saturation of  $R_H(T)$  at the lowest temperatures. Sample differences are assumed to arise from slight variations during the crystal growth. In detail, the actual value of  $R_H(T)$  depends sensitively on the ratio of the scattering rates of the individual two bands, which are of opposite character and almost compensate each other [289]. Therefore, the sample dependences are assumed to be related to changes in the relative scattering rates.

Finally, it should be mentioned that quantum critical behavior and unconventional superconductivity are often found in close vicinity in the class of heavy fermion materials. For instance,  $\text{CeCu}_2\text{Si}_2$  is considered the first material in which superconductivity was observed in an inherently magnetic environment [267]. In the case of  $\text{YbRh}_2\text{Si}_2$ , heavy-electron superconductivity has been observed very recently by E. Schuberth *et al.* with a concomitantly emerging nuclear antiferromagnetic order slightly above 2 mK, i.e., at extremely low temperatures [294].

Besides standard resistivity and Hall effect measurements, fluctuation spectroscopy may provide further insight into charge carrier dynamics related to the interplay between the Kondo lattice, crystal electric field excitations and quantum criticality in  $\text{YbRh}_2\text{Si}_2$ . In this context, the structuring of  $\text{YbRh}_2\text{Si}_2$  single crystals by means of a focused ion beam allows for an investigation of the noise properties of a heavy fermion system. In the following section, it will be described how the resistance of a single-crystalline sample can be increased in order to reveal  $1/f$ -type fluctuations and thus overcome the thermal noise background of the experimental setup.

## 6.2 Sample geometry optimization and preparation

In order to facilitate resistance noise measurements of low-resistive samples, a first approach is given by cutting or polishing the sample with the aim of enhancing its resistance. In general, Hooge's law (Eq. (2.35)) implies that

$$S_V \propto \frac{V^2}{\Omega} \propto \frac{R^2}{\Omega} = \frac{(\rho l/A)^2}{lA} \propto \frac{l}{A^3}, \quad (6.5)$$

where  $\Omega$  corresponds to the sample volume,  $l$  denotes the length of the sample,  $A$  the cross-sectional area and  $\rho$  the resistivity. Therefore, it is beneficial to cut the sample in such a way that the length  $l$  is maximized, while the cross-sectional area  $A$  is reduced. As a consequence, polishing a single crystal to a thin platelet can already lead to a significant enhancement of the resistance. This was successfully demonstrated in the bachelor's thesis of T. Hagen, which was carried out in the scope of the present work and focused on single crystals of the predicted topological Kondo insulator  $\text{SmB}_6$  [295]. Here, simultaneously with the work of S. Biswas *et al.* [296], the very first noise measurements on a predicted topological insulator

were carried out. Although in this case it was sufficient to polish a single crystal to a thin platelet, a rod- or wire-type geometry is generally preferred after Eq. (6.5). An example is given by the noise studies on the ferromagnetic semimetal  $\text{EuB}_6$  [5, 73]. However, in the case of the heavy-fermion system  $\text{YbRh}_2\text{Si}_2$ , the resistance of single crystals is typically far too low in order to allow for noise measurements, which is why a new method of geometry optimization will be presented in the following.

The investigated  $\text{YbRh}_2\text{Si}_2$  single crystal was synthesized in the group of Prof. Dr. C. Krellner at the Goethe University Frankfurt by applying an indium-flux-growth technique as described in Refs. [270, 297]. The subsequent sample preparation process has been performed in the group of Dr. M. Brando at the Max Planck Institute for Chemical Physics of Solids in Dresden. A similar process was performed at the Goethe University Frankfurt in collaboration with the group of Prof. Dr. M. Huth for a  $\text{MnSi}$  single crystal, which had also been grown in the group of Prof. Dr. C. Krellner. Although electronic transport investigations on  $\text{MnSi}$  are beyond the scope of the present thesis work, the following description is based on the attempts on  $\text{MnSi}$ , but, importantly, is equivalent to the preparation process performed in Dresden.

After the growth and polishing of the sample, the single crystal is embedded into an epoxy (e.g., Araldite), a sufficient amount of which has been spread on an insulating substrate such as a piece of a GaAs or Si wafer. The crystal is required to be immersed into the epoxy in such a way that the upper side of the sample remains free and is aligned with the surface of the epoxy drop. The choice of a suitable epoxy is of major importance in order to ensure a good balance between its frictional force and the gravitational force pulling the sample downwards. The aforementioned arrangement allows to deposit several thin gold contacts by means of a thermal evaporator. For this purpose, the crystal and the surrounding epoxy are covered with aluminum foil acting as a shadow mask, except a small region on which the desired gold contact will be evaporated. Since the lateral dimensions of the crystal are typically very small, it is difficult to cut and attach appropriate pieces of aluminum foil, and thus it is advisable to deposit each gold contact individually. After a successful deposition procedure, the substrate with the sample on top of it is attached to a sample holder with GE low-temperature varnish and electrical contacts are made by gold wires which are fixed by using conductive silver paste or soldering. As the next step, a meander-shaped geometry is etched into the crystal by means of a high-energy focused ion beam (FIB) inside a standard scanning electron microscope system. In the case of the polished  $\text{MnSi}$  platelet with a thickness of only about  $10\ \mu\text{m}$ , a gallium FIB has been utilized with an acceleration voltage and ion beam current of 30 kV and 20 nA, respectively. The structure is designed in such a way that the only possible current path through the crystal will be given by the specified meander tracks. Therefore, since the effective length of the sample is drastically increased while the cross-sectional area is reduced, the total resistance can be strongly enhanced. In other words, a higher number and a lower thickness of the meanders will both lead to a



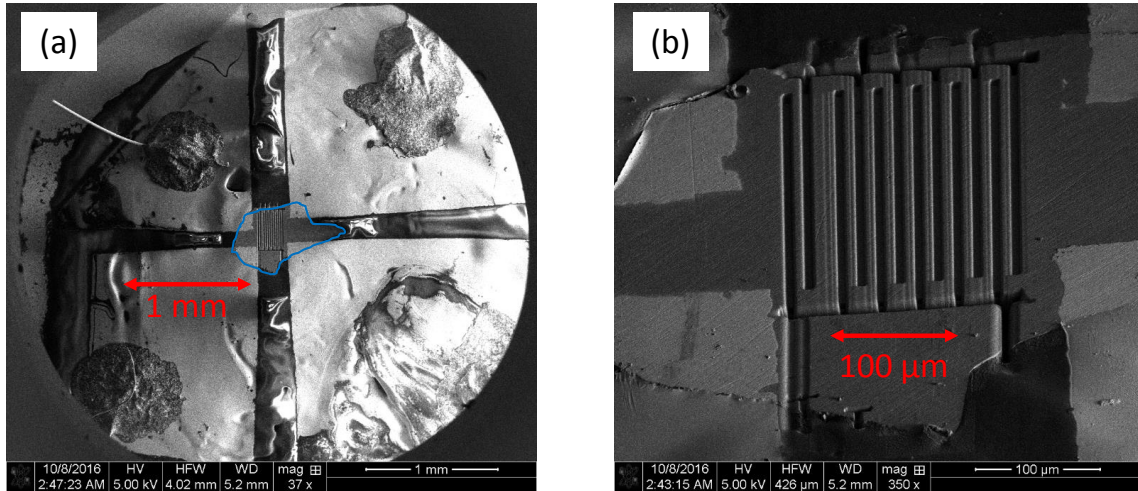


Figure 6.2.1: Exemplary scanning electron microscope images of an electrically contacted MnSi single crystal with a meander-shaped geometry created by means of a focused ion beam. In panel (a), the blue line clarifies the sample contours. Pictures by courtesy of R. Sachser from the group of Prof. Dr. M. Huth (Goethe University Frankfurt).

higher resistance. Here, the defined current path consists of 11 straight wire-like segments with dimensions of about  $300 \mu\text{m} \times 5 \mu\text{m}$  each. The duration of the FIB etching process was nearly 7 h. Moreover, the pitch was 213.5 nm, the dwell time was set to  $1 \mu\text{s}$  and the number of passes was 74617 [298]. Importantly, the resistance can be read out in situ during the etching process in order to verify a smooth operation. Fig. 6.2.1 contains two exemplary scanning electron microscope images of an electrically contacted MnSi single crystal. In Fig. 6.2.1 (a), the four symmetrically arranged gold contacts are visible. The single crystal is located in the center of the image and the meanders are further magnified in Fig. 6.2.1 (b). Note that the blue line in panel (a) clarifies the sample contours.

This procedure has been the first approach of generating a meander geometry in a single crystal at the Goethe University Frankfurt, but in spite of further subsequent FIB etching processes with ion beam currents of 1 nA, the resistance of the present MnSi sample has not increased as expected. We assume that, due to an incomplete removal or redeposition of MnSi, the meander-shaped structure depicted in Fig. 6.2.1 is electrically shorted in some way. It will be a matter of future studies to further establish this procedure in Frankfurt.

In contrast to MnSi, in the case of  $\text{YbRh}_2\text{Si}_2$ , a patterned sample has been provided by the group of Dr. M. Brando from the Max Planck Institute for Chemical Physics of Solids in Dresden. Although first patterning approaches were also made by utilizing a Ga FIB, the sample considered in the present work was structured by means of a Xe plasma FIB. Apart from the facilitation of noise measurements, the patterning of an  $\text{YbRh}_2\text{Si}_2$  single crystal by means of FIB etching allows for precise resistance measurements even below temperatures

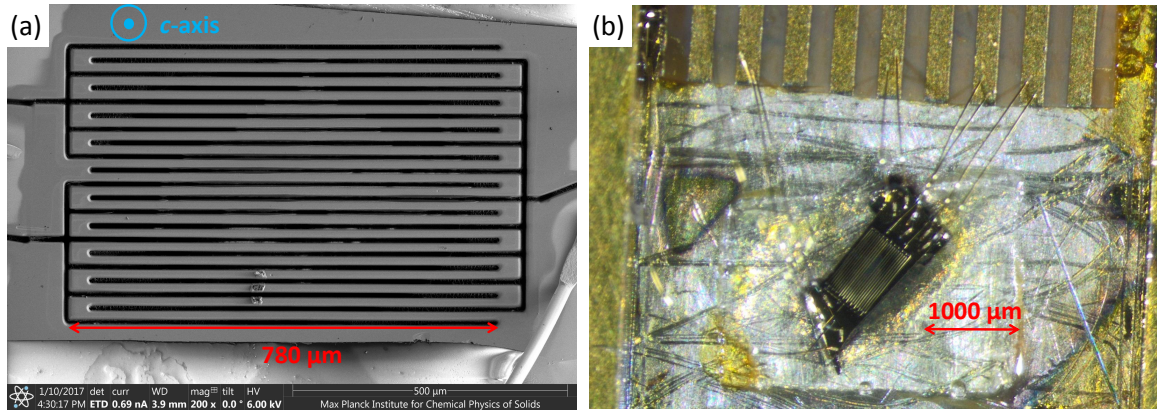


Figure 6.2.2: (a) Electron microscope image of an  $\text{YbRh}_2\text{Si}_2$  single crystal with a meander-shaped geometry created by means of a focused ion beam. The direction of the crystallographic  $c$  axis is also shown. (b) Optical microscope image providing an overview over the connections of all five electrical contacts to the sample. Pictures by courtesy of Dr. A. Steppke from the Max Planck Institute for Chemical Physics of Solids in Dresden.

of 10 mK, where standard four-terminal measurements on as-grown single crystals fail due to the extremely small residual resistivity. Although a possible alternative to standard four-terminal resistance measurements appears to be given by measurements of the Johnson noise originating from the sample [299], this method requires relatively high sample resistances, which, however, in reality are typically smaller than the contact resistances. Therefore, the geometrical optimization of the single crystal is a crucial step in order to allow for high-resolution electronic transport measurements at low temperatures, e.g., around the superconducting transition in  $\text{YbRh}_2\text{Si}_2$ . Alternative microstructuring methods including milling or laser cutting are more flexible, but, however, exhibit clear disadvantages compared to focused ion beam etching. For instance, laser cutting causes parts of the crystal to melt and thus leads to changes of the crystalline structure due to the high amount of introduced heat power. On the other hand, milling also potentially damages the crystal and, moreover, does not allow for such small channel widths as compared to FIB etching [300]. As also reported in a work by P. Moll *et al.* on the structuring of thin  $\text{PdCoO}_2$  platelets [301], FIB etching is a suitable tool in order to shape samples on micrometer dimensions without altering their physical properties.

Electron and optical microscope images of the patterned  $\text{YbRh}_2\text{Si}_2$  sample are shown in Fig. 6.2.2. Figure 6.2.2 (a) shows an electron microscope image of the meander tracks. The meander structure consists of 20 straight wire-like segments with dimensions of  $L \times W \approx 800 \mu\text{m} \times 15 \mu\text{m}$  each, resulting in a total wire length of approximately 16 mm. The original size of the flat  $\text{YbRh}_2\text{Si}_2$  crystal is  $L \times W \approx 2 \text{ mm} \times 1 \text{ mm}$ . Furthermore, the determined thickness of the platelet ranges from  $12 \mu\text{m}$  to  $17 \mu\text{m}$ . The optical microscope picture in Fig.

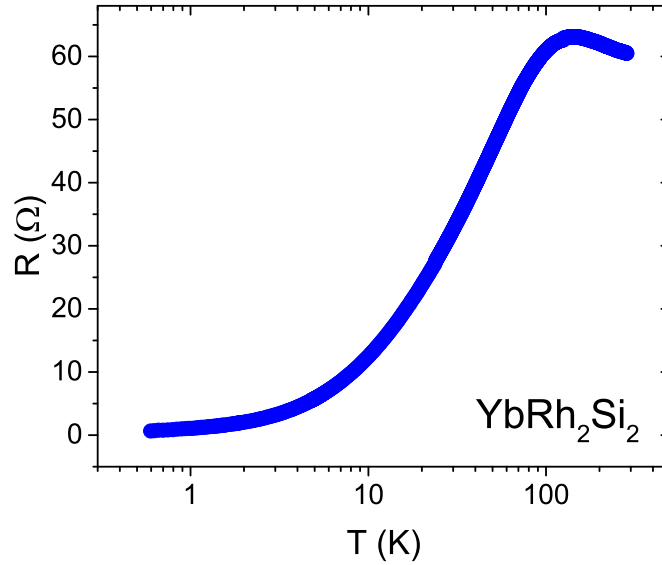


Figure 6.2.3: Resistance  $R$  plotted against the temperature  $T$  between 0.6 K and 285 K for the  $\text{YbRh}_2\text{Si}_2$  sample with a meander-shaped geometry. Clearly, the magnitude of the absolute resistance is considerably higher than for standard single-crystalline samples, while the qualitative behavior remains the same.

6.2.2 (b) gives an overview of the sample and its electrical connections. It can be seen that, in contrast to the  $\text{MnSi}$  single crystal shown in Fig. 6.2.1, there is a further middle contact which may be used for five-terminal AC noise measurements, cf. Sec. 3.2.4. As clarified in Fig. 6.2.2 (b), the wires leading away from the sample were connected to conducting gold tracks by means of ultrasonic bonding, which are then connected to the sample holder by further wires (not shown). Despite the fifth contact, all noise measurements presented in the subsequent section were performed in a four-terminal AC configuration, since a further connection between the arrangement shown in Fig. 6.2.2 (b) and the sample holder would have been required. Finally, it should be mentioned that, since  $\text{YbRh}_2\text{Si}_2$  single crystals are grown as platelets in the crystallographic  $a$ - $b$  plane, the  $c$  axis is oriented perpendicular to the platelet plane as indicated in Fig. 6.2.2 (a).

The resistance of the structured  $\text{YbRh}_2\text{Si}_2$  crystal is depicted in Fig. 6.2.3 between 0.6 K and 285 K. As can be seen, the absolute resistance is significantly higher than for standard single crystals of  $\text{YbRh}_2\text{Si}_2$ , where typical values of  $R$  are found to be considerably lower than 0.1  $\Omega$  at room temperature. Therefore, the FIB structuring technique allows for an enhancement of the resistance by at least two or three orders of magnitude, which, particularly with regard to noise measurements, where  $S_R \propto R^2$ , constitutes an enormous difference. As expected for FIB-etched samples, the qualitative behavior remains the same, i.e., an increase of  $R(T)$  is observed between room temperature and  $\sim 130$  K, where a maximum occurs. As discussed in Sec. 6.1.2, this maximum originates from the development of coherence between screened magnetic

sites, but it is also influenced by crystal electric field splitting. Upon further cooling the resistance decreases to values of less than  $1\ \Omega$  at the lowest temperatures. It should be noted that at higher temperatures parallel conductivity through the Si substrate may lead to the observation that the resistance data for bulk samples and structured crystals do not perfectly scale. However, since the substrate becomes strongly insulating at low temperatures, the signatures of the quantum critical point and the antiferromagnetic phase do not change significantly compared to other single-crystalline samples [300]. The residual-resistance ratio (RRR), which usually is defined as the ratio of the resistance at room temperature and the extrapolated value at 0 K, can—in the case of the considered meander structure—be approximated as

$$\text{RRR} = \frac{R(300\ \text{K})}{R(0\ \text{K})} \approx \frac{R(285\ \text{K})}{R(0.6\ \text{K})} = \frac{60.5\ \Omega}{0.67\ \Omega} \approx 90. \quad (6.6)$$

Compared to the RRR of other  $\text{YbRh}_2\text{Si}_2$  single crystals from Ref. [271], where the resistance at room temperature was divided by the resistance at the lowest measured temperature of  $T = 17\ \text{mK}$  and values of 40, 70, and 120 were obtained, the estimated RRR of the present sample can be classified as very high and thus the crystal is of excellent quality. In the following section, the electronic noise characteristics of the investigated  $\text{YbRh}_2\text{Si}_2$  meander sample will be presented and analyzed in detail.

### 6.3 Fluctuation spectroscopy results

Fluctuation spectroscopy measurements on low-resistive samples such as  $\text{YbRh}_2\text{Si}_2$  are extremely difficult because even at high current densities the observed noise spectra only reflect the background noise of the experimental setup. However, as demonstrated in Fig. 6.3.1, the noise spectra measured on the structured  $\text{YbRh}_2\text{Si}_2$  single crystal are clearly of  $1/f$ -type. In panel (a), the voltage noise PSD  $S_V$  is plotted as a function of frequency for various currents at a temperature of 25 K, where the sample resistance is only  $28.5\ \Omega$ . As expected, there is a current-dependent shift of the  $1/f$  noise spectra, which clearly lie above the background noise (blue curve) below 1 Hz.

Although the resistance of this structured sample is considerably higher than the one of standard single crystals, relatively high currents of several hundred microamperes are still required in order to detect and shift the  $1/f$  spectrum above the background noise. As proven in Fig. 6.3.1 (b), where  $S_R = S_V/I^2$  is plotted for three different currents and all spectra lie on top of each other at low frequencies, the scaling of the noise is in good agreement with Hooge's law (see Eq. (2.35)). All noise measurements presented in this section were performed in a four-terminal AC configuration using the SR554 preamplifier, which constitutes an appropriate choice for low-resistive samples (see Fig. 3.2.4 in Sec. 3.2.2).

An overview of the temperature-dependent noise characteristics is given in Fig. 6.3.2. In detail, Fig. 6.3.2 (a) shows the normalized resistance noise PSD  $S_R/R^2$  evaluated at 1 Hz

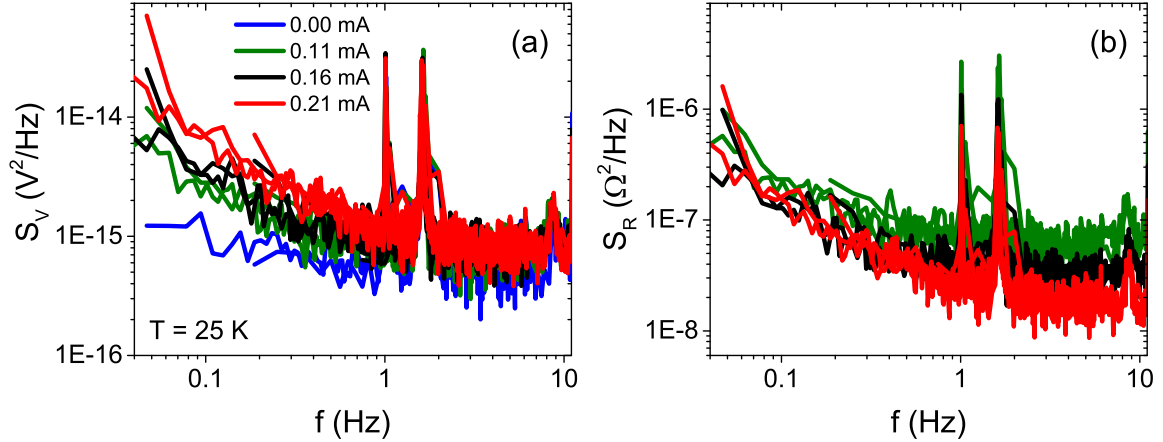


Figure 6.3.1: (a) Current-dependent voltage noise PSD  $S_V(f)$  for the  $\text{YbRh}_2\text{Si}_2$  sample at 25 K. (b) Calculated resistance noise PSD  $S_R = S_V/I^2$ .

between 3.7 K and 160 K. Noise data were recorded for different externally applied magnetic fields between 0 T and 10 T. Panel (b) includes the corresponding frequency exponent  $\alpha$  as a function of temperature.

Considering the normalized PSD  $S_R/R^2$  at 1 Hz, a very similar trend is observed for all four curves. While the noise magnitude displays only a weak temperature dependence between 100 K and 160 K, a clear decrease occurs between 100 K and 25 K upon cooling. Between 15 K and 25 K, all curves exhibit a pronounced minimum, which is followed by a sharp increase towards lower temperatures. Although the changes in  $S_R(1 \text{ Hz})/R^2$  as a function of temperature can be considered relatively small, namely less than one order of magnitude, an excellent reproducibility is observed—particularly at low temperatures. On the other hand, this implies that no clear magnetic field dependence down to the lowest temperatures of measurement ( $\sim 3.7 \text{ K}$ ) can be deduced from the results shown in Fig. 6.3.2. Between 70 K and 160 K it appears as if a weak field dependence is present. However, there is no consistent systematics and the mutual deviations are relatively small. Interestingly, a few noise spectra around 100 K have shown indications for a spectral wandering, that is, a time-dependence of the  $1/f$  spectrum itself. Therefore, in future investigations it may be worthwhile to study the second spectrum in this temperature range (see Sec. 2.5). Although the analysis in Fig. 6.3.2 is solely based on reproducible noise spectra, spectral wandering may still lead to an increased error in determining  $S_R(1 \text{ Hz})/R^2$  and the frequency exponent  $\alpha$  and thus may explain weak deviations for different measurement cycles. In order to ensure a best possible consistency of the data, all noise measurements were performed upon warming.

Interestingly, the pronounced minimum in  $S_R(1 \text{ Hz})/R^2$  between 15 K and 25 K appears in the range of the single-ion Kondo temperature of  $T_K \approx 25 \text{ K}$ , where local  $f$ -electrons and conduction electrons are expected to form composite heavy quasiparticles. As can be seen in Fig. 6.3.2 (b), the frequency exponent  $\alpha(T)$ , which remains rather constant around  $\alpha = 1$

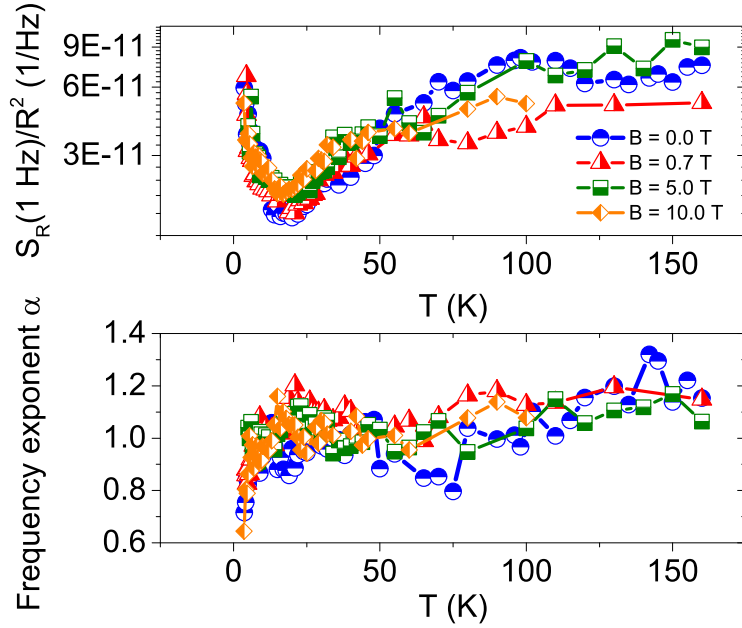


Figure 6.3.2: (a) Normalized resistance noise PSD  $S_R/R^2$  evaluated at  $f = 1 \text{ Hz}$  plotted against the temperature  $T$  with a pronounced minimum in the vicinity of the Kondo temperature  $T_K \approx 25 \text{ K}$ . (b) Frequency exponent  $\alpha$  as a function of  $T$ . All data points were acquired upon warming.

between 20 K and 160 K, begins to steadily decrease at 15–20 K down to the lowest measured temperatures. Therefore, below  $T_K$ , spectral weight is shifted towards higher frequencies. A more detailed analysis of the frequency dependence is presented in the following.

In Fig. 6.3.3, the normalized resistance noise PSD  $S_R/R^2$  is evaluated at different frequencies between 0.001 Hz and 100 Hz. Strikingly, only a weak feature in  $S_R/R^2$  below  $T_K$  is observable for the three lowest frequencies, 0.001 Hz, 0.01 Hz and 0.1 Hz. By contrast, an ever sharper increase occurs towards higher frequencies from 1 Hz to 10 Hz and up to 100 Hz. This corroborates the assumption that the sharp increase is mainly caused by fluctuations at higher frequencies.

Subsequently, the calculated spectral weight  $\text{SW} = \langle (\delta R)^2 \rangle / R^2$  is presented in Fig. 6.3.4 for four different frequency decades between 0.01 Hz and 100 Hz. After Eq. (2.16), the spectral weight is defined as the integrated PSD in a certain frequency range. Here, panels (a)–(d) show the results for different magnetic fields. First of all, it can be seen again that in the majority of cases the spectral weight calculated at higher frequencies shows a sharper increase than the one at lower frequencies. Only for an externally applied magnetic field of 5 T it appears not to be the case, but, however, in this case a reliable analysis could not be performed down to the lowest temperature of 3.7 K. Due to this fact, a few data points are missing at very low temperatures and thus care has to be taken for a comparison with other magnetic fields. Moreover, while the observed frequency dependence is only weak

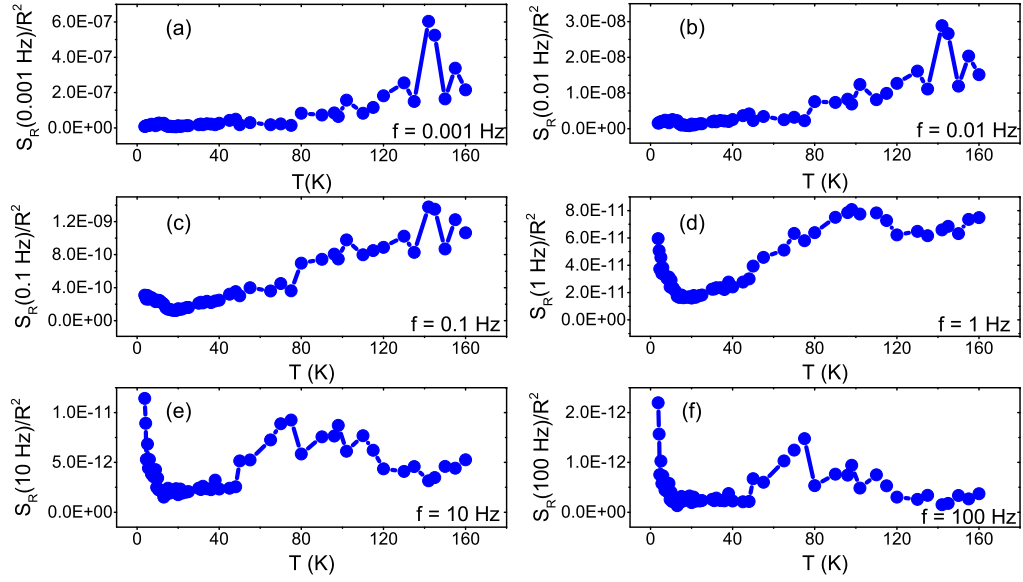


Figure 6.3.3: Normalized resistance noise PSD  $S_R/R^2$  evaluated at different frequencies  $f$  plotted against the temperature  $T$  for  $B = 0$  T. A sharp increase below  $T_K$  is only observed for higher frequencies.

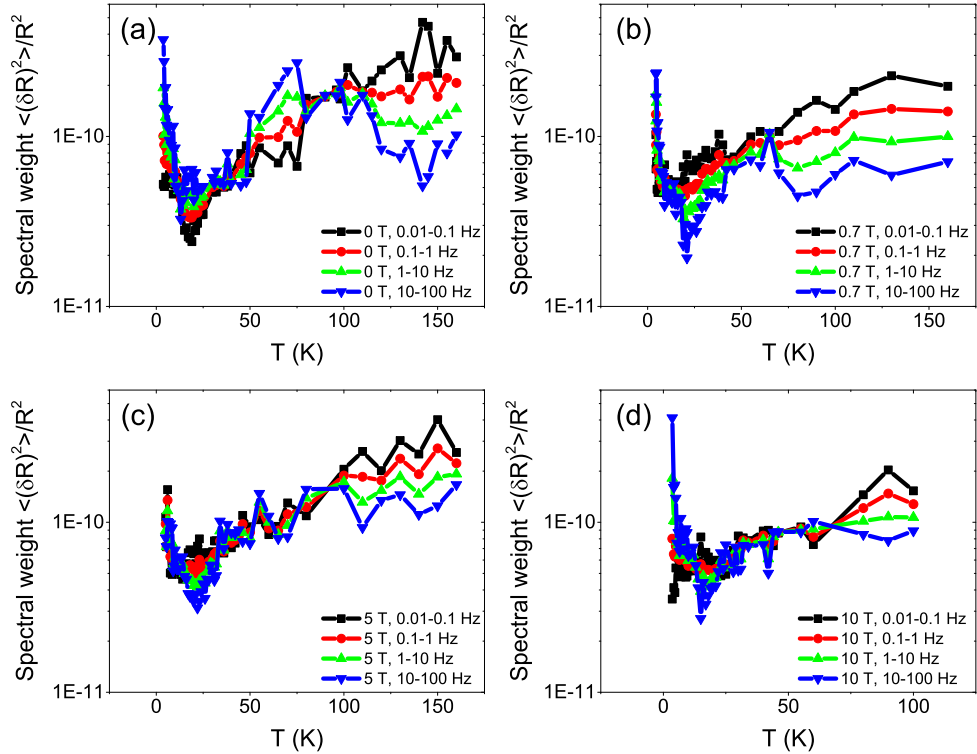


Figure 6.3.4: Calculated spectral weight  $\langle(\delta R)^2\rangle/R^2$  for four different frequency decades. Panels (a)–(d) show the results for different magnetic fields.

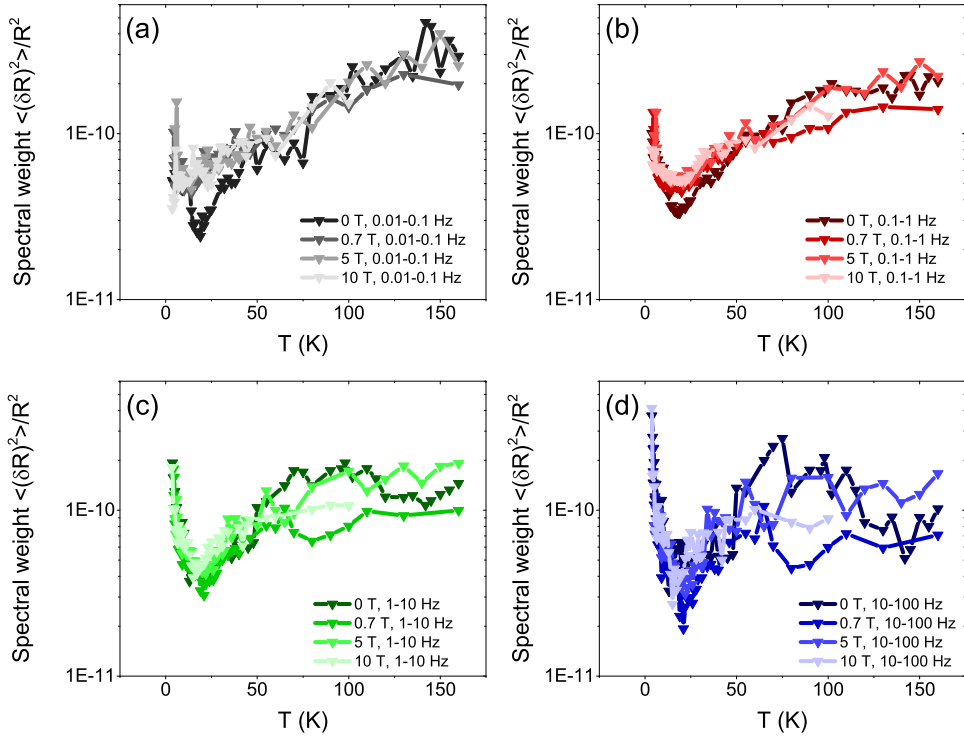


Figure 6.3.5: Calculated spectral weight  $\langle(\delta R)^2\rangle/R^2$  for different externally applied magnetic fields. Panels (a)–(d) show the results for different frequency decades.

at intermediate temperatures, for all magnetic fields a systematic behavior can be observed between about 80–100 K and 160 K. In this temperature range, the spectral weight decreases towards increasing frequencies. This is the same temperature range where a maximum in the resistance occurs due to the onset of coherence between screened magnetic sites and the influence of crystal electric field effects. However, no clear magnetic field dependence can be deduced from the present analysis. This is corroborated by the representation in Fig. 6.3.5, where the identical data are arranged in a different way. Here, each of the diagrams (a)–(d) contains the spectral weight in a particular frequency decade for different magnetic fields. Even though the individual curves in panels (b)–(d) do not perfectly lie on top of each other above 50 K, there is no clear systematics in terms of the magnetic field.

To summarize, for the first time a low-frequency  $1/f$  noise dataset has been acquired on a heavy fermion material. A pronounced minimum in the normalized resistance noise magnitude in the vicinity of the Kondo temperature  $T_K \approx 25$  K, as well as a shift of spectral weight towards higher frequencies, indicate a correlation between the investigated electronic noise and the Kondo physics in  $\text{YbRh}_2\text{Si}_2$ . As discussed in Sec. 6.1.3, the Hall coefficient  $R_H(T)$  displays a plateau or a shoulder for different  $\text{YbRh}_2\text{Si}_2$  samples (see Fig. 6.1.4) in exactly the same temperature range, while the resistance does not exhibit any prominent



features around  $T_K$ . In order to allow for unambiguous conclusions, we suggest further noise studies on other systems with different Kondo temperatures  $T_K$ . It can only be speculated that the observed features in the noise analysis performed in the present thesis work are related to changes in the microscopic mechanisms involved in the charge transport. After a rather constant behavior between 100 K and 160 K, the decrease in the noise magnitude down to about 25 K may be related to the Kondo effect developing coherence, that is, a coherent scattering of charge carriers off the Kondo singlets. At the Kondo temperature  $T_K \approx 25$  K, the hybridization of localized  $f$  electrons with the conduction electrons leads to an enhanced effective mass of the charge carriers. The onset of correlations and changes in the scattering mechanisms may explain the enhancement of the  $1/f$  noise magnitude below  $T_K$ . However, further measurements down to lower temperatures are required for a better understanding. In this respect, it should be noted that S. Kambe et al. report on coexisting Fermi liquid and non-Fermi liquid states in  $\text{YbRh}_2\text{Si}_2$  which were observed in NMR measurements [302]. It will be a matter of future noise studies to clarify whether the observed increase in the PSD can be related to this type of two-state coexistence, which is assumed to emerge at temperatures below 1 K.

As can be seen in Fig. 6.3.6, the application of the phenomenological DDH model (see Sec. 2.4.4) does not lead to an overall agreement between calculated and experimentally determined values of the frequency exponent  $\alpha$  in the case of  $\text{YbRh}_2\text{Si}_2$ . This is true for utilizing the noise PSD at 1 Hz or 1000 Hz for the calculation of the respective frequency exponents within the framework of the DDH model, as the comparison between panels (a) and (b) shows. In detail, the low temperature data can be better reproduced when considering the PSD at 1000 Hz, but in both cases the experimental frequency exponent at higher temperatures cannot be reproduced by the DDH model. The application of the DDH model for other frequencies than 1 Hz and 1000 Hz does not lead to a better agreement (not shown). Therefore, the calculation of the distribution of activation energies  $D(E)$  is not possible and thus information about relevant energy scales for the  $1/f$ -type fluctuations in  $\text{YbRh}_2\text{Si}_2$  is still lacking. In addition, future investigations towards even lower temperatures are expected to provide further information about the quantum-critical behavior in  $\text{YbRh}_2\text{Si}_2$ . Finally, we emphasize that the meander tracks appear to be very sensitive to mechanical, electric or thermal stress. After the acquisition of the noise data presented above, it was aimed at connecting the fifth contact of the sample with the sample holder by means of soldering in order to allow for further noise measurements at temperatures below 3.7 K, where the four-terminal noise setup fails due to the extremely low sample resistance. However, it was observed that a permanent interruption of the meander structure possibly caused by electrostatic discharge or thermal heating appeared. Therefore, for future measurements a new  $\text{YbRh}_2\text{Si}_2$  meander sample has to be prepared.

In conclusion, this project has laid the foundation stone to measure resistance noise fluctuations in strongly correlated metals as well as in other extremely metallic condensed

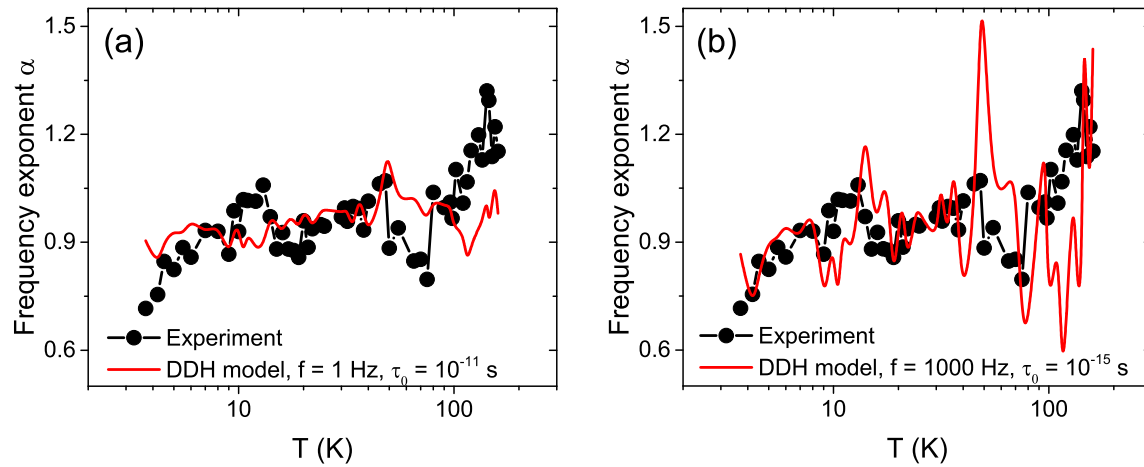


Figure 6.3.6: Application of the DDH model (red curves) to the experimental data (black points) taking into account the noise PSD at (a) 1 Hz and (b) 1000 Hz. No overall agreement is found for neither of the two frequencies. The attempt times  $\tau_0$  are indicated in each case.

matter systems. Based on this work, the implementation of noise measurements on systems which exhibit exotic magnetic states, so-called magnetic skyrmions, will be pursued in future projects.

## 7 Conclusion and Outlook

In the present thesis work, it was aimed to further develop the fluctuation spectroscopy technique and to investigate novel condensed matter systems of current interest. Generally speaking, the noise properties of metallic, semiconducting and insulating compounds were investigated by means of different measurement techniques. It was pointed out that each system requires a different approach in order to reliably detect the inherent  $1/f$ -type fluctuations. In detail, metallic or semiconducting thin films may be structured by means of optical lithography combined with wet chemical etching in order to reduce the active noise volume and thus to increase the sample resistance, leading to an enhancement of the desired noise magnitude. In addition, this well-defined geometry also allows for precise measurements of the (anomalous) Hall effect and the magnetoresistance. In the case of single crystals, two other methods have been proven to be suitable for an enhancement of the sample resistance. Firstly, polishing the sample to a thin platelet as in the case of  $\text{SmB}_6$  [295] may be sufficient to shift the noise magnitude above the background noise originating from the experimental setup. On the other hand, as successfully demonstrated for the heavy-fermion compound  $\text{YbRh}_2\text{Si}_2$ , in the case that the  $1/f$ -type fluctuations are too weak to be measured on a standard platelet sample, generating a meander-shaped geometry by means of focused ion beam etching may be required to further enhance the sample resistance. By contrast, the approach for studying the noise properties of highly insulating samples is entirely different. As demonstrated on the example of hafnia- and yttria-based memristor devices, a two-terminal DC noise setup is the method of choice for highly insulating samples. A very different approach can be the investigation of dielectric polarization noise, which is mainly based on the fluctuation-dissipation theorem. In this context, an experimental setup was established and successfully tested in the group of Prof. Dr. S. Nair at IISER, Pune. On the basis of the gathered experiences, an experimental setup for dielectric polarization noise measurements on organic charge transfer salts will be realized in Frankfurt in the near future, while the setup in Pune will allow for temperature-dependent measurements of relaxor ferroelectrics. To summarize, substantial progress has been made in terms of further development of noise measurement techniques. This progress, together with fruitful collaborations with other institutes, allowed for instructive contributions to open questions in condensed matter physics. A major project presented in this thesis is the comprehensive electronic transport study on thin films of the diluted magnetic semiconductors (DMSs)  $\text{Ga}_{1-x}\text{Mn}_x\text{As}$  and  $\text{Ga}_{1-x}\text{Mn}_x\text{P}$ , which are potential candidates for future spintronics applications. Here, the comparison of the temperature-dependent noise

characteristics of metallic and insulating samples has confirmed the theoretical prediction by A. Kaminski and S. Das Sarma that the ferromagnetic transition in a DMS with localized charge carriers is a percolation transition [3, 4]. Pronounced maxima in the temperature-dependent noise magnitude  $S_R(1\text{ Hz})/R^2$ , a characteristic scaling behavior  $S_R(1\text{ Hz})/R^2 \propto R^w$  and clear deviations in the vicinity of the Curie temperature between the experimentally determined frequency exponent  $\alpha$  and calculations by means of the phenomenological DDH model provide strong evidence for a percolative transition. By contrast, for metallic samples no characteristic features were found in the noise around the ferromagnetic transition temperature. Instead, it was concluded that the observed  $1/f$  fluctuations can be attributed to capture and emission processes of charge carriers involving crystalline defects such as Mn interstitials or As antisites. This idea is supported by the results obtained on He-ion irradiated samples, where, without changes of the Mn content  $x$ , the defect landscape and thus the charge carrier density in  $\text{Ga}_{1-x}\text{Mn}_x\text{As}$  could be tuned in an elegant manner. Furthermore, the comparison of the noise properties of various metallic  $\text{Ga}_{1-x}\text{Mn}_x\text{As}$  samples yielded a strong variation of the noise magnitude as a function of the Mn content and the defect distribution in the respective films. For instance, the noise magnitude in thermally annealed  $\text{Ga}_{1-x}\text{Mn}_x\text{As}$  epilayers was found to be entirely different as compared to as-grown films, which could be related to the out-diffusion of Mn interstitial atoms towards the surface. In addition, the observation of Lorentzian spectra for selected samples allowed for an accurate calculation of characteristic activation energies, which are in the range of typical defect binding energies in the studied DMSs. Finally, other physical quantities than the resistance noise such as the (anomalous) Hall effect and the magnetoresistance were analyzed in the scope of this work, and a good agreement with results from literature was achieved. This indicates a high quality of the investigated samples and thus points to a strong reliability and general validity of the conducted noise data analysis. In conclusion, it was shown that fluctuation spectroscopy is an ideal technique in order to study the physics of defects and electronic phase separation in magnetic semiconductors. Consequently, future projects will involve noise studies on other magnetic semiconductors which are supposed to exhibit percolation transitions or an electronic phase separation such as  $\text{In}_{1-x}\text{Mn}_x\text{As}$  or  $\text{Mn}_x\text{Ge}_{1-x}$  [185].

Further potential systems for novel data storage approaches investigated in the present thesis work were hafnia- and yttria-based resistive random-access memories (RRAMs). For this purpose, fluctuation spectroscopy measurements were established and realized in the group of Prof. Dr. L. Alff at the Technical University Darmstadt. It was demonstrated that electronic noise measurements constitute an ideal method in order to study the charge transport through the conducting filament located in the oxide layer of the RRAM. Our results indicate that trap-assisted tunneling is the main conduction mechanism in stoichiometric and oxygen deficient hafnium oxide devices and at the same time dominates the noise characteristics. In addition to the noise analysis in frequency space, the time signal was analyzed and it was shown that strong random telegraph noise originating from capture and emission processes of charge

---

carriers at traps located in the vicinity of the (ruptured) conducting filament is abundantly present in the high resistance state of the investigated hafnia-based devices. In addition, anomalous random telegraph noise was observed in hafnium oxide RRAMs and could be explained by an oxygen interstitial diffusion model as suggested by F. Puglisi *et al.* [239]. Our results indicate that the occurrence of random telegraph signals and Lorentzian spectra is enhanced in stoichiometric  $\text{HfO}_2$  devices as compared to oxygen deficient  $\text{HfO}_x$  systems, which is related to the enhanced presence of oxygen vacancies in  $\text{HfO}_x$ . More importantly, in the case of  $\text{Y}_2\text{O}_3$  RRAM devices, the noise behavior appears to be dominated by a different conduction mechanism, namely Schottky emission. This is related to the fact that mostly  $1/f$ -type noise or only weak Lorentzian contributions were observed in samples based on  $\text{Y}_2\text{O}_3$ . In future, temperature-dependent noise measurements are expected to shed further light on the relevant electronic transport mechanisms in RRAMs based on these different oxide materials.

Compared to the aforementioned compounds, an entirely different type of physics has been investigated in chapter 6, where the emphasis is put on strongly correlated materials, particularly the heavy fermion compound  $\text{YbRh}_2\text{Si}_2$ . In spite of the differences in terms of the underlying physics, the observed fluctuations are also of  $1/f$ -type, which is another proof of the ubiquity of low-frequency  $1/f$  noise in nature as stated in lots of previous works. In the case of  $\text{YbRh}_2\text{Si}_2$ , a pronounced minimum in the noise magnitude was found in the vicinity of the Kondo temperature  $T_K = 25$  K, indicating a strong correlation between the observed  $1/f$ -type fluctuations and the Kondo physics. In addition, the analysis of the frequency dependence of the noise yields a shift of spectral weight towards higher frequencies below this temperature, which may be related to the formation of composite quasiparticles. Further noise studies towards temperatures below  $\sim 3$  K and on related material systems are expected to provide new insights about the nature and origin of the  $1/f$ -type fluctuations, as well as new findings about the quantum criticality in  $\text{YbRh}_2\text{Si}_2$ . In conclusion, the structuring of single crystals by means of focused ion beam etching has paved the way to measure resistance fluctuations in further strongly correlated metals, which had not been possible so far.

All together, this work contributes to a further development of the fluctuation spectroscopy technique and a better understanding of charge transport in various materials. Moreover, it provides an important basis for more advanced investigations on magnetic semiconductors, oxide-based RRAMs and strongly-correlated electron materials.



# Deutsche Zusammenfassung

Die vorliegende Arbeit beschäftigt sich mit dem elektronischen Rauschen in kondensierter Materie. Obwohl das Rauschen häufig als eine Störgröße angesehen wird, welche die Auflösung eines wissenschaftlichen Experiments limitiert, können elektronische Fluktuationen auch als das eigentliche Messsignal aufgefasst werden, welches wertvolle Informationen über die intrinsischen dynamischen Eigenschaften der Ladungsträger enthält. Zwar sind Fluktuationen zunächst einmal rein zufälliger Natur, allerdings ist die sogenannte spektrale Leistungsdichte der Fluktuationen eine statistisch stationäre Größe, die wiederum – über eine Fourier-Transformation – mit der Autokorrelationsfunktion der Schwankungsgröße verknüpft ist. Diese Korrelationsfunktion ist eine nicht-zufällige Größe, welche die Kinetik der statistischen Prozesse beschreibt. Im Allgemeinen existieren verschiedene Arten des Rauschens: Schrotrauschen und thermisches Rauschen, welche beide aufgrund der nicht vorhandenen Frequenzabhängigkeit der spektralen Leistungsdichte als weißes Rauschen bezeichnet werden, sowie Telegraphenrauschen und  $1/f$ -Rauschen [28]. In dieser Arbeit sind hauptsächlich  $1/f$ -artige Fluktuationen von großer Bedeutung. Diese werden in der Festkörperphysik üblicherweise als Überlagerung einer Vielzahl von thermisch aktivierten Zwei-Niveau-Prozessen mit unterschiedlichen charakteristischen Zeitkonstanten modelliert. Allerdings treten diese  $1/f$ -artigen Fluktuationen auch in anderen Bereichen der Natur auf, beispielsweise bei Messungen der Intensität von Quasaren [38], in der Verteilung von Primzahlen [40], bei Untersuchungen von Erdbeben und Gewittern [35] sowie in den Schwankungen der menschlichen Herzfrequenz [41].

Die Messung und Analyse von elektronischen Fluktuationen in Feststoffen, auch als Fluktuationsspektroskopie bezeichnet, hat sich in den letzten Jahrzehnten als wichtige Methode in der Festkörperphysik etabliert. Diese konnte bereits auf verschiedene Systeme angewandt werden, wie beispielsweise Metalle, Halbleiter, Isolatoren, Supraleiter oder magnetische Materialien. In der Arbeitsgruppe von Prof. Dr. J. Müller haben sich insbesondere die sogenannten organischen Ladungstransfersalze als erfolgreiches Anwendungsgebiet etabliert [28, 9, 10]. Darüber hinaus konnte festgestellt werden, dass sich die Fluktuationsspektroskopie sehr gut für solche Systeme eignet, welche in einem bestimmten Temperaturbereich elektronische Inhomogenitäten aufweisen. Dabei steht eine beobachtete elektronische Phasenseparation häufig in Zusammenhang mit Perkolationseffekten, wie beispielsweise im Falle der Perkolation magnetischer Polaronen in  $\text{EuB}_6$  oder bei der perkolativen Supraleitung in  $\kappa\text{-(BEDT-TTF)}_2\text{Cu[N(CN)}_2\text{]Cl}$  [5, 80]. Solche Phänomene wurden in der vorliegenden Ar-

beit an einer weiteren Materialklasse, den verdünnten magnetischen Halbleitern, untersucht. Die beiden Schwerpunkte dieser Arbeit waren einerseits die Untersuchung aktueller Fragestellungen der Festkörperphysik mit Hilfe der Fluktuationsspektroskopie und andererseits die Weiterentwicklung dieser Messtechnik. Im Hinblick auf den erstgenannten Aspekt standen wie zuvor erwähnt insbesondere verdünnte magnetische Halbleiter im Vordergrund, welche bereits gut erforschte halbleitende mit magnetischen Eigenschaften verbinden und dadurch ein großes Potential für die Anwendung im Rahmen der sogenannten Spintronik bergen. Bei der Spintronik handelt es sich um ein relativ junges Forschungsgebiet, in welchem der Spin des Elektrons neben dessen Ladung als Grundlage zur Verarbeitung und Speicherung von Daten verwendet wird. Im Zuge dieser Arbeit wurden systematische Rauschmessungen an dünnen Filmen der beiden Verbindungen  $\text{Ga}_{1-x}\text{Mn}_x\text{As}$  [114, 115] und  $\text{Ga}_{1-x}\text{Mn}_x\text{P}$  [208] durchgeführt. Obwohl diese Materialien in den letzten beiden Jahrzehnten bereits extensiv untersucht wurden, sind die Ursachen für das Auftreten einer spontanen Magnetisierung und die elektronische Struktur immer noch nicht vollständig geklärt. Eine von A. Kaminski und S. Das Sarma entwickelte Theorie nimmt eine Perkolation gebundener magnetischer Polaronen als Ursache für die spontane Magnetisierung in verdünnten magnetischen Halbleitern im Grenzfall starker Ladungsträgerlokalisierung an [3, 4]. Im Rahmen der vorliegenden Arbeit konnten starke Hinweise auf diesen perkolutiven Übergang in der Nähe der Curie-Temperatur  $T_C$  gefunden werden. Für isolierende  $\text{Ga}_{1-x}\text{Mn}_x\text{As}$ - und  $\text{Ga}_{1-x}\text{Mn}_x\text{P}$ -Proben mit stark lokalisierten Ladungsträgern wurde ein ausgeprägtes Maximum in der normierten spektralen Leistungsdichte der Widerstandsfluktuationen  $S_R(1\text{Hz})/R^2$  bei  $T_C$  beobachtet. Zudem skaliert die spektrale Leistungsdichte wie  $S_R/R^2 \propto R^w$ , wobei  $R$  den Probenwiderstand und  $w$  einen kritischen Perkolationsexponenten bezeichnen. Dieses Potenzgesetzverhalten wird nach verschiedenen theoretischen Modellen für zufällige Widerstandsnetzwerke, die Perkulationsphänomene aufweisen, erwartet. Einen weiteren Hinweis für das Auftreten von Perkolationseffekten liefern Abweichungen zwischen dem experimentell bestimmten Frequenzexponenten  $\alpha(T)$  – einer weiteren wichtigen Charakteristik von  $1/f$ -artigen Fluktuationen – und berechneten Werten für  $\alpha(T)$  nach dem phänomenologischen Modell von P. Dutta, P. Dimon und P. Horn (DDH-Modell) [62] in der Nähe der Curie-Temperatur. Im Gegensatz dazu wurden für metallische  $\text{Ga}_{1-x}\text{Mn}_x\text{As}$ -Proben keine signifikanten Änderungen im Rauschen am ferromagnetischen Übergang beobachtet. Stattdessen konnte festgestellt werden, dass die  $1/f$ -artigen Fluktuationen hauptsächlich durch den kurzzeitigen Einfang und die anschließende Emission von Ladungsträgern an Defekten und die damit verbundenen Schwankungen der Ladungsträgerdichte bestimmt werden. Hierzu wurden unter anderem mit Helium-Ionen bestrahlte  $\text{Ga}_{1-x}\text{Mn}_x\text{As}$ -Proben systematisch auf ihr Rauschverhalten untersucht. Die Bestrahlung führt zu einer größeren Anzahl an Defekten und somit zu einer höheren Unordnung in den jeweiligen Proben, wodurch sich die effektive Ladungsträgerdichte insgesamt verringert. Es wurde gezeigt, dass die erzeugten Defekte einen starken Einfluss auf das



Rauschverhalten haben. Die wichtige Rolle von Defekten für das Widerstandsrauschen wird auch darin deutlich, dass sich die spektrale Leistungsdichte für unterschiedliche metallische  $\text{Ga}_{1-x}\text{Mn}_x\text{As}$ -Proben mit verschiedenen Parametern wie z.B. dem Mn-Gehalt um mehrere Größenordnungen unterscheidet. Da ein Großteil der untersuchten dünnen magnetischen Filme mittels Molekularstrahlepitaxie bei relativ niedrigen Temperaturen gewachsen wurde, um Fremdphasen zu verhindern und einen möglichst hohen Mn-Gehalt zu erzielen, ist die Anzahl der auftretenden Defekte im Vergleich zu anderen Materialien relativ hoch. Um die Dichte der Defekte nach der Herstellung zu verringern und somit die Curie-Temperatur weiter zu erhöhen, existieren verschiedene Ansätze der Nachbearbeitung, wovon sicherlich die nachträgliche Wärmebehandlung (engl.: thermal annealing) die bekannteste ist. In dieser Arbeit wurden vergleichende Messungen zwischen unbehandelten und behandelten Proben durchgeführt. Dabei wurde festgestellt, dass sich das Rauschverhalten aufgrund der veränderten Verteilung und Anzahl der Defekte, insbesondere bedingt durch die Ausdiffusion von Mn-Zwischengitteratomen, deutlich unterscheidet. Die Qualitätsunterschiede zwischen den Proben werden bereits in anderen Größen deutlich, wie zum Beispiel am spezifischen Widerstand, am (anormalen) Hall-Effekt oder am Magnetwiderstand, welche im Rahmen dieser Arbeit ebenfalls systematisch untersucht worden sind. Insgesamt wurde gezeigt, dass die Fluktuationsspektroskopie eine ideale Methode darstellt, um einerseits die Physik von Defekten in magnetischen Halbleitern zu untersuchen, andererseits aber auch elektronische Inhomogenitäten und die Perkolation magnetischer Polaronen.

Ein weiteres, in Zusammenarbeit mit der Arbeitsgruppe von Prof. Dr. L. Alff (Technische Universität Darmstadt) untersuchtes System sind auf  $\text{HfO}_2$  und  $\text{Y}_2\text{O}_3$  basierende RRAMs (engl.: Resistive Random Access Memory) [33, 32, 233]. Diese Metall-Isolator-Metall-Schichten weisen ungewöhnliche Strom-Spannungs-Kennlinien auf, welche durch die Erzeugung und teilweise Zerstörung eines leitfähigen Filaments, bestehend aus Sauerstoff-Fehlstellen, erklärt werden können. Im Rahmen dieser Arbeit wurden erstmals vergleichende Rauschmessungen an stöchiometrischem  $\text{HfO}_2$  sowie Sauerstoff-defizitärem  $\text{HfO}_x$  durchgeführt. Des Weiteren wurde zum ersten Mal das Rauschverhalten von  $\text{Y}_2\text{O}_3$  RRAMs untersucht, welche ebenso wie Hafniumoxid-Strukturen mittels Molekularstrahlepitaxie hergestellt werden. Da der Aufbau zur Charakterisierung von RRAMs in Darmstadt nicht von Grund auf für Rauschmessungen konzipiert worden ist, mussten zunächst einige technische Hürden, wie beispielsweise die korrekte Erdung des Aufbaus und der Probe, überwunden werden. Diese werden im Rahmen dieser Arbeit ausführlich erläutert. Anschließend wurden Rauschmessungen an verschiedenen Proben und bei verschiedenen Widerständen im sogenannten High Resistance State durchgeführt, in welchem das leitfähige Filament immer teilweise zerstört ist. Nachdem der gewünschte Zustand des RRAMs präpariert wurde, wurden über zwei mit der Probe in Kontakt stehende Messspitzen eine konstante Gleichspannung angelegt und die Stromfluktuationen mittels eines Signalanalysators gemessen, um daraus die entsprechenden Rauschspektren zu berechnen. Zeitgleich wurde hierbei auch das Zeitsignal des Stromes

$I(t)$  aufgezeichnet. Dabei wurde in Hafniumoxid-Proben häufig ein Telegraphenrauschen beobachtet, welches dem Einfang und der anschließenden Emission von Ladungsträgern an Defekten zuzuschreiben ist, die sich in der Nähe des Filaments und insbesondere zwischen dem zerstörten Ende des Filaments und der metallischen Elektrode befinden. Darüber hinaus wurde festgestellt, dass sich häufig die Rauschcharakteristik als Funktion der Zeit ändert. Im Detail handelt es sich dabei um ein sogenanntes anomales Telegraphenrauschen [239], welches aufgrund der Diffusion von Sauerstoffatomen zustande kommt und im fluktuierenden Zeitsignal insoweit beobachtet werden kann, als einzelne Zwei-Niveau-Prozesse verschwinden und gegebenenfalls nach einer gewissen Zeit wieder auftreten. Es gibt erste Hinweise darauf, dass in stöchiometrischem  $\text{HfO}_2$  verstärkt Telegraphenrauschen auftritt, während im Falle von  $\text{HfO}_x$  häufiger reine  $1/f$ -Spektren beobachtet wurden. Dies konnte durch die unterschiedliche Anzahl und Verteilung der Sauerstoff-Fehlstellen begründet werden. Während es in  $\text{HfO}_x$  viele Fehlstellen gibt, die zu Fluktuationsprozessen mit verschiedenen Zeitkonstanten beitragen können, kommt es im Falle des stöchiometrischen  $\text{HfO}_2$  zu weniger einzelnen Zwei-Niveau-Prozessen. Somit überlagern sich die vielen Einzelprozesse im ersten Fall zu einem  $1/f$ -artigen Spektrum, wohingegen im zweiten Fall häufig Telegraphenrauschen beobachtet werden kann. Insgesamt ist das Auftreten von Telegraphenrauschen in beiden Fällen dennoch ein Hinweis darauf, dass es sich bei dem wichtigsten Mechanismus für Ladungstransport im High Resistance State von Hafniumoxid um Tunnelprozesse handelt, welche durch die Defekte in der Nähe des leitfähigen Filaments begünstigt werden (engl.: trap-assisted tunneling). Schließlich wurden erste Rauschmessungen an RRAMs, welche auf  $\text{Y}_2\text{O}_3$  basieren, durchgeführt. Dabei wurde sehr häufig reines  $1/f$ -Rauschen beobachtet, und die nur selten auftretenden Lorentz-Spektren waren im Vergleich zu Hafniumoxid deutlich schwächer ausgeprägt. Da auch das Skalierungsverhalten der normierten spektralen Leistungsdichte mit dem Widerstand schwächer ausgeprägt war als im Falle von Hafniumoxid, ist es naheliegend, dass die durchgeführten Rauschmessungen die Modelle aus der Literatur bestätigen, welche in Yttriumoxid die sogenannte Schottky-Emission als Hauptmechanismus für den Ladungstransport annehmen [245, 244]. Da für die Schottky-Emission in  $\text{Y}_2\text{O}_3$  im Vergleich zu den oben beschriebenen Tunnelprozessen in  $\text{HfO}_2$  eine stärkere Temperaturabhängigkeit zu erwarten ist [234], sollen in Zukunft temperaturabhängige Rauschmessungen durchgeführt werden. Mit der Etablierung der Rauschmessungen an der Technischen Universität Darmstadt besteht nun außerdem die Möglichkeit, weiterführende Messungen an RRAMs durchzuführen und die Abhängigkeit der elektronischen Fluktuationen von weiteren, bisher nicht berücksichtigten Parametern zu untersuchen. Der zweite Schwerpunkt der vorliegenden Arbeit beinhaltet die Weiterentwicklung der Fluktuationsspektroskopie. Im Allgemeinen gestalten sich Rauschmessungen an besonders isolierenden oder an stark metallischen Systemen als schwierig. Wie in dieser Arbeit demonstriert, können im Falle von metallischen Verbindungen Optimierungen an der Probengeometrie vorgenommen werden. Die Anwendung eines fokussierten Ionenstrahls erlaubt es,

einen Teil des ursprünglich gewachsenen Einkristalls in eine mäanderförmige Geometrie zu bringen. Dabei wird der Widerstand der Probe signifikant erhöht, was im Idealfall dazu führt, dass die zu messenden, relativ schwachen  $1/f$ -artigen Fluktuationen über den Rauschuntergrund des experimentellen Aufbaus gehoben werden. Diese Art von Strukturierung wurde in Zusammenarbeit mit Dr. M. Brando und Dr. A. Steppke vom Max-Planck-Institut für Chemische Physik fester Stoffe, sowie mit den Arbeitsgruppen von Prof. Dr. C. Krellner und Prof. Dr. M. Huth vom Physikalischen Institut der Goethe-Universität Frankfurt, etabliert. An einem klassischen Schwere-Fermionen-System,  $\text{YbRh}_2\text{Si}_2$  [270, 272], wurde gezeigt, dass die beschriebene Strukturierung Rauschmessungen überhaupt erst ermöglichen kann. Zudem konnten an diesem System erste temperaturabhängige Messungen durchgeführt werden. Dabei gibt es starke Hinweise darauf, dass die Beobachtungen im elektronischen Rauschen stark mit dem Kondo-Effekt zusammenhängen. Für ein besseres Verständnis müssen jedoch in Zukunft weitere Messungen an diesem und verwandten Systemen mit unterschiedlicher Kondo-Temperatur durchgeführt werden.

Schließlich wurde mit den Messungen der dielektrischen Polarisationsfluktuationen ein Ansatz für Rauschmessungen an stark isolierenden Proben vorgestellt. Im Rahmen der vorliegenden Arbeit wurde nach dem Vorbild der Arbeit von J. Schindele *et al.* [86] ein experimenteller Aufbau in der Arbeitsgruppe von Prof. Dr. S. Nair am Indian Institute of Science Education and Research (IISER) in Pune (Indien) realisiert und erfolgreich getestet. Dies geschah sowohl an realen physikalischen Proben als auch an einer Parallelschaltung aus einem Widerstand und einem Kondensator, wodurch eine reale Probe simuliert wurde. Dabei wurde das Polarisationsrauschen einer sich in einem Kondensator befindlichen Probe als Spannungs- oder Stromrauschen an den beiden Kondensatorplatten gemessen. Dies ermöglicht es, Rückschlüsse über die strukturelle Dynamik des Systems zu ziehen und die Gültigkeit des Fluktuations-Dissipations-Theorems, beispielsweise im Falle von Relaxor-Ferroelektrika, zu überprüfen. Im Falle der bisher nur bei Raumtemperatur untersuchten Proben entsprachen die gemessenen Rauschspektren immer dem aus dielektrischen Messungen vorhergesagten Verlauf. Außerdem werden die hieraus gewonnenen Erkenntnisse in die zukünftige Realisierung eines neuen Aufbaus für die Messung des dielektrischen Polarisationsrauschens an organischen Ladungstransfersalzen an der Universität Frankfurt einfließen.

Somit wurden neben den neuen Erkenntnissen an magnetischen Halbleitern, RRAMs, und Schwere-Fermionen-Systemen durch die technischen Weiterentwicklungen im Rahmen dieser Arbeit die Grundlagen gelegt, um in Zukunft Rauschmessungen an Systemen durchzuführen, die mittels dieser Methode bisher nicht zugänglich waren. Des Weiteren wurden die Stärken und insbesondere die Vielfältigkeit der Fluktuationsspektroskopie anhand der Experimente an verschiedensten Systemen der Festkörperphysik demonstriert.



# Bibliography

- [1] F. M. Vidal. Statistics in particle physics - the role it played in discovering Higgs boson. *Mètode Science Studies Journal*, 5:167–173, 2015. 1
- [2] B. Raquet. Electronic Noise in Magnetic Materials and Devices. In *Spin Electronics*, Chapter: "Electronic Noise in Magnetic Materials and Devices", pages 232–273. Springer, Heidelberg, 2001. 1, 13, 15, 16, 19, 20, 24
- [3] A. Kaminski and S. Das Sarma. Polaron percolation in diluted magnetic semiconductors. *Phys. Rev. Lett.*, 88(24):247202, 2002. 2, 63, 73, 74, 75, 104, 110, 156, 160
- [4] A. Kaminski and S. Das Sarma. Magnetic and transport percolation in diluted magnetic semiconductors. *Phys. Rev. B*, 68(23):235210, 2003. 2, 63, 73, 74, 75, 104, 105, 110, 156, 160
- [5] P. Das, A. Amyan, J. Brandenburg, J. Müller, P. Xiong, S. von Molnár, and Z. Fisk. Magnetically driven electronic phase separation in the semimetallic ferromagnet  $\text{EuB}_6$ . *Phys. Rev. B*, 86(18):184425, 2012. 2, 5, 29, 30, 31, 63, 104, 144, 159
- [6] V. Podzorov, M. Uehara, M. E. Gershenson, T. Y. Koo, and S-W. Cheong. Giant  $1/f$  noise in perovskite manganites: Evidence of the percolation threshold. *Phys. Rev. B*, 61(6):R3784–R3787, 2000. 2, 29, 30, 63, 106
- [7] J. Müller, S. von Molnár, Y. Ohno, and H. Ohno. Decomposition of  $1/f$  Noise in  $\text{Al}_x\text{Ga}_{1-x}\text{As}/\text{GaAs}$  Hall Devices. *Phys. Rev. Lett.*, 96(18):186601, 2006. 5
- [8] J. Müller, Y. Li, S. von Molnár, Y. Ohno, and H. Ohno. Single-electron switching in  $\text{Al}_x\text{Ga}_{1-x}\text{As}/\text{GaAs}$  Hall devices. *Phys. Rev. B*, 74(12):125310, 2006. 5, 13, 14
- [9] B. Hartmann, D. Zielke, J. Polzin, T. Sasaki, and J. Müller. Critical slowing down of the charge carrier dynamics at the Mott metal-insulator transition. *Physical Review Letters*, 114(21), 2015. 5, 24, 159
- [10] J. Brandenburg, J. Müller, and J. A Schlueter. Sudden slowing down of charge carrier dynamics at the Mott metal-insulator transition in  $\kappa\text{-(D}_8\text{-BEDT-TTF)}_2\text{Cu}[\text{N}(\text{CN})_2]\text{Br}$ . *New Journal of Physics*, 14(2):023033, 2012. 5, 159

- [11] S. Kogan. *Electronic Noise and Fluctuations in Solids*. Cambridge University Press, 1996. 5, 9, 13, 19, 24, 28, 32, 105, 116
- [12] R. Müller. *Rauschen*. Springer-Verlag Berlin, Heidelberg, 1990. 5, 8, 10, 32
- [13] B. Hartmann. *Ladungsträgerdynamik am Mott-Übergang*. PhD Thesis, Goethe University Frankfurt, 2017. 5, 21, 48, 52
- [14] J. Brandenburg. *Fluktuationsspektroskopie an organischen Ladungstransfersalzen*. PhD Thesis, Goethe-Universität Frankfurt am Main, 2010. 5, 6, 12, 51, 52
- [15] J. B. Johnson. Thermal Agitation of Electricity in Conductors. *Nature*, 119(2984):50–51, 1927. 11
- [16] H. Nyquist. Thermal agitation of electric charge in conductors. *Phys. Rev.*, 32(1):110–113, 1928. 11
- [17] P. L. Garrity. Spectroscopy of electronic thermal noise as a direct probe of absolute thermoelectric coefficients. *Journal of Applied Physics*, 109(7):073701, 2011. 11
- [18] L.B. Kish. To the problem of zero-point energy and thermal noise. *Solid State Communications*, 67(7):749–751, 1988. 11
- [19] L. B. Kish, G. A. Niklasson, and C. G. Granqvist. Zero-point term and quantum effects in the Johnson noise of resistors: a critical appraisal. *Journal of Statistical Mechanics: Theory and Experiment*, 2016(5):054006, 2016. 11
- [20] E. T. Patronis, H. Marshak, C. A. Reynolds, V. L. Sailor, and F. J. Shore. Low-temperature thermal noise thermometer. *Review of Scientific Instruments*, 30(7):578–580, 1959. 13
- [21] D. Rothfuß, A. Reiser, A. Fleischmann, and C. Enss. Noise thermometry at ultra low temperatures. *Applied Physics Letters*, 103(5):052605, 2013. 13
- [22] W. Schottky. Über spontane Stromschwankungen in verschiedenen Elektrizitätsleitern. *Ann. Phys.*, 362(23):541–567, 1918. 13
- [23] C. Beenakker and C. Schönberger. Quantum shot noise. *Physics Today*, 56(5):37–42, 2003. 13
- [24] F. Lefloch, C. Hoffmann, M. Sanquer, and D. Quirion. Doubled full shot noise in quantum coherent superconductor-semiconductor junctions. *Physical Review Letters*, 90(6), 2003. 13
- [25] L. Saminadayar, D. C. Glattli, Y. Jin, and B. Etienne. Observation of the  $e/3$  Fractionally Charged Laughlin Quasiparticle. *Physical Review Letters*, 79(13):2526–2529, 1997. 13

- 
- [26] P. Y. Yu and M. Cardona. Fundamentals in semiconductors: Physics and materials properties. Springer Berlin/Heidelberg, 3 edition, 2004. 14
- [27] S. Machlup. Noise in semiconductors: Spectrum of a two-parameter random signal. *J. Appl. Phys.*, 25(3):341, 1954. 14
- [28] J. Müller. Fluctuation Spectroscopy: A New Approach for Studying Low-Dimensional Molecular Metals. *ChemPhysChem*, 12(7):1222–1245, 2011. 15, 18, 159
- [29] M. Lonsky, S. Heinz, M. V. Daniel, M. Albrecht, and J. Müller. Electronic transport in thermoelectric  $\text{Yb}_2\text{Co}_4\text{Sb}_{12}$  Skutterudite thin films studied by resistance noise spectroscopy. *J. Appl. Phys.*, 120(14):142101, 2016. 15, 46, 47
- [30] A. Anane, B. Raquet, S. von Molnár, L. Pinsard-Godart, and A. Revcolevschi. Electrical noise from phase separation in  $\text{Pr}_{2/3}\text{Ca}_{1/3}\text{MnO}_3$  single crystal. *Journal of Applied Physics*, 87(9):5025–5027, 2000. 15
- [31] R. D. Merithew, M. B. Weissman, F. M. Hess, P. Spradling, E. R. Nowak, J. O. Donnell, J. N. Eckstein, Y. Tokura, and Y. Tomioka. Mesoscopic thermodynamics of an inhomogeneous colossal-magnetoresistive phase. *Physical Review Letters*, 84(15):3442–3445, 2000. 15
- [32] W. Yi, S. E. Savelev, G. Medeiros-Ribeiro, F. Miao, M.-X. Zhang, J. J. Yang, A. M. Bratkovsky, and R. S. Williams. Quantized conductance coincides with state instability and excess noise in tantalum oxide memristors. *Nature Communications*, 7:11142, 2016. 15, 54, 116, 118, 119, 128, 161
- [33] S. Yu, R. Jeyasingh, Y. Wu, and H.-S. P. Wong. Characterization of low-frequency noise in the resistive switching of transition metal oxide  $\text{HfO}_2$ . *Physical Review B*, 85(4), 2012. 15, 54, 116, 117, 120, 127, 131, 161
- [34] J. B. Johnson. The Schottky effect in low frequency circuits. *Phys. Rev.*, 26(1):71–85, 1925. 16
- [35] S. Machlup. Proc. 6th Int. Conf. on Noise in Physical Systems, Chapter Earthquakes, thunderstorms, and other  $1/f$  noises, page 157. MD, Gaithersburg, 1981. 16, 159
- [36] M. Gardner. Mathematical Games. *Scientific American*, 238(4):16–32, 1978. 16
- [37] R. F. Voss and J. Clarke.  $1/f$  - noise in music and speech. *Nature*, 258(5533):317–318, 1975. 16
- [38] W. H. Press. Flicker Noise in Astronomy and Elsewhere. *Comments Astrophysics and Space Physics*, 7:103, 1978. 16, 18, 159

- [39] T. Musha and H. Higuchi. The  $1/f$  fluctuation of a traffic current on an expressway. *Japanese Journal of Applied Physics*, 15(7):1271, 1976. 16
- [40] M. Wolf.  $1/f$  noise in the distribution of prime numbers. *Physica A: Statistical Mechanics and its Applications*, 241(3-4):493–499, 1997. 16, 159
- [41] C.-K. Peng, J. Mietus, J. M. Hausdorff, S. Havlin, H. E. Stanley, and A. L. Goldberger. Long-range anticorrelations and non-Gaussian behavior of the heartbeat. *Physical Review Letters*, 70(9):1343–1346, 1993. 16, 159
- [42] R. F. Voss and J. Clarke. Flicker  $1/f$  noise: Equilibrium temperature and resistance fluctuations. *Physical Review B*, 13(2):556–573, 1976. 16
- [43] H. G. E. Beck and W. P. Spruit.  $1/f$  noise in the variance of johnson noise. *Journal of Applied Physics*, 49(6):3384–3385, 1978. 16
- [44] G. P. Zhigal'skii. Nonequilibrium  $1/f$  noise in conducting films and contacts. *Physics-Uspekhi*, 46(5):449, 2003. 16, 19, 109
- [45] M. A. Caloyannides. Microcycle spectral estimates of  $1/f$  noise in semiconductors. *J. Appl. Phys.*, 45(1):307, 1974. 16, 17, 18
- [46] A. Einstein. Über die von der molekularkinetischen Theorie der Wärme geforderte Bewegung von in ruhenden Flüssigkeiten suspendierten Teilchen. *Annalen der Physik*, 322(8):549–560, 1905. 17, 32
- [47] A. Einstein. Eine neue Bestimmung der Moleküldimensionen. *Annalen der Physik*, 324(2):289–306, 1906. 17, 32
- [48] M. J. Buckingham. *Noise in electronic devices and systems*. Ellis Horwood Ltd, 1983. 19
- [49] F. N. Hooge.  $1/f$  noise is no surface effect. *Physics Letters A*, 29(3):139–140, 1969. 19, 82
- [50] F. N. Hooge.  $1/f$  noise. *Physica B*, 83(1):14–23, 1976. 19, 82
- [51] F. N. Hooge, T. G. M. Kleinpenning, and L. K. J. Vandamme. Experimental studies on  $1/f$  noise. *Reports on Progress in Physics*, 44(5):479, 1981. 19
- [52] J. L. Williams and I. L. Stone. Current noise in thin discontinuous films. *Journal of Physics C: Solid State Physics*, 5(16):2105, 1972. 19, 109
- [53] M. B. Weissman.  $1/f$  noise and other slow, nonexponential kinetics in condensed matter. *Reviews of Modern Physics*, 60(2):537–571, 1988. 20



- 
- [54] P. Dutta and P. M. Horn. Low-frequency fluctuations in solids:  $1/f$  noise. *Reviews of Modern Physics*, 53(3):497–516, 1981. 20, 116
- [55] P. Drude. Zur Elektronentheorie der Metalle. *Annalen der Physik*, 306(3):566–613, 1900. 20
- [56] M. B. Weissman. Relations between geometrical factors for noise magnitudes in resistors. *Journal of Applied Physics*, 51(11):5872–5875, 1980. 20
- [57] R. D. Black, P. J. Restle, and M. B. Weissman. Hall effect, anisotropy, and temperature-dependence measurements of  $1/f$  noise in silicon on sapphire. *Physical Review B*, 28(4):1935–1943, 1983. 20
- [58] H. M. J. Vaes and T. G. M. Kleinpenning. Hall-effect noise in semiconductors. *Journal of Applied Physics*, 48(12):5131–5134, 1977. 20
- [59] F. K. Du Pré. A suggestion regarding the spectral density of flicker noise. *Phys. Rev.*, 78(5):615–615, 1950. 22
- [60] A. Van Der Ziel. On the noise spectra of semi-conductor noise and of flicker effect. *Physica*, 16(4):359–372, 1950. 22
- [61] A. L. McWhorter. *Semiconductor Surface Physics*, Chapter  $1/f$  noise and germanium surface properties, pages 207–228. University of Philadelphia Press, 1957. 22
- [62] P. Dutta, P. Dimon, and P. M. Horn. Energy Scales for Noise Processes in Metals. *Phys. Rev. Lett.*, 43(9):646–649, 1979. 22, 23, 24, 160
- [63] D. M. Fleetwood, T. Postel, and N. Giordano. Temperature dependence of the  $1/f$  noise of carbon resistors. *J. Appl. Phys.*, 56(11):3256, 1984. 23
- [64] J. H. Scofield, D. H. Darling, and W. W. Webb. Exclusion of temperature fluctuations as the source of  $1/f$  noise in metal films. *Phys. Rev. B*, 24(12):7450–7453, 1981. 24
- [65] J. Pelz and J. Clarke. Dependence of  $1/f$  Noise on Defects Induced in Copper Films by Electron Irradiation. *Physical Review Letters*, 55(7):738–741, 1985. 24
- [66] H. T. Hardner, M. B. Weissman, M. Jaime, R. E. Treece, P. C. Dorsey, J. S. Horwitz, and D. B. Chrisey. Non-Gaussian noise in a colossal magnetoresistive film. *Journal of Applied Physics*, 81(1):272–275, 1997. 25
- [67] S. Kar, A. K. Raychaudhuri, A. Ghosh, H. v. Löhneysen, and G. Weiss. Observation of Non-Gaussian Conductance Fluctuations at Low Temperatures in Si:P(B) at the Metal-Insulator Transition. *Physical Review Letters*, 91(21), 2003. 25

- [68] M.B. Weissman, N.E. Israeloff, and G.B. Alers. Spin-glass fluctuation statistics: mesoscopic experiments in Mn. *Journal of Magnetism and Magnetic Materials*, 114(1-2):87–130, 1992. 25
- [69] M. B. Weissman. What is a spin glass? A glimpse via mesoscopic noise. *Reviews of Modern Physics*, 65(3):829–839, 1993. 25
- [70] S. Ottersbach. Fluktuationsspektroskopie mittels schneller Datenerfassung und softwaregestützter Datenanalyse – Anwendung auf den Ladungsordnungsübergang in Nickelaten. Master’s Thesis, Goethe University Frankfurt, 2013. 25
- [71] D. Zielke. Fluktuationsspektroskopie an quasi-zweidimensionalen molekularen Metallen. Master’s Thesis, Goethe University Frankfurt, 2014. 25
- [72] S. R. Broadbent and J. M. Hammersley. Percolation processes. *Mathematical Proceedings of the Cambridge Philosophical Society*, 53(03):629, 1957. 26
- [73] A. Amyan. Elektronische und magnetische Phasenseparation in  $\text{EuB}_6$ . PhD Thesis, Goethe-Universität Frankfurt am Main, 2013. 26, 104, 144
- [74] A. Bunde and J. W. Kantelhardt. Diffusion in Condensed Matter – Methods, Materials, Models, Chapter Diffusion and conduction in percolation systems – Theory and Applications, pages 895–914. Springer Verlag Berlin, 2005. 28
- [75] R. Rammal, C. Tannous, P. Breton, and A. M. S. Tremblay. Flicker (1/f) Noise in Percolation Networks: A New Hierarchy of Exponents. *Phys. Rev. Lett.*, 54(15):1718–1721, 1985. 27, 28, 29, 105
- [76] B. Raquet, A. Anane, S. Wirth, P. Xiong, and S. von Molnár. Noise Probe of the Dynamic Phase Separation in  $\text{La}_{2/3}\text{Ca}_{1/3}\text{MnO}_3$ . *Phys. Rev. Lett.*, 84(19):4485–4488, 2000. 29
- [77] V. Podzorov, M. E. Gershenson, M. Uehara, and S-W. Cheong. Phase separation and 1/f noise in low- $T_{\text{MI}}$  colossal magnetoresistance manganites. *Physical Review B*, 64(11), 2001. 29
- [78] A. Amyan, P. Das, J. Müller, and Z. Fisk. Electronic phase separation due to magnetic polaron formation in the semimetallic ferromagnet  $\text{EuB}_6$  — A weakly-nonlinear-transport study. *Journal of the Korean Physical Society*, 62(10):1489–1494, 2013. 29
- [79] R. S. Manna, P. Das, M. de Souza, F. Schnelle, M. Lang, J. Müller, S. von Molnár, and Z. Fisk. Lattice Strain Accompanying the Colossal Magnetoresistance Effect in  $\text{EuB}_6$ . *Physical Review Letters*, 113(6), 2014. 29

- 
- [80] J. Müller, J. Brandenburg, and J. A. Schlueter. Magnetic-Field Induced Crossover of Superconducting Percolation Regimes in the Layered Organic Mott System  $\kappa$ -(BEDT-TTF)<sub>2</sub>Cu[N(CN)<sub>2</sub>]Cl. *Physical Review Letters*, 102(4), 2009. 29, 159
- [81] O. Levy and D. J. Bergman. Critical behavior of the weakly nonlinear conductivity and flicker noise of two-component composites. *Physical Review B*, 50(6):3652–3660, 1994. 30
- [82] K. W. Yu and P. M. Hui. Percolation effects in two-component nonlinear composites: Crossover from linear to nonlinear behavior. *Physical Review B*, 50(18):13327–13335, 1994. 30
- [83] A.-M. S. Tremblay, S. Feng, and P. Breton. Exponents for 1/f noise, near a continuum percolation threshold. *Physical Review B*, 33(3):2077–2080, 1986. 30, 31, 106
- [84] N. E. Israeloff. Dielectric polarization noise through the glass transition. *Physical Review B*, 53(18):R11913–R11916, 1996. 31
- [85] N. E. Israeloff and X. Wang. High-sensitivity dielectric polarization noise measurements. *Review of Scientific Instruments*, 68(3):1543–1546, 1997. 31, 32
- [86] J. Schindele, A. Reiser, and C. Enss. Fluctuation-dissipation theorem in liquid and glassy glycerol: Frequency-dependent dielectric permittivity and dielectric polarization fluctuation measurements. *Physical Review Letters*, 107(9), 2011. 31, 32, 38, 54, 55, 56, 61, 163
- [87] R Kubo. The fluctuation-dissipation theorem. *Reports on Progress in Physics*, 29(1):255–284, 1966. 32
- [88] J. Schindele. Dielektrische Polarisationsfluktuationen von organischen Glasbildnern. Master’s Thesis, Ruprecht-Karls-Universität Heidelberg, 2009. 32, 54, 56, 57, 61
- [89] T. S. Grigera and N. E. Israeloff. Observation of fluctuation-dissipation-theorem violations in a structural glass. *Physical Review Letters*, 83(24):5038–5041, 1999. 32
- [90] K. P. O’Brien. Dielectric Noise Spectroscopy of Relaxor Ferroelectrics. PhD Thesis, University of Illinois, 1997. 32
- [91] E. Vidal Russell and N. E. Israeloff. Direct observation of molecular cooperativity near the glass transition. *Nature*, 408(6813):695–698, 2000. 32
- [92] E. Vidal Russell, N. E. Israeloff, L. E. Walther, and H. Alvarez Gomariz. Nanometer scale dielectric fluctuations at the glass transition. *Physical Review Letters*, 81(7):1461–1464, 1998. 32

- [93] L. E. Walther, E. Vidal Russell, N. E. Israeloff, and H. Alvarez Gomariz. Atomic force measurement of low-frequency dielectric noise. *Applied Physics Letters*, 72(24):3223–3225, 1998. 32
- [94] P. Lunkenheimer and A. Loidl. Dielectric spectroscopy on organic charge-transfer salts. *Journal of Physics: Condensed Matter*, 27(37):373001, 2015. 33, 34
- [95] P. Debye. Polare molekeln. *Zeitschrift für Elektrochemie und angewandte physikalische Chemie*, 36(11):944–944, 1930. 34
- [96] S. Jenewein. Dielektrisches Polarisationsrauschen am Glasübergang. Master's Thesis, Ruprecht-Karls-Universität Heidelberg, 2008. 35, 36
- [97] N. H. Balshaw. *Practical Cryogenics - An Introduction to Laboratory Cryogenics*. Oxford Instruments. 42
- [98] N. Leps. Rauschmessungen an hochorientiertem pyrolytischen Graphit. Diplomarbeit, Universität Leipzig, 2006. 43
- [99] H. O. McMahon and W. E. Gifford. Closed-cycle helium refrigeration. *Solid-State Electronics*, 1(4):273–278, 1960. 44
- [100] J. R. Kirtley, T. N. Theis, P. M. Mooney, and S. L. Wright. Noise spectroscopy of deep level (DX) centers in GaAs-Al<sub>x</sub>Ga<sub>1-x</sub>As heterostructures. *J. Appl. Phys.*, 63(5):1541, 1988. 46
- [101] S. Heinz. 1/f and Random Telegraph Noise in Thermoelectric Yb<sub>x</sub>Co<sub>4</sub>Sb<sub>12</sub> Skutterudites. Master's Thesis, Goethe University Frankfurt, 2015. 47
- [102] Stanford Research Systems. *Manual for the Model SR560 Low-Noise Preamplifier*, 2013. 48
- [103] Stanford Research Systems. *Manual for the Model SR554 Transformer Preamplifier*, 2004. 48
- [104] J. H. Scofield. AC method for measuring low-frequency resistance fluctuation spectra. *Rev. Sci. Instrum.*, 58(6):985, 1987. 50, 51, 53
- [105] J. Briaire and L. K. J. Vandamme. Uncertainty in Gaussian noise generalized for cross-correlation spectra. *Journal of Applied Physics*, 84(8):4370–4374, 1998. 53
- [106] Keithley Instruments. *Model 428 Current Amplifier Instruction Manual*, 1990. 54
- [107] Burr-Brown Corporation. *Ultra Low Input Bias Current Instrumentation Amplifier*, 1995. 57, 58

- 
- [108] J. Kumar, S. N. Panja, S. Dengre, and S. Nair. Identification of a Griffiths singularity in a geometrically frustrated antiferromagnet. *Physical Review B*, 95(5), 2017. 60
- [109] S. N. Panja, J. Kumar, S. Dengre, and S. Nair. Relieving geometrical frustration through doping in the  $\text{Dy}_{1-x}\text{Ca}_x\text{BaCo}_4\text{O}_7$  swedenborgites. *Journal of Physics: Condensed Matter*, 28(48):486001, 2016. 60
- [110] J. Kumar and A. M. Awasthi. Glassy domain wall matter in  $\text{KH}_2\text{PO}_4$  crystal: Field-induced transition. *Applied Physics Letters*, 103(13):132903, 2013. 60
- [111] T. Chakrabarty and P. L. Paulose. Comparative NMR studies on  $\text{Ca}_3\text{LiRuO}_6$  and  $\text{Ca}_3\text{NaRuO}_6$ . *Journal of Physics: Condensed Matter*, 28(23):236001, 2016. 61
- [112] H. Munekata, H. Ohno, S. von Molnar, A. Segmüller, L. L. Chang, and L. Esaki. Diluted magnetic III-V semiconductors. *Physical Review Letters*, 63(17):1849–1852, 1989. 63
- [113] H. Ohno, H. Munekata, T. Penney, S. von Molnár, and L. L. Chang. Magnetotransport properties of p-type (In,Mn)As diluted magnetic III-V semiconductors. *Phys. Rev. Lett.*, 68(17):2664–2667, 1992. 63, 74
- [114] H. Ohno, A. Shen, F. Matsukura, A. Oiwa, A. Endo, S. Katsumoto, and Y. Iye. (Ga,Mn)As: A new diluted magnetic semiconductor based on GaAs. *Appl. Phys. Lett.*, 69(3):363, 1996. 63, 66, 160
- [115] H. Ohno. Making nonmagnetic semiconductors ferromagnetic. *Science*, 281(5379):951–956, 1998. 63, 67, 160
- [116] L. Chen, S. Yan, P. F. Xu, J. Lu, W. Z. Wang, J. J. Deng, X. Qian, Y. Ji, and J. H. Zhao. Low-temperature magnetotransport behaviors of heavily Mn-doped (Ga,Mn)As films with high ferromagnetic transition temperature. *Appl. Phys. Lett.*, 95(18):182505, 2009. 63, 66
- [117] N. Samarth. Ferromagnetic semiconductors: Battle of the bands. *Nature Materials*, 11(5):360–361, 2012. 63, 72, 73
- [118] T. Dietl and H. Ohno. Dilute ferromagnetic semiconductors: Physics and spintronic structures. *Reviews of Modern Physics*, 86(1):187–251, 2014. 64
- [119] T. Jungwirth, J. Wunderlich, V. Novák, K. Olejník, B. L. Gallagher, R. P. Campion, K. W. Edmonds, A. W. Rushforth, A. J. Ferguson, and P. Němec. Spin-dependent phenomena and device concepts explored in (Ga,Mn)As. *Reviews of Modern Physics*, 86(3):855–896, 2014. 64

- [120] T. Jungwirth, J. Sinova, J. Mašek, J. Kučera, and A. H. MacDonald. Theory of ferromagnetic (III,Mn)V semiconductors. *Reviews of Modern Physics*, 78(3):809–864, 2006. 64
- [121] S. Das Sarma, E.H. Hwang, and A. Kaminski. How to make semiconductors ferromagnetic: a first course on spintronics. *Solid State Communications*, 127(2):99–107, 2003. 64, 66, 74
- [122] K. Sato, L. Bergqvist, J. Kudrnovský, P. H. Dederichs, O. Eriksson, I. Turek, B. Sanyal, G. Bouzerar, H. Katayama-Yoshida, V. A. Dinh, T. Fukushima, H. Kizaki, and R. Zeller. First-principles theory of dilute magnetic semiconductors. *Reviews of Modern Physics*, 82(2):1633–1690, 2010. 64
- [123] S. Frank. Einfluss der Materialeigenschaften auf den Ferromagnetismus von GaMnAs. PhD Thesis, Universität Ulm, 2005. 64, 88
- [124] M. Glunk. Elektrische und magnetische Eigenschaften des verdünnten magnetischen Halbleiters (Ga,Mn)As. PhD Thesis, Universität Ulm, 2011. 64
- [125] M. Reinwald. Herstellung und Charakterisierung von ferromagnetischem GaMnAs auf der GaAs (001)- und (311)A-Oberfläche. PhD Thesis, Universität Regensburg, 2005. 64
- [126] M. Utz. Epitaxie von (Ga,Mn)As. PhD Thesis, Universität Regensburg, 2012. 64
- [127] F. Hoffmann. Magnetic anisotropies of (Ga,Mn)As films and nanostructures. PhD Thesis, Universität Regensburg, 2010. 64, 71
- [128] M. Lonsky, J. Teschabai-Oglu, K. Pierz, S. Sievers, H. W. Schumacher, Y. Yuan, R. Böttger, S. Zhou, and J. Müller. Investigation of a possible electronic phase separation in the magnetic semiconductors  $\text{Ga}_{1-x}\text{Mn}_x\text{As}$  and  $\text{Ga}_{1-x}\text{Mn}_x\text{P}$  by means of fluctuation spectroscopy. *Physical Review B*, 97(5), 2018. 64
- [129] M. Lonsky, J. Teschabai-Oglu, K. Pierz, S. Sievers, H. W. Schumacher, Y. Yuan, R. Böttger, S. Zhou, and J. Müller. Charge carrier dynamics in  $\text{Ga}_{1-x}\text{Mn}_x\text{As}$  studied by resistance noise spectroscopy. *Acta Physica Polonica A* (accepted), 2017. 64, 93
- [130] J. S. Blakemore. Thermal activation energy of manganese acceptors in gallium arsenide as a function of impurity spacing. *J. Appl. Phys.*, 44(7):3352, 1973. 64
- [131] R. A. Chapman and W. G. Hutchinson. Photoexcitation and Photoionization of Neutral Manganese Acceptors in Gallium Arsenide. *Phys. Rev. Lett.*, 18(12):443–445, 1967. 64
- [132] M. Linnarsson, E. Janzén, B. Monemar, M. Kleverman, and A. Thilderkvist. Electronic structure of the  $\text{GaAs:Mn}_{\text{Ga}}$  center. *Phys. Rev. B*, 55(11):6938–6944, 1997. 64

- 
- [133] L. J. Vieland. Behavior of manganese in GaAs. *J. Appl. Phys.*, 33(6):2007, 1962. 64
- [134] F. Matsukura, H. Ohno, and T. Dietl. *Handbook on Magnetic Materials*, Volume 14, pages 1–87. Elsevier, Amsterdam, 2002. 64, 65
- [135] H. Ohldag, V. Solinus, F. U. Hillebrecht, J. B. Goedkoop, M. Finazzi, F. Matsukura, and H. Ohno. Magnetic moment of Mn in the ferromagnetic semiconductor  $\text{Ga}_{0.98}\text{Mn}_{0.02}\text{As}$ . *Applied Physics Letters*, 76(20):2928–2930, 2000. 64
- [136] M. Kobayashi, H. Niwa, Y. Takeda, A. Fujimori, Y. Senba, H. Ohashi, A. Tanaka, S. Ohya, P. N. Hai, M. Tanaka, Y. Harada, and M. Oshima. Electronic Excitations of a Magnetic Impurity State in the Diluted Magnetic Semiconductor (Ga,Mn)As. *Physical Review Letters*, 112(10), 2014. 65
- [137] S. Souma. Spintronics development gets boost with new findings into ferromagnetism in Mn-doped GaAs. Published online (<http://www.tohoku.ac.jp/en/press>, access on May 21st, 2017), 2016. 65
- [138] K. W. Edmonds, P. Bogusławski, K. Y. Wang, R. P. Campion, S. N. Novikov, N. R. S. Farley, B. L. Gallagher, C. T. Foxon, M. Sawicki, T. Dietl, M. Buongiorno Nardelli, and J. Bernholc. Mn Interstitial Diffusion in (Ga,Mn)As. *Phys. Rev. Lett.*, 92(3):037201, 2004. 65, 83
- [139] A. Wolos, M. Kaminska, M. Palczewska, A. Twardowski, X. Liu, T. Wojtowicz, and J. K. Furdyna. Properties of arsenic antisite defects in  $\text{Ga}_{1-x}\text{Mn}_x\text{As}$ . *Journal of Applied Physics*, 96(1):530–533, 2004. 65
- [140] R. C. Myers, B. L. Sheu, A. W. Jackson, A. C. Gossard, P. Schiffer, N. Samarth, and D. D. Awschalom. Antisite effect on hole-mediated ferromagnetism in (Ga,Mn)As. *Physical Review B*, 74(15):155203, 2006. 65
- [141] J. Blinowski and P. Kacman. Spin interactions of interstitial Mn ions in ferromagnetic GaMnAs. *Phys. Rev. B*, 67(12):121204(R), 2003. 65
- [142] V. Novák, K. Olejník, J. Wunderlich, M. Cukr, K. Výborný, A. W. Rushforth, K. W. Edmonds, R. P. Campion, B. L. Gallagher, J. Sinova, and T. Jungwirth. Curie Point Singularity in the Temperature Derivative of Resistivity in (Ga,Mn)As. *Phys. Rev. Lett.*, 101(7), 2008. 66, 76, 84
- [143] K. W. Edmonds, K. Y. Wang, R. P. Campion, A. C. Neumann, N. R. S. Farley, B. L. Gallagher, and C. T. Foxon. High-Curie-temperature  $\text{Ga}_{1-x}\text{Mn}_x\text{As}$  obtained by resistance-monitored annealing. *Appl. Phys. Lett.*, 81(26):4991, 2002. 66, 83

- [144] M. A. Mayer, P. R. Stone, N. Miller, H. M. Smith, O. D. Dubon, E. E. Haller, K. M. Yu, W. Walukiewicz, X. Liu, and J. K. Furdyna. Electronic structure of  $\text{Ga}_{1-x}\text{Mn}_x\text{As}$  analyzed according to hole-concentration-dependent measurements. *Physical Review B*, 81(4):045205, 2010. 67
- [145] E. H. C. P. Sinnecker, G. M. Penello, T. G. Rappoport, M. M. Sant'Anna, D. E. R. Souza, M. P. Pires, J. K. Furdyna, and X. Liu. Ion-beam modification of the magnetic properties of  $\text{Ga}_{1-x}\text{Mn}_x\text{As}$  epilayers. *Phys. Rev. B*, 81(24):245203, 2010. 67, 68, 80, 100
- [146] S. Zhou, L. Li, Y. Yuan, A. W. Rushforth, L. Chen, Y. Wang, R. Böttger, R. Heller, J. Zhao, K. W. Edmonds, R. P. Campion, B. L. Gallagher, C. Timm, and M. Helm. Precise tuning of the Curie temperature of (Ga,Mn)As-based magnetic semiconductors by hole compensation: Support for valence-band ferromagnetism. *Phys. Rev. B*, 94(7):075205, 2016. 67, 68, 78, 79, 80, 96
- [147] T. E. Winkler, P. R. Stone, T. Li, K. M. Yu, A. Bonanni, and O. D. Dubon. Compensation-dependence of magnetic and electrical properties in  $\text{Ga}_{1-x}\text{Mn}_x\text{P}$ . *Appl. Phys. Lett.*, 98(1):012103, 2011. 67, 80, 101
- [148] S. T. B. Goennenwein, T. A. Wassner, H. Huebl, M. S. Brandt, J. B. Philipp, M. Opel, R. Gross, A. Koeder, W. Schoch, and A. Waag. Hydrogen control of ferromagnetism in a dilute magnetic semiconductor. *Physical Review Letters*, 92(22):227202, 2004. 67
- [149] L. Thevenard, L. Largeau, O. Mauguin, A. Lemaître, K. Khazen, and H. J. von Bardeleben. Evolution of the magnetic anisotropy with carrier density in hydrogenated  $\text{Ga}_{1-x}\text{Mn}_x\text{As}$ . *Physical Review B*, 75(19):195218, 2007. 67
- [150] H. Ohno, D. Chiba, F. Matsukura, T. Omiya, E. Abe, T. Dietl, Y. Ohno, and K. Ohtani. Electric-field control of ferromagnetism. *Nature*, 408(6815):944–946, 2000. 67
- [151] J. Ziegler, J. Biersack, and U. Littmark. *The Stopping and Range of Ions in Solids*. Pergamon Press, New York, 1985. 67, 80
- [152] M. A. Scarpulla, O. D. Dubon, K. M. Yu, O. Monteiro, M. R. Pillai, M. J. Aziz, and M. C. Ridgway. Ferromagnetic  $\text{Ga}_{1-x}\text{Mn}_x\text{As}$  produced by ion implantation and pulsed-laser melting. *Applied Physics Letters*, 82(8):1251–1253, 2003. 68
- [153] S. Zhou. Dilute ferromagnetic semiconductors prepared by the combination of ion implantation with pulse laser melting. *Journal of Physics D: Applied Physics*, 48(26):263001, 2015. 68, 69, 78, 80, 81
- [154] Y. Yuan, C. Xu, R. Hübner, R. Jakiela, R. Böttger, M. Helm, M. Sawicki, T. Dietl, and S. Zhou. Interplay between localization and magnetism in (Ga,Mn)As and (In,Mn)As. *Physical Review Materials*, 1(5):054401, 2017. 68, 73, 78, 80, 81, 100, 103, 110



- 
- [155] P. J. Wellmann, J. M. Garcia, J.-L. Feng, and P. M. Petroff. Formation of nanoscale ferromagnetic MnAs crystallites in low-temperature grown GaAs. *Applied Physics Letters*, 71(17):2532–2534, 1997. 68
- [156] J. Shi, J. M. Kikkawa, R. Proksch, T. Schäffer, D. D. Awschalom, G. Medeiros-Ribeiro, and P. M. Petroff. Assembly of submicrometre ferromagnets in gallium arsenide semiconductors. *Nature*, 377(6551):707–710, 1995. 68
- [157] M. Khalid, S. Prucnal, M. O. Liedke, K. Gao, S. Facsko, W. Skorupa, M. Helm, and S. Zhou. Synthesis and characterization of MnAs and MnP nanoclusters embedded in III–V semiconductors. *Materials Research Express*, 1(2):026105, 2014. 68
- [158] Y. J. Cho, M. A. Scarpulla, Y. Y. Zhou, Z. Ge, X. Liu, M. Dobrowolska, K. M. Yu, O. D. Dubon, and J. K. Furdyna. Magnetic anisotropy of ferromagnetic  $\text{Ga}_{1-x}\text{Mn}_x\text{As}$  formed by Mn ion implantation and pulsed-laser melting. *Journal of Applied Physics*, 104(4):043902, 2008. 69
- [159] J. Sadowski and J. Z. Domagala. Influence of defects on the lattice constant of GaMnAs. *Physical Review B*, 69(7), 2004. 69
- [160] L. X. Zhao, C. R. Staddon, K. Y. Wang, K. W. Edmonds, R. P. Campion, B. L. Gallagher, and C. T. Foxon. Intrinsic and extrinsic contributions to the lattice parameter of GaMnAs. *Applied Physics Letters*, 86(7):071902, 2005. 69
- [161] T. Dietl, H. Ohno, F. Matsukura, J. Cibert, and D. Ferrand. Zener Model Description of Ferromagnetism in Zinc-Blende Magnetic Semiconductors. *Science*, 287(5455):1019–1022, 2000. 70, 71, 72, 75
- [162] H. Ohno and T. Dietl. Spin-transfer physics and the model of ferromagnetism in (Ga,Mn)As. *Journal of Magnetism and Magnetic Materials*, 320(7):1293–1299, 2008. 70, 72, 110
- [163] C. Zener. Interaction Between the d Shells in the Transition Metals. *Phys. Rev.*, 81(3):440–444, 1951. 70, 71
- [164] M. A. Ruderman and C. Kittel. Indirect exchange coupling of nuclear magnetic moments by conduction electrons. *Phys. Rev.*, 96(1):99–102, 1954. 70
- [165] T. Kasuya. A Theory of Metallic Ferro- and Antiferromagnetism on Zeners Model. *Progress of Theoretical Physics*, 16(1):45–57, 1956. 70
- [166] K. Yosida. Magnetic Properties of Cu-Mn Alloys. *Physical Review*, 106(5):893–898, 1957. 70

- [167] S. Blundell and D. Thouless. Magnetism in condensed matter. *Am. J. Phys.*, 71(1):94, 2003. 70
- [168] T. Dietl, H. Ohno, and F. Matsukura. Hole-mediated ferromagnetism in tetrahedrally coordinated semiconductors. *Phys. Rev. B*, 63(19):195205, 2001. 70, 71, 72
- [169] T. Dietl, J. Cibert, P. Kossacki, D. Ferrand, S. Tatarenko, A. Wasiela, Y. Merle d'aubigne, F. Matsukura, N. Akiba, and H. Ohno. Ferromagnetism induced by free carriers in p-type structures of diluted magnetic semiconductors. *Physica E: Low-dimensional Systems and Nanostructures*, 7(3-4):967–975, 2000. 71
- [170] M. Abolfath, T. Jungwirth, J. Brum, and A. H. MacDonald. Theory of magnetic anisotropy in  $\text{III}_{1-x}\text{Mn}_x\text{V}$  ferromagnets. *Physical Review B*, 63(5), 2001. 71
- [171] T. Dietl. Ferromagnetic semiconductors. *Semiconductor Science and Technology*, 17(4):377, 2002. 71
- [172] K. Y. Wang. Influence of the Mn interstitial on the magnetic and transport properties of (Ga,Mn)As. *J. Appl. Phys.*, 95(11):6512, 2004. 72
- [173] M. Dobrowolska, K. Tivakornsasithorn, X. Liu, J. K. Furdyna, M. Berciu, K. M. Yu, and W. Walukiewicz. Controlling the Curie temperature in (Ga,Mn)As through location of the Fermi level within the impurity band. *Nature Materials*, 11(5):444–449, 2012. 72, 73
- [174] F. Matsukura, H. Ohno, A. Shen, and Y. Sugawara. Transport properties and origin of ferromagnetism in (Ga,Mn)As. *Phys. Rev. B*, 57(4):R2037–R2040, 1998. 72, 76, 77, 84, 85
- [175] T. Jungwirth, J. Sinova, A. H. MacDonald, B. L. Gallagher, V. Novák, K. W. Edmonds, A. W. Rushforth, R. P. Campion, C. T. Foxon, L. Eaves, E. Olejník, J. Mašek, S.-R. Eric Yang, J. Wunderlich, C. Gould, L. W. Molenkamp, T. Dietl, and H. Ohno. Character of states near the Fermi level in (Ga,Mn)As: Impurity to valence band crossover. *Phys. Rev. B*, 76(12):125206, 2007. 72, 73, 74, 110
- [176] C. Timm. Disorder effects in diluted magnetic semiconductors. *Journal of Physics: Condensed Matter*, 15(50):R1865, 2003. 72, 75, 76
- [177] J.-M. Tang and M. Flatté. Multiband Tight-Binding Model of Local Magnetism in  $\text{Ga}_{1-x}\text{Mn}_x\text{As}$ . *Physical Review Letters*, 92(4), 2004. 73
- [178] P. Mahadevan and A. Zunger. Trends in ferromagnetism, hole localization, and acceptor level depth for Mn substitution in GaN, GaP, GaAs, and GaSb. *Applied Physics Letters*, 85(14):2860–2862, 2004. 73

- 
- [179] S. C. Erwin and A. G. Petukhov. Self-Compensation in Manganese-Doped Ferromagnetic Semiconductors. *Physical Review Letters*, 89(22), 2002. 73
- [180] Y. J. Cho, K. M. Yu, X. Liu, W. Walukiewicz, and J. K. Furdyna. Effects of donor doping on  $\text{Ga}_{1-x}\text{Mn}_x\text{As}$ . *Applied Physics Letters*, 93(26):262505, 2008. 73
- [181] K. S. Burch, D. B. Shrekenhamer, E. J. Singley, J. Stephens, B. L. Sheu, R. K. Kawakami, P. Schiffer, N. Samarth, D. D. Awschalom, and D. N. Basov. Impurity band conduction in a high temperature ferromagnetic semiconductor. *Physical Review Letters*, 97(8), 2006. 73
- [182] A. Oiwa, S. Katsumoto, A. Endo, M. Hirasawa, Y. Iye, H. Ohno, F. Matsukura, A. Shen, and Y. Sugawara. Nonmetal-metal-nonmetal transition and large negative magnetoresistance in  $(\text{Ga,Mn})\text{As}/\text{GaAs}$ . *Solid State Communications*, 103(4):209–213, 1997. 73
- [183] S. Kumar, W. Paschoal, A. Johannes, D. Jacobsson, C. Borschel, A. Pertsova, C.-H. Wang, M.-K. Wu, C. M. Canali, C. Ronning, L. Samuelson, and H. Pettersson. Magnetic Polarons and Large Negative Magnetoresistance in GaAs Nanowires Implanted with Mn Ions. *Nano Letters*, 13(11):5079–5084, 2013. 74, 105
- [184] P. A. Wolff, R. N. Bhatt, and A. C. Durst. Polaron-polaron interactions in diluted magnetic semiconductors. *Journal of Applied Physics*, 79(8):5196, 1996. 74
- [185] Y. D. Park. A Group-IV Ferromagnetic Semiconductor:  $\text{Mn}_x\text{Ge}_{1-x}$ . *Science*, 295(5555):651–654, 2002. 74, 156
- [186] X. Chen, M. Na, M. Cheon, S. Wang, H. Luo, B. D. McCombe, X. Liu, Y. Sasaki, T. Wojtowicz, J. K. Furdyna, S. J. Potashnik, and P. Schiffer. Above-room-temperature ferromagnetism in GaSb/Mn digital alloys. *Applied Physics Letters*, 81(3):511–513, 2002. 74
- [187] N. F. Mott and R. Peierls. Discussion of the paper by de Boer and Verwey. *Proceedings of the Physical Society*, 49(4S):72, 1937. 75
- [188] N. F. Mott. *Metal-Insulator Transitions*. Taylor and Francis, London/Philadelphia, 1990. 75
- [189] C. Timm, F. Schäfer, and F. von Oppen. Correlated defects, metal-insulator transition, and magnetic order in ferromagnetic semiconductors. *Physical Review Letters*, 89(13), 2002. 75
- [190] S.-R. Eric Yang and A. H. MacDonald. Disorder and ferromagnetism in diluted magnetic semiconductors. *Physical Review B*, 67(15), 2003. 75
-

- [191] P. W. Anderson. Absence of diffusion in certain random lattices. *Physical Review*, 109(5):1492–1505, 1958. 76
- [192] H. v. Löhneysen. Metal-insulator transition in heavily doped semiconductors. *Current Opinion in Solid State and Materials Science*, 3(1):5–15, 1998. 76
- [193] A. Richardella, P. Roushan, S. Mack, B. Zhou, D. A. Huse, D. D. Awschalom, and A. Yazdani. Visualizing Critical Correlations Near the Metal-Insulator Transition in  $\text{Ga}_{1-x}\text{Mn}_x\text{As}$ . *Science*, 327(5966):665–669, 2010. 76
- [194] A. Richardella. Character of the electronic states near the metal-insulator transition in gallium manganese arsenide. PhD Thesis, University of Illinois at Urbana-Champaign, 2009. 76
- [195] L. Bergqvist, O. Eriksson, J. Kudrnovský, V. Drchal, P. Korzhavyi, and I. Turek. Magnetic percolation in diluted magnetic semiconductors. *Physical Review Letters*, 93(13), 2004. 76
- [196] C. P. Moca, B. L. Sheu, N. Samarth, P. Schiffer, B. Janko, and G. Zarand. Scaling Theory of Magnetoresistance and Carrier Localization in  $\text{Ga}_{1-x}\text{Mn}_x\text{As}$ . *Physical Review Letters*, 102(13), 2009. 76
- [197] M. E. Fisher and J. S. Langer. Resistive anomalies at magnetic critical points. *Phys. Rev. Lett.*, 20(13):665–668, 1968. 76
- [198] M. Wang, R. A. Marshall, K. W. Edmonds, A. W. Rushforth, R. P. Campion, and B. L. Gallagher. Three-dimensional Heisenberg critical behavior in the highly disordered dilute ferromagnetic semiconductor  $(\text{Ga,Mn})\text{As}$ . *Physical Review B*, 93(18), 2016. 76
- [199] Y. Iye, A. Oiwa, A. Endo, S. Katsumoto, F. Matsukura, A. Shen, H. Ohno, and H. Munekata. Metal-insulator transition and magnetotransport in III-V compound diluted magnetic semiconductors. *Materials Science and Engineering: B*, 63(1-2):88–95, 1999. 77
- [200] K. W. Edmonds, R. P. Campion, K. Y. Wang, A. C. Neumann, B. L. Gallagher, C. T. Foxon, and P. C. Main. Magnetoresistance and Hall effect in the ferromagnetic semiconductor  $\text{Ga}_{1-x}\text{Mn}_x\text{As}$ . *J. Appl. Phys.*, 93(10):6787, 2003. 77
- [201] J. Smit. The spontaneous Hall effect in ferromagnetics I. *Physica*, 21(6-10):877–887, 1955. 77
- [202] J. Smit. The spontaneous Hall effect in ferromagnetics II. *Physica*, 24(1-5):39–51, 1958. 77

- 
- [203] L. Berger. Side-Jump Mechanism for the Hall Effect of Ferromagnets. *Phys. Rev. B*, 2(11):4559–4566, 1970. 77
- [204] M. Berry. The geometric phase. *Scientific American*, 26, 1988. 77
- [205] T. Jungwirth, Q. Niu, and A. H. MacDonald. Anomalous Hall Effect in Ferromagnetic Semiconductors. *Phys. Rev. Lett.*, 88(20), 2002. 77
- [206] T. Jungwirth, J. Sinova, J. Mašek, J. Kučera, and A. H. MacDonald. Theory of ferromagnetic (III,Mn)V semiconductors. *Reviews of Modern Physics*, 78(3):809–864, 2006. 78
- [207] B Clerjaud. Transition-metal impurities in III-V compounds. *Journal of Physics C: Solid State Physics*, 18(19):3615, 1985. 78
- [208] M. A. Scarpulla, B. L. Cardozo, R. Farshchi, W. M. Hlaing Oo, M. D. McCluskey, K. M. Yu, and O. D. Dubon. Ferromagnetism in  $\text{Ga}_{1-x}\text{Mn}_x\text{P}$ : Evidence for Inter-Mn Exchange Mediated by Localized Holes within a Detached Impurity Band. *Phys. Rev. Lett.*, 95(20):207204, 2005. 78, 101, 103, 160
- [209] N. Theodoropoulou, A. F. Hebard, M. E. Overberg, C. R. Abernathy, S. J. Pearton, S. N. G. Chu, and R. G. Wilson. Unconventional Carrier-Mediated Ferromagnetism above Room Temperature in Ion-Implanted (Ga,Mn)P:C. *Physical Review Letters*, 89(10):107203, 2002. 78
- [210] A. Ben Hamida, S. Sievers, F. Bergmann, A. Racu, M. Bieler, K. Pierz, and H. W. Schumacher. Magnetotransport and magnetization dynamics of GaMnAs thin films and magnetic tunnel junctions. *Phys. Status Solidi B*, 251(9):1652–1662, 2014. 78
- [211] Y. Yuan, R. Hübner, F. Liu, M. Sawicki, O. Gordan, G. Salvan, D. R. T. Zahn, D. Banerjee, C. Baehtz, M. Helm, and S. Zhou. Ferromagnetic Mn-Implanted GaP: Microstructures vs Magnetic Properties. *ACS Applied Materials & Interfaces*, 8(6):3912–3918, 2016. 78, 81
- [212] M. Wang, R. P. Campion, A. W. Rushforth, K. W. Edmonds, C. T. Foxon, and B. L. Gallagher. Achieving high Curie temperature in (Ga,Mn)As. *Applied Physics Letters*, 93(13):132103, 2008. 79, 81
- [213] D. Pons and J. C. Bourgoin. Irradiation-induced defects in GaAs. *Journal of Physics C: Solid State Physics*, 18(20):3839, 1985. 80
- [214] Y. J. Cho, M. A. Scarpulla, X. Liu, Y. Y. Zhou, O. D. Dubon, and J. K. Furdyna. Magnetic cluster phases of Mn-interstitial-free (Ga,Mn)As. In *AIP Conference Proceedings*. AIP, 2007. 81

- [215] J. Teschabai-Oglu. Charakterisierung elektronischer Transporteigenschaften dünner  $\text{Ga}_{1-x}\text{Mn}_x\text{As}$ -Filme. Master's Thesis, Goethe-Universität Frankfurt, 2016. 82, 83, 86, 88, 89, 93, 97
- [216] E. Kamińska, A. Piotrowska, A. Kamińska, and M. Klimkiewicz. Etching procedures for GaP surfaces. *Surface Technology*, 12(2):205–215, 1981. 83
- [217] A. R. Clawson. Guide to references on III–V semiconductor chemical etching. *Materials Science and Engineering: R: Reports*, 31(1–6):1 – 438, 2001. 83
- [218] H. T. He, C. L. Yang, W. K. Ge, J. N. Wang, X. Dai, and Y. Q. Wang. Resistivity minima and Kondo effect in ferromagnetic GaMnAs films. *Appl. Phys. Lett.*, 87(16):162506, 2005. 84
- [219] K. W. Edmonds, K. Y. Wang, R. P. Campion, A. C. Neumann, C. T. Foxon, B. L. Gallagher, and P. C. Main. Hall effect and hole densities in  $\text{Ga}_{1-x}\text{Mn}_x\text{As}$ . *Appl. Phys. Lett.*, 81(16):3010, 2002. 88
- [220] M. Zhu, X. Li, G. Xiang, and N. Samarth. Random telegraph noise from magnetic nanoclusters in the ferromagnetic semiconductor (Ga,Mn)As. *Phys. Rev. B*, 76(20):201201, 2007. 89, 91, 93, 98
- [221] D. M. Fleetwood. *1/f Noise and Defects in Microelectronic Materials and Devices*. *IEEE Transactions on Nuclear Science*, 62(4):1462–1486, 2015. 90
- [222] G. B. Bachelet, M. Schlüter, and G. A. Baraff.  $\text{As}_{\text{Ga}}$  antisite defect in GaAs. *Phys. Rev. B*, 27(4):2545–2547, 1983. 92
- [223] D. J. Chadi and K. J. Chang. Metastability of the isolated arsenic-antisite defect in GaAs. *Phys. Rev. Lett.*, 60(21):2187–2190, 1988. 92
- [224] N. F. Mott. Conduction in non-crystalline materials. *Philosophical Magazine*, 19(160):835–852, 1969. 97
- [225] J. Kondo. Resistance Minimum in Dilute Magnetic Alloys. *Progress of Theoretical Physics*, 32(1):37–49, 1964. 97, 135, 138
- [226] B. I. Shklovskii.  $1/f$  noise in variable range hopping conduction. *Physical Review B*, 67(4), 2003. 97
- [227] M. A. Scarpulla, P. R. Stone, I. D. Sharp, E. E. Haller, O. D. Dubon, J. W. Beeman, and K. M. Yu. Nonmagnetic compensation in ferromagnetic  $\text{Ga}_{1-x}\text{Mn}_x\text{As}$  and  $\text{Ga}_{1-x}\text{Mn}_x\text{P}$  synthesized by ion implantation and pulsed-laser melting. *Journal of Applied Physics*, 103(12):123906, 2008. 101

- 
- [228] Y. Yagil and G. Deutscher. Third-harmonic generation in semicontinuous metal films. *Phys. Rev. B*, 46(24):16115–16121, 1992. 106
- [229] C. Barone, S. Pagano, I. Pallecchi, E. Bellingeri, M. Putti, and C. Ferdeghini. Thermal and voltage activated excess  $1/f$  noise in  $\text{FeTe}_{0.5}\text{Se}_{0.5}$  epitaxial thin films. *Physical Review B*, 83(13), 2011. 109
- [230] T. Dietl. Origin of ferromagnetism and nano-scale phase separations in diluted magnetic semiconductors. *Physica E: Low-dimensional Systems and Nanostructures*, 35(2):293–299, 2006. 110
- [231] V. G. Storchak, D. G. Eshchenko, E. Morenzoni, T. Prokscha, A. Suter, X. Liu, and J. K. Furdyna. Spatially Resolved Inhomogeneous Ferromagnetism in  $(\text{Ga},\text{Mn})\text{As}$  Diluted Magnetic Semiconductors: A Microscopic Study by Muon Spin Relaxation. *Physical Review Letters*, 101(2), 2008. 110
- [232] S. Bae and H. Raebiger. Critical metal-insulator transition due to nuclear quantum effects in Mn-doped GaAs. *Phys. Rev. B*, 94(24):241115, 2016. 110
- [233] S. U. Sharath, S. Vogel, L. Molina-Luna, E. Hildebrandt, C. Wenger, J. Kurian, M. Duerrschabel, T. Niermann, G. Niu, P. Calka, M. Lehmann, H.-J. Kleebe, T. Schroeder, and L. Alff. Control of Switching Modes and Conductance Quantization in Oxygen Engineered  $\text{HfO}_x$  based Memristive Devices. *Advanced Functional Materials*, 27(32):1700432, 2017. 113, 114, 115, 128, 131, 161
- [234] E. Lim and R. Ismail. Conduction mechanism of valence change resistive switching memory: A survey. *Electronics*, 4(3):586–613, 2015. 114, 131, 162
- [235] S. U. Sharath, T. Bertaud, J. Kurian, E. Hildebrandt, C. Walczyk, P. Calka, P. Zaumseil, M. Sowinska, D. Walczyk, A. Gloskovskii, T. Schroeder, and L. Alff. Towards forming-free resistive switching in oxygen engineered  $\text{HfO}_{2-x}$ . *Applied Physics Letters*, 104(6):063502, 2014. 114
- [236] C.-K. Lee, E. Cho, H.-S. Lee, C. S. Hwang, and S. Han. First-principles study on doping and phase stability of  $\text{HfO}_2$ . *Physical Review B*, 78(1), 2008. 114
- [237] A. Buckow, R. Retzlaff, J. Kurian, and L. Alff. Growth of superconducting epitaxial  $\text{LaNi}_x\text{Bi}_2$  pnictide thin films with a Bi square net layer by reactive molecular beam epitaxy. *Superconductor Science and Technology*, 26(1):015014, 2012. 115
- [238] Y. Li, S. Long, Y. Liu, C. Hu, J. Teng, Q. Liu, H. Lv, J. Suñé, and M. Liu. Conductance Quantization in Resistive Random Access Memory. *Nanoscale Research Letters*, 10(1), 2015. 116

- [239] F. M. Puglisi, L. Larcher, A. Padovani, and P. Pavan. Anomalous random telegraph noise and temporary phenomena in resistive random access memory. *Solid-State Electronics*, 125:204–213, 2016. 116, 124, 125, 157, 162
- [240] M. Nardone, V. I. Kozub, I. V. Karpov, and V. G. Karpov. Possible mechanisms for  $1/f$  noise in chalcogenide glasses: A theoretical description. *Physical Review B*, 79(16), 2009. 116
- [241] S. B. Lee, S. Park, J. S. Lee, S. C. Chae, S. H. Chang, M. H. Jung, Y. Jo, B. Kahng, B. S. Kang, M.-J. Lee, and T. W. Noh. Large  $1/f$  noise of unipolar resistance switching and its percolating nature. *Applied Physics Letters*, 95(12):122112, 2009. 116, 119
- [242] Y. Song, H. Jeong, J. Jang, T.-Y. Kim, D. Yoo, Y. Kim, H. Jeong, and T. Lee.  $1/f$  noise scaling analysis in unipolar-type organic nanocomposite resistive memory. *ACS Nano*, 9(7):7697–7703, 2015. 116, 119
- [243] D. Basak and S. K. Sen. Electrical conduction in aluminium/yttrium oxide/aluminium sandwich structure. *Physica Status Solidi a*, 142(1):K37–K40, 1994. 116, 129
- [244] D. Basak and S.K. Sen. Electrical, dielectric and optical properties of  $M/Y_2O_3/M$  devices. *Thin Solid Films*, 254(1-2):181–186, 1995. 116, 129, 131, 162
- [245] T.-M. Pan, K.-M. Chen, and C.-H. Lu. Resistive Switching Behavior in the  $Ru/Y_2O_3/TaN$  Nonvolatile Memory Device. *Electrochemical and Solid-State Letters*, 14(1):H27, 2011. 116, 129, 131, 162
- [246] S. Kuriki, A. Noya, and G. Matsumoto. Electroforming and conduction in thin anodized  $Y_2O_3$  films. *Thin Solid Films*, 48(1):27–41, 1978. 116, 129
- [247] F. M. Puglisi and P. Pavan. Guidelines for a reliable analysis of random telegraph noise in electronic devices. *IEEE Transactions on Instrumentation and Measurement*, 65(6):1435–1442, 2016. 116
- [248] F. M. Puglisi, L. Larcher, A. Padovani, and P. Pavan. Characterization of anomalous random telegraph noise in resistive random access memory. In *2015 45th European Solid State Device Research Conference (ESSDERC)*. IEEE, 2015. 116
- [249] F. M. Puglisi, L. Larcher, G. Bersuker, A. Padovani, and P. Pavan. An empirical model for RRAM resistance in low- and high-resistance states. *IEEE Electron Device Letters*, 34(3):387–389, 2013. 116, 127
- [250] F. M. Puglisi and P. Pavan. RTN analysis with FHMM as a tool for multi-trap characterization in  $HfO_x$  RRAM. In *2013 IEEE International Conference of Electron Devices and Solid-state Circuits*. IEEE, 2013. 116



- 
- [251] M. Reznikov, M. Heiblum, H. Shtrikman, and D. Mahalu. Temporal correlation of electrons: Suppression of shot noise in a ballistic quantum point contact. *Physical Review Letters*, 75(18):3340–3343, 1995. 119
- [252] F. Verbakel, S. C. J. Meskers, and R. A. J. Janssen. Electronic memory effects in diodes of zinc oxide nanoparticles in a matrix of polystyrene or poly(3-hexylthiophene). *Journal of Applied Physics*, 102(8):083701, 2007. 119
- [253] D. R. Islamov, V. A. Gritsenko, C. H. Cheng, and A. Chin. Percolation conductivity in hafnium sub-oxides. *Applied Physics Letters*, 105(26):262903, 2014. 119
- [254] B. I. Shklovskii and A. L. Éfros. Percolation theory and conductivity of strongly inhomogeneous media. *Soviet Physics Uspekhi*, 18(11):845–862, 1975. 119
- [255] A. S. Foster, A. L. Shluger, and R. M. Nieminen. Mechanism of interstitial oxygen diffusion in hafnia. *Physical Review Letters*, 89(22), 2002. 125
- [256] T. Nagumo, K. Takeuchi, S. Yokogawa, K. Imai, and Y. Hayashi. New analysis methods for comprehensive understanding of random telegraph noise. In *2009 IEEE International Electron Devices Meeting (IEDM)*. IEEE, 2009. 125
- [257] Y. Song, H. Jeong, S. Chung, G. H. Ahn, T.-Y. Kim, J. Jang, D. Yoo, H. Jeong, A. Javey, and T. Lee. Origin of multi-level switching and telegraphic noise in organic nanocomposite memory devices. *Scientific Reports*, 6(1), 2016. 125
- [258] F. M. Puglisi, P. Pavan, A. Padovani, L. Larcher, and G. Bersuker. Random telegraph signal noise properties of HfO<sub>x</sub> RRAM in high resistive state. In *2012 Proceedings of the European Solid-State Device Research Conference (ESSDERC)*. IEEE, 2012. 125, 129
- [259] N. Mahmud, A. J. Narasimham, and J. R. Lloyd. 1/f noise analysis of hafnium oxide based ReRAM devices using ac + dc measurement technique. In *2016 IEEE International Integrated Reliability Workshop (IIRW)*. IEEE, 2016. 127
- [260] D. Veksler, G. Bersuker, L. Vandelli, A. Padovani, L. Larcher, A. Muraviev, B. Chakrabarti, E. Vogel, D. C. Gilmer, and P. D. Kirsch. Random telegraph noise (RTN) in scaled RRAM devices. In *2013 IEEE International Reliability Physics Symposium (IRPS)*. IEEE, 2013. 129
- [261] F.-C. Chiu. A Review on Conduction Mechanisms in Dielectric Films. *Advances in Materials Science and Engineering*, 2014:1–18, 2014. 131
- [262] V. Maccaronio, F. Crupi, L.M. Procel, L. Goux, E. Simoen, L. Trojman, and E. Miranda. DC and low-frequency noise behavior of the conductive filament in bipolar HfO<sub>2</sub>-based resistive random access memory. *Microelectronic Engineering*, 107:1–5, 2013. 132

- [263] P. A. Lee, N. Nagaosa, and X.-G. Wen. Doping a Mott insulator: Physics of high-temperature superconductivity. *Reviews of Modern Physics*, 78(1):17–85, 2006. 135
- [264] T. Kimura, T. Goto, H. Shintani, K. Ishizaka, T. Arima, and Y. Tokura. Magnetic control of ferroelectric polarization. *Nature*, 426(6962):55–58, 2003. 135
- [265] M. Imada, A. Fujimori, and Y. Tokura. Metal-insulator transitions. *Reviews of Modern Physics*, 70(4):1039–1263, 1998. 135
- [266] L. Balents. Spin liquids in frustrated magnets. *Nature*, 464(7286):199–208, 2010. 135
- [267] F. Steglich, J. Aarts, C. D. Bredl, W. Lieke, D. Meschede, W. Franz, and H. Schäfer. Superconductivity in the Presence of Strong Pauli Paramagnetism:  $\text{CeCu}_2\text{Si}_2$ . *Physical Review Letters*, 43(25):1892–1896, 1979. 135, 143
- [268] P. Coleman. Heavy fermions: electrons at the edge of magnetism. *Handbook of Magnetism and Advanced Magnetic Materials*, 2006. 135
- [269] L. Landau. The Theory of a Fermi Liquid. *Sov. Phys. JETP*, 6:920–925, 1957. 135
- [270] O. Trovarelli, C. Geibel, S. Mederle, C. Langhammer, F. M. Grosche, P. Gegenwart, M. Lang, G. Sparn, and F. Steglich.  $\text{YbRh}_2\text{Si}_2$ : Pronounced Non-Fermi-Liquid Effects above a Low-Lying Magnetic Phase Transition. *Physical Review Letters*, 85(3):626–629, 2000. 136, 137, 144, 163
- [271] S. Friedemann. Elektrischer Transport und Quantenkritikalität in reinem und substituiertem  $\text{YbRh}_2\text{Si}_2$ . PhD Thesis, Technische Universität Dresden, 2009. 136, 148
- [272] J. Custers, P. Gegenwart, H. Wilhelm, K. Neumaier, Y. Tokiwa, O. Trovarelli, C. Geibel, F. Steglich, C. Pépin, and P. Coleman. The break-up of heavy electrons at a quantum critical point. *Nature*, 424(6948):524–527, 2003. 136, 163
- [273] P. Gegenwart, Q. Si, and F. Steglich. Quantum criticality in heavy-fermion metals. *Nature Physics*, 4(3):186–197, 2008. 137, 140, 141
- [274] P. Gegenwart, J. Custers, C. Geibel, K. Neumaier, T. Tayama, K. Tenya, O. Trovarelli, and F. Steglich. Magnetic-Field Induced Quantum Critical Point in  $\text{YbRh}_2\text{Si}_2$ . *Physical Review Letters*, 89(5), 2002. 137
- [275] A. J. Millis. Effect of a nonzero temperature on quantum critical points in itinerant fermion systems. *Physical Review B*, 48(10):7183–7196, 1993. 137, 141
- [276] U. Köhler, N. Oeschler, F. Steglich, S. Maquilon, and Z. Fisk. Energy scales of  $\text{Lu}_{1-x}\text{Yb}_x\text{Rh}_2\text{Si}_2$  by means of thermopower investigations. *Physical Review B*, 77(10), 2008. 137, 138

- 
- [277] O. Stockert, M.M. Koza, J. Ferstl, A.P. Murani, C. Geibel, and F. Steglich. Crystalline electric field excitations of the non-Fermi-liquid. *Physica B: Condensed Matter*, 378-380:157–158, 2006. 137
- [278] C. Krellner. Ferromagnetische Korrelationen in Kondo-Gittern: YbT<sub>2</sub>Si<sub>2</sub> und CeTPO (T=Übergangsmetall). PhD Thesis, Technische Universität Dresden, 2009. 138
- [279] J. Ferstl. New Yb-based systems: From an intermediate-valent to a magnetically ordered state. PhD Thesis, Technische Universität Dresden, 2007. 138
- [280] Y. Lassailly, A. K. Bhattacharjee, and B. Coqblin. Low-temperature resistivity and magnetoresistivity of cerium compounds. *Physical Review B*, 31(11):7424–7429, 1985. 139
- [281] K. Kummer, S. Patil, A. Chikina, M. Güttler, M. Höppner, A. Generalov, S. Danzenbächer, S. Seiro, A. Hannaske, C. Krellner, Y. Kucherenko, M. Shi, M. Radovic, E. Rienks, G. Zwicknagl, K. Matho, J.W. Allen, C. Laubschat, C. Geibel, and D.V. Vyalikh. Temperature-Independent Fermi Surface in the Kondo Lattice YbRh<sub>2</sub>Si<sub>2</sub>. *Physical Review X*, 5(1), 2015. 139, 140, 141
- [282] S. Doniach. The Kondo lattice and weak antiferromagnetism. *Physica B+C*, 91:231–234, 1977. 139, 140
- [283] J. W. Allen, S. J. Oh, M. B. Maple, and M. S. Torikachvili. Large Fermi-level resonance in the electron-addition spectrum of CeRu<sub>2</sub> and CeIr<sub>2</sub>. *Physical Review B*, 28(9):5347–5349, 1983. 140
- [284] K. Andres, J. E. Graebner, and H. R. Ott. 4f-Virtual-Bound-State Formation in CeAl<sub>3</sub> at Low Temperatures. *Physical Review Letters*, 35(26):1779–1782, 1975. 140
- [285] S. Ernst, S. Kirchner, C. Krellner, C. Geibel, G. Zwicknagl, F. Steglich, and S. Wirth. Emerging local Kondo screening and spatial coherence in the heavy-fermion metal YbRh<sub>2</sub>Si<sub>2</sub>. *Nature*, 474(7351):362–366, 2011. 140
- [286] F. Steglich, H. Pfau, S. Lausberg, S. Hamann, P. Sun, U. Stockert, M. Brando, S. Friedemann, C. Krellner, C. Geibel, S. Wirth, S. Kirchner, E. Abrahams, and Q. Si. Evidence of a Kondo Destroying Quantum Critical Point in YbRh<sub>2</sub>Si<sub>2</sub>. *Journal of the Physical Society of Japan*, 83(6):061001, 2014. 141
- [287] J. A. Hertz. Quantum critical phenomena. *Physical Review B*, 14(3):1165–1184, 1976. 141
- [288] S. Paschen, T. Lühmann, S. Wirth, P. Gegenwart, O. Trovarelli, C. Geibel, F. Steglich, P. Coleman, and Q. Si. Hall-effect evolution across a heavy-fermion quantum critical point. *Nature*, 432(7019):881–885, 2004. 141, 142

- [289] S. Friedemann, S. Wirth, N. Oeschler, C. Krellner, C. Geibel, F. Steglich, S. MaQuilon, Z. Fisk, S. Paschen, and G. Zwicknagl. Hall effect measurements and electronic structure calculations on  $\text{YbRh}_2\text{Si}_2$  and its reference compounds  $\text{LuRh}_2\text{Si}_2$  and  $\text{YbIr}_2\text{Si}_2$ . *Physical Review B*, 82(3), 2010. 141, 142, 143
- [290] G. A. Wigger, F. Baumberger, Z.-X. Shen, Z. P. Yin, W. E. Pickett, S. Maquilon, and Z. Fisk. Electronic band structure and Kondo coupling in  $\text{YbRh}_2\text{Si}_2$ . *Physical Review B*, 76(3), 2007. 141
- [291] S. Nair, S. Wirth, S. Friedemann, F. Steglich, Q. Si, and A. J. Schofield. Hall effect in heavy fermion metals. *Advances in Physics*, 61(5):583–664, 2012. 141, 142
- [292] A. Fert and P. M. Levy. Theory of the hall effect in heavy-fermion compounds. *Physical Review B*, 36(4):1907–1916, 1987. 142
- [293] K. Ishida, K. Okamoto, Y. Kawasaki, Y. Kitaoka, O. Trovarelli, C. Geibel, and F. Steglich.  $\text{YbRh}_2\text{Si}_2$ : Spin Fluctuations in the Vicinity of a Quantum Critical Point at Low Magnetic Field. *Physical Review Letters*, 89(10), 2002. 143
- [294] E. Schuberth, M. Tippmann, L. Steinke, S. Lausberg, A. Steppke, M. Brandt, C. Krellner, C. Geibel, R. Yu, Q. Si, and F. Steglich. Emergence of superconductivity in the canonical heavy-electron metal  $\text{YbRh}_2\text{Si}_2$ . *Science*, 351(6272):485–488, 2016. 143
- [295] T. Hagen. Electronic Transport of  $\text{SmB}_6$  Studied by Resistance Noise Spectroscopy. Bachelor's Thesis, 2017. Goethe University Frankfurt. 143, 155
- [296] S. Biswas, M. C. Hatnean, G. Balakrishnan, and A. Bid. Probing the interplay between surface and bulk states in the topological Kondo insulator  $\text{SmB}_6$  through conductance fluctuation spectroscopy. *Physical Review B*, 95(20), 2017. 143
- [297] P. C. Canfield and Z. Fisk. Growth of single crystals from metallic fluxes. *Philosophical Magazine Part B*, 65(6):1117–1123, 1992. 144
- [298] R. Sachser. Private communication, 2018. 145
- [299] R. A. Webb, R. P. Giffard, and J. C. Wheatley. Noise thermometry at ultralow temperatures. *Journal of Low Temperature Physics*, 13(3-4):383–429, 1973. 146
- [300] A. Steppke. Private communication, 2018. 146, 148
- [301] P. J. W. Moll, P. Kushwaha, N. Nandi, B. Schmidt, and A. P. Mackenzie. Evidence for hydrodynamic electron flow in  $\text{PdCoO}_2$ . *Science*, 351(6277):1061–1064, 2016. 146
- [302] S. Kambe, H. Sakai, Y. Tokunaga, G. Lapertot, T. D. Matsuda, G. Knebel, J. Flouquet, and R. E. Walstedt. Degenerate Fermi and non-Fermi liquids near a quantum critical phase transition. *Nature Physics*, 10(11):840–844, 2014. 153

# Acknowledgements

An erster Stelle gilt mein Dank meinem Doktorvater Prof. Dr. Jens Müller für seine wissenschaftliche und persönliche Unterstützung während der vergangenen Jahre. Ich habe es nie als selbstverständlich angesehen, dass seine Tür trotz vieler anderer Verpflichtungen stets offen stand und dass er immer ein offenes Ohr für die Sorgen und Nöte seiner Mitarbeiter hatte. Zudem stellte sein Enthusiasmus für die Festkörperphysik eine immerwährende Motivation für mich und für diese Arbeit dar. Es war und ist mir ein Vergnügen, aber auch eine große Ehre, ein Teil der "AG Müller" zu sein.

Weiterhin danke ich Prof. Dr. Cornelius Krellner für äußerst lehrreiche Diskussionen über  $\text{YbRh}_2\text{Si}_2$  sowie für das Interesse an meiner Arbeit und die freundliche Übernahme des Zweitgutachtens.

Mein außerordentlicher Dank gilt allen aktuellen und ehemaligen Mitgliedern der Arbeitsgruppe von Prof. Dr. Jens Müller. Bei Dr. Merlin Pohlitz und Dr. Benedikt Hartmann möchte ich mich für die zahlreichen physikalischen und nicht-physikalischen Diskussionen, für das vermittelte Wissen sowie einfach nur für eine schöne gemeinsame Zeit in den letzten Jahren bedanken. Außerdem danke ich Tatjana Thomas und Merlin Mitschek für die Unterstützung bei meiner Arbeit. Schließlich danke ich Jan Teschabai-Oglu und Sven Heinz, deren eigene Arbeiten stark zum Gelingen meiner Doktorarbeit beigetragen haben.

The present thesis work would not have been possible without all the fruitful collaborations on various research topics. In the following, I would like to express my gratitude to all collaborators. My sincere thanks goes to Dr. Shengqiang Zhou and Dr. Ye Yuan from HZDR for a very successful collaboration on magnetic semiconductors, for the provided samples and for their continuous support. Genauso möchte ich mich bei PD Dr. Hans Werner Schumacher sowie Dr. Klaus Pierz für die zur Verfügung gestellten Proben und eine sehr erfolgreiche Zusammenarbeit bedanken.

I am grateful to Prof. Dr. Sunil Nair and his group at IISER Pune, in particular to Charu Garg and Soumendhra Nath Panja, for the fruitful collaboration, for being exceptionally good hosts, and for contributing to the present thesis work. In this respect, I would like to cordially thank the DAAD and DST for the financial support and for making the exchange project possible. On this occasion, I would also like to thank Prof. Dr. Pintu Das, who was an excellent host in Delhi and provided valuable insight into the research at the IIT.

Furthermore, I would like to thank Prof. Dr. Lambert Alff and his entire group at the TU Darmstadt for the unique opportunity to work in the exciting field of RRAMs. My sincere thanks goes to Eszter Piros for the insightful collaboration, helpful discussions and for much patience during the noise measurements carried out in Darmstadt.

Mein Dank gilt Dr. Manuel Brando und Dr. Alexander Steppke vom MPI-CPfS für die zur Verfügung gestellte  $\text{YbRh}_2\text{Si}_2$  Probe sowie für sehr aufschlussreiche Diskussionen und eine hervorragende Zusammenarbeit.

Weiterhin bedanke ich mich bei Prof. Dr. Manfred Albrecht und Dr. Marcus Daniel für die sehr interessante Kollaboration an thermoelektrischem  $\text{CoSb}_3$ . Auch wenn dieses Thema leider keinen Platz mehr in dieser Arbeit gefunden hat, belegen die zwei gemeinsam publizierten Artikel den Erfolg dieser exzellenten Zusammenarbeit.

An dieser Stelle möchte ich mich bei Prof. Dr. Steffen Wirth und Thomas Hagen für die gemeinsame Arbeit an  $\text{SmB}_6$  sowie die damit verbundenen lehrreichen Diskussionen bedanken.

Allen Mitgliedern des Physikalischen Instituts an der Goethe-Universität Frankfurt danke ich für die direkte und indirekte Unterstützung bei meiner Arbeit. Ich danke Prof. Dr. Michael Huth, Prof. Dr. Cornelius Krellner, Roland Sachser und Sebastian Witt für die sehr gute Zusammenarbeit hinsichtlich der Strukturierung von MnSi Einkristallen. Ebenso danke ich Prof. Dr. Michael Lang und seiner Arbeitsgruppe für einen regen Austausch und hilfreiche Gespräche.

Insbesondere möchte ich mich bei den Herren Florian Hohmann und Knut Pfeiffer von der mechanischen Werkstatt sowie Andreas Holzmann und Bernd Gärtner von der Elektronik-Werkstatt für immer schnelle und kompetente Hilfe bedanken. Außerdem danke ich Herrn Siegfried Rapphahn für seinen unermüdlichen Einsatz und die zuverlässige Versorgung mit flüssigem Helium. Darüber hinaus danke ich Herrn Thomas Dübel für die Hilfe bei allen Fragen rund um Computer und Technik. Herrn Bernhard Klug danke ich für die Unterstützung bei der Arbeit im Reinraum des Instituts. Schließlich gilt mein Dank Frau Birgit Scherff für die kontinuierliche Unterstützung bei Dienstreisen und anderen administrativen Aspekten. Ganz besonders möchte ich an dieser Stelle auch meiner Familie und meinen Freunden für die unermüdliche Stärkung und Motivation danken.

# Curriculum Vitae

## Personal Details

Name	Martin Lonsky
Date of Birth	April 9th, 1989
Place of Birth	Hanau (Germany)
Nationality	German

## School and University Education

2013–2018	PhD work in the group of Prof. Dr. J. Müller, Goethe University Frankfurt
2011–2013	Master in Physics, Goethe University Frankfurt, Master's Thesis: <i>Hall-Magnetometrie an ferromagnetischen Mikro-Teilchen</i> . Supervisor: Prof. Dr. J. Müller
2008–2011	Bachelor in Physics, Goethe University Frankfurt, Bachelor's Thesis: <i>Aufbau eines Stereo-ATI-Spektrometers zur Messung der Carrier-Envelope-Phase ultrakurzer Laserpulse</i> . Supervisor: Prof. Dr. R. Dörner
1999–2008	Abitur, Albert-Einstein-Gymnasium, Maintal

## List of Publications

- *Investigation of a possible electronic phase separation in the magnetic semiconductors  $Ga_{1-x}Mn_xAs$  and  $Ga_{1-x}Mn_xP$  by means of fluctuation spectroscopy*  
M. Lonsky, J. Teschabai-Oglu, K. Pierz, S. Sievers, H. W. Schumacher, Y. Yuan, R. Böttger, S. Zhou, and J. Müller  
Physical Review B 97, 054413 (2018)

- *Charge Carrier Dynamics in  $Ga_{1-x}Mn_xAs$  Studied by Resistance Noise Spectroscopy*  
M. Lonsky, J. Teschabai-Oglu, K. Pierz, S. Sievers, H. W. Schumacher, Y. Yuan, R. Böttger, S. Zhou, and J. Müller  
accepted in Acta Physica Polonica A (2018)
- *Electronic transport in thermoelectric  $Yb_zCo_4Sb_{12}$  skutterudite thin films studied by resistance noise spectroscopy*  
M. Lonsky, S. Heinz, M. V. Daniel, M. Albrecht, and J. Müller  
Journal of Applied Physics 120, 142101 (2016)
- *Magnetization dynamics and frustration in the multiferroic double perovskite  $Lu_2MnCoO_6$*   
V. Zapf, B. G. Ueland, M. Laver, M. Lonsky, M. Pohlit, J. Müller, T. Lancaster, J. S. Möller, S. J. Blundell, J. Singleton, J. Mira, S. Yanez-Vilar, and M. A. Senaris-Rodriguez  
Physical Review B 93, 134431 (2016)
- *$1/f$ - and random telegraph noise of thermoelectric  $CoSb_3$  skutterudite thin films*  
M. Lonsky, S. Heinz, M. V. Daniel, M. Albrecht, and J. Müller  
IEEE International Conference on Noise and Fluctuations (2015)

## Conference Contributions and Invited Talks

- |      |  |
|------|--|
| 2017 | Frontiers in Materials Science Conference, Greifswald (Germany), invited talk;<br>Physics of Magnetism Conference, Poznan (Poland), contribution: talk;<br>DPG spring meeting, Dresden (Germany), contribution: poster |
| 2016 | Invited talk in the condensed matter physics seminar at Indian Institute of Technology Delhi (India);<br>DPG spring meeting, Regensburg (Germany), contribution: talk  |
| 2015 | International Conference on Noise and Fluctuations, Xi'an (China), contribution: talk;<br>DPG spring meeting, Berlin (Germany), contribution: poster   |
| 2014 | DPG spring meeting, Dresden (Germany), contribution: talk  |
| 2013 | DPG spring meeting, Regensburg (Germany), contribution: poster   |



---

## Research Visits

January 2018	Research stay in the group of Prof. Dr. L. Alff at Technical University Darmstadt, Germany (2 weeks)
August 2017	Research stay in the group of Prof. Dr. L. Alff at Technical University Darmstadt, Germany (1 week)
September/October 2016	Research stay in the group of Prof. Dr. S. Nair at Indian Institute of Science Education and Research (IISER) Pune, India (4 weeks)
November/December 2015	Research stay in the group of Prof. Dr. S. Nair at Indian Institute of Science Education and Research (IISER) Pune, India (4 weeks)

## Teaching Experience

2009–2018	Teaching assistant and tutor for > 10 undergraduate courses in solid state physics, computer science, and mathematics at Goethe University Frankfurt
2015–2017	Tutor for an experiment in the advanced lab course of the Institute of Physics at Goethe University Frankfurt
2013–2018	Co-guidance of 2 Master's and 2 Bachelor's theses in experimental solid state physics in the group of Prof. Dr. J. Müller at Goethe University Frankfurt